Modeling of isolated and coalescing neutron stars

Rahul Somasundaram

To cite this version:

Rahul Somasundaram. Modeling of isolated and coalescing neutron stars. Astrophysics [astro-ph]. Université de Lyon, 2022. English. NNT : 2022LYSE1135 . tel-04217464

HAL Id: tel-04217464
https://theses.hal.science/tel-04217464

Submitted on 25 Sep 2023

THÈSE de DOCTORAT DE L'UNIVERSITÉ DE LYON
Opérée au sein de :
l'Université Claude Bernard Lyon 1

Ecole Doctorale ED52
de Physique et Astrophysique

Spécialité de doctorat : Physique Théorique
Discipline : Astrophysique nucléaire

Soutenue publiquement le 04/07/2022, par :
Rahul Somasundaram

Modeling of Isolated and Coalescing Neutron Stars

Devant le jury composé de :

GASCON Jules, Professeur, Université Lyon 1	Président
BLASCHKE David, Professeur, University of Wroclaw	Rapporteur
GULMINELLI Francesca, Professeure, ENSICAEN	Rapporteur
BOMBACI Ignazio, Professeur, University of Pisa	Examinateur
PROVIDÊNCIA Constança, Professeure, University of Coimbra	Examinatrice

MARGUERON Jérôme, Directeur de Recherche CNRS, IP2I	Directeur de thèse
HANSEN Hubert, Maître de Conférences, Université Lyon 1	Co-Directeur de thèse

Abstract

Understanding the properties of dense matter is one of the most outstanding challenges in nuclear (astro)physics. The purpose of this thesis is to contribute to this understanding in the framework of the study of neutron stars. Neutron stars are ideal realizations of dense matter. They contain dilute matter and inhomogeneous clusters in their crusts whereas the inner cores of neutron stars explore matter at the largest densities in the universe, about $5 - 8\rho_{\rm sat}$ where $\rho_{\rm sat} \approx 2.6 \times 10^{14}$g cm^{-3}. The study of such neutron star matter is presented in this thesis in three parts.

In part I, we study the behaviour of dense matter by employing a meta-modeling approach. This allows us to tightly constrain the nuclear symmetry energy, a key quantity in nuclear and astrophysics. We confront the standard quadratic isospin expansion of the equation of state with explicit asymmetric nuclear-matter calculations based on a set of commonly used Hamiltonians including two- and three-nucleon forces derived from chiral effective-field theory. We study, in particular, the importance of nonquadratic contributions to the symmetry energy. Our results suggest that the nonquadratic contribution to the symmetry energy can be systematically determined from the various Hamiltonians employed, and we obtain $0.74^{+0.11}_{-0.08}$ MeV at nuclear saturation density. Furthermore, we perform a detailed analysis of the implications of these calculations for the crust of neutron stars. In order to do so, a compressible liquid drop model is employed to model the finite-sized clusters in the neutron star crust. Our analysis allows us to investigate the model dependence of the crust properties, and in particular the effects of the behaviour of neutron matter at low density.

In Part II of the thesis, we emphasize the need to develop relativistic models of nuclear matter which allow for a link between the fundamental properties of QCD, such as chiral symmetry breaking and confinement, and the natural nucleonic degrees of freedom. In this regard, we present and explore a model in which chiral symmetry is incorporated within the Walecka type Relativistic Mean Field (RMF) model as well as the effect of confinement through the nucleon response. The parameters of this model are controlled by properties such as the chiral potential, the Lattice-QCD predictions, the quark structure, and two saturation properties (density and energy). As a next step, the predictions of this chiral+confinement model are compared to two other models: another chiral model - but without confinement effect - and the original RMF model. For these three models, we additionally take care of parameter uncertainties and propagate them to our predictions for dense matter properties employing Bayesian statistics. We show that the combination of chiral potential with nucleon response represents a microscopically motivated and economical way to treat in-medium corrections and accurately reproduces the other two models which are directly fitted to the empirical properties of nuclear matter. Finally, we find that, while these models are calibrated to the same properties at saturation density, they differ in their predictions as the density increases.

Part III of this thesis is devoted to the study of phase transitions that could lead to the existence of exotic degrees of freedom in the inner cores of neutron stars. We begin with a focus on first-order phase transitions, which often softens the EoS and consequently reduces the maximum mass as well as the radii of NSs. We challenge this conventional expectation by constructing explicit examples of EoSs undergoing a first-order phase transition, but which are much stiffer than their purely hadronic counterparts. We also provide comparisons with the recently proposed quarkyonic EoS which suggests a strong repulsion in the core of NSs, and we show that their stiffness can be realistically masqueraded by first-order phase transitions to exotic matter. Furthermore, we enunciate the fact that phase transitions could be indicated by non-trivial structures in the density behavior of the speed of sound such as jumps and sharp peaks. We thus employ a physics-agnostic approach to model the speed of sound in neutron stars and study to which extent the existence of non-trivial structures can be inferred from existing astrophysical observations of neutron stars. We conclude that astrophysical information to date does not necessarily require a phase transition to quark matter. Finally, the implications of perturbative QCD calculations for the equation of state of neutron star matter are discussed.

Résumé

La compréhension des propriétés de la matière dense est l'un des challenges les plus importants de la physique nucléaire et de l'astrophysique des étoiles compactes. L'objectif de cette thèse est de contribuer à cette compréhension dans le cadre de l'étude des étoiles à neutrons. Les étoiles à neutrons sont des réalisations idéales de la matière dense. Elles contiennent de la matière diluée dans leur croûte alors que les cœurs des étoiles à neutrons contiennent de la matière aux densités les plus élevées de l'univers. L'étude de cette matière des étoiles à neutrons est présentée dans cette thèse en trois parties.

Dans la partie I, nous étudions le comportement de la matière dense en utilisant une approche de méta-modélisation de la matière nucléonique. Ceci nous permet de fixer des contraintes strictes sur l'énergie de symétrie nucléaire, une quantité clé en (astro)physique nucléaire. Nous comparons l'expansion quadratique en isospin de l'équation d'état avec des calculs explicites de matière nucléaire asymétrique basés sur un ensemble d'hamiltoniens couramment utilisés, y compris les forces à deux et trois nucléons dérivées de la théorie du champ effectif chirale («chiral effective-field theory»). Nous étudions, en particulier, l'importance des contributions non quadratiques à l'énergie de symétrie. Nos résultats suggèrent que la contribution non quadratique à l'énergie de symétrie peut être systématiquement déterminée à partir des divers hamiltoniens employés, et nous obtenons $0.74^{+0.11}_{-0.08}$ MeV à la densité de saturation nucléaire. En outre, nous effectuons une analyse détaillée des implications de ces calculs pour la croûte des étoiles à neutrons. Pour cela, le modèle de la goutte liquide compressible est employé pour modéliser les agrégats dans l'écorce des étoiles à neutrons. Notre analyse nous permet d'étudier la dépendance au modèle des propriétés de l'écorce, et en particulier les effets du comportement de la matière neutronique à basse densité.

Dans la partie II de la thèse, nous soulignons la nécessité de développer des modèles relativistes de la matière nucléaire qui permettent un lien entre les propriétés fondamentales de la QCD, telles que la brisure de symétrie chirale et le confinement, et les degrés de liberté nucléoniques naturels. À cet égard, nous présentons et explorons un modèle dans lequel la symétrie chirale est incorporée dans le modèle de champ moyen relativiste («Relativistic Mean Field», RMF) de type Walecka, ainsi que l'effet du confinement par la réponse du nucléon. Les paramètres de ce modèle sont déterminés par des propriétés telles que le potentiel chiral, les prédictions de QCD sur réseau, la structure des quarks et deux propriétés de saturation (densité et énergie). Dans un deuxième temps, les prédictions de ce modèle chiral+confinement sont comparées à deux autres modèles : un autre modèle chiral - mais sans effet de confinement - et le modèle RMF original. Pour ces trois modèles, nous prenons en compte les incertitudes sur les paramètres et les propageons à nos prédictions pour les propriétés de la matière dense en utilisant l'analyse bayésienne. Nous montrons que la combinaison du potentiel chiral avec la réponse du nucléon représente une manière économique et justifiée au niveau microscopique de traiter les corrections du milieu de l'équation scalaire du mouvement, reproduisant avec précision les deux autres modèles qui sont directement adaptés aux propriétés empiriques de la matière nucléaire. Enfin, nous constatons que, si ces modèles sont calibrés sur les mêmes propriétés à la densité de saturation, ils diffèrent dans leurs prédictions lorsque la densité augmente.

La partie III de cette thèse est consacrée à l'étude des transitions de phase qui pourraient conduire à l'existence de degrés de liberté exotiques dans les cœurs des étoiles à neutrons. Nous

commençons par nous concentrer sur les transitions de phase de premier ordre, qui souvent adoucissent l'EoS et par conséquent réduisent la masse maximale ainsi que les rayons des NSs. Nous remettons en question cette hypothèse conventionnelle en construisant des exemples explicites d'EoSs subissant une transition de phase de premier ordre, mais qui sont beaucoup plus rigides que leurs homologues purement hadroniques. Nous établissons également des comparaisons avec l'EoS quarkyonique récemment proposée, qui suggère une forte répulsion au cœur des NSs, et nous montrons que leur rigidité peut aussi être déguisé de manière réaliste par des transitions de phase du premier ordre vers de la matière exotique. De plus, nous montrons que les transitions de phase pourraient être mise en évidence par des structures non triviales dans le comportement en densité de la vitesse du son, comme des sauts ou des bosses. Nous employons donc une approche agnostique de la physique pour modéliser la vitesse du son dans les étoiles à neutrons et nous étudions dans quelle mesure l'existence de structures non triviales peut être déduite des observations astrophysiques existantes des étoiles à neutrons. Nous concluons que les informations astrophysiques obtenues à ce jour ne démontrent pas nécessairement qu'il existe une transition de phase vers la matière de quarks. Enfin, nous discutons des implications des calculs de QCD perturbative pour l'équation d'état de la matière des étoiles à neutrons.

Acknowledgements

I would like to thank Jérôme Margueron for his outstanding supervision and encouragement over the past three years. I thank him for everything he has taught me and I will always remember the warm and nurturing environment he provided that allowed me to enjoy carrying out my thesis. I am also very grateful to my co-advisor Hubert Hansen, for his constant help and support.

I would also like to thank Guy Chanfray for many useful and enthusiastic discussions. I hope we will continue to work together in the future. I owe a lot to many senior colleagues who have taught me so much over the past years. In particular, I extend a special thanks to Ingo Tews for his collaboration, help and kindness. I also thank Elias Khan for the innumerable informative discussions.

My PhD experience would not have been the same without my friendships with Guilherme Grams and Mohamad Chamseddine. I am indebted to them for all the experiences we have shared together, both at and outside work. I also thank all my fellow PhD students, especially Paul Proust, Philippe Da Costa and Jean-Francois Coupechoux.

I thank my family for their constant support. Finally, and most importantly, I thank Sonali, my closest friend and wife. This thesis is dedicated to her.

Contents

Chapter 1

Introduction to Dense Matter Physics

Understanding the nature of matter when subjected to extreme conditions of temperature and density is one of the biggest outstanding problems in physics. Our present understanding of the phases of matter that appear at such thermodynamic conditions is summarized in Fig. 1.1. This figure is called the phase diagram of Quantum chromodynamics (QCD) [1] since the properties of matter at such densities and temperatures are directly linked with the physics of the strong interaction as described by QCD [2, 3, 4]. Much progress in the understanding of the phase diagram at finite temperature (and low density) has been made in recent years due to both experiment and theory [5, 6, 7]. For instance, heavy ion collisions performed at laboratories like the Relativistic Heavy Ion Collider (RHIC) [8] and the Facility for Antiproton and Ion Research (FAIR) [9] allow for the exploration of this region of the phase diagram, as shown in Fig. 1.1. The purpose of this thesis is, however, primarily to study low-temperature matter at finite densities where our understanding is still quite limited.

In Fig. 1.1, the horizontal density axis is normalized such that the typical densities explored in the bulk of atomic nuclei is indicated by $\rho_{\rm sat}$. For reasons that we will discuss later, this density is referred to as the *saturation density* of nuclear matter. The properties of matter, composed of neutrons and protons in roughly equal numbers, around this density $\rho_{\rm sat}$ can mostly be inferred from the characteristics of heavy nuclei [10, 11] and is therefore relatively well understood despite the fact that the connection to QCD is still difficult, see discussion in Sec. 1.3. On the other hand, matter at much larger densities $\rho \gg \rho_{\rm sat}$ is still poorly understood and a proper understanding of such dense matter remains one of the most important unanswered questions in nuclear and hadronic physics. While, in principle, these dense matter properties are determined by QCD, it has been very difficult to extract the QCD predictions for dense matter due to its non-perturbative nature [12]. Ab-initio numerical lattice calculations, while having been extremely successful at finite temperature, fail at finite density due to the ubiquitous sign problem [5, 6]. Furthermore, the lack of terrestrial experiments that probe high density matter make this problem a very challenging one.

The only empirical evidence we have about cold matter at higher baryon densities comes from the study of Neutron Stars (NS) [13]. NSs are astrophysical objects of extremes and an introduction to these fascinating objects is given in Sec. 1.1. Here we only remark that it is well understood that NSs contain matter up to $5\rho_{\rm sat}$ to $8\rho_{\rm sat}$. The study of the composition of NSs is therefore directly linked with the study of QCD at the highest densities encountered in the universe. This makes NSs an ideal laboratory for the study of dense matter. Furthermore, in recent years, enormous progress has been made in the experimental observations of NSs, see

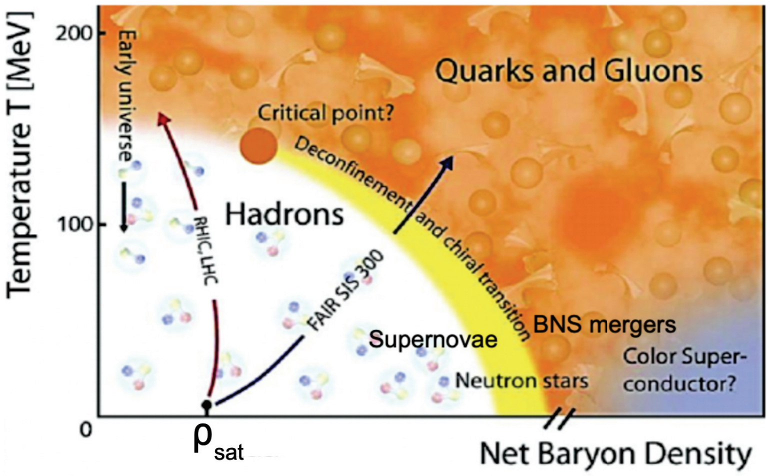

Figure 1.1: The schematic phase diagram of QCD showing the phases of matter at different temperatures and densities, as well as the experiments and astrophysical sites that probe them. The first order transition line between the hadronic and quark phases is shown in yellow and the endpoint of this line i.e. the critical point [14] is shown as an orange dot.

Sec. 1.2. This makes the study of NSs extremely timely and exciting. The purpose of this thesis is to contribute to this effort, namely the study of the nature of matter present in NSs.

The rest of this chapter is organized as follows. In Sec 1.1 we discuss the physics of NSs and establish the astrophysical context of this work. In Sec. 1.2 the recent experimental observations that have ushered in the so-called multi-messenger era is discussed. In Sec. 1.3 we discuss the connection between the dense matter constrained by astrophysical NS observations and the constraints one obtains at lower densities via terrestrial nuclear experiments. We will conclude in Sec. 1.4 where a summary of the rest of the thesis is given.

1.1 The physics of neutron stars

NSs contain matter at the largest densities in the universe [13]. They therefore act as astrophysical sites where a fascinating interplay of nuclear physics, particle physics, hadronic physics, astrophysics, relativistic gravitational physics and magnetohydrodynamics occurs. NSs may exhibit conditions and phenomena not observed elsewhere. For instance, exotic phases such as hyperon-dominated matter, deconfined quark matter, superfluidity and superconductivity might occur in NSs only. Furthermore, during dynamic stages of their lives, NSs exhibit opaqueness to neutrinos and also explore matter at finite temperature. The surface magnetic fields might be in excess of 10^{13} Gauss and some NSs rotate several hundreds of times per second, inducing general relativistic effects such as frame-dragging. In this section, we will give a brief introduction to some of these phenomena. Let us first begin with the birth of NSs.

1.1.1 The birth of NSs

NSs are sometimes dubbed as ‘Cosmic Zombies’ because they are the dead remnants of massive ‘normal’ stars. All normal stars, with our sun being the most prominent example, have thermonuclear lives during which a series of light elements undergo nuclear fusion. The energy released in the fusion processes balances the star's gravitational attraction, establishing equilibrium. A star's first thermonuclear stage is the fusion of hydrogen into helium in its hot core. With the exhaustion of hydrogen at the core, the star then proceeds to shell hydrogen burning, and then to core helium burning. The ashes of the latter are predominantly carbon and oxygen. What happens next is strongly dependent of the mass of the star [15].

Most stars, including our Sun, will die leaving behind carbon/oxygen white dwarfs with radii close to the Earth's radius and masses near 0.5 – 1.0 $\mathrm{M}_{\odot}$. These white dwarfs are born slowly over hundreds to thousands of years through the ejection of the dying star's heavy outer mantle. There is no explosion. Note that the formation of helium white dwarfs is possible if the progenitor's mass is insufficient to support helium burning and, in the same spirit, heavier stars might lead to the formation of neon or magnesium white dwarfs. These white dwarfs support themselves against gravity by electron degeneracy pressure. Due to the Pauli exclusion principle, at the densities achieved by massive white dwarfs, their electrons are relativistic. Unlike a non-relativistic gas, a relativistic gas is more easily compressed by the force of gravity. The electron degeneracy pressure is therefore only sufficient to stabilize white dwarfs up to a certain maximum mass, the so-called Chandrasekhar mass [16]. The Chandrasekhar limit depends on the composition of the star and is typically around 1.4 $\mathrm{M}_{\odot}$.

On the other hand, stars with masses around 8 to 20 $\mathrm{M}_{\odot}$ have an entirely different evolution [17, 18]. There is no quiet mantle ejection and the thermonuclear cycle continues during which heavier elements like neon, oxygen, and silicon are created. Finally, these products ignite to produce iron and its isotopes near the peak of the nuclear binding energy curve. At this stage, the core of these stars is essentially an iron or oxygen-neon-magnesium white dwarf, with the mass of the core continuously increasing due to the above mentioned fusion processes. At a certain stage, the core white dwarf exceeds the Chandrasekhar limit and the core collapses. In less than one second the core of the star, which has a radius that is roughly equal to the radius of our planet, implodes to a radius of about 10 km, achieving densities in excess of nuclear matter densities and velocities one-fourth the speed of light. One of the most remarkable aspects is that neutrinos become dynamically trapped during a timescale of the order of the star's collapse time. Also, the gravitational binding energy released in the collapse of the progenitor star's white dwarf-like core to a neutron star is about 3×10^{53} ergs [19, 20], which is about 10% of its total mass.

The density in the core rises rapidly as the collapse progresses. When the density reaches typical nuclear matter densities, core collapse halts abruptly due to the large value of the nuclear incompressibility. This triggers a bounce which results in a shock wave that propagates to about 100 to 200 km before it stalls. Neutrinos from the core, assisted perhaps by rotation, convection, magnetic fields and hydrodynamical instabilities such as the Standing Accretion Shock Instability (SASI) [21, 22], eventually resuscitate the shock and help it to overcome the imploding mantle in order to launch a type II supernova explosion. The violent explosion throws several heavy elements such as oxygen, carbon, magnesium and silicon into the interstellar medium. The luminosity display of this event can be comparable to that of its parent galaxy for months [23, 24].

The remnant that is left behind is called a proto-neutron star. These objects are rich in leptons and are initially hot. Further, proto-neutron stars absorb a large part of the angular momentum and the magnetic field of the initial star and thus can have strong magnetic fields

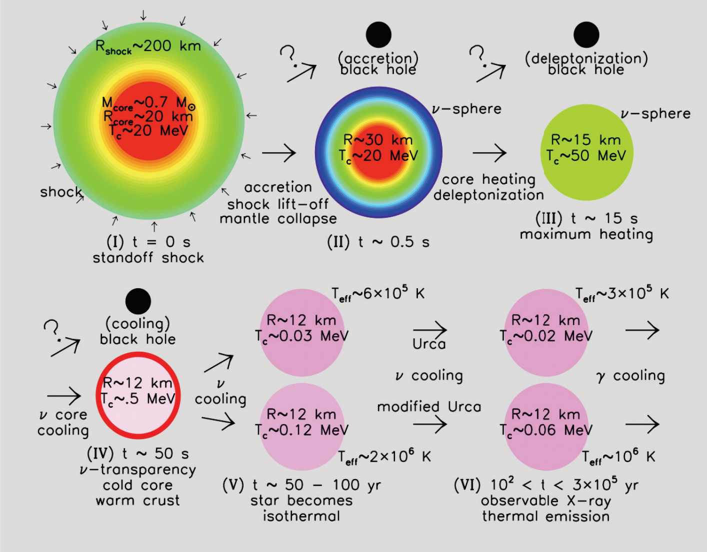

Figure 1.2: The main stages of the birth and evolution of a NS taken from Ref. [13].

and high rotation frequencies, and can be detected by their emitted radio signals. This angular momentum is gradually lost due to electromagnetic emissions whereas the proto-neutron star cools via neutrino emission. Ultimately a cold, slowly-rotating neutron star is finally formed. The main stages of the evolution described in this section is showed in Fig. 1.2.

1.1.2 Global structure of NSs: The mass-radius relation

General Relativity (GR) connects certain properties of dense matter with the relation between the radius and the mass of neutron stars. Rotation, magnetic fields, and finite temperature make only small corrections to the mass-radius (M-R) relation. The M-R relation is determined by the equations of hydrostatic equilibrium. For a spherical object in GR, they were first derived by Tolman [25] and later by Oppenheimer and Volkov [26], giving their names to the so-called TOV (Tolman-Oppenheimer-Volkov) equations

$$\begin{aligned} \frac{dm(r)}{dr} &= 4\pi r^2 \epsilon(r), \qquad (1.1)\\ \frac{dp(r)}{dr} &= -\epsilon(r)c^2\left(1+\frac{p(r)}{\epsilon(r)c^2}\right)\frac{d\Phi(r)}{dr}, \\ \frac{d\Phi(r)}{dr} &= \frac{Gm(r)}{c^2r^2}\left(1+\frac{4\pi p(r)r^3}{m(r)c^2}\right)\left(1-\frac{2Gm(r)}{rc^2}\right)^{-1}, \end{aligned}$$

where G is the gravitational constant, r is the radial distance to the center, c the speed of light, $p(r)$ the total pressure, $m(r)$ the enclosed mass, $\epsilon(r)$ is the total mass-energy density and $\Phi(r)$ the gravitational field. Note that in order to solve this system of coupled equations, the relationship between p and ϵ has to be known. This link $p(\epsilon)$ is called the *Equation of State* (EoS). For

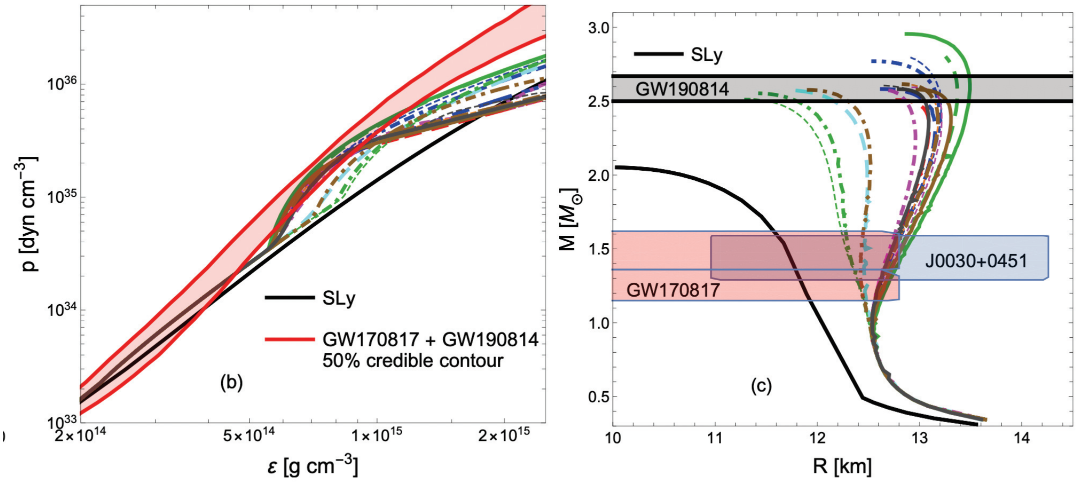

Figure 1.3: Examples of several EoSs (left panel) and their associated mass-radius relations (right panel). The curves of different colors correspond to different EoS models whereas the different line-styles are obtained by varying the parameters of a given model. Figure taken from Ref. [27].

NSs, the EoS needs to be known across several orders of magnitude in densities. While at densities around saturation density the EoS is known fairly well, the uncertainties in the EoS grows rapidly as the density increases. This originates from the fact that the degrees of freedom that constitute dense matter and their corresponding interactions are poorly understood. Therefore, we see that a solid understanding of the EoS is an extremely challenging but exciting task.

Regarding the numerical solution of Eqs. (1.1), one integrates numerically from the center of the star $r = 0$ to the boundary $r = \mathrm{R}$, with R being the radius of the NS. The boundary is defined to be the value of the radial coordinate such that the pressure vanishes, i.e. $P(r = \mathrm{R}) = 0$. Furthermore, a certain value for the central density ρ_c has to be chosen for this numerical integration. The obtained solution then gives the gravitational mass $\mathrm{M} = m(\mathrm{R})$ and radius R for the chosen value of ρ_c. This procedure can then be iterated for different values of ρ_c, allowing for the construction of a sequence of NSs, each with a specific mass and radius. This sequence lies on a curve in the mass-radius plane and is called the M-R relation.

Fig. 1.3 shows examples of several EoSs (left panel) with their associated mass-radius relations (right panel) obtained by solving the TOV equations (1.1). We see that different EoSs give different M-R relations and therefore a simultaneous measurement of mass and radius of a NS could help to discriminate among possible EoSs. In the next section, we will see several experimental advances in this regard. Also, note that for every EoS, the associated M-R curve terminates at a certain maximum value of the NS mass. Beyond this mass, stable NSs cannot exist as matter would collapse to form a black hole. This upper limit on the NS mass is called the TOV limit and is denoted as $\mathrm{M_{TOV}}$. The existence of $\mathrm{M_{TOV}}$ is a consequence of GR and is a characteristic feature of Eqs. (1.1) due to the pole at $r = 2Gm(r)/c^2$. However, its exact value depends on the EoS, indicating that constraints on $\mathrm{M_{TOV}}$ would immediately translate into constraints on the underlying EoS.

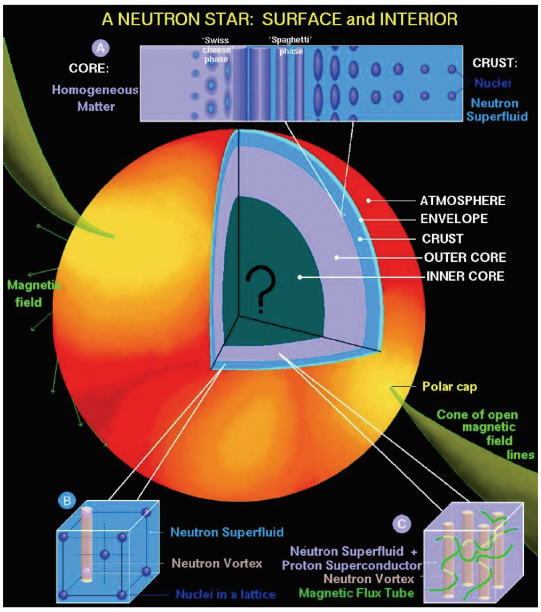

Figure 1.4: The major regions and composition inside a NS. The top bar illustrates expected geometric transitions from homogenous matter at high densities in the core to nuclei at low densities in the crust. Figure taken from Ref. [13].

1.1.3 NS composition

As shown in Fig. 1.4, a NS has five major regions, the inner and the outer cores, the inner crust and the outer crust (the envelope), and the atmosphere [13, 15, 28]. The atmosphere is very thin, up to a few centimeters and contains a negligible amount of mass. It is primarily composed of hydrogen and helium. The outer crust extends from the bottom of the atmosphere up to some hundreds of meters. This layer of the crust is constituted by a degenerate electron gas as well as a lattice of neutron rich nuclei with atomic number $Z \approx 30$. In this region the pressure primarily originates from the electron degeneracy pressure. The electron Fermi energy increases with the density which causes the nuclei to become more neutron rich. At some point, the neutron chemical potential is zero and the neutrons start dripping out off the nuclei, creating a dilute neutron gas. The point at which this occurs is where the outer crust transitions to the inner crust [29].

The inner crust is about one kilometer thick. It consists of neutron rich nuclei, an electron gas and also a neutron gas. As the density increases, more matter exists in the gaseous state than inside nuclear clusters. Also, close to the transition point between the crust and the core, the nuclei are expected to be drastically deformed. As shown in Fig. 1.4, it is expected that the nuclei undergo a series of continuous deformations from spherical nuclei to 2-D cylindrical nuclei to 1-D slabs of nuclei. This is called the nuclear pasta phase [13].

At roughly half saturation density, nuclei disintegrate completely and matter exists in a completely homogeneous liquid state [28]. This region is called the core and it accounts for 99% of the mass of the NS. Its radius is about 10-15 kms. Based on the composition of the homogeneous matter, the core can be divided into the outer core and the inner core. In the outer core, matter exists in a uniform state of neutrons, protons, electrons and muons which appear around saturation density. The conditions of beta equilibrium, baryon number conservation and charge neutrality determine the different particle fractions. The electrons and muons can be approximated as quantum ideal gases, whereas the interaction between the nucleons has to be taken into account for a realistic description of the outer core.

After about twice saturation density, we have the ultimate layer of the NS, the inner core. Densities in this region can extend up to 5 to 8 times nuclear saturation density. The composition of the inner core remains largely unknown and therefore serves as an exciting platform for active research. It is possible that the inner core, like the outer core, consists of only neutrons and protons (along with leptons) but with their interactions being significantly different at these larger densities. On the other hand, it is expected that other 'exotic' degrees of freedom such as hyperons appear in the inner core [30]. Other possibilities include the presence of pion and/or kaon condensates [31, 32]. Another tantalizing possibility is the appearance of deconfined quark matter composed of almost massless u and d quarks and even s quarks [33]. The transition from 'normal' nuclear matter to these exotic phases might occur via a strong first-order phase transition or a smooth crossover. A lot of research remains to be done in order to answer these extremely interesting questions about the nature of the inner core of NSs.

1.2 Era of multi-messenger NS astronomy

The study of NSs and the dense QCD matter that they contain has undergone a major revolution in recent years. This is due to recent advances in technology and experimental methods that have allowed for unprecedented and remarkable observations of NSs. These observations include detections of X-rays, radio waves and gravitational waves (GW). For this reason, the present age is called the era of multi-messenger NS astronomy. In this section, we will elaborate on three of these major experimental breakthroughs.

1.2.1 Gravitational waves

The first Binary Neutron Star (BNS) system was discovered by Hulse and Taylor almost four decades ago and is called PSR B1913+16 [34]. Detailed observations of this BNS system found that its orbital angular momentum was decreasing continuously due to the emission of gravitational waves, providing the first indirect evidence of their existence [35]. Since the Hulse-Taylor discovery, radio pulsar surveys have found several more BNS systems in our galaxy [36] and detailed modeling based on these observations indicated that a direct detection of GWs from a BNS merger was close at hand [37]. Finally, On 17 August 2017, the LIGO and Virgo observatories made the first direct detection of GWs from the coalescence of a BNS system [38, 39]. The GW signal was produced during the final minutes of the inspiral phase before the two NSs finally merged together. Unlike the five previous GW detections, which were of merging black holes not expected to produce a detectable electromagnetic signal, the aftermath of this merger was also seen by 70 observatories on 7 continents and in space, across the electromagnetic spectrum, marking a significant breakthrough for multi-messenger astronomy [40].

This GW event, called GW170817 allowed for stringent constraints on the EoS of dense matter. Such constraints are possible because the GW emitted from two merging NSs is different from that emitted from a system of two black holes. The most prominent effect of the NS matter during the observed binary inspiral comes from the tidal deformation that each star's gravitational field induces on its companion. We will therefore briefly summarize the theory of tidal deformations of NSs.

Tidal deformability

When a neutron star is placed in a perturbing tidal gravitational field its shape is distorted, expressed through an induced quadrupole moment [41, 42, 43]. Compact binaries that are detectable with gravitational waves provide a natural stage for this interaction: the neutron star binary component is subject to the gravitational field generated by its companion compact star. The induced quadrupole moment of the neutron star will, in turn, affect the characteristics of the GW as compared to GWs emitted from binary black holes.

The tidal deformability of a neutron star is a single parameter λ that quantifies how easily the star is deformed when subject to an external tidal field. In general, a larger tidal deformability signals a larger, less compact star that is easily deformable. On the other hand, a star with a smaller tidal deformability parameter is smaller, more compact, and it is more difficult to deform. Traditionally one can expresses the tidal deformability as

$$\lambda = \frac{2}{3} k_2 \mathrm{R}^5 \tag{1.2}$$

where R is the radius and k_2 is the dimensionless love number that depends on the EoS. The parameter λ depends on the EoS due to the dependence of both R and k_2 on the EoS. A related quantity that is commonly also used is the dimensionless tidal deformability defined as

$$\Lambda = \frac{\lambda}{\mathrm{M}^5} \tag{1.3}$$

where M is the mass of the star. Tidal effects are expected to impact both the amplitude and the phase of the emitted signal, however the latter is typically better measured for GWs. The GW signal can be expressed as a post-Newtonian expansion which is a series expansion in the velocity of the inspiralling NSs u. This velocity is small compared to the speed of light during the early stages of the inspiral. A term proportional to u^{2N} relative to the leading order term is referred to as an NPN contribution. In this framework, the tidal contribution scales as $\approx u^{10}$, i.e. it is 5PN correction compared to the leading Newtonian term. This shows why tidal effects are negligible when the stars' separation is large, but become more important as the binary approaches the later stages of its coalescence where velocities increase [41].

While the tidal deformability can be measured from GW signals, one needs to be capable of computing the tidal deformability from an underlying EoS so that constraints on the EoS can be obtained from GW signals. It turns out that with a given EoS, the love number k_2 can be calculated from the so-called pulsation equation at the surface of NSs [42, 43],

$$\begin{aligned} k_2 \;=\; & \frac{8C^5}{5}\left(1-2C\right)^2\left(2-y_R+2C(y_R-1)\right) \\ & \times\Big(2C(6-3y_R+3C(5y_R-8)) \\ & +4C^3\left(13-11y_R+C(3y_R-2)+2C^2(1+y_R)\right) \\ & +3(1-2C)^2\left(2-y_R+2C(y_R-1)\right)\ln(1-2C)\Big)^{-1}, \end{aligned} \tag{1.4}$$

where C is the compactness of the NS, y_R is the value of the y function at radius R, $y_R = y(r = \mathrm{R})$, and $y(r)$ is the solution of the following differential equation,

$$r\frac{dy}{dr} + y^2 + yF(r) + r^2Q(r) = 0\,, \tag{1.5}$$

with the boundary condition $y(0) = 2$ and the functions $F(r)$ and $Q(r)$ defined as,

$$\begin{aligned} F(r) &= \frac{1 - 4\pi r^2 G[\epsilon(r) - p(r)]/c^4}{1 - 2M(r)G/(rc^2)}\,, \qquad (1.6)\\ r^2Q(r) &= \frac{4\pi r^2 G}{c^4}\left(5\epsilon(r) + 9p(r) + \frac{\partial\epsilon(r)}{\partial p(r)}[\epsilon(r) + p(r)]\right)\\ &\times\left(1 - 2M(r)G/(rc^2)\right)^{-1} - 6\left(1 - 2M(r)G/(rc^2)\right)^{-1}\\ &-\frac{4G^2}{r^2c^8}\left(M(r)c^2 + 4\pi r^3 p(r)\right)^2\left(1 - 2M(r)G/(rc^2)\right)^{-2}\,. \end{aligned} \tag{1.7}$$

EoS constraints from GW170817

As mentioned earlier, the first GW from a BNS system was detected on 17 August, 2017 and is called GW170817. The detection of the signal corresponding to the final stages of the inspiral phase allowed for the determination of Λ_1 and Λ_2, where these two parameters are the dimensionless tidal deformabilities, see Eq. (1.3), of each component of the binary. The marginalized posterior for the tidal deformabilities are shown in the left panel of Fig. 1.5 obtained from Ref. [39]. In this figure the shaded green region represents the probability density obtained using certain EoS-insensitive relations that relate Λ_1 and Λ_2 [1]. More details regarding the other features of this plot can be found in Ref. [39].

Tidal deformabilities of NSs are closely related to their radii and therefore a constraint on the tidal deformability can be converted into a constraint on the radius. In order to do this Ref. [39] used a piecewise polytropic model for the EoS whose parameters can be varied in a physics-agnostic manner. Tidal deformabilities and radii were computed consistently for each EoS sample using Eqs. (1.1) and (1.4). This allows for the representation of the GW constraint on the mass-radius plane as shown in the right panel of Fig. 1.5. We see that at the 90% confidence level, the radius is constrained to be $\approx 12 \pm 1.5$ km.

In this section, we have summarized briefly how constraints on the EoS can be obtained from the inspiral phase of the GW signal. As an example, we discussed the analysis performed by Ref. [39] on the first ever BNS GW event GW170817. See Refs. [44, 45, 46] for other examples of constraints on the EoS obtained from GW170817 as calculated by several independent groups.

Post-merger remnant of GW170817

Another fascinating aspect of GW170817, and BNS mergers in general, is the physics of the remnant that is created due to the merger. It is widely accepted that the GW170817 binary-merger remnant underwent gravitational collapse to a black hole marked by the observation of

---

[1] In fact, the EoS-insensitive relation relates Λ_a and Λ_s, where $\Lambda_s \equiv \frac{\Lambda_1+\Lambda_2}{2}$ and $\Lambda_a \equiv \frac{\Lambda_2-\Lambda_1}{2}$ [39]

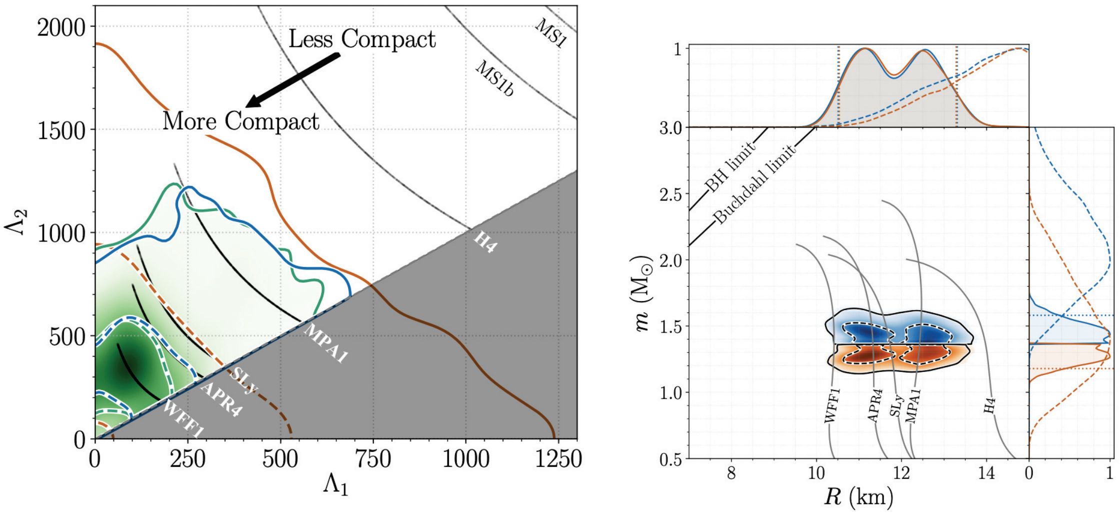

Figure 1.5: The left panel shows the marginalized posterior for the tidal deformabilities Λ_1 and Λ_2 of the two binary components of GW170817. The right panel depicts the posteriors for the mass and radius of each binary component using a parametrized EoS approach. Figure taken from Ref. [39] where more details can be found.

a gamma ray burst [44]. This assumption can be used to obtain constraints on the maximum mass that non-rotating NSs can have, $\mathrm{M_{TOV}}$. Recall from Sec. 1.1.2 that while the existence of the maximum mass for non-rotating NSs $\mathrm{M_{TOV}}$ is a consequence of GR, the exact value of $\mathrm{M_{TOV}}$ depends on the EoS since different EoSs predict different values for $\mathrm{M_{TOV}}$. Therefore a constraint on $\mathrm{M_{TOV}}$ serves as a strong constraint on the EoS.

It should first be noted that neutron stars with masses exceeding the maximum mass of non-rotating configurations, $\mathrm{M_{TOV}}$, can exist if such masses are supported by rotation effects. There also exists an upper limit on the maximum mass that can be supported by uniform rotation and, following Ref. [47], we shall call this $\mathrm{M_{max}}$. Neutron stars with masses between $\mathrm{M_{TOV}}$ and $\mathrm{M_{max}}$ are referred to as supramassive NSs, while the ones with mass higher than $\mathrm{M_{max}}$ are called hypermassive NSs. The latter configurations can only be supported by differential rotation.

Regarding the GW170817 event, there are indications that the collapse to a black hole likely took place in a time frame of order 1-2 s. Based on this, the authors of Ref. [47] argued that the GW170817 post-merger remnant collapsed to a black hole when its mass was close to $\mathrm{M_{max}}$. Then, using EoS-insensitive relations between $\mathrm{M_{TOV}}$ and $\mathrm{M_{max}}$, where the latter can be inferred from the measurement of the total mass in the GW170817 event, the authors of Ref. [47] obtained $\mathrm{M_{TOV}} < 2.16^{+0.17}_{-0.15}\ \mathrm{M_\odot}$. A similar analysis of Ref. [48] found that $\mathrm{M_{TOV}} \lesssim 2.3\ \mathrm{M_\odot}$.

It is thus clear from this section that GWs provide a extremely interesting constraints on the EoS. New observations will set sharper boundaries in the probability distributions over tidal deformabilities and radii and also tighten estimates for the maximum mass $\mathrm{M_{TOV}}$.

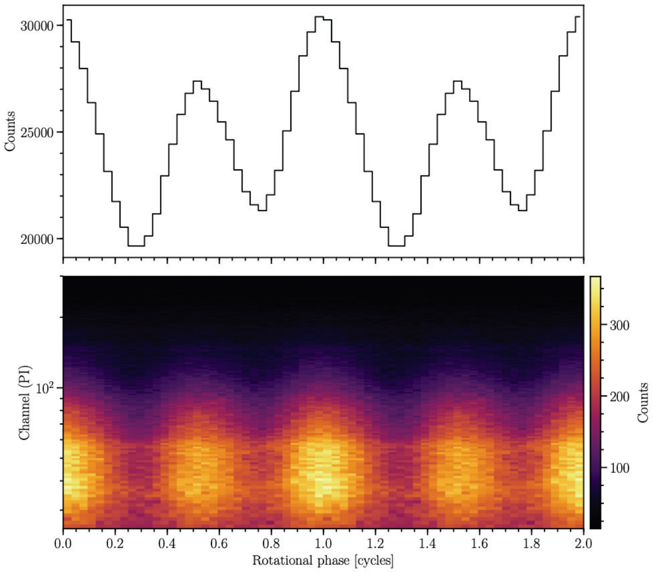

Figure 1.6: A sample pulse-profile observed by the NICER telescope for PSR J0030+0451. Figure taken from Ref. [51] where more details can be found.

1.2.2 NICER observations

NASA's Neutron Star Interior Composition Explorer (NICER) is an X-ray telescope installed on the International Space Station in 2017 [49, 50, 51, 52]. Its primary use is to estimate masses and radii of NSs using pulse-profile modeling of rotation-powered pulsars. Pulse-profile modeling is a technique that probes GR effects on thermal X-ray emission from localized hot regions on the stellar surface [53]. The X-ray that is emitted from the hot regions undergo GR effects due to the curvature of spacetime around the NS. These effects include the usual bending of light, gravitational redshift and frame-dragging. As the star rotates, the X-ray beam is observed by the NICER telescope as a periodic signal called a pulse-profile (X-ray counts per rotational phase bin). A sample pulse-profile observed by the NICER telescope is shown in Fig. 1.6. A significant amount of modeling is required to correlate the observation of the pulse-profile to the global properties of the pulsar such as its mass and radius. Among these, the relativistic ray-tracing of the X-ray through the spacetime around the rotating pulsar is well understood. However, since the NICER telescope cannot resolve the spatial structure of the star, a model for the surface comoving temperature field along with a model for the atmosphere is required. The model dependencies arising from these two aspects are the primary sources of uncertainty in the measurement of the star's mass and radius. Finally, by coupling such surface emission models to statistical sampling software, the NICER collaboration uses Bayesian inference to calculate posterior probability distributions for parameters such as the mass and equatorial radius directly from the pulse-profile data.

The first NS that the NICER telescope observed was PSR J0030+0451. From the above mentioned pulse-profile modelling techniques, Ref. [51] estimated the mass and radius of this pulsar. The obtained results were sensitive to the modeling of the surface temperature field and the assumption of a fully ionized hydrogen atmosphere. Regarding the temperature field, the pulse-profile data seemed to indicate that there were two distinct hot regions which were nonantipodal and non-identical. Ref. [51] considered various shapes for the hot regions including circles, rings and crescents, with each hot region associated with a single temperature. For the family of models considered, the configuration favoured by the data seemed to be the one in which the hot regions consist of a small hot spot with angular extent of only a few degrees, and a more extended hot crescent, both in the same rotational hemisphere. For this configuration, the inferred mass and equatorial radius are $\mathrm{M} = 1.34^{+0.15}_{-0.16}\ \mathrm{M}_{\odot}$ and $\mathrm{R} = 12.71^{+1.14}_{-1.19}$ km. The compactness $\mathrm{M/R} = 0.156^{+0.008}_{-0.010}$ is much more tightly constrained. See also Ref. [49] which performed an independent analysis of the same data set using different modeling choices [2] and methodology. More details on the modeling of the observed profile of PSR J0030+0451 can be found in Ref. [54].

Later in 2021, the NICER collaboration announced results based on their observation of PSR J0740+6620. Unlike the previous PSR J0030+0451 measurement, the mass of this pulsar was already known thanks to radio observations, see Sec. 1.2.3. Furthermore, the mass of this pulsar is around $2\ \mathrm{M}_{\odot}$, making this the heaviest known NS. Therefore the NICER results for this pulsar were received with much enthusiasm. The same data set was analysed independently by both Ref. [52] and Ref. [50]. The authors of Ref. [52] obtained $\mathrm{R} = 12.39^{+1.30}_{-0.98}$ km whereas Ref. [50] obtained $\mathrm{R} = 13.7^{+2.6}_{-1.5}$ km. There are many differences in the modelling choices made by the two groups. In particular, the prior on the radius assumed by Ref. [50] is much larger, which explains the larger uncertainties in their results.

The results for the two pulsars PSR J0030+0451 and PSR J0740+6620 are shown in Fig. 1.7. The green contours are obtained using the analyses of the Amsterdam collaboration [51, 52] and the brown contours from the Illinois group [49, 50]. Note that constraints from GW170817, as discussed in the previous section, are also shown here. This figure clearly illustrates the influence the multi-messenger era has already had on our knowledge of the global properties of NSs and consequently our understanding of the EoS of dense matter.

1.2.3 Mass measurements of heavy pulsars

While joint mass-radius measurements are very helpful, accurate mass measurements of certain pulsars have also allowed us to gain valuable insight into the EoS of dense matter. Very accurate measurements of NS masses are possible thanks to pulsar timing of radio signals. Fig. 1.8 displays the masses of several NSs present in binary systems measured using radio timing methods. The associated uncertainties are shown as well.

Among these mass measurements, in recent years, NSs with masses around $2\ \mathrm{M}_{\odot}$ have been reported. In 2019, Ref. [56] observed a pulsar PSR J0740+6620 and reported its mass to be $\mathrm{M} = 2.14^{+0.10}_{-0.09}\ \mathrm{M}_{\odot}$. This mass measurement has been refined more recently by Ref. [57] which gives an updated mass $\mathrm{M} = 2.08^{+0.07}_{-0.07}\ \mathrm{M}_{\odot}$. They used a technique called relativistic Shapiro delay, which is observable when a pulsar passes behind its stellar companion during its orbital motion. This creates a small delay in the pulse arrival time induced by the curvature of spacetime in the vicinity of the companion star. For a pulsar–white dwarf binary, the full delay is of the order of 10 micro seconds. This pulsar is now recognized as the heaviest NS that has ever been observed.

Earlier, in 2010, Ref. [58] reported the discovery of a $2\ \mathrm{M}_{\odot}$ pulsar, J1614-2230 (though

---

[2] In particular, Ref. [49] concluded that the best modeling choices for the surface temperature field were models with either two oval hotspots or three oval hotspots

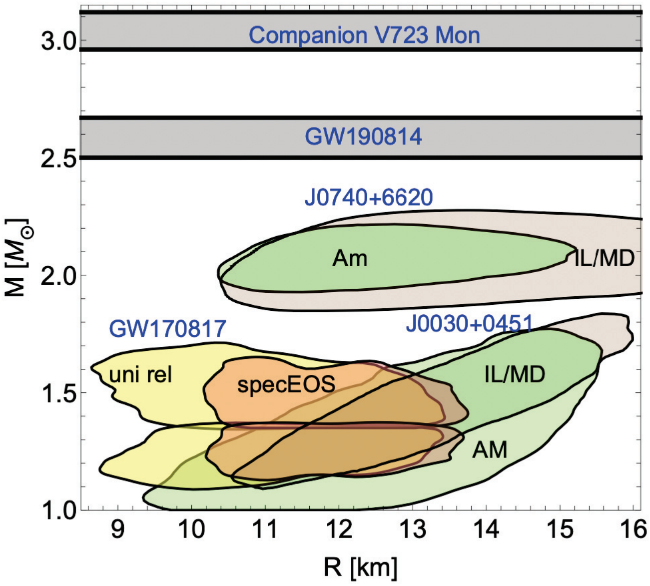

Figure 1.7: Figure from Ref. [55] displaying constraints from NICER [49, 50, 51, 52] as well as from GW170817 [39].

the originally reported mass was $1.97 \pm 0.04\ \mathrm{M}_\odot$, continued timing has led to a more precise mass measurement of $1.928 \pm 0.017\ \mathrm{M}_\odot$ by Ref. [59]), also using the shapiro delay method. In 2013, Ref. [60] used optical techniques in combination with timing of the orbital period to yield a mass measurement of $2.01 \pm 0.04\ \mathrm{M}_\odot$ for the pulsar J0348+0432. Finally, the existence of extremely massive ($> 2.4\ \mathrm{M}_\odot$) neutron stars has been suggested through optical spectroscopic and photometric observations by Ref. [61]. However these measurements, in contrast with radio timing methods, come with larger uncertainties.

As discussed earlier in Sec. 1.1.2, the determination of $\mathrm{M}_{\mathrm{TOV}}$ would place a significant constraint on the EoS. Observations of such heavy pulsars imply that $\mathrm{M}_{\mathrm{TOV}} > 2\ \mathrm{M}_\odot$. This immediately rules out several EoSs that are not repulsive enough to support such massive NSs.

1.3 Dense matter from terrestrial experiments

As mentioned earlier, only NSs can provide us with information regarding matter at several times nuclear densities. On the other hand, the behaviour of matter close to nuclear densities is interesting in its own right. Further, properties of matter at these lower densities can be shown to be correlated with global properties of NSs [63]. Information regarding matter at nuclear densities can be obtained based on the study of heavy finite nuclei.

The connection between the properties of finite nuclei and the physics of NSs is facilitated by the concept of nuclear matter. We will discuss nuclear matter in full detail in chapter 2. For the moment, we remark that nuclear matter is an idealized homogeneous infinite system of neutrons and protons. In this medium, the ratio of the number density of protons to the number density of neutrons can take arbitrary values. However, two interesting cases appear naturally: (i) nuclear matter with an equal number of neutrons and protons, the so-called Symmetric Nu-

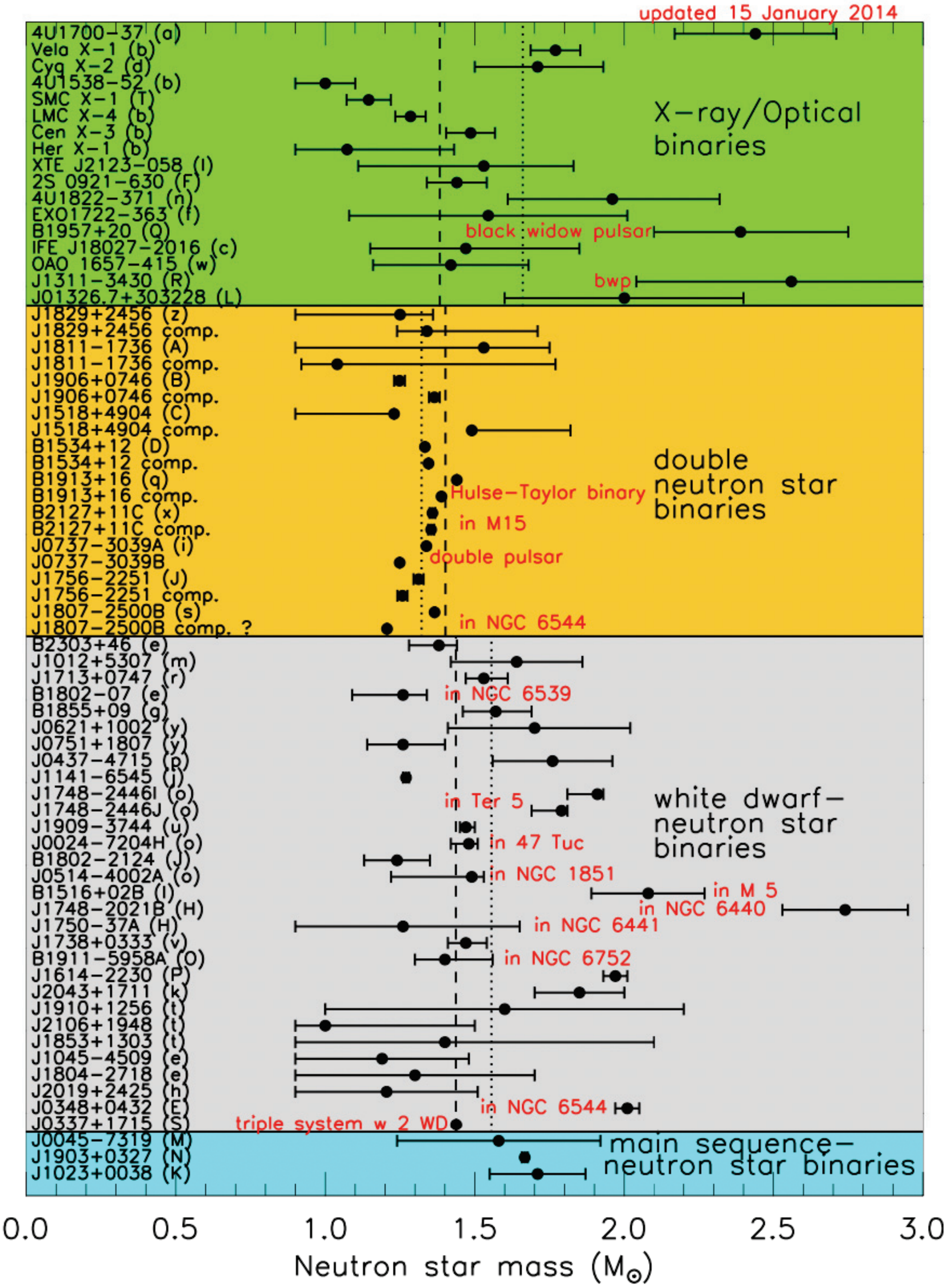

Figure 1.8: Observed neutron-star masses from Ref. [62].

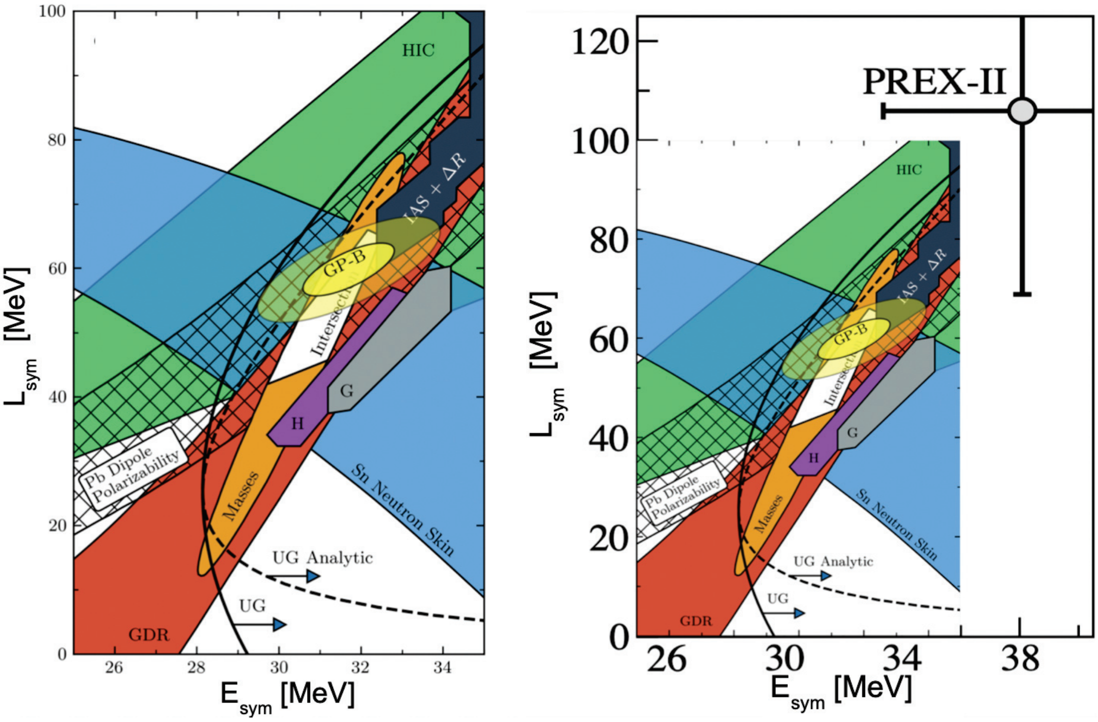

Figure 1.9: Constraints on the correlation between E_{sym} and L_{sym} from different experiments and theoretical considerations. The left panel is taken from Ref. [65] where more details can be found. The right panel is taken from Ref. [66]. The two panels are the same except that the right panel additionally shows the latest PREX-II results [66].

clear Matter (SNM) and (ii) matter with only neutrons, or Pure Neutron Matter (PNM). As we will see in chapter 2, the binding energy per nucleon in PNM is larger than in SNM, i.e. it costs energy to convert a proton into a neutron. This required energy in nuclear matter is called the nuclear symmetry energy. Knowledge of the symmetry energy allows us to connect the physics of the matter explored in the bulk of atomic nuclei to the properties of neutron rich matter existing in NSs. In this section, we will give a brief review of how terrestrial experiments can help constrain the symmetry energy, postponing its precise definition till chapter 2.

The symmetry energy $e_{\text{sym}}(n)$, with n being the number density, can be expanded in a Taylor expansion about the so-called nuclear saturation density n_{sat} [3],

$$e_{\text{sym}}(n) = E_{\text{sym}} + L_{\text{sym}} x + \dots , \tag{1.8}$$

where $x = (n - n_{\text{sat}})/3n_{\text{sat}}$. Here E_{sym} is the symmetry energy at saturation density and L_{sym} is its slope at this point. Therefore several terrestrial experiments that attempt to constrain the symmetry energy and its density dependence aim to measure the values of the parameters E_{sym} and L_{sym}. Different experimental constraints on E_{sym} and L_{sym} are shown in Fig. 1.9. We will now discuss some of these experiments.

---

[3] This density $n_{\text{sat}} \approx 0.16\,\text{fm}^{-3}$ [64] is defined as the density at which the pressure in SNM is zero. More details are given in chapter 2.

Nuclear Binding energies

In 1935, Bethe and Weizsäcker proposed a very successful formula for the nuclear binding energies [67, 68]. In their formalism, the binding energy $B(N, Z)$ is obtained as a function of proton number Z and neutron number N with mass number $A = N + Z$,

$$B(N, Z) = a_{\text{vol}}A - a_{\text{surf}}A^{2/3} - a_c\frac{Z^2}{A^{1/3}} - a_{\text{sym}}(A)\frac{(N-Z)^2}{A}, \tag{1.9}$$

where the different terms correspond to the volume, surface, Coulomb and symmetry energies. A fit of this equation to known atomic masses across the nuclear chart can, in principle, yield the symmetry energy. However, since the symmetry energy contribution to the total binding energy can be small relative to those from the other terms, the unambiguous determination of E_{sym} and L_{sym} has proven difficult. To overcome this issue several refinements to the Bethe-Weizacker mass formula such as the Finite Range Droplet Model [69] have been proposed. These include additional microscopic features such as shell effects as well as macroscopic features such as axially asymmetric nuclear ground states . Finally, when nuclear masses where reproduced to within 0.1%, the parameters E_{sym} and L_{sym} were constrained with an accuracy of about 1.5% and 20% respectively [11], see Fig. 1.9.

Isobaric Analog State energies

Fits of nuclear binding energies to mass models must address ambiguities stemming from the similarities in the influences of the different terms in Eq. (1.9) over the range of experimentally measured masses. These ambiguities in the determination of the symmetry energy can be removed by taking advantage of the charge independence of nuclear interactions, i.e. to a very good approximation, strong interactions between nucleons do not depend on whether the nucleons are protons or neutrons. For example, the nucleus ^{12}C($Z = N = 6$) has the same wavefunction and nuclear contribution to the binding energy as the nucleus ^{12}B($Z = 5, N = 7$). The ^{12}C nucleus is called the "isobaric analog" of ^{12}B. It follows from Eq. (1.9) that the energy differences between two such isobaric analogs are given solely by the symmetry energy, apart from a trivial Coulomb contribution that can be fixed by fitting to the whole mass table.

Therefore, by fitting to the excitation energies of isobaric analog states, Ref. [70] obtained constraints on E_{sym} and the L_{sym} parameter. Fig. 1.9 shows these constraints, labelled IAS+ΔR, after a refinement including the diffusivity of the neutron skin was taken into account in the calculation [71].

Neutron skin thickness measurements

In light and intermediate mass nuclei with N approximately equal to Z, the neutrons and protons have similar density distributions. With increasing neutron number, the radius of the neutron density distribution becomes larger than that of the protons, reflecting the influence of the symmetry energy. The difference δR of the neutron and proton root mean square radii is called the neutron skin, i.e.

$$\delta R = \langle r^2\rangle_n^{1/2} - \langle r^2\rangle_p^{1/2}. \tag{1.10}$$

Proton radii have been determined accurately for many nuclei using electron scattering experiments [72]. This accuracy is due to the accuracy of perturbative treatments of the electromagnetic process. The neutron density distribution is more difficult to measure. Recently, the neutron radius in ^{208}Pb has been measured by the PREX experiment in Jefferson Laboratory. This experiment extracts the neutron radius in ^{208}Pb via parity violating electron scattering. Since parity violating scattering is mediated only by the weak interaction, this experiment measures the weak charge distribution in the ^{208}Pb nucleus. Furthermore, the weak charge inside the nucleus arises dominantly from the neutrons since the contribution from the protons is suppressed by the Weinberg angle [73]. Thus a measurement of the parity violating amplitude allows for an accurate determination of the neutron skin thickness.

Due to technical problems in the initial run of the experiment, uncertainties obtained by the PREX collaboration were quite significant with the measured $\delta R = 0.33^{+0.16}_{-0.18}$ fm [74]. However, in 2021 the updated PREX measurement, PREX-II delivered on the promise to determine the neutron radius of ^{208}Pb with a precision of nearly 1%. They reported a value of $\delta R = 0.283 \pm 0.071$ fm [75]. Subsequently Ref. [66] analysed the implications of this measurement on the value of the E_{sym} and L_{sym} parameters. They found that $E_{\text{sym}} = 38.1 \pm 4.7$ MeV and $L_{\text{sym}} = 106 \pm 37$ MeV. The discrepancy between this result as compared to other measurements is made clear in the right panel of Fig. 1.9. The astonishingly large value for L_{sym} has stirred much debate in the community recently [76].

1.4 Summary and the structure of the thesis

In this chapter, the basic purpose of this thesis i.e. the study of the nature of dense matter was introduced. We discussed that NSs serve as unique laboratories which allow us to study dense and cold matter. Furthermore, we stressed that recent incredible measurements of NSs have ushered in the era of multi-messenger NS astronomy, making this period an ideal time to explore the physics of NSs. Finally, we clarified how experimental data probing matter in the bulk of atomic nuclei can be helpful in understanding the neutron rich matter present in NSs.

The rest of this thesis is organized as follows. In chapters 2 and 3, we will analyse the nuclear symmetry energy in detail. While, the symmetry energy was introduced briefly in Sec. 1.3, we will define and study this quantity in a much more rigorous manner. For this analysis, we will use a certain microscopic ab-initio calculation that is referred to as chiral Effective Field Theory (EFT). In chapter 4, we will build upon the analyses of chapters 2 and 3 in order to apply the results of chiral EFT in the study of the crust of NSs. In this process, we will also enunciate on the concept of an unified EoS that is applicable to both the crust and the core of NSs. Chapters 2 to 4 constitute part I of this thesis.

Partly motivated by the fact that the sound speed in NSs is expected to be a significant fraction of the speed of light, part II of this thesis will be focused on the development of relativistic models for nuclear matter. In particular, we will focus on relativistic models in which the connection to the underlying properties of QCD, such as chiral symmetry and confinement, are well established. We will confront such models against other models that do not have such a clear connection to QCD. In contrast to chiral EFT, these relativistic models will be more phenomenological in nature, i.e. at least some of the model parameters will be fit to empirical saturation properties. However, the work developed in this part of the thesis will serve as a useful tool in future analyses that attempt to study dense matter in a Lorentz-covariant approach while keeping the connection to fundamental QCD properties.

In part III of this thesis, we will work on the question of phase transitions in NSs. It is certainly possible that at some densities explored in NSs, exotic degrees of freedom other than nucleons appear. It will be the purpose of this part of the thesis to study different kinds of transitions in dense matter. In particular, we will focus on first order phase transitions to exotic matter as well as a crossover transition to quarkyonic matter. We will then attempt to determine if astrophysical observations require the presence of these kinds of phase transitions in a physics-agnostic manner. Finally, the implications of perturbative QCD calculations for the equation of state of neutron star matter are also discussed at the end of this part.

Most of the results presented in this thesis have been published in the following articles.

- R. Somasundaram, C. Drischler, I. Tews, and J. Margueron, *Constraints on the nuclear symmetry energy from asymmetric-matter calculations with chiral NN and 3N interactions.*
  Published in: Phys.Rev.C 103 (2021) 4, 045803.
- G. Grams, J. Margueron, R. Somasundaram, and S. Reddy, *Confronting a set of Skyrme and Chiral EFT predictions for the crust of neutron stars.*
  Published in: Eur.Phys.J.A 58 (2022) 3, 56.
- G. Grams, R. Somasundaram, J. Margueron, and S. Reddy, *Properties of the neutron star crust: Quantifying and correlating uncertainties with improved nuclear physics.*
  Published in: Phys.Rev.C 105 (2022) 3, 035806.
- G. Grams, J. Margueron, R. Somasundaram, and S. Reddy, *Properties of Neutron Star Crust with Improved Nuclear Physics: Impact of Chiral EFT Interactions and Experimental Nuclear Masses.*
  Published in: Few-Body Syst 62, 116 (2021).
- R. Somasundaram, J. Margueron, G. Chanfray, and H. Hansen, *Confrontation of Different Relativistic Descriptions of Nuclear Matter.*
  Published in: Eur.Phys.J.A 58 (2022) 5, 84.
- R. Somasundaram and J. Margueron, *Impact of massive neutron star radii on the nature of phase transitions in dense matter.*
  Published in: EPL 138 (2022) 1, 14002.
- R. Somasundaram, I. Tews, and J. Margueron, *Investigating Signatures of Phase Transitions in Neutron-Star Cores.*
  e-Print: 2112.08157 [nucl-th].
- R. Somasundaram, I. Tews, and J. Margueron, *Perturbative QCD and the Neutron Star Equation of State.*
  e-Print: 2204.14039 [nucl-th].

Part I

Analysis and Implications of Chiral EFT Calculations

Chapter 2

Nuclear-Matter Equation of State and the Symmetry Energy

2.1 Introduction

Since the discovery of Neutron Stars (NSs) in 1967, the accurate prediction of the properties of nuclear matter has become of great importance and a lot of effort, both from theory and experiment, has been devoted to this aim. Further, the *Equation of State* (EoS) of nuclear matter connects neutron-rich matter inside NSs with the bulk properties of atomic nuclei [77, 78], making it extremely valuable for nuclear physics, see recent reviews [79, 80, 81] and references therein.

As mentioned in Sec. 1.3, nuclear matter is characterized by the total baryon number density $n = n_n + n_p$ and the isospin asymmetry $\delta = (n_n - n_p)/n$, where n_n (n_p) denotes the neutron (proton) number density. The EoS of nuclear matter is primarily a description of the energy per particle in this infinite medium as a function of density and isospin asymmetry, i.e. $e(n, \delta)$. In particular, the isospin dependence of the EoS is very important as it can be shown to, for example, govern the proton fraction in beta-equilibrium, determine the pressure in the core of NSs, and hence, the NS mass-radius relation [82, 83, 84], and cooling via the direct URCA process [85]. This isospin dependence of the EoS is represented by a quantity called the nuclear *symmetry energy*. Due to its importance for many physical systems, the symmetry energy was identified as a key quantity for nuclear (astro)physics in the 2015 DOE/NSF Nuclear Science Advisory Committee Long Range Plan for Nuclear Science [86], and is actively investigated by combining information from nuclear theory, astrophysics, and experiments.

Because NS observations still come with sizable uncertainties, the symmetry energy and its density dependence cannot be inferred from NS properties alone [85]. Hence, various constraints on the symmetry energy have be been inferred from experimental data, e.g., determinations of neutron skins in lead (PREX) and calcium (CREX) [74, 87], collective modes such as giant dipole resonances [88], and heavy-ion collisions [11, 63], see Sec. 1.3 for a discussion of some of these experiments. The determination of the symmetry energy is on the road-map for several future experiments conducted at rare-isotope beam facilities such as FRIB at MSU, SPIRAL2 at GANIL, and FAIR at GSI.

An extraction of the symmetry energy from nuclear theory as well as from nuclear experiments and astrophysical programs requires that the measured quantities in these different approaches, as well as their relations, are well defined. Different approximations for the symmetry energy are commonly used. It is, therefore, important to clarify whether the symmetry energy measured in laboratory experiments is the same quantity as the one inferred from NS properties. The energy per particle of nuclear matter at zero temperature can be represented as an isospin-asymmetry expansion from symmetric nuclear matter (SNM, $\delta = 0$) to pure neutron matter (PNM, $\delta = 1$),

$$e(n,\, \delta) \approx e(n,\, \delta = 0) + \delta^2\, e_{\text{sym},2}(n) + \delta^4\, e_{\text{sym},4}(n) + \mathcal{O}(\delta^6)\,. \tag{2.1}$$

Here $e_{\text{sym},2}(n)$ and $e_{\text{sym},4}(n)$ are the quadratic and quartic contributions to the symmetry energy, respectively. Given the expansion (2.1), the quadratic contribution to the symmetry energy is defined by the second derivative

$$e_{\text{sym},2}(n) = \frac{1}{2}\frac{\partial^2 e(n,\delta)}{\partial \delta^2}\bigg|_{\delta=0}\,, \tag{2.2}$$

similar to the empirical Bethe-Weizsäcker mass formula for finite nuclei. Hence, $e_{\text{sym},2}(n)$ is often referred to as the symmetry energy, and used in nuclear experiments. In practice, however, the more commonly used definition of the symmetry energy is given by the difference between the energy per particle in PNM and SNM,

$$e_{\text{sym}}(n) = e_{\text{PNM}}(n) - e_{\text{SNM}}(n)\,. \tag{2.3}$$

While definition (2.3) requires the EoS only in the limits of PNM and SNM, Eq. (2.2) necessitates explicit calculations of isospin-asymmetric nuclear matter (ANM). Both $e_{\text{sym},2}(n)$ and $e_{\text{sym}}(n)$ are equal if the isospin dependence of the energy per particle is *purely* quadratic, i.e., non-quadratic terms in the expansion (2.1) vanish. However, there is no *a priori* argument why this should be the case. In fact, non-quadratic terms have been found to be relevant for, e.g., accurate studies of nuclear matter in beta-equilibrium at supra-saturation density [89, 90, 91, 92] and the crust-core transition density in NSs [91, 93].

In chapters 2 and 3, we will confront the expansion (2.1) with the explicit ANM calculations based on chiral nucleon-nucleon (NN) and three-nucleon (3N) interactions reported in Ref. [94] and quantify the impact of non-quadratic contributions to the symmetry energy. We also investigate to which extent uncertainties in the microscopic approach affect the extraction of non-quadratic contributions to the symmetry energy. In more details, Sec. 2.2 gives an overview of previous studies of non-quadratic contributions to the symmetry energy. In Sec. 2.3, we present our computational setup where we explain the details of the microscopic models that we have chosen to analyse and, in Sec. 2.3.2, we compare it with other calculations. The complete analysis of the EoS will be presented in chapter 3.

2.2 Previous studies of non-quadratic contributions

As stated above, there is no *a priori* reason for the isospin-asymmetry expansion to be purely quadratic. In general, even the free Fermi gas (FFG) energy per particle, given by

$$e^{\text{FFG}}(n) = \frac{t_{\text{SNM}}^{\text{sat}}}{2} \left(\frac{n}{n_{\text{sat}}}\right)^{2/3} \left[(1+\delta)^{5/3} + (1-\delta)^{5/3}\right] , \tag{2.4}$$

with $t_{\text{SNM}}^{\text{sat}} = \frac{3}{5m_N}\left(\frac{3\pi^2}{2}n_{\text{sat}}\right)^{2/3} \approx 22.1\,\text{MeV}$, leads to non-quadratic contributions to the expansion (2.1). Here, n_{sat} is the empirical saturation density.

The quartic term,

$$e_{\text{sym},4}^{\text{FFG}}(n) \simeq 0.45\,\text{MeV} \times \left(\frac{n}{n_{\text{sat}}}\right)^{2/3} , \tag{2.5}$$

represents a $\approx 3.5\%$ correction to the FFG symmetry energy at n_{sat}. Nuclear interactions also contribute to non-quadratic terms; for example, the phenomenological Skyrme interaction [95] gives the following quartic contribution to the symmetry energy:

$$e_{\text{sym},4}^{\text{Skyrme}}(n) \simeq e_{\text{sym},4}^{\text{FFG}}(n) + \frac{k_{\text{F}}^5}{972\pi^2}\left[3t_1(1+x_1) + t_2(1-x_2)\right] , \tag{2.6}$$

where k_{F} is the Fermi momentum. The Skyrme parameters (t_1, t_2) represent the correction to the bare nucleon mass generated by in-medium effects. Since the Skyrme in-medium mass is generally $\approx 30-40\%$ lower than the bare mass [95], these terms increase the $e_{\text{sym},4}^{\text{FFG}}$ by $\approx 30-40\%$ to $\approx (0.7-0.8)\,\text{MeV}$. In a recent work, Cai and Li [92] found $e_{\text{sym},4}(n_{\text{sat}}) = (7.2 \pm 2.5)$ MeV, which indicates a rather significant difference between e_{sym} and $e_{\text{sym},2}$. They employed an empirically constrained isospin-dependent single-nucleon momentum distribution and the EoS of PNM near the unitary limit. Subsequently, Bulgac *et al.* found that $e_{\text{sym},4}(n = 0.1\,\text{fm}^{-3}) = 2.635$ MeV is necessary in order to reproduce properties of both finite nuclei and the PNM EoS as calculated in Ref. [96]. In contrast, previous works, e.g., based on Brueckner-Hartree-Fock (BHF) approaches and hard-core interactions [97, 98, 99, 100] obtained only small non-quadratic contributions to the symmetry energy.

In a recent study of nuclear matter in many-body perturbation theory (MBPT) with contributions from 1π-exchange, 2π-exchange, and three-body terms involving virtual $\Delta(1232)$-isobars, Kaiser [101] could not confirm such large values for $e_{\text{sym},4}$. Instead, Kaiser found $e_{\text{sym},4} \simeq 1.5$ MeV at n_{sat}, which is still about three times larger than the FFG contribution. Moreover, Kaiser found contributions to the energy per particle whose fourth derivative with respect to δ are singular at $\delta = 0$. This was further substantiated by analytic MBPT calculations based on an S-wave contact interaction, which gave rise to a singular term $\propto \delta^4 \log|\delta|$—a term that only contributes to the ANM EoS when $\delta \neq 0$ and $\delta \neq 1$, and which will be referred to as the leading-order logarithmic term in the following.

Subsequently, Wellenhofer *et al.* performed a more detailed analysis of such divergences by examining the δ dependence of the nuclear EoS as a function of density and temperature [102]. They found that the asymmetry expansion is hierarchically ordered, i.e., the lower-order coefficients are dominant at high temperature and low density, but the expansion diverges at $\delta = 0$

with alternating sign in the zero-temperature limit. Around saturation density, their results indicate that the convergence of the series expansion is restored for $T \gtrsim 3$ MeV. Moreover, they have argued that the logarithmic term at leading order considerably improves the isospin-asymmetry expansion at zero temperature and suggested to include this term in future fits of the EoS.

While mathematically well-defined, it is not clear whether the aforementioned divergence of the series expansion in δ substantially impacts the practical usability of the expansion (2.1), because corrections remain small at nuclear densities. Our knowledge of the symmetry energy, and, more fundamentally, of the nuclear interaction itself, is limited by experimental precision and by the theoretical understanding of strongly interacting systems. As a consequence, while the series expansion in the isospin asymmetry can be determined with high accuracy when the nuclear interaction and the many-body treatment are fixed (with numerical limitations as discussed in Ref. [102]), current theoretical uncertainties reduce our ability to accurately determine high-order contributions in general. In this part of the thesis, we analyze the impact of these uncertainties on the determination of the symmetry energy.

2.3 Computation of the Equation of State

We will use the explicit ANM calculations of Ref. [94] at zero temperature to study the importance of non-quadratic contributions to the symmetry energy. The authors of Ref. [94] computed the EoS for ANM using a set of chiral NN and 3N interactions. We will therefore begin with a brief overview of Chiral Effective Field Theory (χEFT).

2.3.1 Overview of Chiral Effective Field Theory

Chiral symmetry is one of the most prominent low-energy features of the gauge theory of colored quarks and gluons (QCD) established in the 1970's. The $\mathrm{SU}(\mathrm{N_f}=2)$ chiral symmetry of QCD means that, in the limit of zero quark masses (called the chiral limit), light (u,d) quarks [1] with opposite parity are indistinguishable from each other. At energies relevant for nuclear physics, chiral symmetry is spontaneously broken due to the condensation of quark-antiquark pairs, mixing left handed and right handed quarks in the QCD vacuum: QCD prefers quark-antiquark pairs with negative parity to the quark-quark pairs with positive parity [103]. Furthermore, according to Goldstone's theorem, spontaneous symmetry breaking leads to Goldstone bosons, which are massless excitations of the vacuum. These Goldstone bosons of spontaneously broken chiral symmetry are associted with the pions.

In addition to the spontaneous chiral symmetry breaking one expects a small but explicit symmetry breaking originating from finite quark masses. For small masses indeed, as it is the case in the physical world, chiral symmetry is explicitly broken. In reality the "Goldstone" bosons are therefore quasi-Goldstone bosons with small masses. This explains why the quasi-Goldstone boson, identified as the pion, has a small mass $\simeq 140$ MeV compared to the other mesons. The Gellmann-Oakes-Renner relation, $f_\pi^2 m_\pi^2 = -2m_q \left<\bar{q}q\right>_{vac}$, relates the pion mass m_π to m_q, the small but finite mass of the light u and d quarks.

---

[1] For the description of hyper-nuclei, this concept of chiral symmetry can be extended to the s quark within $\mathrm{SU}(\mathrm{N_f}=3)$. In the present study, we however limit ourself to the $\mathrm{SU}(2)$ case.

These chiral properties can be implemented in chiral perturbation theory. In this chiral EFT framework initiated by Weinberg [104], the most general Lagrangian is expressed in terms of the pionic degrees of freedom, dictated by symmetries, e.g. chiral symmetry. Nucleons can be introduced as heavy sources coupled to pions, see Ref. [105] for a recent review, while heavy mesons and nucleon resonances are integrated out and replaced by corresponding counter-terms in the Lagrangian, since their masses happen to be much higher than the designed resolution scale of the model. This effective approach is however unable to fix the parameters of the Lagrangian, which are fitted to vacuum data. Within these limitations, the resulting EFT is expected to be equivalent to QCD at low energy.

2.3.2 Nuclear Matter calculations from Chiral Lagrangians

As mentioned earlier, we use the explicit ANM calculations of Ref. [94] at zero temperature to study the importance of non-quadratic contributions to the symmetry energy. The authors of Ref. [94] used chiral NN and 3N interactions to compute the EoS in the framework of Many Body Perturbation Theory (MBPT). Specifically, we analyze their results obtained with the improved (angle averaging) approximation for normal ordering 3N forces and in a Hartree-Fock single-particle spectrum. The calculations in Ref. [94] are based on the set of six chiral NN and 3N interactions summarized in Table 2.1. These interactions are also commonly used in nuclear-structure calculations [106, 108, 109, 110, 111, 112, 113, 114, 115, 107]. They combine the N^3LO NN potential EM $500\,\mathrm{MeV}$ [116] evolved to lower momentum scales λ using the similarity renormalization group (SRG) with bare N^2LO 3N forces regularized by a nonlocal regulator with momentum cutoff $\Lambda_{3\mathrm{N}}$. Hebeler *et al.* then fit the two 3N low-energy couplings c_D and c_E for the different combinations of λ and $\Lambda_{3\mathrm{N}}$ shown in Table 2.1 to the triton binding energy as well as the charge radius of ^{4}He [117]. Assuming N^2LO 3N forces provide a sufficiently complete operator basis, and the long-range low-energy couplings c_1, c_3, and c_4 are SRG-invariant, this approach captures dominant contributions from induced three–body forces due to the SRG transformation. Note that the c_i's appear both in the NN and 3N interactions at N^2LO. As discussed in Ref. [94], the spread in the energy per particle obtained from these nuclear interactions can serve as a simple uncertainty estimate—though with limited statistical meaning.

The energy per particle in PNM obtained in Ref. [94] is depicted in panel (a) of Fig. 2.1 by blue dots whereas panel (b) represents the ratio of the energy per particle over the FFG energy. In this work, we perform least-squares fits of nonlinear functions to this data. Each fit parameter is guided by a (Bayesian) prior, which distinguishes our parametric fits[2] from a standard χ^2 minimization. The parametric fits result in the posterior distributions shown as dark (light) red bands corresponding to 68% (95%) confidence intervals in Fig. 2.1.

In Fig. 2.1, we also provide comparisons with the variational calculation of Ref. [119] (APR), Fock-space formulated Quantum Monte Carlo (QMC) calculations of Ref. [96] (Wlazlowski *et al.* 2014), and continuum QMC calculations using auxiliary field diffusion Monte Carlo of Ref. [120] (Tews *et al.* 2016). These calculations were not only conducted using different many-body approaches, but also different nuclear interactions: the APR result uses the Argonne v_{18} (AV18) NN potential [122] and the Urbana IX (UIX) 3N force [123], Ref. [96] employs the nonlocal momentum-space chiral N^3LO NN interactions of Ref. [124] combined

---

[2] These fits were performed using the LSQFIT Python package [121]

Table 2.1: Nonlocal $\mathrm{N^3LO}$ NN and $\mathrm{N^2LO}$ 3N interactions used in the MBPT calculations of Ref. [94]. The interactions are based on the $\mathrm{N^3LO}$ NN potential EM $500\,\mathrm{MeV}$ [116] evolved to the SRG resolution scale λ. The low-energy couplings c_D and c_E were subsequently fit to the triton binding energy and the charge radius of ^{4}He in Ref. [117] for different combinations of λ and the 3N cutoff $\Lambda_{3\mathrm{N}}$. The 3N two-pion exchange is governed by the πN low-energy couplings c_1, c_3, and c_4, which were taken from the NN potential, except for H7 which uses the values obtained from the NN partial-wave analysis (PWA) of Ref. [118]. Hamiltonian H6 has been excluded as discussed in Section IV B of Ref. [94].

label	$\lambda\ [\mathrm{fm}^{-1}]$	$\Lambda_{3\mathrm{N}}\ [\mathrm{fm}^{-1}]$	3N $c_{1,3,4}$	c_D	c_E
H1	1.8	2.0	NN potential	$+1.264$	-0.120
H2	2.0	2.0	NN potential	$+1.271$	-0.131
H3	2.0	2.5	NN potential	-0.292	-0.592
H4	2.2	2.0	NN potential	$+1.214$	-0.137
H5	2.8	2.0	NN potential	$+1.278$	-0.078
H7	2.0	2.0	PWA [118]	-3.007	-0.686

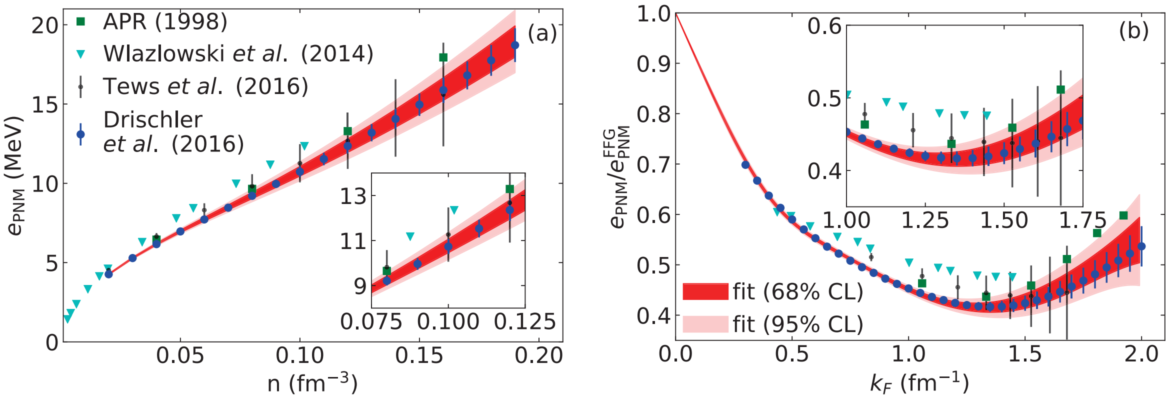

Figure 2.1: Comparison of the MBPT predictions for the (a) energy per particle in PNM [94] (blue points) with the APR EoS [119] (green squares), QMC calculations of Wlazlowski *et al.* (2014) [96] (cyan triangles), and Tews *et al.* (2016) [120] (black dots) using different chiral EFT Hamiltonians with NN and 3N forces. The latter points include simple estimates for the EFT truncation error of the chiral expansion. We also show our fit posterior at 68% (95%) confidence level as dark (light) red bands. (b) The same comparison but with a different scaling.

with $\mathrm{N^2LO}$ 3N forces as specified in Ref. [125], and Ref. [120] uses local coordinate-space chiral interactions constructed in Refs. [126, 127, 128]. The first two calculations do not provide theoretical uncertainties, while the latter estimates the standard EFT uncertainty [129]. Note that, in general, order-by-order calculations are required for estimating EFT truncation errors. Such calculations are not possible with the chiral Hamiltonians given in Table 2.1.

When comparing the approaches using chiral EFT interactions, the QMC calculations of Ref. [120] agree with the MBPT approach employed in this work within uncertainties above $n \approx 0.08\,\mathrm{fm}^{-3}$, while QMC finds slightly higher energies at lower densities. In contrast, the QMC calculations of Ref. [96] find a higher PNM energy per particle at all densities, by about ≈ 1 MeV. We also compare the ratio $e_{\mathrm{PNM}}/e^{\mathrm{FFG}}_{\mathrm{PNM}}$ as a function of neutron Fermi momentum k_{F} for the various calculations in the bottom panel of Fig. 2.1. In the figure, we can identify the density region where the ratio exhibits a plateau, indicating a similar scaling of e_{PNM} and e^{FFG} with k_{F}. For the MBPT calculation, we find the ratio at the plateau to be $\approx 0.42(1)$ in PNM at momenta $k_{\mathrm{F}} \approx 1.3(2)\,\mathrm{fm}^{-1}$, which describes densities at $\approx n_{\mathrm{sat}}/2$.

The comparison of the different results in Fig. 2.1 provides a qualitative illustration of the uncertainties originating from the nuclear interactions as well as from the different many-body approaches. While the MBPT results of Ref. [94] provide a simple uncertainty estimate, they do not quantify EFT truncation errors, which can be significant at $n \gtrsim n_0$. Future order-by-order calculations of ANM will enable statistically robust EFT uncertainty estimates using the Bayesian framework recently developed by the BUQEYE collaboration [65, 130]. In the present analysis, however, such systematic ANM calculations are not available. Therefore, we follow the approach in Ref. [94], and consider the spread of the EoSs due to the Hamiltonians in Table 2.1 as an uncertainty estimate.

2.4 Summary

In this chapter, we have discussed the importance of the nuclear-matter EoS and the symmetry energy. We introduced the isospin expansion of the energy per particle (2.1) which allowed us to clarify the difference between the quadratic symmetry energy (2.2) and the total symmetry energy (2.3). The importance and the need to distinguish these two quantities were enunciated and we then reviewed the literature on non-quadratic contributions to the symmetry energyin Sec. 2.2. The following chapter 3 will be focused on a detailed computation of both e_{sym} and $e_{\mathrm{sym},2}$ as well as an analysis of the EoS in the limits of SNM and PNM. The reference microscopic calculations used to perform this analysis are those of Ref. [94] which used chiral NN and 3N interactions to compute the EoS in the framework of many-body perturbation theory. Therefore, in this chapter, we also briefly reviewed the basic principles of chiral EFT (in Sec. 2.3.1) and discussed the details of the chiral Hamiltonians used in our work. Additionally we compared our results for the EoS in PNM with some other state-of-the-art ab-initio calculations in Sec. 2.3.2.

Chapter 3

Meta-Model Analysis of the Equation of State from Chiral EFT

After the introduction of the nuclear-matter Equation of State discussed in the previous chapter, we will now focus on a detailed Bayesian analysis of the EoS using the *meta-model* [64, 131]. Let us first review the isospin expansion of the energy per particle introduced in Chapter 2. This will allow us to generalize this expansion which, in turn, will be useful for the up-coming analysis.

3.1 Energy expansion in the isospin asymmetry parameter δ

A general expression for the expansion (2.1) of energy observables in nuclear matter was suggested in Ref. [102], from which we consider all contributions up to δ^4, including the logarithmic term, and rewrite it as

$$y(n,\delta) \approx y_{\text{SNM}}(n) + y_{\text{sym},2}(n)\delta^2 + y_{\text{sym},4}(n)\delta^4 + y_{\text{sym,log}}(n)\delta^4 \log|\delta| \,, \tag{3.1}$$

see Eq. (27) of Ref. [102] for more details. In the following, we will treat this expression as a parametrization of the EoS's δ dependence, in which the coefficients are determined by parametric fits, rather than a formal expansion in δ. The term $y_{\text{sym,log},4}\delta^4 \log|\delta|$ originates from the second-order contribution in the many-body expansion, as explained in Ref [102].

The corresponding contribution to the symmetry energy y_{sym} is defined as

$$y_{\text{sym}}(n) \quad = \quad y_{\text{PNM}}(n) - y_{\text{SNM}}(n) \,. \tag{3.2}$$

The non-quadratic contribution to the symmetry energy is defined as

$$y_{\text{sym,nq}}(n) \quad = \quad y_{\text{sym}}(n) - y_{\text{sym},2}(n) \,. \tag{3.3}$$

Note, that since the logarithmic term vanishes in SNM and PNM, it also does not contribute to the non-quadratic term (3.3).

The quantity y in Eq. (3.1) can be the energy per particle e, as originally suggested by Kaiser [101], or any other energy contribution. For instance, it can be the potential energy

$y = e^{\text{pot}}$ or the effective potential energy $y = e^{\text{pot}*}$ defined as

$$e^{\text{pot}}(n,\delta) \;=\; e(n,\delta) - t(n,\delta)\,, \tag{3.4}$$

$$e^{\text{pot}*}(n,\delta) \;=\; e(n,\delta) - t^*(n,\delta)\,, \tag{3.5}$$

where t and t^* are the kinetic and effective kinetic energies (see Eq. (3.12) below) respectively. In the following, we use these notations for analyzing the δ-dependence of the total, potential, and effective potential energies.

The rest of this chapter is organized as follows. In Sec. 3.2, the derivation of the Landau effective mass from the single-particle energy is presented. We then discuss the EoS in the limits of PNM and SNM in Sec. 3.3, followed by the symmetry energy in Sec. 3.4. Finally, we conclude in Sec. 3.5. The Python codes used to perform the analysis and generate the figures are publicly available on GitHub [132].

3.2 Landau mass contribution to the symmetry energy

Non-trivial contributions to the symmetry energy can arise due to the effective mass, see for instance Eq. (2.6). Therefore we characterize these effects here before commencing our analysis of the energy per particle. The calculations performed here will allow us to introduce the effective kinetic energy t^* which is necessary to compute the quantity $y = e^{\text{pot}*}(n,\delta)$ introduced in Sec. 3.1. We start with the single-particle energy $\epsilon_\tau(k)$ in a Hartree-Fock spectrum (as in Ref. [94]),

$$\epsilon_\tau(k,n,\delta) \approx \frac{k^2}{2m_\tau} + \Sigma^{(1)}(k,n,\delta)\,. \tag{3.6}$$

The first term in Eq. (3.6) is the single-particle kinetic energy, while the second term $\Sigma^{(1)}$ denotes the spin-isospin-averaged first-order self-energy. We refer the reader to, e.g., Refs. [133, 94] for more details.

First, we consider the single particle energies calculated from Eq. (3.6). Figure 3.1 shows the single-particle energy $\epsilon_n(k)$ in SNM and PNM evaluated at $n_{\text{sat}}^{\text{emp}}$. The left (right) panel depicts the NN-only (NN+3N) results, and the vertical lines mark the position of the neutron Fermi momentum in SNM ($k_{F,\text{SNM}} = 1.33\,\text{fm}^{-3}$) and PNM ($k_{F,\text{PNM}} = 1.68\,\text{fm}^{-3}$) associated with the nuclear saturation density, $n_{\text{sat}}^{\text{emp}}$. The different curves show the results for the six Hamiltonians H1 to H7 specified in Table 2.1. The spread is larger in SNM (about 15 MeV) compared to PNM (about 5 MeV) because the 3N short- and intermediate-range contributions governed by c_D and c_E do not contribute to the PNM EoS for nonlocal regulator functions. As expected, SNM is more attractive than PNM, as a result of the attractive contributions from the $T = 0$ channels, which are absent in PNM.

The momentum dependence of the nuclear interactions can be absorbed by modifying the nucleon mass, which gives rise to the so-called in-medium effective mass and the Landau mass. Specifically, Eq. (3.6) can be approximated as,

$$\epsilon_\tau(k,n,\delta) \approx \frac{k^2}{2m^*_\tau(k,n,\delta)} + \Sigma^{(1)}(k=0,n,\delta), \tag{3.7}$$

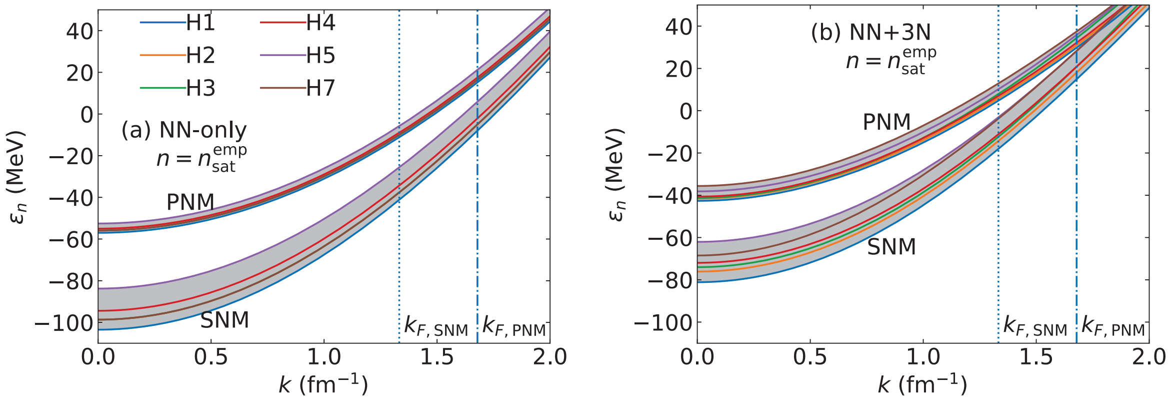

Figure 3.1: The neutron single-particle energies $\epsilon_n(k)$ as a function of the momentum k calculated at $n_{\rm sat}^{\rm emp}$, and extracted from the MBPT calculations of Ref. [94]. The different colors correspond to the six Hamiltonians as labeled in the legend. We show the single particle energies obtained from (a) only NN forces and (b) when including 3N contributions. In each panel, we present results for both SNM and PNM.

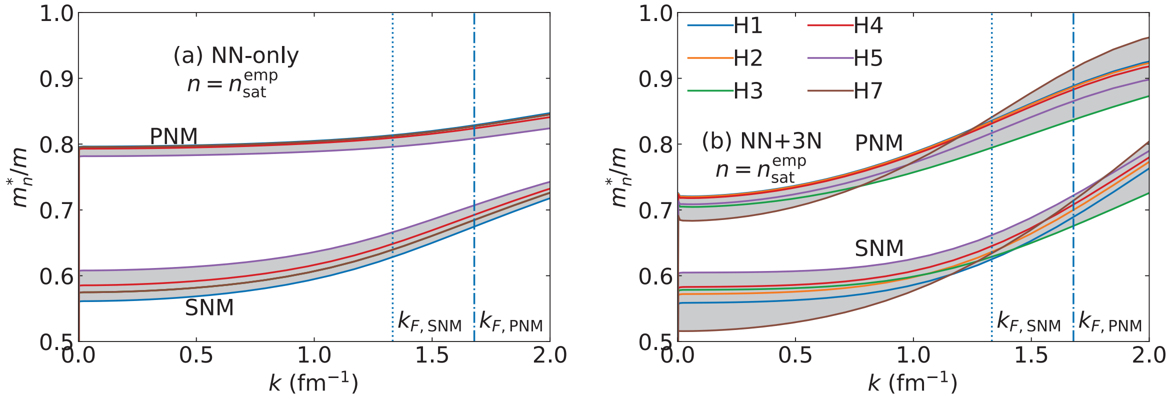

Figure 3.2: Same as Fig. 3.1 but for the neutron effective mass as function of the momentum k.

where the in-medium effective mass is defined as [134],

$$\frac{m_\tau^*(k,n,\delta)}{m_\tau} = \frac{k}{m_\tau}\left(\frac{d\epsilon_\tau(k,n,\delta)}{dk}\right)^{-1}. \tag{3.8}$$

Finally, the Landau mass is defined as the effective mass (3.8) evaluated at $k{=}k_{\rm F}$.

The effective masses in SNM and PNM are shown in Fig. 3.2 as functions of the momentum k at a fixed density $n_{\rm sat}^{\rm emp}$. The effective masses are lower in SNM compared to PNM, in agreement with BHF calculations [97, 135, 136]. We find that the inclusion of 3N forces leads to several interesting effects on the effective mass: (a) 3N forces generate a stronger momentum dependence compared with NN-only calculations, and (b) 3N forces have a larger impact on PNM than on SNM. Furthermore, the dispersion among the different Hamiltonians is slightly larger when 3N forces are included. From Fig. 3.2, we find for the Landau mass $m_n^*/m(\delta{=}0) = 0.64(2)$ in SNM and $m_n^*/m(\delta{=}1) = 0.88(4)$ in PNM when 3N forces are

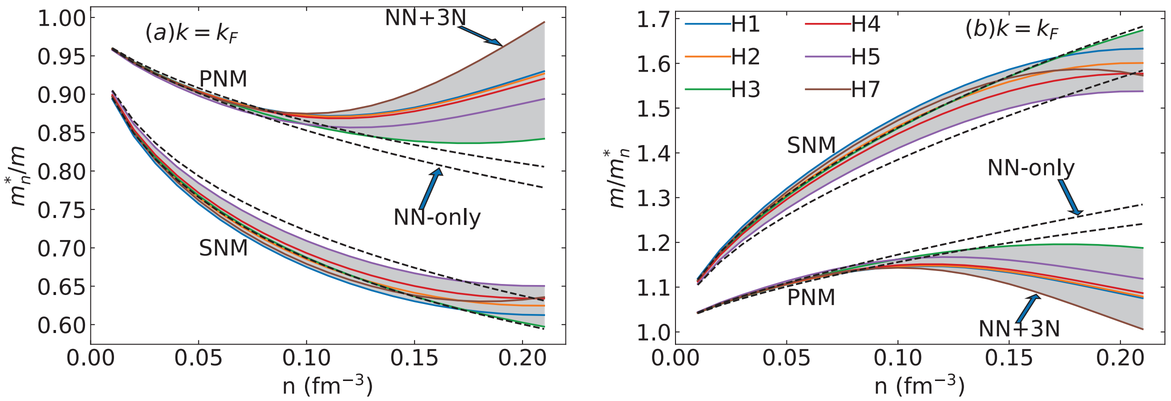

Figure 3.3: (a) Landau effective mass and (b) its inverse in SNM and PNM as a function of the density. The black-dashed lines represent the upper and lower limits when only NN forces are considered, while the grey-shaded regions show the results with 3N forces included. The different colors correspond to the six Hamiltonians as labeled in the legend.

included. The difference between the Landau mass in PNM and SNM at saturation density, defined as

$$Dm^*_{n,\text{sat}} = m^*_n(n_\text{sat}, \delta = 1) - m^*_n(n_\text{sat}, \delta = 0)\,, \tag{3.9}$$

is about $Dm^*_{n,\text{sat}} = 0.24(5)$ at n_sat.

In Fig. 3.3, we show the Landau mass (left) and its inverse (right) considering NN-only forces (dashed lines) and NN and 3N forces (gray bands) in SNM and PNM as a function of the density, n. The difference of the Landau masses in PNM and SNM, $Dm^*_n(n)$, increases with density, and is found to be about 0.24 at saturation density, see also Fig. 3.2. While it is usually found that the Landau mass decreases with density [97, 135, 136], we find that in PNM the Landau mass first decreases at lower density, but increases again for $n > 0.1\,\text{fm}^{-3}$ (except for Hamiltonian H3, which has a higher momentum cutoff applied to the 3N forces). This effect is due to the inclusion of 3N interactions in the Hamiltonian.

Because many energy density functional (EDF) approaches approximate the inverse of the Landau mass by a linear function in density [95], we show the inverse Landau mass in the right panel of Figure 3.3. In contrast to the EDFs approaches, we find that the density dependence of the inverse Landau mass is not linear, and that 3N forces enhance the nonlinear behavior. To describe the inverse of the Landau mass as function of the density n and asymmetry parameter δ. We consider the following functional form:

$$\left(\frac{m^*_\tau}{m}(n,\delta)\right)^{-1} = 1 + \left(\frac{\kappa_\text{sat}}{n_\text{sat}} + \tau_3\delta\frac{\kappa_\text{sym}}{n_\text{sat}}\right) n + \left(\frac{\kappa_{\text{sat},2}}{n^2_\text{sat}} + \tau_3\delta\frac{\kappa_{\text{sym},2}}{n^2_\text{sat}}\right) n^2\,, \tag{3.10}$$

where $\tau_3 = 1(-1)$ for neutrons (protons). Note that we have neglected terms of higher order in δ in Eq. (3.10). The parameters κ_sat, $\kappa_{\text{sat},2}$, κ_sym, and $\kappa_{\text{sym},2}$ are obtained from fitting the expression (3.10) (in SNM and PNM) to the results computed using Eq. (3.8). The details of our parametric fits are discussed in Appendix A. The relevant fit parameters, p_α, are

$$p_\alpha = \{\kappa_\text{sat}/n_\text{sat}, \kappa_{\text{sat},2}/n^2_\text{sat}, \kappa_\text{PNM}/n_\text{sat}, \kappa_{\text{PNM},2}/n^2_\text{sat}\}\,. \tag{3.11}$$

Table 3.1: Fit parameters of the inverse Landau mass considering linear and quadratic density expansions. The fits are compared to three Skyrme-type interactions: NRAPR [77], LNS5 [137], and SAMI [138].

	$\kappa_{\text{sat}}/n_{\text{sat}}$ [fm^3]	$\kappa_{\text{sat},2}/n_{\text{sat}}^2$ [fm^6]	$\kappa_{\text{PNM}}/n_{\text{sat}}$ [fm^3]	$\kappa_{\text{PNM},2}/n_{\text{sat}}^2$ [fm^6]
linear	$3.33(18)$	–	$0.89(19)$	–
quadratic	$6.25(35)$	$-16.9(16)$	$2.63(14)$	$-11.1(19)$
NRAPR [77]	2.75	–	1.40	–
LNS5 [137]	4.12	–	2.19	–
SAMI [138]	3.03	–	2.87	–

These fit parameters are determined from the predicted Landau effective masses for each of the six Hamiltonians. The results of the fits for the inverse of the Landau mass are given in Table 3.1, where we have considered both, a linear and a quadratic fit function. The prior distribution for each of the fit parameters is given by a normal distribution with mean 0 and standard deviation 100, providing an uninformative prior. The fits are compared to three Skyrme-type interactions: NRAPR [77], LNS5 [137], and SAMI [138] that satisfy the following conditions: $0.6 \leqslant m^*/m(\text{SNM}) \leqslant 0.7$, $\Delta m^*/m > 0$ and $40\,\text{MeV} < L_{\text{sym}} < 60\,\text{MeV}$.

In Fig. 3.4, we compare the posterior distribution functions for the Landau mass in SNM (top panel) and PNM (bottom panel), and the input data. The predictions from the six Hamiltonians are plotted as solid lines, and, at each density, we calculate the centroid and 1σ interval given the six Hamiltonians (black points with error bars). The $\pm 1\sigma$ ($\pm 2\sigma$) contours of the posterior, corresponding to the 68% (95%) confidence region, are depicted in red (light red) for the quadratic fit and dark blue (light blue) for the linear fit. We have fit the models to the data in the range $n = 0.15 - 0.17\,\text{fm}^{-3}$ for the linear fit (3 data points) and from $n = 0.07 - 0.20\,\text{fm}^{-3}$ for the quadratic fit (14 data points). These values are chosen to allow for the ranges to be as large as possible while, at the same time, ensuring that the fits reproduce the data around saturation density. While the quadratic fit performs well even outside the fit interval, down to $n \approx 0.05\,\text{fm}^{-3}$ in SNM and PNM, the linear fit does not because of the strong curvature of the Landau mass. The differences between the linear and quadratic fits are further analyzed in Sec. 3.4.

The fact that the Landau mass induces non-trivial contributions to the symmetry energy can be seen by explicitly including it in the effective kinetic energy

$$t^*(n,\delta) = \frac{t_{\text{SNM}}^{\text{sat}}}{2}\left(\frac{n}{n_{\text{sat}}}\right)^{2/3}\left[\frac{m}{m_n^*(\delta)}(1+\delta)^{5/3} + \frac{m}{m_p^*(\delta)}(1-\delta)^{5/3}\right]. \tag{3.12}$$

We have used this expression for t^* (3.12) in order to present our generalized framework to

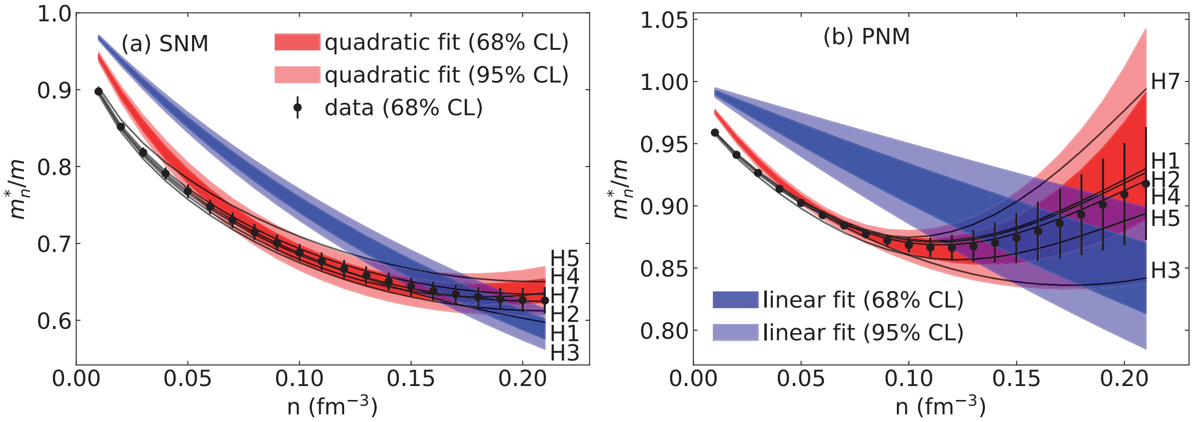

Figure 3.4: Results of the Bayesian parametric fits of the Landau mass in (a) SNM and (b) PNM. The 68% (95%) confidence levels for the posterior distribution functions are shown as dark-shaded (light-shaded) bands. The black lines represent the individual Hamiltonians, and the black points show the average over the six Hamiltonians with $\pm 1\sigma$ uncertainty bands.

analyze the EoS in the Sec. 3.1.

Finally, we study the splitting of the neutron and proton Landau masses in ANM, defined as

$$\Delta m^*_{\text{sat}}(\delta) = m^*_n(n_{\text{sat}}, \delta) - m^*_p(n_{\text{sat}}, \delta)\,. \tag{3.13}$$

In PNM ($\delta = 1$), this splitting can be expressed in terms of the difference Dm^*_{sat}, see Eq. (3.9), as

$$\frac{\Delta m^*_{\text{sat}}}{m}(\text{PNM}) \approx \frac{Dm^*_{n,\text{sat}}}{m} + \mathcal{O}\left(\left(\frac{\kappa_{\text{sym}} + \kappa_{\text{sym},2}}{1 + \kappa_{\text{sat}} + \kappa_{\text{sat},2}}\right)^2\right)\,. \tag{3.14}$$

From our fits estimated in Sec. 3.2, we can estimate that the neglected terms account for about 5% of the splitting (more precisely, 7% for the linear fit of the effective mass, and 3% for the quadratic fit), which is small considering the present uncertainty of this quantity. The splitting of the Landau mass is, thus, approximately given by the difference of the Landau mass between PNM and SNM. The splitting of the Landau mass obtained here is compatible with the one obtained in the literature for BHF [97, 139, 140] and Dirac-BHF [135, 136] approaches.

3.3 Meta-Model for Symmetric and Neutron matter

To describe the MBPT data for the energy per particle in SNM and PNM, we use in this work a functional form described by a Meta-Model (MM) for nuclear matter similar to the one suggested in Ref. [64], but generalized to a potential energy with non-quadratic δ dependence. The MM is adjusted to MBPT data sampled on a given grid in the asymmetry parameter δ [94]. This is in contrast to Ref. [102], who used a finite difference method [141] on an adjustable grid to determine all derivatives with respect to δ of interest. The MM, instead, provides a flexible polynomial-type approach to nuclear matter, which allows us to accurately determine the higher-order coefficients in the δ expansion, even for the fixed grid considered here.

For SNM and PNM, the energy per particle in the MM reads

$$e_\alpha^{\text{MM}}(n) \;=\; t_\alpha^*(n) + e_\alpha^{\text{pot}*}(n)\,, \tag{3.15}$$

where α stands for either SNM or PNM. The kinetic energy is determined by Eq. (3.12) with the Landau mass, see Sec. 3.2. The potential energies are expanded about n_{sat} in terms of the parameter

$$x \equiv \frac{n - n_{\text{sat}}}{3n_{\text{sat}}}$$

as follows

$$\begin{aligned}
e_{\text{SNM}}^{\text{pot}*}(n) \;&=\; \sum_{j=0}^{N} \frac{1}{j!} v_{\text{SNM},j} x^j + v_{\text{SNM}}^{\text{low}-\text{n}}\, x^{N+1} e^{-b_{\text{sat}} \frac{n}{n_{\text{sat}}^{\text{emp}}}}\,, \\
e_{\text{PNM}}^{\text{pot}*}(n) \;&=\; \sum_{j=0}^{N} \frac{1}{j!} v_{\text{PNM},j} x^j + v_{\text{PNM}}^{\text{low}-\text{n}}\, x^{N+1} e^{-b_{\text{PNM}} \frac{n}{n_{\text{sat}}^{\text{emp}}}}\,,
\end{aligned}$$

where the second term on the right-hand side is a low-density correction. This correction represents the low-density contribution of all higher-order terms neglected in the summation, and scales like x^{N+1} at leading order, where N is the upper limit of the power in the density expansion. In the original nucleonic MM of Ref. [64], the low-density EoS correction was simply parameterized by a fixed coefficient $b = b_{\text{sat}} = b_{\text{PNM}} \approx 6.93$. In the improved MM considered here, we introduce two parameters (b_{sat} and b_{PNM}) controlling the density dependence of the low-density corrections in PNM and SNM separately. It was suggested in Ref. [64] that using an expansion up to $N = 4$ allows for the reproduction of the pressure and sound speed of about 50 known energy density functional (EDF) up to about $4n_{\text{sat}}$. In principle, it is not necessary to consider such a high N in the present analysis. The inclusion of high-order contributions, however, affects the determination of the low-order ones, as discussed in Ref. [142], even if the data does not constrain the high-order terms themselves.

Imposing that the energies per particle vanish at $n = 0\,\text{fm}^{-3}$, we obtain the following relations

$$e_\alpha^{\text{pot}*}(n) \;=\; \sum_{j=0}^{N} \frac{1}{j!} v_{\alpha,j}\, x^j\, u_{\alpha,j}(x)\,, \tag{3.16}$$

where

$$u_{\alpha,j}(x) = 1 - (-3x)^{N+1-j} e^{-b_\alpha n / n_{\text{sat}}^{\text{emp}}}\,, \tag{3.17}$$

and α indicates either SNM or PNM, and the corresponding b_{sat} or b_{PNM}. As an aside, we note that the energy per particle in SNM receives contributions from cluster formation, such as alpha clustering, at very low densities [143]. Such effects are not included in this work, however an analysis of the EoS of clusterized matter relevant to the crust of NSs is presented in chapter 4.

In the MM, the coefficients $v_{\alpha,1}$ to $v_{\alpha,N}$ are related to the nuclear empirical parameters (NEPs), such as E_{sat}, K_{sat}, E_{sym}, L_{sym}, etc. The NEPs for SNM are defined by the density expansion

$$e_{\text{SNM}}(n) = E_{\text{sat}} + \frac{1}{2}K_{\text{sat}}x^2 + \frac{1}{6}Q_{\text{sat}}x^3 + \frac{1}{24}Z_{\text{sat}}x^4 + \dots , \tag{3.18}$$

whereas the NEPs for PNM are defined by

$$e_{\text{PNM}}(n) = E_{\text{PNM}} + L_{\text{PNM}}x + \frac{1}{2}K_{\text{PNM}}x^2 + \frac{1}{6}Q_{\text{PNM}}x^3 + \frac{1}{24}Z_{\text{PNM}}x^4 + \dots . \tag{3.19}$$

We use the following relations between the MM parameters and the NEPs for the isoscalar parameters controlling the SNM EoS:

$$\begin{aligned}
v_{\text{SNM},0} &= E_{\text{sat}} - t_{\text{SNM}}(1 + \kappa_{\text{sat}} + \kappa_{\text{sat},2}) , \\
v_{\text{SNM},1} &= -t_{\text{SNM}}(2 + 5\kappa_{\text{sat}} + 8\kappa_{\text{sat},2}) , \\
v_{\text{SNM},2} &= K_{\text{sat}} - 2t_{\text{SNM}}(-1 + 5\kappa_{\text{sat}} + 20\kappa_{\text{sat},2}) , \\
v_{\text{SNM},3} &= Q_{\text{sat}} - 2t_{\text{SNM}}(4 - 5\kappa_{\text{sat}} + 40\kappa_{\text{sat},2}) , \\
v_{\text{SNM},4} &= Z_{\text{sat}} - 8t_{\text{SNM}}(-7 + 5\kappa_{\text{sat}} - 10\kappa_{\text{sat},2}) ,
\end{aligned} \tag{3.20}$$

while the isovector parameters describing the PNM EoS are

$$\begin{aligned}
v_{\text{PNM},0} &= E_{\text{PNM}} - 2^{\frac{2}{3}}t_{\text{SNM}}(1 + \kappa_{\text{PNM}} + \kappa_{\text{PNM},2}) , \\
v_{\text{PNM},1} &= L_{\text{PNM}} - 2^{\frac{2}{3}}t_{\text{SNM}}(2 + 5\kappa_{\text{PNM}} + 8\kappa_{\text{PNM},2}) , \\
v_{\text{PNM},2} &= K_{\text{PNM}} - 2^{\frac{5}{3}}t_{\text{SNM}}(-1 + 5\kappa_{\text{PNM}} + 20\kappa_{\text{PNM},2}) , \\
v_{\text{PNM},3} &= Q_{\text{PNM}} - 2^{\frac{5}{3}}t_{\text{SNM}}(4 - 5\kappa_{\text{PNM}} + 40\kappa_{\text{PNM},2}) , \\
v_{\text{PNM},4} &= Z_{\text{PNM}} - 2^{\frac{11}{3}}t_{\text{SNM}}(-7 + 5\kappa_{\text{PNM}} - 10\kappa_{\text{PNM},2}) .
\end{aligned} \tag{3.21}$$

These relations represent another difference to the original nucleonic MM of Ref. [64], where the isovector coefficients were determined assuming a quadratic isospin-asymmetry dependence of the symmetry energy. The isovector contribution of the present MM is built on the global symmetry energy (2.3), which allows for possible non-quadratic contributions to the symmetry energy. These contributions will be estimated from the difference between the global symmetry energy and its quadratic contribution, as detailed in Sec. 3.4.

In our MM there are five NEPs in SNM, including n_{sat}, and five additional NEPs in PNM. Considering the two parameters controlling the low-density EoS, b_{sat} and b_{PNM}, there is a total of 12 parameters that need to be determined. Note, that these parameters carry uncertainties that reflect the current lack of knowledge of the nuclear EoS. In our Bayesian fits, we use the priors for the NEPs from the analysis presented in Refs. [64, 131] and summarized in Table 3.2. Here, we additionally vary the parameters b_{sat} and b_{PNM} to reproduce the low-density behavior of the energy per particle in SNM and PNM.

We show the fitted parameters in Table 3.2. Note, that both the posterior and prior of each parametric fit is a normal distribution with mean value and standard deviation (printed in parenthesis). The posteriors we obtain for the NEPs may depend on the exact representation of the data points, i.e., if the data is equidistant in n or k_{F}. To gauge the sensitivity to this choice, we investigate in the following three possible data representations. Figure 3.5 shows the results for these so-called scalings.

Since we require a good representation of low-density nuclear matter in order to fix b_{sat} and

Table 3.2: Priors and posteriors of the NEPs from analyses of SNM and PNM. We report results for the different scalings described in the text. Values within parentheses represent the error bars at the $\pm 1\sigma$ level. NEPs for the following three Skyrme-type interactions are given: NRAPR [77], LNS5 [137] and SAMI [138].

Scaling	n_{sat}	E_{sat}		K_{sat}	Q_{sat}	Z_{sat}	b_{sat}
	(fm^{-3})	(MeV)		(MeV)	(MeV)	(MeV)	
prior	0.160(10)	$-15.50(100)$		230(20)	$-300(400)$	1300(500)	0(50)
1	0.166(8)	$-15.48(58)$		211(14)	$-573(133)$	1055(474)	17(5)
2	0.163(8)	$-15.07(57)$		227(18)	$-172(243)$	1287(499)	9(5)
3	0.163(8)	$-15.07(57)$		227(18)	$-172(243)$	1287(499)	9(5)
3*	0.161(7)	$-15.17(57)$		226(18)	$-306(186)$	1324(497)	17†
NRAPR [77]	0.161	-15.85		226	-363	1611	
LNS5 [137]	0.160	-15.57		240	-316	1255	
SAMI [138]	0.159	-15.93		245	-339	1330	
Scaling	n_{sat}	E_{PNM}	L_{PNM}	K_{PNM}	Q_{PNM}	Z_{PNM}	b_{PNM}
	(fm^{-3})	(MeV)	(MeV)	(MeV)	(MeV)	(MeV)	
prior	–	16.00(300)	50(10)	100(100)	0(400)	$-500(500)$	0(50)
1	0.166(8)††	16.61(93)	48(5)	40(37)	$-320(224)$	$-388(494)$	42(4)
2	0.163(8)††	16.30(93)	47(5)	75(40)	34(285)	$-504(497)$	15(9)
3	0.163(8)††	16.30(93)	47(5)	75(40)	34(285)	$-504(497)$	15(9)
3*	0.161(7)††	16.16(89)	46(5)	57(34)	$-110(206)$	$-450(492)$	42†
NRAPR [77]	0.161	18.33	65	108	-52	-236	
LNS5 [137]	0.160	15.29	57	130	-34	-416	
SAMI [138]	0.159	13.32	47	127	35	-873	

† Fixed parameter. †† Quoted values are the n_{sat} priors considered in PNM and obtained from SNM posteriors.

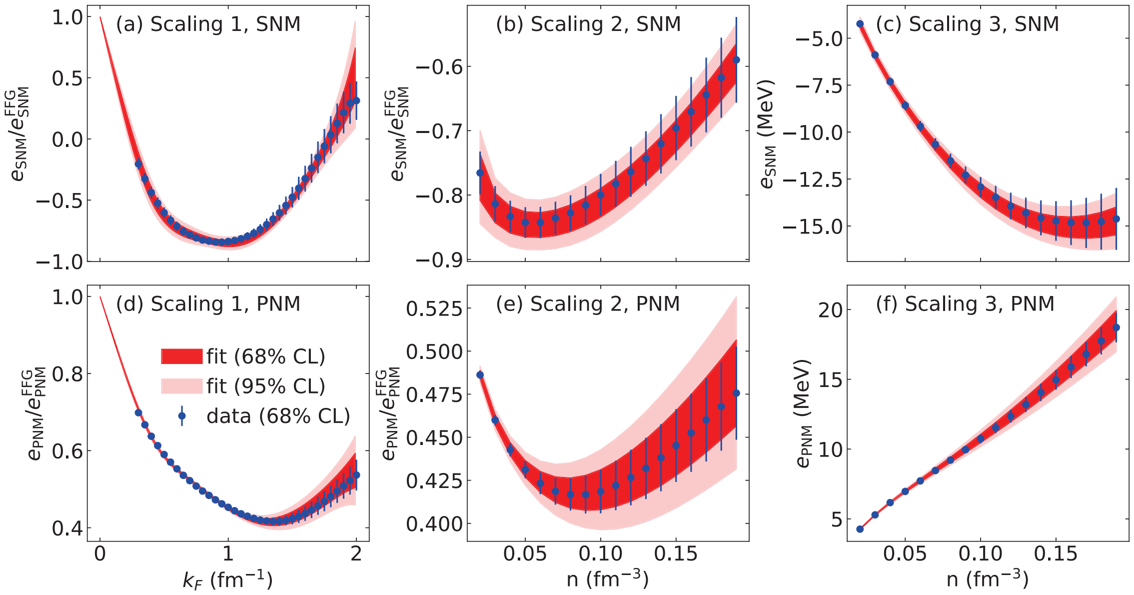

Figure 3.5: Comparison of the Bayesian inference results for the MM of this work (red bands) with the MBPT data (blue points) for SNM (panels (a),(b),(c)) and PNM (panels (d),(e),(f)) and the three different scalings described in the main text. The bands are given at the 65% (dark-shaded) and 95% confidence level (light-shaded), whereas the data points are shown with the $\pm 1\sigma$ uncertainty estimate.

$b_{\rm PNM}$, we adopt for scaling 1 the representation of $e/e^{\rm FFG}$ as a function of the Fermi momentum $k_{\rm F}$. Scaling 1 provides the best representation for analyzing the low-density properties of the energy per particle because an equidistant grid in $k_{\rm F}$ leads to a very dense data set at low densities. Note that the original MBPT data [94] is provided on an equidistant grid in $k_{\rm F}$. The scaling of the y-axis normalizes the energies to the same order of magnitude at all $k_{\rm F}$. For scaling 2, we choose the representation of $e/e^{\rm FFG}$ on an equidistant grid in density. We use cubic splines to interpolate the energies per particle from the original Fermi momentum grid to a equally spaced density grid. By switching from the equidistant grid in momentum to one in density, scaling 2 reduces the weight for the low-density data points and, therefore, is more appropriate to fit the NEPs, which are determined around saturation density. Finally, scaling 3 represents the energy per particle on an equidistant grid in density, as it is more often presented in the literature. Hence, the only difference to scaling 2 is the normalization of the energy. The results for each of the three scalings are shown in Fig. 3.5 for SNM and PNM, while the posteriors for the NEPs are given in Table 3.2. Note, that the NEP $n_{\rm sat}$ is only meaningful in SNM, while its uncertainty influences the determination of the NEPs in PNM. In our approach, we therefore vary $n_{\rm sat}$ in PNM within the posterior uncertainty obtained from the fit in SNM. In this way, the NEPs in PNM naturally include the uncertainty in $n_{\rm sat}$.

In the case of Scaling 1, when simultaneously varying the 12 MM parameters, we find $b_{\rm SNM} = 17(5)$ and $b_{\rm PNM} = 42(4)$ as well as the values for the 10 NEPs given in Table 3.2. The density dependence of the low-density correction is, thus, very different in SNM and PNM, in contrast to the original MM of Ref. [64]. We find some differences between the NEPs obtained from scaling 1 and scalings 2 and 3. These differences are usually small compared to the

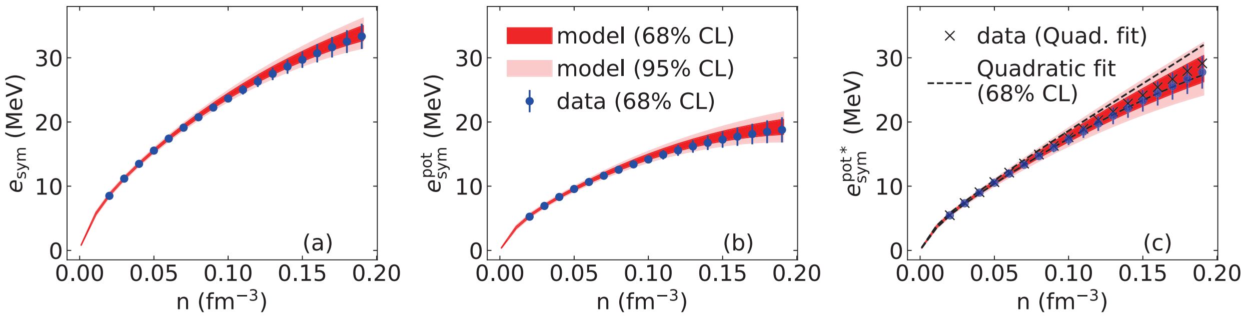

Figure 3.6: Results for the (a) symmetry energy, $e_{\text{sym}}(n)$, (b) its potential contribution $e_{\text{sym}}^{\text{pot}}$, and (c) the effective potential $e_{\text{sym}}^{\text{pot}*}$ using (3.22) - (3.23). The meaning of the individual bands and points is the same as in Fig. 3.5. In the right panel, the light- and dark-shaded red bands and the data (blue points) correspond to calculations where the Landau mass is represented by a linear polynomial. The black squares (without error bars) and the black dashed lines (enclosing a band) represent calculations where the Landau mass is represented by a quadratic fit.

uncertainties, except for Q_{sat} in SNM, as well as Q_{PNM} in PNM. We note that the fits from scalings 2 and 3 are identical and, hence, the scaling of the energy with respect to e^{FFG} has a negligible effect.

Finally, we fix the values for b_{sat} and b_{PNM} from scaling 1, and re-fit all remaining NEPs considering scaling 3. The results are referred to as scaling 3*. Fixing b_{SNM} and b_{PNM} has the largest impact on Q_{sat} and Q_{PNM}, as expected, but differences between scaling 3 and 3* are small compared to the overall uncertainties. Hence, we conclude that the parameters b_{SNM} and b_{PNM} do not have a significant impact on the determination of the NEPs, and can be fixed from the fit to low-density matter (scaling 1). We stress that for the higher-order NEPs Z_{sat} and Z_{PNM} our analysis simply returns the prior, which implies that they are not constrained by our data. This is because the density range of the MBPT data is limited to densities $n \lesssim 0.21$ fm^{-3}. However, they contribute to the uncertainty of the other NEPs [142].

For the NEPs describing nuclear saturation we obtain from scaling 3, $n_{\text{sat}} = 0.161(7)\,\text{fm}^{-3}$, $E_{\text{sat}} = -15.17(57)$ MeV, and $K_{\text{sat}} = 226(18)$ MeV. The results are consistent with the original analysis in Ref. [94], which obtained $n_{\text{sat}} = 0.143 - 0.190\,\text{fm}^{-3}$, $E_{\text{sat}} = -(15.1 - 18.3)$ MeV, and $K_{\text{sat}} = 223 - 254$ MeV using a Hartree-Fock spectrum. However, our uncertainties are generally smaller because we explicitly guide the fits in Fig. 3.5 by empirical (or “expert”) knowledge [64] through prior distributions of the fit parameters. In PNM, where empirical constraints are lacking, the fits are therefore closer to the MBPT data.

3.4 Symmetry energy

Using the results obtained in Secs. 3.2 and 3.3, we now determine the properties of the symmetry energy and the relative contributions of the quadratic and non-quadratic terms.

3.4.1 Global symmetry energy e_{sym}

The global symmetry energy e_{sym} is determined from our fits in PNM and SNM, see Eq. (2.3) and Sec. 3.3, and the contributions of the potential energies $e_{\text{sym}}^{\text{pot}}$, and $e_{\text{sym}}^{\text{pot}*}$ are obtained from e_{sym} following,

$$\begin{aligned} e_{\text{sym}}^{\text{pot}}(n) &= e_{\text{sym}}(n) - t_{\text{PNM}}(n) + t_{\text{SNM}}(n)\,, & (3.22)\\ e_{\text{sym}}^{\text{pot}*}(n) &= e_{\text{sym}}(n) - t^*_{\text{PNM}}(n) + t^*_{\text{SNM}}(n)\,. & (3.23)\end{aligned}$$

We use the fits of the Landau mass discussed in Sec. 3.2 to determine t^*, including its uncertainties, as explained in the following.

We present these quantities in Fig. 3.6 as functions of the density n. For e_{sym}, the data points are obtained from the PNM and SNM data, and their uncertainties are defined by the arithmetic average of the PNM and SNM error bars. For the model, we employ the symmetry energy determined from the MM, which is defined as

$$e_{\text{sym}}^{\text{MM}}(n) = e_{\text{PNM}}^{\text{MM}}(n) - e_{\text{SNM}}^{\text{MM}}(n)\,. \tag{3.24}$$

The results shown in Fig. 3.6 are obtained from the best fits to SNM and PNM (scaling $3*$ in Table 3.2), where the width of the bands is defined as the arithmetic average of the widths in SNM and PNM. The model results, therefore, depend on the choice of prior in SNM and PNM, in particular, on the prior knowledge of the saturation density and energy considered in SNM, see the discussion of Fig. 3.5. For this reason, the MM uncertainty for the symmetry energy is slightly smaller than the uncertainty of the data in Fig. 3.6. At nuclear saturation density, $n_{\text{sat}} = 0.161(7)\,\text{fm}^{-3}$, the data suggest $e_{\text{sym}} = 30.70(140)$ MeV, while the MM leads to $e_{\text{sym}} = 31.33(106)$ MeV. Our values for the symmetry energy are in good agreement with the fiducial value of 31.6 ± 2.7 MeV in Ref. [144], with the recent Bayesian analysis in Refs. [65, 130] that fully quantifies correlated EFT truncation errors with chiral NN and 3N interactions up to N^{3}LO, $30.9(11)$ MeV at the canonical saturation density, with the value of $30(3)$ MeV in Ref. [145] ($E\mathbb{1}$), and the range $29 - 35$ MeV obtained in Ref. [146]. Similarly, we predict $L_{\text{sym}} = 46.2(49)$ MeV, while $L_{\text{sym}} = 58.9(160)$ MeV was found in Ref. [144], $L_{\text{sym}} = 58.4(48)$ MeV in Refs. [65, 130] at the canonical saturation density, and the range $L_{\text{sym}} \in [43, 67]$ MeV in Ref. [146]. The determination of L_{sym}, however, is sensitive to the densities at which the value is extracted as well as to the interactions employed.

The data for $e_{\text{sym}}^{\text{pot}}$ and $e_{\text{sym}}^{\text{pot}*}$ are obtained from e_{sym} using Eqs. (3.22) and (3.23). In the case of $e_{\text{sym}}^{\text{pot}*}$, the effective mass is fixed to be the best fit using either the linear or the quadratic density expansion (depicted by dashed lines in the right panel), and the uncertainty of $e_{\text{sym}}^{\text{pot}*}$ is defined as the arithmetic average of the uncertainties of e_{sym}, t^*_{PNM} and t^*_{SNM}. Therefore, the uncertainty of $e_{\text{sym}}^{\text{pot}*}$ also includes the uncertainties in the Landau mass parameters κ_{sat} and κ_{PNM}. We observe that there is a large impact of the Landau mass on $e_{\text{sym}}^{\text{pot}*}$, compared to $e_{\text{sym}}^{\text{pot}}$ with the bare mass. At n_{sat}, we obtain $e_{\text{sym}}^{\text{pot}} = 18.1(7)$ MeV and $e_{\text{sym}}^{\text{pot}*} = 25.7(14)$ MeV. Hence, the Landau mass increases the potential part of the symmetry energy by about $30-40\%$ as discussed in the introduction. These numbers are compatible with the expectations for the complementary contribution from the kinetic energy. We find $t_{\text{PNM}}(n_{\text{sat}}^{\text{emp}}) - t_{\text{SNM}}(n_{\text{sat}}^{\text{emp}}) = 13.0$ MeV and $t^*_{\text{PNM}}(n_{\text{sat}}^{\text{emp}}) - t^*_{\text{SNM}}(n_{\text{sat}}^{\text{emp}}) = 5.4(13)$ MeV.

For $e_{\text{sym}}^{\text{pot}*}$, we expect a difference when using either a Landau mass that is linear or quadratic

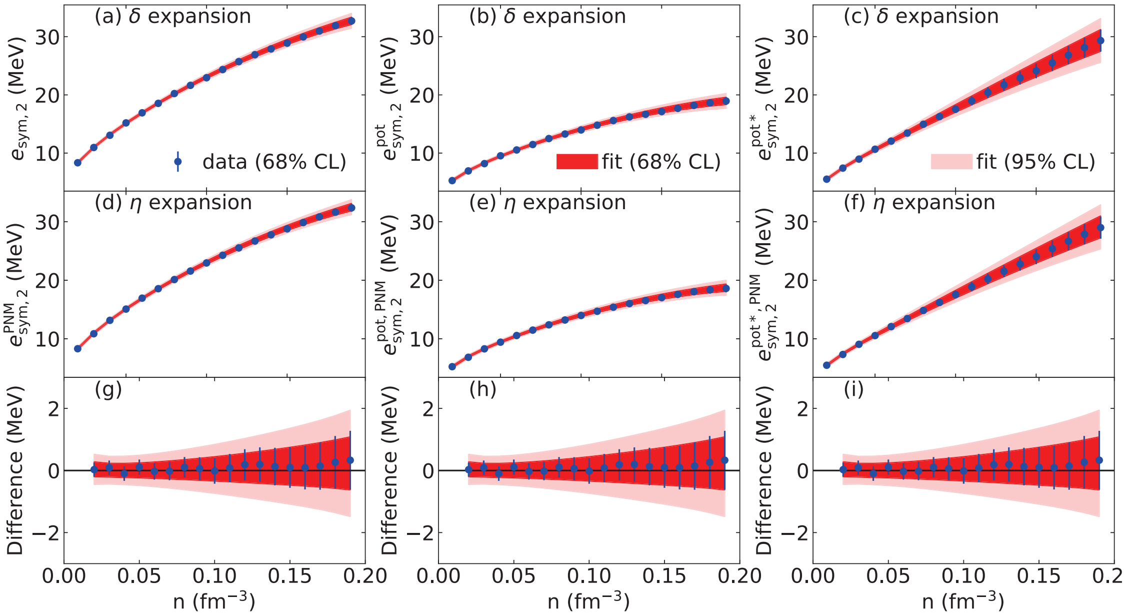

Figure 3.7: Comparison of the extracted $e_{\rm sym,2}$, $e^{\rm pot}_{\rm sym,2}$, and $e^{\rm pot*}_{\rm sym,2}$ using Eqs. (3.25), (3.27), and (3.28) (panels (a), (b) and (c)) and via an expansion around PNM, i.e., using Eq. (3.33) (panels (d), (e) and (f)). Panels (g), (h) and (i) show the difference between the δ and η expansions.

in density, see Fig. 3.4. In Fig. 3.6 we show two results for $e^{\rm pot*}_{\rm sym}$. The blue data points and the dark-shaded (light-shaded) red bands correspond to the results at 68% (95%) confidence level when using a Landau mass linear in density. The black squares and the black-dashed lines, encompassing the corresponding 68% confidence interval, represent calculations with a Landau mass quadratic in density. Interestingly, the values for $e^{\rm pot*}_{\rm sym}$ obtained from these two functions for the Landau mass differ only by about 1.8%, which is quite small. We, therefore, use only the linear fit for the Landau mass in the following.

3.4.2 Quadratic contribution to the symmetry energy

The quadratic contribution to the symmetry energy, $e_{\rm sym,2}$, is defined in Eq. (2.2) as the local curvature in the isospin-asymmetry parameter δ in SNM. In the following, we extract $e_{\rm sym,2}$ using this expansion around SNM, but also suggest obtaining $e_{\rm sym,2}$ from an expansion around PNM. We demonstrate that both definitions provide comparable results.

Expansion around SNM

The quadratic contribution to the symmetry energy is defined by Eq. (2.2) relative to the SNM EoS. To determine this contribution directly from the MBPT data, we employ Eq. (2.1) up to the fourth order in δ, and fit the coefficients $e_{\rm sym,2}$ and $e_{\rm sym,4}$ using a standard least-squares minimization. The fits are performed in the range, $\delta = 0.0 - 0.5$. We have checked that the results are insensitive (within variations of about 0.1 MeV) to the upper limit of this range—as long as it is chosen to be $\delta \geqslant 0.5$.

For the model, we express $e_{\text{sym},2}(n)$ as a function of the density using the MM contribution to the quadratic symmetry energy,

$$e^{\text{MM}}_{\text{sym},2}(x) = \frac{5}{9} t_{\text{SNM}}(x) + \sum_{j=0}^{N} \frac{x^j}{j!} \left[v_{\text{sym2},j} u_j(x, \delta = 0) - v_{\text{SNM,j}} \big(u_j(x, \delta = 0) - 1 \big)(1 + 3x) b_{\text{sym}} \right] , \tag{3.25}$$

where the parameters $v_{\text{sym2},i}$ are determined using a Bayesian parametric fit, as before for other quantities. They are related to the quadratic symmetry energy NEPs as follows:

$$\begin{aligned}
v_{\text{sym2},0} &= E_{\text{sym2}} - \frac{5}{9} t^{\text{sat}}_{\text{SNM}} [1 + \kappa_{\text{sat}} + 3\kappa_{\text{sym}} + \kappa_{\text{sat},2} + 3\kappa_{\text{sym},2}] , &(3.26)\\
v_{\text{sym2},1} &= L_{\text{sym2}} - \frac{5}{9} t^{\text{sat}}_{\text{SNM}} [2 + 5(\kappa_{\text{sat}} + 3\kappa_{\text{sym}}) + 8(\kappa_{\text{sat},2} + 3\kappa_{\text{sym},2})] ,\\
v_{\text{sym2},2} &= K_{\text{sym2}} - \frac{10}{9} t^{\text{sat}}_{\text{SNM}} [-1 + 5(\kappa_{\text{sat}} + 3\kappa_{\text{sym}}) + 20(\kappa_{\text{sat},2} + 3\kappa_{\text{sym},2})] ,\\
v_{\text{sym2},3} &= Q_{\text{sym2}} - \frac{10}{9} t^{\text{sat}}_{\text{SNM}} [4 - 5(\kappa_{\text{sat}} + 3\kappa_{\text{sym}}) + 40(\kappa_{\text{sat},2} + 3\kappa_{\text{sym},2})] ,\\
v_{\text{sym2},4} &= Z_{\text{sym2}} - \frac{40}{9} t^{\text{sat}}_{\text{SNM}} [-7 + 5(\kappa_{\text{sat}} + 3\kappa_{\text{sym}}) - 10(\kappa_{\text{sat},2} + 3\kappa_{\text{sym},2})] .
\end{aligned}$$

These relations generalize the ones in Ref. [64] for a quadratic density-dependent Landau mass. The parameter $b_{\text{sym}} \equiv b_{\text{PNM}} - b_{\text{SNM}}$ is fixed by the 3^* fit.

The contributions to the symmetry energy due to the potential energy are determined from the following expressions,

$$e^{\text{pot}}_{\text{sym},2}(n) = e_{\text{sym},2}(n) - \frac{5}{9} t_{\text{SNM}}(n) , \tag{3.27}$$

$$e^{\text{pot}*}_{\text{sym},2}(n) = e_{\text{sym},2}(n) - \frac{5}{9} t_{\text{SNM}}(n) \left[1 + (\kappa_{\text{sat}} + 3\kappa_{\text{sym}}) \left(\frac{n}{n_{\text{sat}}} \right) + (\kappa_{\text{sat},2} + 3\kappa_{\text{sym},2}) \left(\frac{n}{n_{\text{sat}}} \right)^2 \right] . \tag{3.28}$$

Our results for $e_{\text{sym},2}$, $e^{\text{pot}}_{\text{sym},2}$, and $e^{\text{pot}*}_{\text{sym},2}$ are shown in the first row of Fig. 3.7. At $n^{\text{emp}}_{\text{sat}}$, we find $e_{\text{sym},2}(n^{\text{emp}}_{\text{sat}}) = 30.0(4)$ MeV, $e^{\text{pot}}_{\text{sym},2}(n^{\text{emp}}_{\text{sat}}) = 17.7(4)$ MeV and $e^{\text{pot}*}_{\text{sym},2}(n^{\text{emp}}_{\text{sat}}) = 26.4(1.7)$ MeV (with the linear density-dependent model for the Landau mass). The large value of $e^{\text{pot}*}_{\text{sym},2}(n^{\text{emp}}_{\text{sat}})$, almost 90% of $e_{\text{sym},2}(n^{\text{emp}}_{\text{sat}})$, originates from the isospin dependence of the Landau mass, encoded by κ_{sym}.

From the fit model (3.25), we obtain an estimate for the NEPs that govern the quadratic contribution to the symmetry energy at the inferred value of n_{sat}. The values are given in the first row of Table 3.3. Our result for $E_{\text{sym},2}$ is about 1 MeV below the total symmetry energy, E_{sym}—the difference is due to non-quadratic contributions.

Expansion around PNM

An alternative approach is to determine the contribution $e_{\text{sym},2}$ from an expansion around PNM. Since the MBPT approach used here is able to explore asymmetric matter with arbitrary δ, we

Table 3.3: Posteriors of empirical parameters obtained from the analysis of the δ and η expansions for $e_{\text{sym},2}$. Values inside parentheses represent error bars at the $\pm 1\sigma$ level. Results for the following three Skyrme-type interactions are given: NRAPR [77], LNS5 [137] and SAMI [138].

Expansion	n_{sat} (fm^{-3})	$E_{\text{sym},2}$ (MeV)	$L_{\text{sym},2}$ (MeV)	$K_{\text{sym},2}$ (MeV)	$Q_{\text{sym},2}$ (MeV)	$Z_{\text{sym},2}$ (MeV)	b_{sym}
Prior	-	31.50(350)	50(10)	−130(110)	−300(600)	−1800(800)	
δ (SNM)	0.161(7)†	30.16(83)	47(3)	−146(43)	90(334)	−1865(793)	25††
η (PNM)	0.161(7)†	30.02(82)	46(3)	−149(46)	93(352)	−1875(793)	25††
NRAPR [77]	0.161	32.78	60	−123	312	−1836	
LNS5 [137]	0.160	29.15	51	−119	286	−1672	
SAMI [138]	0.159	28.16	44	−120	372	−2180	

† Priors taken from the SNM posteriors in Table 3.2. †† Fixed value.

can test the accuracy of this alternative expansion.

To this end, we introduce the parameter

$$\eta = 1 - \delta = 2n_p/n\,, \tag{3.29}$$

which is twice the proton fraction. Equation (2.1) can now be re-expressed in terms of the this parameter,

$$\begin{aligned} e(\eta) \;&=\; e_{\text{PNM}} - 2(e_{\text{sym},2} + 2e_{\text{sym},4})\eta + (e_{\text{sym},2} + 6e_{\text{sym},4})\eta^2 \\ &\quad -4e_{\text{sym},4}\eta^3 + e_{\text{sym},4}\eta^4 + O(\eta^5)\,. \end{aligned} \tag{3.30}$$

From Eq. (3.30), it follows then

$$e^{\text{PNM}}_{\text{sym},2}(n) = -\frac{3}{4}\frac{\partial e}{\partial \eta}\bigg|_{\eta=0} - \frac{1}{4}\frac{\partial^2 e}{\partial \eta^2}\bigg|_{\eta=0}\,. \tag{3.31}$$

We determine $e^{\text{PNM}}_{\text{sym},2}$ and $e^{\text{PNM}}_{\text{sym},4}$ from fitting the function

$$e(n,\eta) \;=\; e_{\text{PNM}}(n) + a_1(n)\eta + a_2(n)\eta^2 + \mathcal{O}(\eta^3)\,. \tag{3.32}$$

with

$$e^{\text{PNM}}_{\text{sym},2}(n) \;=\; -\frac{1}{4}\left[3a_1(n) + 2a_2(n)\right]\,, \tag{3.33}$$

$$e^{\text{PNM}}_{\text{sym},4}(n) \;=\; +\frac{1}{8}\left[a_1(n) + 2a_2(n)\right]\,, \tag{3.34}$$

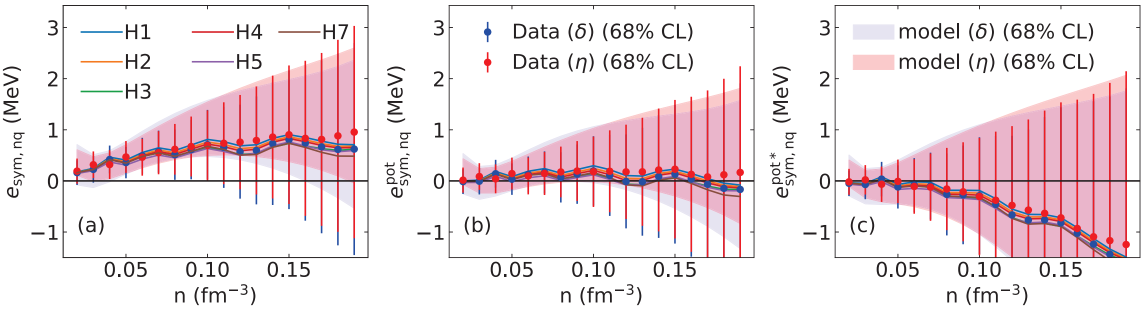

Figure 3.8: Non-quadratic terms (a) $e_{\text{sym},nq}$, (b) $e^{pot}_{\text{sym},nq}$ and (c) $e^{pot*}_{\text{sym},nq}$ calculated via an expansion around SNM (blue) and PNM (red). For panel (c), the Landau mass is described by a linear fit. The coloured lines depict results for the six individual Hamiltonians.

at each density to the computed energies per particle at $\eta = 0.0, 0.1, 0.2,$ and 0.3. Again, we also perform a Bayesian fit using Eq. (3.25). The two quantities are shown in the second row of Fig. 3.7, together with the potential terms $e^{\text{pot,PNM}}_{\text{sym},2}$ and $e^{\text{pot}*,\text{PNM}}_{\text{sym},2}$. The NEPs obtained from Eq. (3.25) are given in the second row of Table 3.3. Note, that the differences between the NEPs extracted around SNM [using Eq. (2.2)] and around PNM [using Eq. (3.31)] are much smaller than the uncertainties of these NEPs, which demonstrates that the two approaches are consistent with one another. This is further illustrated in the third row of Fig. 3.7, where the difference between $e^{\text{SNM}}_{\text{sym},2}$ and $e^{\text{PNM}}_{\text{sym},2}$ is shown to be consistent with zero and a small width of about 1.5 MeV at n_{sat}. Note that the width here is calculated as the arithmetic average of the widths of $e^{\text{SNM}}_{\text{sym},2}$ and $e^{\text{PNM}}_{\text{sym},2}$.

Determining the quadratic contribution to the symmetry energy from an expansion around PNM might be beneficial because PNM can usually be computed with much higher accuracy since the uncertainties in the 3N interactions are reduced. Furthermore, such an extraction is useful for microscopic approaches in which a small proton impurity can be treated more easily than SNM, e.g., the auxiliary-field diffusion Monte Carlo approach [145].

3.4.3 Non-quadratic contribution to the symmetry energy $\mathbf{e_{sym,nq}}$ and $\mathbf{e_{sym,4}}$

We now evaluate the contribution of the non-quadratic terms, defined by Eq. (3.3), using the expansions around SNM and PNM, respectively. For the global symmetry energy, we use our model (3.24), while for describing the quadratic contribution we use the fit (3.25). Figure 3.8 shows our results for the expansion around SNM (blue) and the expansion around PNM (red). Both expansions agree, and the differences are smaller than the uncertainties by a factor of $2-3$. We also show results for the six Hamiltonians. Their spread is much smaller than the uncertainties of the data or the model. This is because the latter are computed as arithmetic averages of the error bars of the global symmetry energy and the quadratic contribution. Such an average neglects the correlations between the two, leading to an overestimation of the error-bars. At $n^{\text{emp}}_{\text{sat}}$, we obtain from our model $e_{\text{sym},nq} = 1.3(10)$ MeV, $e^{pot}_{\text{sym},nq} = 0.6(10)$ MeV, $e^{pot*}_{\text{sym},nq} = -0.5(22)$ MeV. For the individual Hamiltonians, we obtain $e_{\text{sym},nq} = 0.74^{+0.11}_{-0.08}$ MeV, $e^{pot}_{\text{sym},nq} = 0.04^{+0.11}_{-0.08}$ MeV, $e^{pot*}_{\text{sym},nq} = -1.02^{+0.11}_{-0.08}$ MeV, where the error bars are due to the different Hamiltonians.

We find that these non-quadratic contributions represent a correction of about $3-5\%$ to the symmetry energy. They originate mainly from the kinetic energy, since $e^{pot}_{\text{sym},nq}$ remains close to zero across all densities. Our model estimates for the non-quadratic contributions to the symmetry energy and the NEPs are summarized in Table 3.4. We also compare the present NEPs to the three selected Skyrme interactions, showing a good agreement between the microscopic results and the EDF approaches.

We calculate the quartic contribution to the symmetry energy $e_{\text{sym},4}$ using Eq. (3.34), and show the resulting NEPs in Table 3.4. We find that the quartic term to the symmetry energy accounts for about $60-70\%$ of the total non-quadratic contribution, while the remaining $30-40\%$ originate from higher-order contributions. The convergence of these additional contributions is discussed in Ref. [102]. We stress that this does not include any logarithmic contribution because such a contribution would vanish in PNM.

A recent analysis based on a general EDF approach—which was optimized to the properties of finite nuclei—concluded that quartic terms $\propto \delta^4$ have little impact on nuclei [147]. The result was interpreted as a consequence of the fact that the asymmetry δ in finite nuclei is small: for $Z > 8$ it varies between -0.33 and $+0.38$ in the latest Atomic Mass Data Center mass table AME2016 [148]. A quartic term was, however, found to be important to correctly reproduce the PNM energy per particle. In order to reproduce the PNM energy per particle predicted in Ref. [96], Ref. [147] found a quartic term of $e_{\text{sym},4} = 2.635\,\text{MeV}$at $n = 0.1\,\text{fm}^{-3}$. This term was the only non-quadratic contribution considered in Ref. [147], and is consistent within our upper 68% confidence interval for the non-quadratic contribution to the symmetry energy. The higher value for $e_{\text{sym},4}$ obtained in Ref. [147] might be related to the larger value in the PNM energy per particle obtained in Ref. [96], as shown in Fig. 2.1. This affects the symmetry energy because the contribution $e_{\text{sym},4}$ is needed to correctly reproduce the PNM EoS. Both, the PNM energy per particle in Ref. [96] and $e_{\text{sym},4}$ obtained in Ref. [147] are ≈ 1 MeV higher than the values we obtain in the this work.

3.4.4 Logarithmic contribution to the symmetry energy $\mathbf{e_{sym,log}}$

The leading-order logarithmic contribution to the symmetry energy, see Eq. (3.1), was suggested to be of the form $\delta^4 \log|\delta|$ [101, 102]. It, therefore, vanishes in both SNM and PNM, and data at finite isospin asymmetry are required to determine its magnitude. Such a logarithmic term would appear by a characteristic arch-like structure in the δ-dependent residuals between the data and a model without the logarithmic term. Figure 3.9 shows these residuals as a function of δ at three different densities. For asymmetric matter, we use

$$y^{\text{model}}(n,\delta) = y_{\text{SNM}}(n) + y_{\text{sym},2}(n)\delta^2 + y_{\text{sym,nq}}(n)\delta^4\,, \tag{3.35}$$

where e_{SNM}, $e_{\text{sym},2}$ and $e_{\text{sym,nq}}$ are given by Eqs. (3.15), (3.25), and (3.3). Note that in the model (3.35), the fourth-order δ term also includes possible higher-order contributions (like, for instance, a δ^6 term) contained in the term $y_{\text{sym,nq}}$. The different panels in Fig. 3.9 show the residuals at three densities, $n = 0.06$, 0.12, and $0.16\,\text{fm}^{-3}$ (from the top to the bottom panel), and for the three choices for the variable y: e, e^{pot}, and $e^{\text{pot}*}$ (from left to right) as a function of the isospin asymmetry δ. The squares (shaded bands) represent the mean (68% confidence level) of the residuals. The presence of logarithmic terms would appear as a systematic deviation of the these residuals from zero in asymmetric matter. However, this is not what we observe at the three considered densities and for all energy observables. Instead, we find the residuals to

Table 3.4: Posteriors of non-quadratic and quartic NEPs obtained from the analysis of $e_{\text{sym},nq}$ using the δ and η expansions, and $e_{\text{sym},4}$ obtained from the η expansion only. For the extraction of $e_{\text{sym},nq}$ via the η expansion, the values inside the square brackets are obtained from a fit to the data in order to provide a direct comparison to the corresponding analysis of $e_{\text{sym},4}$. Values in parenthesis represent the $\pm 1\sigma$ uncertainties. The NEPs for the following three Skyrme-type interactions are given: NRAPR [77], LNS5 [137], and SAMI [138].

Non-quadratic contribution	$E_{\text{sym},nq}$ (MeV)	$L_{\text{sym},nq}$ (MeV)	$K_{\text{sym},nq}$ (MeV)	$Q_{\text{sym},nq}$ (MeV)	$Z_{\text{sym},nq}$ (MeV)
SNM	$1.2(15)$	$0(6)$	$-24(58)$	$106(426)$	$91(1057)$
PNM	$1.3(15)$	$1(6)$	$-20(60)$	$103(441)$	$101(1058)$
	$[0.84(7)]$	$[0.7(8)]$	$[-9(13)]$	$[32(151)]$	$[167(958)]$
NRAPR [77]	1.40	5	6	-1	-12
LNS5 [137]	1.70	6	9	-4	1
SAMI [138]	1.08	3	2	2	-24

Quartic contribution	$E_{\text{sym},4}$ (MeV)	$L_{\text{sym},4}$ (MeV)	$K_{\text{sym},4}$ (MeV)	$Q_{\text{sym},4}$ (MeV)	$Z_{\text{sym},4}$ (MeV)
PNM	$1.00(8)$	$0.6(6)$	$-7(12)$	$69(145)$	$33(956)$
NRAPR [77]	0.95	3	4	-1	-6
LNS5 [137]	1.17	5	6	-4	3
SAMI [138]	0.70	2	2	1	-15

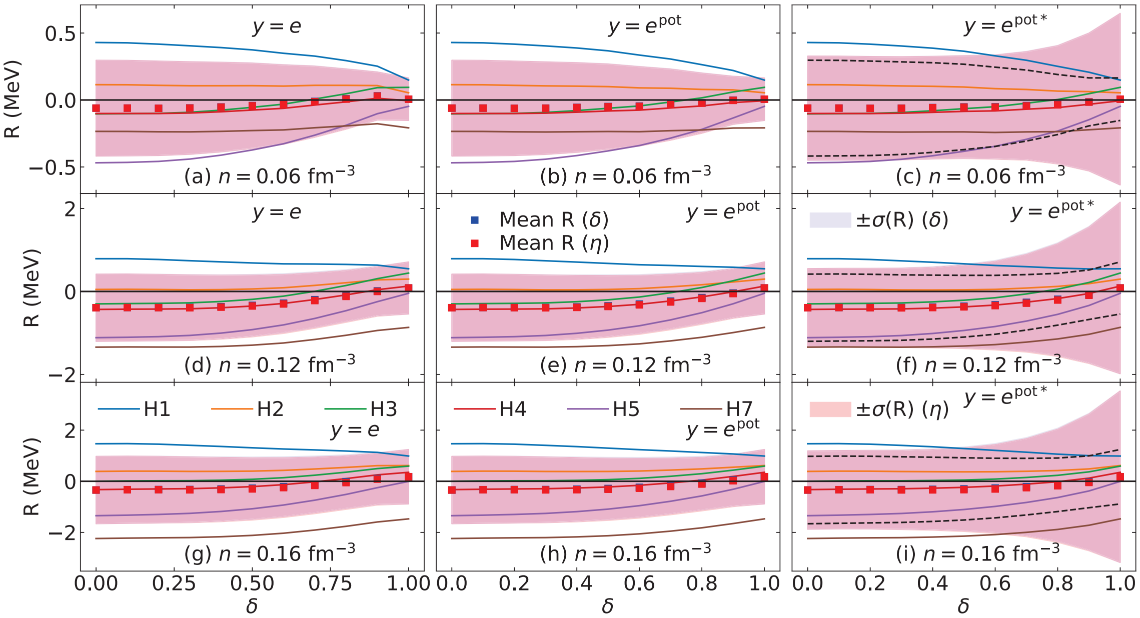

Figure 3.9: Residuals R of the model, see Eq. (3.35), with respect to the data as a function of the asymmetry parameter δ for different values of the density: $n = 0.06\ \mathrm{fm}^{-3}$ (panels (a),(b),(c)), $n = 0.12\ \mathrm{fm}^{-3}$ (panels (d),(e),(f)), and $n = 0.16\ \mathrm{fm}^{-3}$ (panels (g),(h),(i)). The results are shown for the two different calculations of $y_{\mathrm{sym},2}$ and $y_{\mathrm{sym,nq}}$—the expansions around PNM (red) and SNM (blue). The different columns correspond to e, e^{pot}, and $e^{\mathrm{pot},*}$. The coloured lines depict the residuals of the fit for each Hamiltonian. In the last column, the black-dashed lines represent the upper and lower limits of the uncertainty in the residuals, respectively, by disregarding the uncertainties in the effective masses.

be compatible with zero and almost flat as a function of the isospin asymmetry. This is also the case for the results for each Hamiltonian, which we show as coloured lines. The results for the individual Hamiltonians vanish on average, but the uncertainty bands remain quite sizable, about $\pm 1 - 2$ MeV around saturation density. Therefore, our findings suggest that there is no statistically significant indication for a net logarithmic contribution to the symmetry energy for the chiral NN and 3N Hamiltonians used in this work.

Our conclusion about the strength of the logarithmic term is not in contradiction with the findings presented in Refs. [101, 102]. The logarithmic term in Ref. [102] was found to improve the description of the isospin dependence of the energy per particle by at most ≈ 0.1 MeV, shown for one Hamiltonian[1] in Fig. 9 of Ref. [102]. Such contributions of the order of ≈ 0.1 MeV are small compared to the overall theoretical uncertainties in this work, which we estimate by analyzing the six Hamiltonians in Table 2.1.

3.5 Summary and Conclusions

In this chapter, we have analyzed the properties of asymmetric nuclear matter based on MBPT calculations [94] for six commonly used chiral EFT Hamiltonians with NN and 3N interactions.

---

[1] This is the n3lo450 interaction constructed in Refs. [116, 149, 125], which is not considered in this work.

The global symmetry energy, i.e., the difference between EoS in the limits of PNM and SNM, as well as its quadratic and quartic contributions have been determined with theoretical uncertainty estimates. We have calculated the quadratic contribution to the symmetry energy from the usual expansion around SNM, and have also employed a non-standard approach using an expansion for small proton fractions around PNM. The two approaches are in excellent agreement. Furthermore, we have investigated the strength of the non-quadraticities as well as their model dependence. The non-quadratic contribution to the symmetry energy was found to be $0.74^{+0.11}_{-0.08}$ MeV (and $-1.02^{+0.11}_{-0.08}$ MeV for the effective potential part). We have then investigated the leading-order logarithmic term to the symmetry energy, and obtained residuals between our best fit (including quadratic and quartic contributions) and the data to be compatible with zero. In particular, we found that all residuals where flat in the isospin asymmetry δ, indicating no systematic deviation from zero as expected for a logarithmic contribution. However, we also saw that present uncertainties, indicated by the dispersion of the six Hamiltonians of about $1 - 2$ MeV, are too large to precisely determine its strength. For a more recent and complementary approach, see Ref. [150], where the authors have extracted high-order terms using precise modified finite difference methods.

To gauge the full theoretical uncertainties of the non-quadratic contributions to the symmetry energy, future analyses need to explore a wider range of nuclear interactions and additional asymmetric-matter calculations using different many-body approaches and regularization schemes. In particular, this requires the development of improved chiral NN and 3N interactions up to $\mathrm{N}^3\mathrm{LO}$ [151, 152, 153], which will enable order-by-order analyses of the neutron-rich matter EoS with statistically meaningful uncertainty estimates derived from chiral EFT [65, 130].

Finally, at densities beyond those explored in this chapter, heavier baryonic degrees of freedom, such as hyperons, could become relevant. The development and improvement of models that include such degrees of freedom is a crucial task for future work, e.g., along the lines of Refs. [154, 155]; see also Refs. [156, 157] for recent reviews. The work presented in this chapter provides a framework for future investigations of the isospin-dependence of nuclear matter. In the next chapter, we will analyse in detail the implications of the calculations of Ref. [94] for the crust of NSs.

Chapter 4

Implications for the Crust of Neutron Stars

In this chapter, we will analyse the implications of Chiral EFT calculations on the properties of NSs, paying specific attention to the crust. First, in Sec. 4.1, we will build upon the work presented in chapters 2 and 3 to compute the crust-core transition using the spinodal instability criteria. This preparatory calculation will allow us to quantify the impact of non-quadratic symmetry energy terms on the crust-core transition. Although instructive, much of the rich physics of the crust, originating from inhomogenous nuclear clusters are neglected in the spinodal approach. Therefore, a new meta-model analysis is developed in this chapter that allows for the construction of an unified EoS that is applicable to the crust as well as the core in a consistent manner. We thus now move from the study of the *nuclear matter* EoS presented in chapters 2 and 3 to the *neutron star matter* EoS. These concepts are introduced and enunciated in Sec. 4.2. Details of the calibration of the meta-model in uniform matter are given in Sec. 4.3 and the modelling of finite size terms describing nuclear clusters are given in Sec. 4.4. These tools are used to analyse the crust of NSs in detail in Sec. 4.5. Global NS properties such as masses and radii are presented as well in Sec. 4.6. Our conclusions are presented in Sec. 4.7.

4.1 Crust-Core transition in the thermodynamic limit

In this section, we study the impact of the non-quadratic contribution to the symmetry energy on the crust-core transition in neutron stars, for which the symmetry energy plays an important role [158, 159, 160]. This transition occurs at the core-crust transition density n_{cc} with an isospin asymmetry δ_{cc} that is determined by the beta-equilibrium. The parameters n_{cc} and δ_{cc} are obtained from uniform matter by determining the density at which matter becomes unstable with respect to density fluctuations (spinodal instability) [158]. We choose to work only with uniform matter since it allows for a simplified but instructive estimate of the role of the non-quadratic contribution to the symmetry energy. We leave a more complete analysis including the finite-size terms for later parts of this chapter.

In multi-component matter, e.g., matter that consists of neutrons and protons, this spinodal density is determined from the curvature (Hessian) matrix $\mathcal{C}$, defined as the second derivative of the energy density with respect to the component densities [158]. From the eigenvalues of $\mathcal{C}$, one can determine the stability of matter: if all eigenvalues are positive, i.e. if $\mathcal{C}$ is

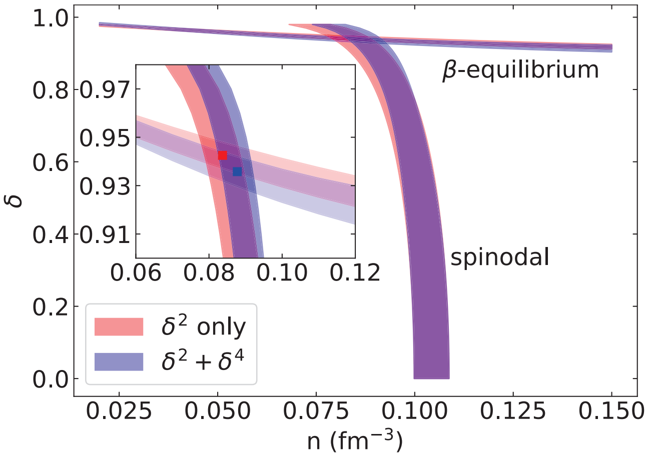

Figure 4.1: Predictions for beta equilibrium in low-density uniform matter obtained by solving Eq. (4.2), and for the spinodal density by solving Eq. (4.1). The intersection denotes the crust-core transition, as indicated by a dot in the inset. The quadratic approximation (red band) is compared to the case where quartic contributions are included (blue band).

positive semi-definite, the matter exhibits a local stability against density fluctuations of all components in any combination, while a change of sign for any eigenvalue triggers an instability with respect to density fluctuations indicated by its associated eigenvector. The change of sign of the eigenvalues can be extracted from the determinant of $\mathcal{C}$, which reads in nuclear matter,

$$\det \mathcal{C}(n,\delta) = \frac{\partial \mu_n}{\partial n_n}\frac{\partial \mu_p}{\partial n_p} - \frac{\partial \mu_n}{\partial n_p}\frac{\partial \mu_p}{\partial n_n}\,, \tag{4.1}$$

where μ_n and μ_p are the neutron and proton chemical potentials. For simplicity, we have neglected the finite-size contribution from the Coulomb interaction as well as the gradient density terms induced by the finite range of nuclear interactions. It is expected that these terms reduce the spinodal density by only ≈ 0.01 fm^{-3} [158, 160].

In sub-saturation asymmetric matter, the equilibrium state is the state that satisfies the chemical potential equilibrium $\mu_n = \mu_p + \mu_e$, at fixed baryon number $n = n_n + n_p$ and charge neutrality $n_e = n_p$. At zero temperature, and considering relativistic electrons, this system of equations reduces to a single non-linear equation,

$$\sqrt{m_e^2 + \left(\frac{3\pi^2}{2}(1-\delta_\beta)n\right)^{2/3}} = 2\frac{\partial e(n,\delta_\beta)}{\partial \delta}\,, \tag{4.2}$$

whose solution, $\delta_\beta(n)$, is obtained by using a combination of the bisection and the secant methods implemented in the Python package of Ref. [161]. Then, we define the crust-core transition as the solution (n_{cc}, δ_{cc}) to both, the instability onset criterion, $\det \mathcal{C} = 0$, and the beta equilibrium condition, e.g., Eq. (4.2). Equivalently, n_{cc} is defined as the spinodal density in beta equilibrium, where $\delta_{cc} = \delta_\beta(n_{cc})$. Figure 4.1 shows the intersection between these two determinations. We investigate the purely quadratic approximation for the symmetry energy, with the NEPs given in Table 3.3, and with the quartic terms from Table 3.4 included. For all cases, the reference MM in SNM is determined by the best fit given in Table 3.2 for the scaling 3^*.

Table 4.1: Crust-core transition density and isospin asymmetry, n_{cc} and δ_{cc}, respectively, for the purely quadratic case (δ^2 only) and for the case including the quartic contribution ($\delta^2 + \delta^4$), see Eq. (3.35).

Model	n_{cc} (fm^{-3})	δ_{cc}
δ^2 only	$0.083(5)$	$0.944(5)$
$\delta^2 + \delta^4$	$0.087(4)$	$0.935(6)$

When we include quartic contributions, the spinodal density in neutron-rich matter is increased compared to the case where only the quadratic term is considered. This is because the quartic term increases the symmetry energy. For the same reason, the isospin asymmetry is decreased when non-quadraticities are included. Our results are summarized in Table 4.1, and depicted in Fig. 4.1 by the blue and red points. They are in agreement with the predictions of, e.g., Refs. [159, 160] with $L_{\text{sym},2} \approx 45$ MeV. From the comparison of our results with and without the quartic term, we find that the mean value of the transition density changes by $\approx 5\%$ while for δ_{cc} the change is only $\approx 1\%$. Note that the 68% confidence intervals of the two results overlap, indicating that the uncertainties in the nuclear interaction are of the same order as the effects of the quartic term on the crust-core transition. For this reason, we will ignore non-quadratic contributions to the effective potential energy $e^{\text{pot}*}$ in the rest of the chapter, focusing instead on the importance of the microscopic nuclear interaction and the finite-size effects of the nuclear clusters in the NS crust.

4.2 Unified EoS modelling for neutron stars

The unified description of the EoS of neutron stars from the crust to the core represents a challenge for modern nuclear and particle physics, as well as for astrophysics [13, 162], see also Ref. [163] for a review. A typical density at the transition between the crust and the core is about half saturation energy-density ($\rho_{\text{sat}} \approx 2.6\ 10^{14}$ g cm^{-3}) while in the core, it reaches up to several times this energy-density. These densities determine NS global equilibrium properties, such as their masses, radii, moment of inertia or tidal deformabilities [28]. Recent observations of NS radii by NICER [49, 52], and tidal deformabilities by the LIGO-Virgo collaboration [38] have also reached the accuracy to sharply constrain the dense matter EoS. These developments motivate the construction of models that can provide a unified description of the EoS of the crust and the core. This is because, while the crust represents a small fraction of the NS, 10% in terms of radius and less than 1% of the mass, it was estimated that the method used to connect the crust and the core could influence the theoretical prediction of the NS radius by 3-5%, or in other words, by a few hundred meters [164]. See also Ref. [165] for a recent study on the impact of non-consistent treatment of the crust and core EoSs on macroscopic NS properties. Presently, the experimental uncertainties in the measurement of NS radii are still larger – about 1-2 km – than this theoretical one. However, anticipating future observational improvements, it is preferable to resolve this source of uncertainty by employing unified models from the crust to the core of NSs, as it has already been suggested by several teams [166, 167, 164].

Regarding homogeneous matter, we will again rely on the meta-model calibrated to chiral EFT calculations, as in chapters 2 and 3. Additionally, we will also use Skyrme forces for our analysis and compare these results with those obtained from Chiral EFT interactions. The reason for doing so is as follows. In Sec. 2.3, we saw that several conceptual milestones have been reached in the prediction of neutron star matter from microscopic ab initio approaches which are based on realistic nuclear Hamiltonians constrained by nucleon scattering data. In particular, as discussed in Sec. 2.3.1, Hamiltonians derived using chiral effective field theory (χEFT) incorporate the symmetries of QCD and provides a systematic expansion of the operators in powers of the nucleon momenta. χEFT has two distinct features: (1) it consistently include three and higher-body interactions along with the two-body interactions that are well constrained by experiments, (2) it provides a robust method to estimate errors associated with the truncation of the momentum expansion when the nucleon p is small compared to the breakdown scale $\Lambda_{\chi\mathrm{EFT}}$ of the χEFT. At sufficiently low densities, neutron matter is well understood because three-body interactions are small, and the two-body neutron-neutron interaction is strongly constrained by the neutron-neutron scattering phase shifts [168, 169]. However, with increasing density and correspondingly larger nucleon momenta, higher-dimension operators including three-body forces begin to play an increasingly important role. For both these reasons the associated uncertainty which can be estimated grows systematically and quite rapidly. The densities up to which χEFT remains useful is still a matter of debate, current expectations are that it breaks down between saturation density (n_{sat}) and twice n_{sat} [170, 171, 172]. Therefore it is necessary to contrast χEFT calculations with phenomenological interactions such as the Skyrme force. The Skyrme interactions, being well calibrated to the properties of finite nuclei, are expected to perform significantly better at and around nuclear matter saturation densities. We expect the predictions of Skyrme forces to be complementary to the χEFT Hamiltonians and we will demonstrate this explicitly in Sec. 4.3.

Unlike the core, NS crusts are composed of finite nuclei, usually referred to as nuclear clusters since their properties are modified by the dense matter environment and differ from those of isolated nuclei probed in terrestrial laboratories, see for instance Ref. [28]. The outer crust is dominated by the presence of an electron gas filling the whole volume in beta-equilibrium with neutrons and protons bound inside nuclear clusters. The nuclear symmetry energy controls the energy difference between neutrons and protons, and thus the isospin asymmetry inside the nuclear clusters. Also, electric charge neutrality is ensured by the presence of electrons, and its rapid increase with density favors the appearance of increasingly neutron-rich nuclear clusters [173]. Nuclear clusters in the inner crust are significantly more neutron-rich and coexist with a neutron fluid which is very likely to be in a superfluid state at low temperature.

These nuclear clusters in the NS crust result from the equilibrium between attractive volume interaction, and repulsive surface and Coulomb interactions, at leading order. Despite recent progress in the description of finite nuclei based on chiral nuclear interaction, it is still computationally not feasible to directly calculate the properties of nuclear clusters in NS crust. Several well-motivated approximations could however be employed to predict and understand the properties of this complex system. Among them, the liquid-drop model (LDM) is a macroscopic approach that allows us to combine together the nuclear matter predictions with finite-size (FS) terms generated from a leptodermous expansion (explained below) of the total energy. On the other hand, the compressible liquid-drop model (CLDM) includes variations of the cluster density from one nucleus to another, through the density dependence of the bulk contribution to the total energy. The LDM and CLDM describe the collective degrees of freedom. They are different from the microscopic approach, like the shell model or the energy-density functional approach, which centers around the single-particle degrees of freedom. Since the microscopic approach is the most general one, it contains the macroscopic one as an average.

In the leptodermous expansion of the total energy [174], the different contributions are sorted by decreasing powers of $A^{1/3}$. The order A belongs to the domain of nuclear matter studies, and can be directly related to the meta-model approach for nuclear matter. The orders $A^{2/3}$ and $A^{1/3}$ characterizes the finite-size contributions, and finally, orders A^0 and below belong to the single-particle contributions, e.g. shell effects or pairing contribution, described by microscopic theories. In this work the CLDM, with the bulk contributions determined by the meta-model and the FS terms generated by the leptodermous expansion, will be employed to describe the nuclear clusters in the crust of NSs. Details of this modeling is given in Sec. 4.4 and implications for the crust are discussed in Sec. 4.5.

4.3 Homogeneous matter

We will now discuss uniform matter properties for the set of models considered in this analysis. Our description of uniform matter is based on the meta-model (MM) [64], as in chapters 2 and 3, which is calibrated on existing models, such as the Skyrme model or the χEFT Hamiltonian.

First let us discuss the calibration of the meta-model to the χEFT Hamiltonians. As in chapters chapters 2 and 3, we analyse Hamiltonians H1-H5 and H7 of Ref. [176]. Additionally we include two recent χ_{EFT} predictions from Ref. [177]: DHS$_{L59}$ and DHS$_{L69}$. The meta-model is fit to these 8 interactions in a manner that is very similar to what was presented in chapter 3 but with one important difference. While, in chapter 3, an average of the interactions was computed and a Bayesian estimate was performed based on this average, in this chapter we make distinct fits to each individual Hamiltonian. This allows us to probe uncertainties in the chiral interactions by monitoring the behaviour of each Hamiltonian. Furthermore, in this approach, one can discard or favour particular models based on confrontation with experimental data. We first compute the Landau effective mass, defined in Sec. 3.2, by fitting Eq. (3.10) to each chiral Hamiltonian. Our results are summarized in the last two columns of the upper half of Table 4.3. Here, m^*_{sat} refers to the nucleon (either proton or neutron) effective mass in Symmetric Matter (SM) at saturation density and Δm^*_{sat} is defined in Eq. (3.13). Note that we have not estimated the effective mass of the DHS$_{L59}$ and DHS$_{L69}$ interactions due to the fact that the single particle energies of these Hamiltonains are not publicly available. Finally, we consider here only the linear effective mass, i.e. the quadratic term in Eq. (3.10) is neglected.

We then fit the meta-model to the energy per particle of each chiral Hamiltonian in the limits of Symmetric matter and Neutron matter (SM and NM). Table 4.2 shows the residual χ^2 values for the fit, where the χ^2 loss function is defined as

$$\chi^2 = \frac{1}{2}\sum_i \left(\frac{e_{\text{data},i} - e_{\text{MM},i}}{\sigma_i}\right)^2, \tag{4.3}$$

where σ_i was taken to be a 10% uncertainty on the data, due to imperfect modeling [178]. The variable e refers to the energy per particle and the subscript MM refers to the meta-model. The fit was performed by minimizing the χ^2 with data in the range $0.4 < k_{Fn} < 1.6$, where

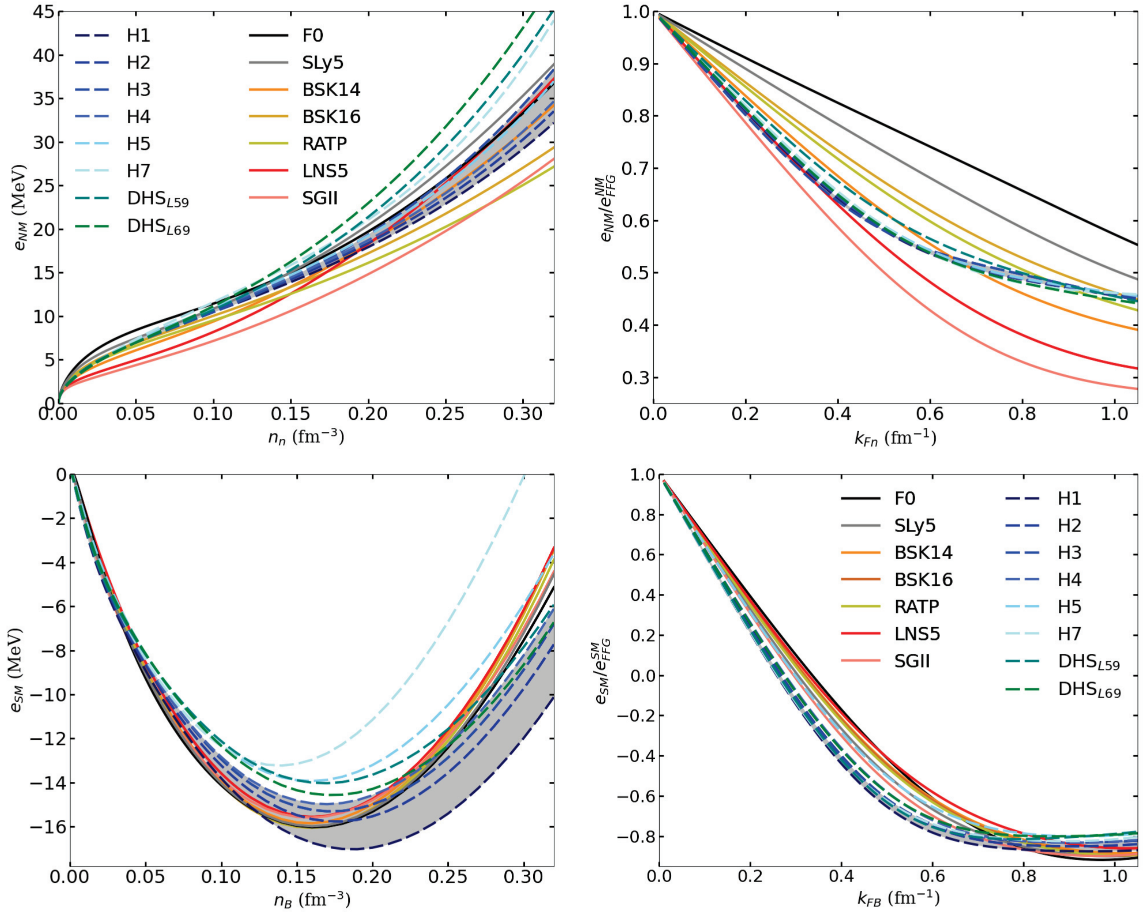

Figure 4.2: Energy per particle in uniform matter (left), for NM (top) and for SM (bottom), normalized by the Free Fermi Gas energy e_{FFG} (right). Plots are drawn as function of the densities, n_n in NM and n_B in SM, as well as function of the Fermi energy, k_{Fn} in NM and k_{FB} in SM. Note that in SM $n_n = n_B/2$ and $k_{Fn} = k_{FB}$. We plot the 8 χEFT Hamiltonians (dashed lines), a gray band for H1-H4, and 7 Skyrme interactions (solid lines), see the legend and the text for more details.

k_{Fn} is the neutron Fermi momentum, by using the standard Levenberg-Marquardt algorithm implemented in Python's scipy package. In Table 4.2, for Hamiltonians H1-H5 and H7, the number of data points N is 11 (11) for SM (NM) when $0.4 < k_{Fn} < 1.0$ and 22 (24) for SM (NM) when $0.4 < k_{Fn} < 1.6$. For the other two Hamiltonians, N is 17 (9) in SM (NM) when $0.4 < k_{Fn} < 1.6$ and 2 (-) for SM (NM) when $0.4 < k_{Fn} < 1.0$. The NEPs obtained in this manner are shown in the upper half of Table 4.3. Note that the third and forth order parameters (Q and Z) are not fir to the chiral interactions, but rather by the requirement that the EoS must be able to support a 2M$_\odot$ NS. We see that the lower order NEPs are consistent with the results presented in Table 3.2.

As for the Skyrme interactions, the reproductions of the predictions for uniform matter is presented in Ref. [64] Note that in the present work, the Skyrme MM adjustment is slightly different from the one shown in Ref. [64] where it was analytically fixed to reproduce Skyrme's predictions at $4\rho_{\text{sat}}$. We replaced this – somehow arbitrary – prescription by a fit over the den-

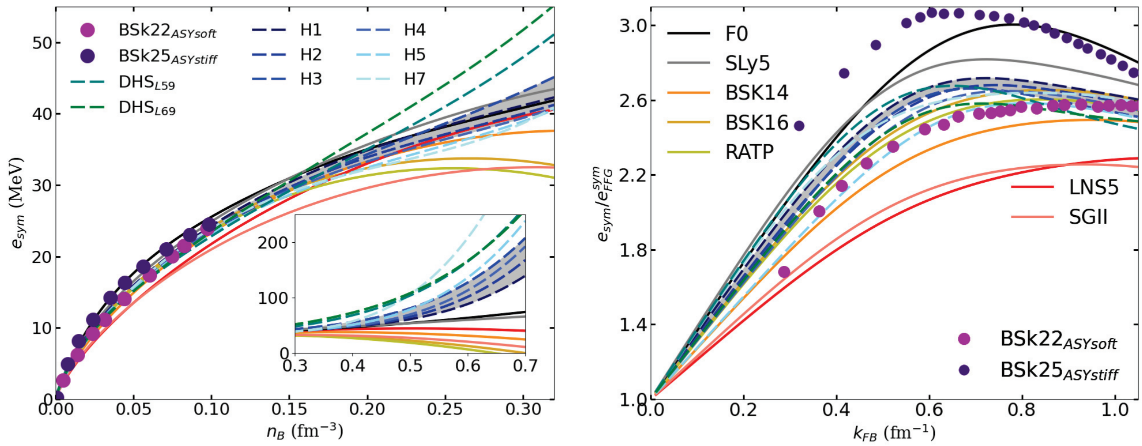

Figure 4.3: Symmetry energy w.r.t to baryon density (left) and normalized by the FFG symmetry energy w.r.t Fermi momentum (right). Inset on left plot shows e_{sym} at high densities. Continuous (dashed) lines shows the meta-model fitted to Skyrme (χEFT) models. Dark purple and magenta dots show predictions from Brussels-Montreal microscopic models BSk22 and BSk25 [175].

sities, from $\rho_{\rm sat}$ up to $10\rho_{\rm sat}$. This new prescription avoids using MM in a region where it was not required to reproduce Skyrme's predictions. In the following, we investigate the following Skyrme models: BSK14[179], BSK16[180], F0[181], LNS5[182], RATP[183], SGII[184], SLy5[185]. The nuclear empirical parameters (NEPs) predicted by these Skyrme models are given in the lower half of Table 4.3. We see that these interactions have wide predictions in NM, reflecting their different predictions for the parameter $L_{\rm sym}$, see Table 4.3.

The predictions in SM and NM are shown in Fig. 4.2, see caption for details. A gray band captures the uncertainties originating from χEFT Hamiltonians H1-H4, which reproduce experimental nuclear masses at best, see the discussion in Sec. 4.4.2. In NM the gray χEFT band is much narrower than the dispersion among the Skyrme models, see top panels of Fig. 4.2. The reason is related to the fact that χEFT is well-suited to describe low-density NM, which is very well constrained by the nucleon-nucleon phase shifts. Skyrme interactions are calibrated using the properties of finite nuclei, which reflect more directly the properties of SM, as it can be seen from Fig. 4.2 (bottom panels), where the χEFT band is now larger than the dispersion among the Skyrme models. At first sight, the predictions from χEFT and Skyrme models are complementary: the former describes NM better, while the latter is better for SM.

The low-density energy per particle is shown in the right panels of Fig. 4.2, as function of the Fermi momentum, $k_{Fn} = (3\pi^2 n_n)^{1/3}$ (NM) and $k_{FB} = (3\pi^2 n_B/2)^{1/3}$ (SM). The Free Fermi Gas (FFG) energy $E^{\rm NM}_{\rm FFG} = 3\hbar^2 k_F^2/(10m)$, where m is the nucleon mass, $k_F = k_{Fn}$ in NM and $k_F = k_{FB}$ in SM, scales the energies shown in the left panels of Fig. 4.2. In this representation, it is clear that the predictions from Skyrme models appear to be almost unconstrained in NM, as already suggested in Ref. [186], while the ones based on χEFT are very consistent among each other. The authors of Ref. [187] compared in detail the χEFT predictions and the SLy4 Skyrme model, which is almost identical to the SLy5 presented here. By investigating other Skyrme models, which perform rather well for the ground state of finite nuclei, we now explore more widely the Skyrme's uncertainties in the predictions for the properties of low-density NM.

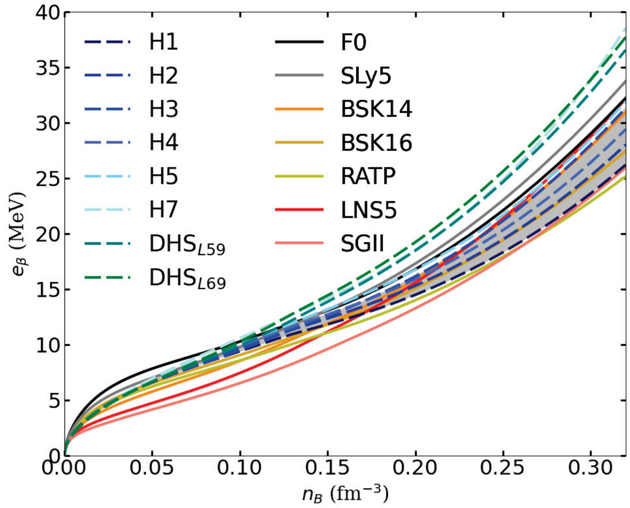

Figure 4.4: Uniform matter energy in β-equilibrium.

These properties are interesting since low-density NM is close to the unitary gas limit [188, 189, 190], which is universal limit that is applicable from nuclear systems to cold atom gas [191].

The symmetry energy, as defined in Eq. (3.24), is shown in Fig. 4.3. Despite the dispersion of χEFT predictions in SM, these models predict symmetry energy in a narrower band compared to the Skyrme's one, since Skyrme models are penalized by their poor reproduction of NM. Similarly to Fig. 4.2, we show in Fig. 4.3 (right panel) the symmetry energy normalized by the FFG prediction as function of the nucleon Fermi momentum. It is interesting to remark the very large deviation from one Skyrme model to the other on the vertical axis, which reflects the influence of the interaction to the symmetry energy (potential and effective mass contributions), see discussion in Ref. [192] for instance. At low density, for instance $k_{FB} = 0.4$ fm^{-1} ($n_B \approx 0.004$ fm^{-3}), the potential term contributes to double the symmetry energy. The potential term in χEFT models increases the normalized symmetry energy up to $k_{FB} = 0.6$-0.7 fm^{-1} ($n_B \approx 0.015$ fm^{-3}), reaching 2.5-2.7, and then it decreases slowly as the Fermi momentum k_{FB} increases. This low-density behavior is however not characteristic of all Skyrme models: Some Skyrme interactions predict the symmetry energy to be lower than the χEFT predictions (BSK14, LNS5, SGII) while some others predict it to be larger than the χEFT predictions (F0, SLy5). In Fig. 4.3 we also show symmetry energy predictions from BSk22 and BSk25 Skyrme interactions [175]. These two models represent the two extreme cases investigated in Ref. [175]: BSk22 is ASYsoft (BSk25 is ASYstiff) below saturation density, as shown in Fig. 4.3. The symmetry energy from BSk22 is similar to the χEFT band, while BSk25 predicts a large value for the symmetry energy below saturation density. In Ref. [175], these two models are used in Hartree-Fock-Bologiubov modeling of the NS crust, as we will discuss in Sec. 4.5.

At high density, as shown in the left panel of Fig. 4.3, several Skyrme models also predict a bending down of the symmetry energy (BSK14, BSK16, RATP, SGII, LNS5) that the χEFT do not predict. The inset in Fig. 4.3 shows that the bending down of the symmetry energy around saturation density of these Skyrme models leads to a crossing of the zero axis at high density. This is a well known feature of phenomenological nuclear interactions such as Skyrme, see for instance Ref. [70] and references therein.

To conclude this section, we show in Fig. 4.4 the energy per particle at β-equilibrium in

χ^2/N	$0.4 < k_{Fn} < 1.6$		$0.4 < k_{Fn} < 1.0$	
Model	SM	NM	SM	NM
H1	0.48	0.02	0.52	0.02
H2	0.48	0.02	0.51	0.02
H3	0.30	0.01	0.41	0.01
H4	0.50	0.03	0.51	0.02
H5	0.51	0.03	0.49	0.04
H7	0.14	0.05	0.23	0.07
DHS$_{L59}$	0.76	0.01	1.6	–
DHS$_{L69}$	1.67	0.09	3.51	–

Table 4.2: Reduced χ^2/N in SM and NM reflecting the residuals between the data and the MM, for $0.4 < k_{Fn} < 1.6$ on the left (used by the fit), and $0.4 < k_{Fn} < 1.0$ fm^{-1} on the right (not used by the fit). All quoted values are dimensionless, see Eq. (4.3).

uniform matter. The condition to fulfill beta-equilibrium (without neutrinos and without muons) is the following: $\mu_n - \mu_p = \mu_e$. In cold catalyzed neutron stars, neutrinos do not contribute to the chemical equilibrium. Muons can however appear when $\mu_\mu \geq m_\mu c^2$ and they contribute to β-equilibrium through the thermodynamical relation: $\mu_e = \mu_\mu$. Charge neutrality is also imposed: $n_e + n_\mu = n_p$. These three conditions complemented by the baryon conservation number $n_B = n_n + n_p$ leads to the unique determination of the composition of npeμ matter. Below saturation density, the dispersion among the Skyrme predictions observed in Fig. 4.4 is very large, much larger than the predictions from χEFT. In the following, we will investigate the impact of this large dispersion among the Skyrme predictions on the crust properties in non-uniform matter. This will be performed in the Sec. 4.5 based on the CLDM approach.

Above saturation density and as the density increases, the χEFT band for the symmetry energy gets larger and larger. While some Skyrme models are close but out of the band, e.g., SLy5 (above) and RATP (bellow), the χEFT band represents a fair estimation of the current uncertainties up to twice saturation density.

4.4 Treatment of finite nuclear systems

The Compressible Liquid Drop Model (CLDM) employed here describes isolated finite nuclei as well as nuclear clusters in the crust of NSs. This approach will also be able to satisfy the prescription where finite systems and infinite nuclear matter are treated consistently. In Sec. 4.4.1, we discuss the details of the CLDM in the context of nuclear clusters present in the crust of NSs, since the limiting case of isolated nuclei is easy to recover. In Sec. 4.4.2, we fit the parameters of the CLDM to experimental nuclear data by considering isolated finite nuclei such as the ones

Table 4.3: Nuclear empirical parameters for the Skryme models and the Hamiltonians derived from χEFT used in the present work. The lower order NEPs are defined at $n_{\rm sat}$ (E, L/n, K), while the higher order ones (Q, Z) are defined from a fit of SM and NM up to $10n_{\rm sat}$ for Skyrme, and a fix to reach $2M_\odot$ for the χEFT models. The last four columns show the low-density correction parameters $b_{\rm sat}$ and $b_{\rm sym}$, and the effective mass $m^*_{\rm sat}$ at saturation in symmetric matter and the effective mass splitting $\Delta m^*_{\rm sat}$, see text for more details.

Model	$E_{\rm sat}$ (MeV)	$n_{\rm sat}$ (fm^{-3})	$K_{\rm sat}$ (MeV)	$Q_{\rm sat}$ (MeV)	$Z_{\rm sat}$ (MeV)	$E_{\rm sym}$ (MeV)	$L_{\rm sym}$ (MeV)	$K_{\rm sym}$ (MeV)	$Q_{\rm sym}$ (MeV)	$Z_{\rm sym}$ (MeV)	$b_{\rm sat}$	$b_{\rm sym}$	$m^*_{\rm sat}$ (m_N)	$\Delta m^*_{\rm sat}$ (m_N)
$\rm H1_{MM}$	-17.0	0.186	261	-220	-200	33.8	46.8	-154	700	500	11.37	10.46	0.59	0.43
$\rm H2_{MM}$	-15.8	0.176	237	-220	-200	32.0	43.9	-144	700	500	9.59	9.34	0.61	0.41
$\rm H3_{MM}$	-15.3	0.173	232	-220	-200	31.8	50.6	-96	700	500	10.35	20.56	0.61	0.34
$\rm H4_{MM}$	-15.0	0.169	223	-220	-200	31.0	42.1	-138	700	500	8.37	8.70	0.63	0.38
$\rm H5_{MM}$	-13.9	0.159	207	-220	-200	29.4	40.2	-128	700	500	6.41	8.24	0.66	0.33
$\rm H7_{MM}$	-13.2	0.139	201	-220	-200	28.1	36.5	-150	700	500	9.40	-1.46	0.67	0.41
$\rm DHS^{\it L59}_{MM}$	-14.0	0.168	200	-220	-200	31.4	58.9	-30	700	500	9.00	10.00	1.0	0.0
$\rm DHS^{\it L69}_{MM}$	-14.6	0.173	216	-220	-200	33.7	69.0	-20	700	500	9.00	10.00	1.0	0.0
$\rm BSK14_{MM}$	-15.9	0.159	239	-88	-896	30.00	43.9	-152	213	-676	1.22	0.01	0.80	0.03
$\rm BSK16_{MM}$	-16.1	0.159	242	-91	-895	30.00	34.9	-187	245	-696	1.22	0.01	0.80	0.04
$\rm F0_{MM}$	-16.0	0.162	230	-124	-749	32.00	42.4	-113	294	-625	1.23	0.06	0.69	-0.19
$\rm LNS5_{MM}$	-15.6	0.160	240	-113	-574	29.15	50.9	-119	195	-853	1.26	0.00	0.60	0.23
$\rm RATP_{MM}$	-16.0	0.160	240	-109	-697	29.26	32.4	-191	266	-923	1.25	-0.00	0.67	0.26
$\rm SGII_{MM}$	-15.6	0.158	215	-90	-874	26.83	37.6	-146	221	-915	1.25	0.00	0.79	0.28
$\rm SLY5_{MM}$	-16.0	0.160	230	-104	-749	32.03	48.3	-112	195	-326	1.26	-0.01	0.70	-0.18

found on earth. Detailed implications for the EoS of the crust of NSs will be given in Sec. 4.5.

4.4.1 The Compressible Liquid Drop Model

In the crust of NSs, we consider the following composition: the nuclear clusters are composed of neutrons and protons, which are described by the mass number $A_{\rm cl}$ and the isospin asymmetry $I_{\rm cl}$. The neutron and proton particle numbers in the nuclear clusters are obtained as $N_{\rm cl} = A_{\rm cl}(1+I_{\rm cl})/2$ and $Z_{\rm cl} = A_{\rm cl}(1-I_{\rm cl})/2$. In addition, clusters are embedded in a gas of electrons and neutrons, described by their uniformly distributed densities n_e and n_{ng}. We have implicitly assumed the r-representation [193] for the Wigner-Seitz cell. In this representation, the particles in the cluster volume $V_{\rm cl}$ are in equilibrium with the ones in the outside volume $V_{\rm WS}-V_{\rm cl}$, where $V_{\rm WS}$ is the Wigner-Seitz volume. There are therefore five variables in total (four particles and one volume), but one is free to choose any combination of these variables. In the present study, we consider the following ones: $A_{\rm cl}$, $I_{\rm cl}$, $n_{\rm cl}$, n_e and n_{ng}, where $n_{\rm cl} = A_{\rm cl}/V_{\rm cl}$ as in Ref. [194].

The total cluster energy in the NS crust is expressed as the sum of the independent contributions from the clusters $E_{\rm cl}$, the electrons E_e and the neutron gas E_{ng},

$$E_{\rm tot}(A_{\rm cl}, I_{\rm cl}, n_{\rm cl}, n_e, n_{ng}) = E_{\rm cl}(A_{\rm cl}, I_{\rm cl}, n_{\rm cl}) + E_e(n_e) + E_{ng}(n_{ng})\,. \tag{4.4}$$

The cluster contribution in the CLDM is expressed as a bulk energy contribution, determined from homogeneous matter, and a finite-size contribution, including Coulomb, surface, curvature terms at leading orders. The cluster binding energy contributing to Eq. (4.4) is given by,

$$E_{\rm cl}(A_{\rm cl}, I_{\rm cl}, n_{\rm cl}, n_e) = E_{\rm bulk}(I_{\rm cl}, n_{\rm cl}) + E_{\rm FS}(A_{\rm cl}, I_{\rm cl}, n_{\rm cl}, n_e)\,, \tag{4.5}$$

with $n_{\rm cl}$ being the cluster density. In the CLDM, the clusters are considered with a uniform density, and the neutron and proton radii, R_n and R_p, are identically equal to the cluster radius $R_{\rm cl}$ (there is no neutron skin in the present model). There is no smooth decrease of the density profile near the cluster radius, at variance with the droplet model [195] or Thomas-Fermi approaches [196, 197]. Further, in the NS crust the total density $n_B = (A_{\rm cl} + N_g)/V_{\rm WS}$ is imposed, N_g being the number of neutrons in the gas phase. This contributes to fix one constraint among the five independent variables. This constraint is treated with the Lagrange multiplier technique, as suggested in Ref. [198].

In the present CLDM, the global asymmetry of the cluster $I_{\rm cl} = (N_{\rm cl} - Z_{\rm cl})/A_{\rm cl}$ coincides with the cluster bulk asymmetry $\delta_{\rm cl} = (n_{{\rm cl},n} - n_{{\rm cl},p})/n_B$, $n_{{\rm cl},n}$ and $n_{{\rm cl},p}$ being the uniform neutron and proton densities in the cluster, since the neutron or proton skin are not considered here. Note however that neutron skins have been considered in Ref. [29] by introducing a fit parameter ζ relating $I_{\rm cl}$ and $\delta_{\rm cl}$, as $\delta_{\rm cl} = \zeta I_{\rm cl}$. If ζ is unity, there is no skin, while if $\zeta < 1$, then all nuclei with $N_{\rm cl} > Z_{\rm cl}$ will have a neutron skin ($R_n > R_p$). In reality, the parameter ζ is function of $A_{\rm cl}$ and $Z_{\rm cl}$, see Ref. [199], as well as of the nuclear interaction, as illustrated by the correlation between the neutron skin in ^{208}Pb and the slope of the symmetry energy $L_{\rm sym}$ [200, 201]. It is thus a strong approximation to impose the relation $\delta_{\rm cl} = \zeta I_{\rm cl}$ with ζ constant that we prefer not to consider here. The skin contribution modifies the Coulomb term by using the proton radius instead of the cluster radius, which modified the Coulomb energy by a factor proportional to the difference between the bulk asymmetry $\delta_{\rm cl}$ and the global asymmetry $I_{\rm cl}$. This term increases with the nuclear size and asymmetry and can be important for nuclear clusters present close to the crust-core transition. However, this modification is small compared to the leading order terms considered here and we follow the procedure of recent works [194, 202] and neglect the presence of neutron skin in the present study. In a future development, a consistent derivation in the spirit of Ref. [199] for instance will be considered.

The CLDM we consider is comparable to the pioneering BBP model [203] and is well suited to analyze the origin of the uncertainties in the predictions of the NS crust. More microscopic models for the crust have indeed been developed, see for instance Ref. [204] and recent efforts in Refs. [205]. While being less accurate than microscopic models in reproducing finite nuclei, the present CLDM allows us a better understanding of the various features influencing the properties of the NS crust, which are difficult to analyze in a microscopic model. There are however missing features, such as shell and pairing effects, but these feature are sub-dominant in the leptodermous expansion: they represent a refinement in the description of experimental binding energies which is of the order of a few MeV in total energy, compared to the leading order contributions which are of the order of hundreds of MeV.

Let us now summarize the various contributions present in the CLDM.

The cluster bulk contribution

The cluster bulk contribution to the energy per particle is the leading order term in the leptodermous expansion (order A_{cl}, the mass term). It is related to the homogeneous matter calculation, represented here by the meta-model energy density $\epsilon_{\text{MM}}(n_n, n_p) = n_B e_{\text{MM}}(n_n, n_p)$, given by

$$e_{\text{bulk}}(I_{\text{cl}}, n_{\text{cl}}) = \frac{1}{n_B}\Big(\epsilon_{\text{MM}}(n_{\text{cl},n}, n_{\text{cl},p}) - n_{\text{cl},n} m_n c^2 - n_{\text{cl},p} m_p c^2\Big) , \tag{4.6}$$

where the neutron and proton masses m_n and m_p are fixed to their bare mass, $m_n c^2 = 939.565346$ MeV and $m_p c^2 = 938.272013$ MeV, and $n_{\text{cl},n}$ and $n_{\text{cl},p}$ are the uniform neutron and proton densities in the cluster.

The finite-size contributions

The finite-size terms incorporates the nuclear contributions to the cluster energy at all orders in the leptodermous expansion. In the present study, we limit ourself to the leading order terms: the Coulomb term is in $Z_{\text{cl}}^2/A_{\text{cl}}^{1/3} \approx A_{\text{cl}}^{5/3}$ (dominant term at large A which prevents super-heavy nuclei to exist), the surface is in $A_{\text{cl}}^{2/3}$, and the curvature term is in $A_{\text{cl}}^{1/3}$. They are expressed as

$$E_{\text{FS}}(A_{\text{cl}}, I_{\text{cl}}, n_{\text{cl}}) = E_{\text{Coul}}(A_{\text{cl}}, I_{\text{cl}}, n_{\text{cl}}) + E_{\text{surf}}(A_{\text{cl}}, I_{\text{cl}}, n_{\text{cl}}) + E_{\text{curv}}(A_{\text{cl}}, I_{\text{cl}}, n_{\text{cl}}). \tag{4.7}$$

The Coulomb term

The Coulomb term for a spherical and uniform distribution of protons is given by the direct and exchange contributions,

$$E_{\text{Coul}} = \mathcal{C}_{\text{Coul}}\left(E_{\text{Coul,Dir}} + E_{\text{Coul,Ex}}\right) , \tag{4.8}$$

with

$$E_{\rm Coul,Dir} = \frac{3}{5}\frac{Z_{\rm cl}^2 e^2}{R_p} f_{\rm Coul}(u) \tag{4.9}$$

$$= a_c \left(\frac{1-I_{\rm cl}}{2}\right)^2 f_{\rm Coul}(u) A^{5/3} \tag{4.10}$$

$$E_{\rm Coul,Ex} = -\frac{3}{4}\left(\frac{3}{2\pi}\right)^{2/3} \frac{Z_{\rm cl}^{4/3} e^2}{R_p} h_{\rm Coul}(u) \tag{4.11}$$

$$= -\frac{5a_c}{4}\left(\frac{3}{2\pi}\right)^{2/3}\left(\frac{1-I_{\rm cl}}{2}\right)^{4/3} h_{\rm Coul}(u) A\,, \tag{4.12}$$

where $e^2 \approx \hbar c/137$ and the functions $f_{\rm Coul}$ and $h_{\rm Coul}$ are defined as: $f_{\rm Coul}(u) = 1-(3/2)u^{1/3} + (1/2)u$ and $h_{\rm Coul}(u) = 1 + u^{1/3}$, with u the volume fraction of the cluster, defined as,

$$u = \frac{V_{\rm cl}}{V_{\rm WS}} = \frac{n_e}{n_{{\rm cl},p}} = \frac{2n_e}{(1-I_{\rm cl})n_{\rm cl}}\,, \tag{4.13}$$

where $n_{{\rm cl},p} = n_{\rm cl}(1-I_{\rm cl})/2$ is defined as the proton density in the cluster. In the function $f_{\rm Coul}$, the first term corresponds to the proton-proton repulsive interaction, the second term is the "lattice contribution" including the electron-proton and electron-electron interaction, under the hypothesis of a globally neutral Wigner-Seitz cell. Then the third term in $f_{\rm Coul}$ stands for the finite-size correction which becomes important when the cluster volume is comparable with the Wigner-Seitz volume. This term is important near the crust-core transition and pushes the transition to nuclear matter towards higher densities. The first term is the only one remaining in the case of isolated nuclei, corresponding to the limit $u = 0$. Since there is no proton-electron contributions to the exchange Coulomb energy, the first (second) term in $h_{\rm Coul}$ corresponds to the proton-proton (electron-electron) contribution.

The coefficient $\mathcal{C}_{\rm Coul}$ in Eq. (4.8) is a variational parameter which is fine tuned over the nuclear mass table. It describes – in an effective way – the effect the diffusive nuclear surface on the Coulomb energy, which is neglected in the sharp drop off density profile that we consider here. Since the diffusive surface is expected to be a small correction, the fit value is expected to remain close to 1, $\mathcal{C}_{\rm Coul} \approx 1$.

Note that the direct Coulomb term scales like $A_{\rm cl}^{5/3}$ and therefore dominates the CLDM energy at large $A_{\rm cl}$. Since the Coulomb term is repulsive, this induces a limitation in the maximum $A_{\rm cl}$ for finite nuclei. However, for most of nuclei in the nuclear chart, the Coulomb interaction remains small compared to the nuclear one. For this reason, the bulk term in $A_{\rm cl}$ and the Coulomb direct contribution in $A_{\rm cl}^{5/3}$ are considered at the same order in the leptodermous expansion. It is also interesting to note that the exchange Coulomb term contributes to two order lower compared to the direct term in the $A_{\rm cl}^{1/3}$ leptodermous expansion. It is thus expected to effectively contribute at one order below the curvature contribution.

Neglecting the difference between the neutron and proton radii – no skin approximation –, we have $R_p = R_{\rm cl} = r_{cl}(n_{\rm cl})A_{\rm cl}^{1/3}$ with $r_{cl}^3(n_{\rm cl}) = 3/(4\pi n_{cl})$, and the Coulomb factor reads,

$$a_c(n_{\rm cl}) = \frac{3}{5}\left(\frac{4\pi}{3}n_{\rm cl}\right)^{1/3} e^2\,. \tag{4.14}$$

Note that the Coulomb factor a_c defined from Eq. (4.14) depends on the cluster density. The Coulomb parameter, a_c, is however often taken as a constant, see for instance Ref. [194], either as a free parameter to be fitted or as function of the constant $n_{\rm sat}$. The different assumptions for a_c give differences on the description of isolated nuclei. Note that if a_c is taken to be constant (often taken to be of the order $\sim$ 0.7 MeV), neither the Coulomb nor the surface energy contributes to nuclear pressure, the pressure derives from the bulk term only. In NS crust however, the Coulomb term contributes to the pressure due to its dependence in the volume fraction u. In this work, we will keep the dependence of this parameter on $n_{\rm cl}$, i.e. $a_c = a_c(n_{\rm cl})$.

The surface energy

The surface energy is proportional to the surface tension $\sigma_{\rm surf}(I_{\rm cl})$ and scales as $A_{\rm cl}^{2/3}$. It reads

$$\begin{aligned} E_{\rm surf}(A_{\rm cl}, I_{\rm cl}, n_{\rm cl}) &= 4\pi R_{\rm cl}^2 \sigma_{\rm surf}(I_{\rm cl}) \qquad (4.15)\\ &= 4\pi r_{\rm cl}^2 \sigma_{\rm surf}(I_{\rm cl}) A_{\rm cl}^{2/3}\,, \qquad (4.16)\end{aligned}$$

with $\sigma_{\rm surf}(I_{\rm cl})$ as expressed, as suggested in [206], as

$$\sigma_{\rm surf}(I_{\rm cl}) = \sigma_{\rm surf,sat} \frac{2^{p_{\rm surf}+1} + b_{\rm surf}}{Y_p^{-p_{\rm surf}} + b_{\rm surf} + (1-Y_p)^{-p_{\rm surf}}}, \qquad (4.17)$$

where $Y_p = Z_{\rm cl}/A_{\rm cl} = (1 - I_{\rm cl})/2$ is the cluster proton fraction and $\sigma_{\rm surf,sat}$ is a parameter that determines the surface tension in symmetric nuclei. The parameter $p_{\rm surf}$ entering into the expression of the surface tension (4.17) plays an important role at large isospin asymmetries. In this work this parameter is fixed to be $p_{\rm surf} = 3$, as usually done in the literature [206], but a small variation around 3 plays an important role at large asymmetries occurring around the core-crust transition densities in NSs [202].

For small asymmetries,

$$\sigma_{\rm surf}(I_{\rm cl}) \approx \sigma_{\rm surf,sat} - \sigma_{\rm surf,sym} I_{\rm cl}^2 \qquad (4.18)$$

with

$$\sigma_{\rm surf,sym} = \sigma_{\rm surf,sat} \frac{2^{p_{\rm surf}} p_{\rm surf}(p_{\rm surf}+1)}{2^{p_{\rm surf}+1} + b_{\rm surf}}\,. \qquad (4.19)$$

One can thus relate the parameter $b_{\rm surf}$ to the surface symmetry energy $\sigma_{\rm surf,sym}$. We have

$$b_{\rm surf} = 2^{p_{\rm surf}} \left[p_{\rm surf}(p_{\rm surf}+1) \frac{\sigma_{\rm surf,sat}}{\sigma_{\rm surf,sym}} - 2 \right]\,. \qquad (4.20)$$

In the following, we prefer to use the parameter $\sigma_{\rm surf,sym}$ instead of $b_{\rm surf}$, since it directly reflects the isospin dependence of the surface tension for small isospin asymmetries, as shown in Eq. (4.18). For this reason the domain of variation of $\sigma_{\rm surf,sym}$ is better constrained than the one for the parameter $b_{\rm surf}$, which eases the determination of the prior for this parameter. Tab. 4.4 suggests a standard value for this parameter obtained by averaging over the usual values used in the literature. See for instance Ref. [202] for a sample of such values associated to various Skyrme interactions.

The curvature energy

The curvature energy is controlled by the curvature tension $\sigma_{\text{curv}}(I)$, and follows [207],

$$E_{\text{curv}}(A_{\text{cl}}, n_{\text{cl}}, I_{\text{cl}}) = 8\pi r_{cl} \sigma_{\text{curv}}(I_{\text{cl}}) A_{\text{cl}}^{1/3}, \tag{4.21}$$

with

$$\sigma_{\text{curv}}(I_{\text{cl}}) = \alpha \sigma_{\text{curv,sat}} \frac{\sigma_{\text{surf}}(I_{\text{cl}})}{\sigma_{\text{surf,sat}}} \left[\beta_{\text{curv}} - \frac{1 - I_{\text{cl}}}{2}\right] . \tag{4.22}$$

The parameter α is fixed to be $\alpha = 5.5$ since we allow the variation of the parameter $\sigma_{\text{curv,sat}}$ in the fit to the binding energy over the nuclear chart, see Sec. 4.4.2. The standard values for the curvature parameters $\sigma_{\text{curv,sat}}$ and β_{curv} are also given in Tab. 4.4.

The authors of Ref. [208] explored the role of the various finite size terms on the properties of NS crusts. This was done by using four different prescriptions, called FS1 to FS4, with each prescription including a certain set of finite size terms and approximations. In this work, we will follow only the FS4 prescription and refer the reader to Ref. [208] for a detailed comparison between the other sets of approximations.

4.4.2 Fit to nuclear masses

We now incorporate experimental nuclear data into the CLDM as follows. We have 5 parameters that need to be fit to data: $\mathcal{C}_{\text{Coul}}$, $\sigma_{\text{surf,sat}}$, $\sigma_{\text{surf,sym}}$, $\sigma_{\text{curv,sat}}$ and β_{curv}. Note that the parameter p_{surf} is fixed to be 3.0 in this work. We now define four other parameters $\mathcal{C}_i$ defined as,

$$\sigma_{\text{surf,sat}} = \mathcal{C}_{\text{surf,sat}} \sigma_{\text{surf,sat}}^{\text{std}} , \tag{4.23}$$

$$\sigma_{\text{surf,sym}} = \mathcal{C}_{\text{surf,sym}} \sigma_{\text{surf,sym}}^{\text{std}} , \tag{4.24}$$

$$\sigma_{\text{curv,sat}} = \mathcal{C}_{\text{curv,sat}} \sigma_{\text{curv,sat}}^{\text{std}} , \tag{4.25}$$

$$\beta_{\text{curv}} = \mathcal{C}_{\beta} \beta_{\text{curv}}^{\text{std}} . \tag{4.26}$$

where the superscript std refers to the standard value of the parameters as given in Tab. 4.4. Thus, ultimately, the five parameters to be fit to the data are $\mathcal{C}_{\text{Coul}}$, $\mathcal{C}_{\text{surf,sat}}$, $\mathcal{C}_{\text{surf,sym}}$, $\mathcal{C}_{\text{curv,sat}}$ and $\mathcal{C}_{\beta}$ The values for these variational parameters are expected to be close to 1, as we show in Table 4.5.

The loss function χ_E, required for the fit, is defined as,

$$\chi_E = \left[\frac{1}{N}\sum_{i=1}^{N}(\tilde{E}^i_{\text{exp}} - E^i_{\text{nuc}})^2\right]^{1/2} , \tag{4.27}$$

where $N = 3375$ is the number of considered nuclei from the experimental nuclear chart and E^i_{nuc} the energy from the CLDM model for the nucleus i. The energy of an isolated nucleus is simply defined from the CLDM as,

$$E_{\text{nuc}}(A_{\text{cl}}, I_{\text{cl}}, n_{\text{cl}}) = E_{\text{bulk}}(A_{\text{cl}}, I_{\text{cl}}, n_{\text{cl}}) + E_{\text{FS}}(A_{\text{cl}}, I_{\text{cl}}, n_{\text{cl}}, n_e = 0) . \tag{4.28}$$

Note that there are only three independent variables in this case, contrary to the 5 variables required to describe the nuclear clusters in the NS crust. There are no electron and neutron gases surrounding the nuclear cluster. In addition, note that the Wigner-Seitz volume $V_{\rm WS}$ is undefined (it is indeed infinite for isolated nuclei) but the cluster volume $V_{\rm cl}$ is. For each nucleus defined by its mass $A_{\rm cl}$ and its charge $Z_{\rm cl}$ localizing it over the nuclear chart, the mechanical equilibrium is imposed: $P_{\rm nuc} = n_{\rm cl}^2 \partial E_{\rm nuc}/\partial n_{\rm cl} = 0$. This variational condition fixes the nuclear cluster density $n_{\rm cl}(A_{\rm cl}, Z_{\rm cl})$ at equilibrium: each nucleus has a different density, and overall they explore the density dependence of the CLDM around saturation density, at variance with the liquid-drop model where the model coefficients are kept constant.

In Eq. 4.27, The quantity $\tilde{E}^i_{\rm exp} = E^i_{\rm exp} - \Delta E^i_{\rm exp}$, where $E^i_{\rm exp}$ is the experimental mass of the nucleus i and $\Delta E^i_{\rm exp}$ is a correction that we have introduced in order the reduce the effect of the odd-even mass staggering in the data. This correction is given by the relation

$$\Delta E^i_{\rm exp} = \left[\Delta_{\rm sat} + \Delta_{\rm sym}\left(\frac{N_i - Z_i}{A_i}\right)^2\right] A_i^{-1/3}\, \delta(N, Z)\,. \tag{4.29}$$

where $\delta(N, Z) = 1$ if N and Z are odd, 0 if either N or Z is odd, and -1 if both N and Z are even [209]. The parameters $\Delta_{\rm sat}$ and $\Delta_{\rm sym}$ are varied together with the CLDM parameters $\mathcal{C}_i$ in the fit to the experimental masses.

By comparing χ_E and $\chi_{E/A}$ (defined as function of E/A instead of E), the impact of the loss function has been shown to be non-negligible in general, but smaller than other uncertainties [208] such as for instance the one coming from varying the model for the bulk. We will thus employ only χ_E for the fit, without considering the uncertainties originating from a different measure of the goodness of the model to reproduce experimental nuclear masses.

The results of the fit to finite nuclei are shown in Table 4.5. The coefficients $\mathcal{C}_i$ are in general of the order of 1, as expected. The odd-even mass staggering parameters $\Delta_{\rm sat}$ and $\Delta_{\rm sym}$ are also shown. The isoscalar parameter $\Delta_{\rm sat}$ is similar to the value suggested in Ref. [210] (7.2 MeV). The isovector parameter $\Delta_{\rm sym}$ however is much smaller than the one suggested in Ref. [210] (-44 MeV), where the fit is done by considering only $A > 40$ nuclei. We indeed found that this quantity is very sensitive to the nuclei which we fit it. When we select only $A > 40$ nuclei $\Delta_{\rm sym}$ change from -7.35 (-11.26) to ≈-16.83 (-16.60) MeV for BSK14 (SLy5). The value of $\Delta_{\rm sym}$ therefore varies from one region of the nuclear chat to another. It is difficult to determine a constant value over the nuclear chart, but its influence is small since nuclei do not explore large isospin asymmetries ($N < 2Z$ for heavy nuclei).

With a loss function $\chi_E \lesssim 3$ MeV, the χEFT models H1 to H4 are the more accurate ones to reproduce the experimental masses. They are comparable with the Skyrme models considered here. Note that our conclusion remains valid even when we do not correct for the odd-even mass staggering in the nuclear data, see number inside the parentheses in the χ_E column in Table 4.5. The nuclear masses however disfavor the χEFT models: H5, H7, DHS$_{L59}$ and DHS$_{L69}$. In the following, Hamiltonians H1-H4 will be considered as our best models and will be marked with a gray band, since they are the best at reproducing the nuclear masses.

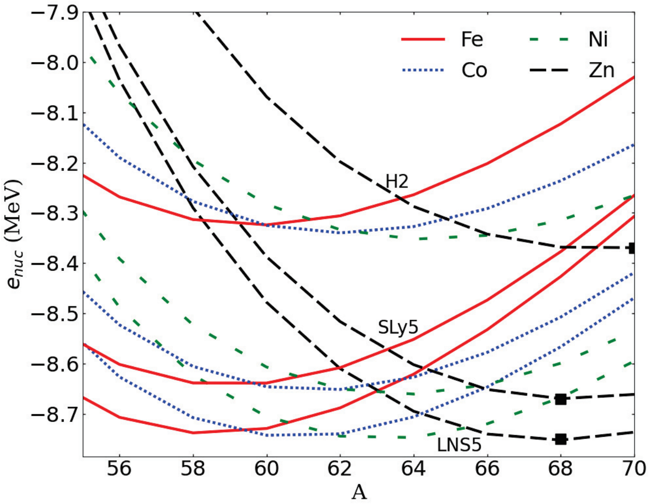

Figure 4.5: Binding energy for the Iron group using the CLDM with SLy5, LNS5 and H2. A black square marks the lowest energy for each model.

The last two columns of Table 4.5 show the minimal energy per particle obtained for each model. This quantity is sometimes used to define the offset of the energy per particle in the crust. Experimentally, the nucleus ^{56}Fe minimizes the energy, but it is a bit model dependent due to the approximation scheme. The search for the minimal energy per particle configuration is illustrated in Fig. 4.5 for a few models (LNS5, SLy5 and H2) and for iron group isotopic chains (Fe, Co, Ni, Zn). For all the Skyrme models, the lowest energy configuration is ^{68}Ni. This is also the lowest energy configuration for H1, H3, H4, while H2 prefers ^{70}Ni and the other χEFT models prefer $^{56-60}$Fe nuclei.

Table 4.4: Standard parameters the surface and curvature terms employed in the CLDM approach considered in this work. Note the associated value $b_{\rm surf} = 29.9$ for $\sigma_{\rm surf,sym}$.

$\sigma^{\rm std}_{\rm surf,sat}$	$\sigma^{\rm std}_{\rm surf,sym}$	$p^{\rm std}_{\rm surf}$	$\sigma^{\rm std}_{\rm curv,sat}$	$\beta^{\rm std}_{\rm curv}$
MeV fm^{-2}	MeV fm^{-2}		MeV fm^{-1}	
1.1	2.3	3.0	0.1	0.7

4.5 The crust of neutron stars

In this section we will use the tools developed in Secs. 4.3 and 4.4 to study the crust of NSs. We first derive the equilibrium equations and then present and discuss our results for the NS equation of state.

Table 4.5: Optimization of the parameters $\mathcal{C}_i$ over the nuclear chart, for $A \geq 12$ and $Z \geq 6$, and considering the experimental energies from the 2016 Atomic Mass Evaluation (AME) [148] for the interactions considered in this work (Skyrme and χEFT). Odd-even mass staggering parameters Δ_{sat} and Δ_{sym}, χ_E for the optimization with (without) odd-even mass staggering. In the two last columns, the minimal energy E_{cl}/A for each model is given together with its position in the nuclear chart $(A, Z)_{\mathrm{min}}$. Experimental binding energy are E/A(^{56}Fe) = -8.79 MeV and E/A(^{68}Zn) = -8.76 MeV.

Model	$\mathcal{C}_{\mathrm{Coul}}$	$\mathcal{C}_{\mathrm{surf,sat}}$	$\mathcal{C}_{\mathrm{surf,sym}}$	$\mathcal{C}_{\mathrm{curv,sat}}$	$\mathcal{C}_{\beta}$	Δ_{sat} (MeV)	Δ_{sym} (MeV)	χ_E (MeV)	$\min(E_{\mathrm{nuc}}/A)$ (MeV)	(A,Z)$_{\mathrm{min}}$
BSK14$_{\mathrm{MM}}$	0.965	1.002	0.890	0.770	1.100	5.75	-7.35	2.61 (2.74)	-8.72	(68,30)
BSK16$_{\mathrm{MM}}$	0.973	1.076	0.876	0.777	0.817	5.68	-4.88	2.66 (2.79)	-8.70	(68,30)
LNS5$_{\mathrm{MM}}$	0.949	0.916	0.668	0.531	1.646	5.69	-4.84	2.66 (2.79)	-8.75	(68,30)
RATP$_{\mathrm{MM}}$	0.970	1.095	0.676	0.583	0.694	5.54	0.22	2.81 (2.93)	-8.70	(68,30)
SGII$_{\mathrm{MM}}$	0.952	0.942	0.406	0.262	1.981	5.42	4.97	2.95 (3.07)	-8.75	(68,30)
F0$_{\mathrm{MM}}$	0.966	1.064	1.264	1.144	0.922	5.82	-10.47	2.60 (2.73)	-8.65	(68,30)
SLy5$_{\mathrm{MM}}$	0.967	1.039	1.257	1.116	0.980	5.85	-11.26	2.59 (2.72)	-8.67	(68,30)
H1$_{\mathrm{MM}}$	0.966	1.582	1.307	0.942	-0.255	5.53	0.22	3.07 (3.18)	-8.17	(68,30)
H2$_{\mathrm{MM}}$	0.927	1.037	1.123	1.053	1.141	5.79	-9.46	2.58 (2.71)	-8.37	(70,30)
H3$_{\mathrm{MM}}$	0.913	0.847	1.095	1.127	1.560	5.94	-14.83	2.65 (2.77)	-8.61	(68,30)
H4$_{\mathrm{MM}}$	0.903	0.716	0.967	1.144	1.833	5.99	-16.85	2.77 (2.89)	-8.84	(68,30)
H5$_{\mathrm{MM}}$	0.868	0.325	0.646	1.215	2.616	6.32	-29.26	3.78 (3.86)	-9.83	(58,26)
H7$_{\mathrm{MM}}$	0.858	0.110	0.339	1.086	3.235	6.61	-43.69	5.32 (4.95)	-10.23	(56,26)
DHS$_{L59,\mathrm{MM}}$	0.853	0.370	1.038	1.686	2.089	6.41	-33.40	4.34 (4.41)	-9.66	(58,26)
DHS$_{L69,\mathrm{MM}}$	0.871	0.567	1.571	1.971	1.649	6.28	-28.51	4.02 (4.10)	-9.10	(60,26)

4.5.1 Equilibrium Equations

The CLDM cluster energy is minimized under the constraint of the baryon density n_B defined as,

$$\begin{aligned} n_B &= \frac{A_{\rm cl}+N_g}{V_{\rm WS}} = n_{\rm cl}u + n_{ng}(1-u)\,, & (4.30)\\ &= n_{ng} + \frac{2n_e}{1-I_{\rm cl}}\left(1-\frac{n_{ng}}{n_{\rm cl}}\right)\,. & (4.31)\end{aligned}$$

In Eq. (4.31), the density n_B is expressed in terms of four of the five independent variables: $A_{\rm cl}$, $I_{\rm cl}$, $n_{\rm cl}$, n_e and n_{ng}. We use the Lagrange multipliers technique, as suggested in Ref. [198], to minimize the μ canonical energy density $\epsilon_{\mu,{\rm can}}$ in the Wigner-Seitz cell,

$$\epsilon_{\mu,{\rm can}} = \epsilon_{\rm tot} - \mu_B n_B\,. \tag{4.32}$$

The total energy reads,

$$\epsilon_{\rm tot}(A_{\rm cl}, I_{\rm cl}, n_{cl}, n_e, n_g) = u\epsilon_{\rm cl} + (1-u)\epsilon_g + n_e(m_pc^2 - m_nc^2) + n_B m_n c^2 + \rho_e\,, \tag{4.33}$$

where $u = V_{\rm cl}/V_{\rm WS}$ is the volume occupied by a nucleus in a Wigner-Seitz cell, ρ_e is the electron energy density (with rest mass), $\epsilon_g = \epsilon_{\rm MM}(n_{ng}=n_g, n_p=0)$ is the neutron gas energy density and $\epsilon_{\rm cl} = \epsilon_{\rm MM}(n_{n,{\rm cl}}, n_{p,{\rm cl}}) + \epsilon_{\rm FS}(A_{\rm cl}, I_{\rm cl}, n_e, n_{\rm cl})$ is the cluster energy density, with the finite-size contributions given by Eq. (4.7) and discussed in the previous section.

In fact $\epsilon_{\mu,{\rm can}}$ coincides with the pressure, $\epsilon_{\mu,{\rm can}} = -P_{\rm tot}$. So minimizing $\epsilon_{\mu,{\rm can}}$ is equivalent to maximizing the total pressure $P_{\rm tot}$. Moreover, minimizing the total energy $E_{\rm tot} \equiv \epsilon_{\rm tot}V_{\rm WS}$ at fixed baryon density n_B is equivalent to minimizing the total Gibbs energy $G_{\rm tot}$ at fixed total pressure, as discussed in Ref. [211].

We define the following thermodynamical quantities ($q = n$, p),

$$\begin{aligned} P_{\rm cl} &\equiv n_{\rm cl}^2 \frac{\partial E_{\rm cl}/A_{\rm cl}}{\partial n_{\rm cl}}\Big|_{A_{\rm cl},I_{\rm cl}}\,, & (4.34)\\ P_g &\equiv -\epsilon_g + n_g\mu_g\,, & (4.35)\\ \mu_{{\rm cl},q} &\equiv \mu_{{\rm nuc},q} + \frac{P_g}{n_B}\,, & (4.36)\\ \mu_e &\equiv \frac{\partial E_e}{\partial N_e}\Big|_{N_{\rm cl},Z_{\rm cl}} + \frac{2n_e}{(1-I_{\rm cl})A_{\rm cl}}\frac{\partial E_{\rm Coul}}{\partial n_e}\,, & (4.37)\end{aligned}$$

with

$$\mu_{{\rm nuc},n} \equiv \frac{\partial E_{\rm nuc}}{\partial N_{\rm cl}}\Big|_{Z_{\rm cl},N_e}\,, \quad \mu_{{\rm nuc},p} \equiv \frac{\partial E_{\rm nuc}}{\partial Z_{\rm cl}}\Big|_{N_{\rm cl},N_e}\,. \tag{4.38}$$

From Eq. (4.34), we deduce,

$$P_{\rm cl} = P_{\rm bulk} + P_{\rm Coul} + P_{\rm surf} + P_{\rm curv}\,, \tag{4.39}$$

with obvious definitions for these partial contributions.

We impose the stationary condition of the canonical potential (4.32) with respect to the five independent variables, considering μ_B as a constant parameter, and obtain the following equilibrium relations [212],

$$
\begin{aligned}
2E_{\mathrm{Coul}} &= E_{\mathrm{surf}} + 2E_{\mathrm{curv}}\,, && (4.40)\\
P_{\mathrm{cl}} &= P_g\,, && (4.41)\\
\mu_{\mathrm{cl},n} &= \mu_g\,, && (4.42)\\
\mu_{\mathrm{cl},n} &= \mu_{\mathrm{cl},p} + \mu_e + \Delta mc^2\,, && (4.43)\\
\mu_B &= \mu_g \\
&\quad + \frac{2n_e}{n_{\mathrm{cl}}A_{\mathrm{cl}}(1-I_{\mathrm{cl}}) - 2n_e}\frac{\partial E_{\mathrm{surf}}}{\partial n_g}\bigg|_{A_{\mathrm{cl}},I_{\mathrm{cl}},n_{\mathrm{cl}}}\,, && (4.44)
\end{aligned}
$$

where $\Delta m = m_p - m_n$. These equilibrium relations have a physical interpretation: Eq. (4.40) is an extension of the virial theorem [203] including the curvature energy, Eq. (4.41) reflects the mechanical equilibrium, Eq. (4.42) describes the chemical equilibrium between the cluster and the gas in the r-representation, and finally Eq. (4.43) assures the β-equilibrium. The last Eq. (4.44) describes the baryon chemical potential which fixes the baryon density.

Equations (4.40)-(4.44) are solved by using the robust Newton-Raphson method. Note that since the surface energy (4.16) is independent of the gas density n_{ng}, Eq. (4.44) reduces to $\mu_B = \mu_g$.

4.5.2 Results for the crust

The energy, pressure, sound speed and volume fraction, $u = V_{\mathrm{cl}}/V_{\mathrm{WS}}$ where V_{cl} is the cluster volume and V_{WS} the Wigner-Seitz cell volume, at β-equilibrium are shown in Fig. 4.6 for a range of densities spanning over the outer (partially) and inner crust. These quantities are sensitive to the properties of low-density NM, as shown in Fig. 4.2. The models LNS5 and SGII (F0 and SLy5), which predict binding energies in low-density NM lower (higher) than the χEFT band, also predict that the binding energy at β-equilibrium is lower (higher) in the density range going from $3\ 10^{-3}$ to 10^{-1} fm^{-3}. The same remarks are applicable for the pressure, the sound speed and the volume fraction at β-equilibrium. Vertical dark gray bands in Fig. 4.6 shows the prediction for the outer-inner crust transition for the models that better reproduce nuclear masses, i.e., all Skyrme models and H1-H4, while light gray band shows the prediction including all models used in this work. Note the importance of reproducing experimental nuclear masses to better constraint the location of the neutron drip.

It can also be remarked that in the outer crust the χEFT Hamiltonians are more spread than the Skyrme models. Since the Skyrme models reproduce better the experimental nuclear binding, they lead to tighter predictions in the outer crust. Note that the gray band localizing the predictions from H1-H4 χEFT Hamiltonians are in full agreement with the Skyrme ones. One can thus conclude that the experimental nuclear masses are important constraints to accurately predict the EoS in NS outer crust. In the inner crust however, since a large amount of neutrons drip off the clusters to form a neutron fluid, some properties such as the binding energy, the pressure, the sound speed and the volume fraction are largely impacted by the properties of uniform NM.

The transition from non-homogeneous matter (crust) to homogeneous matter (core) is obtained by computing the energy per particle for the two phases and comparing their values as the density increases. The state with the lower energy is the favored one. In the bottom-right

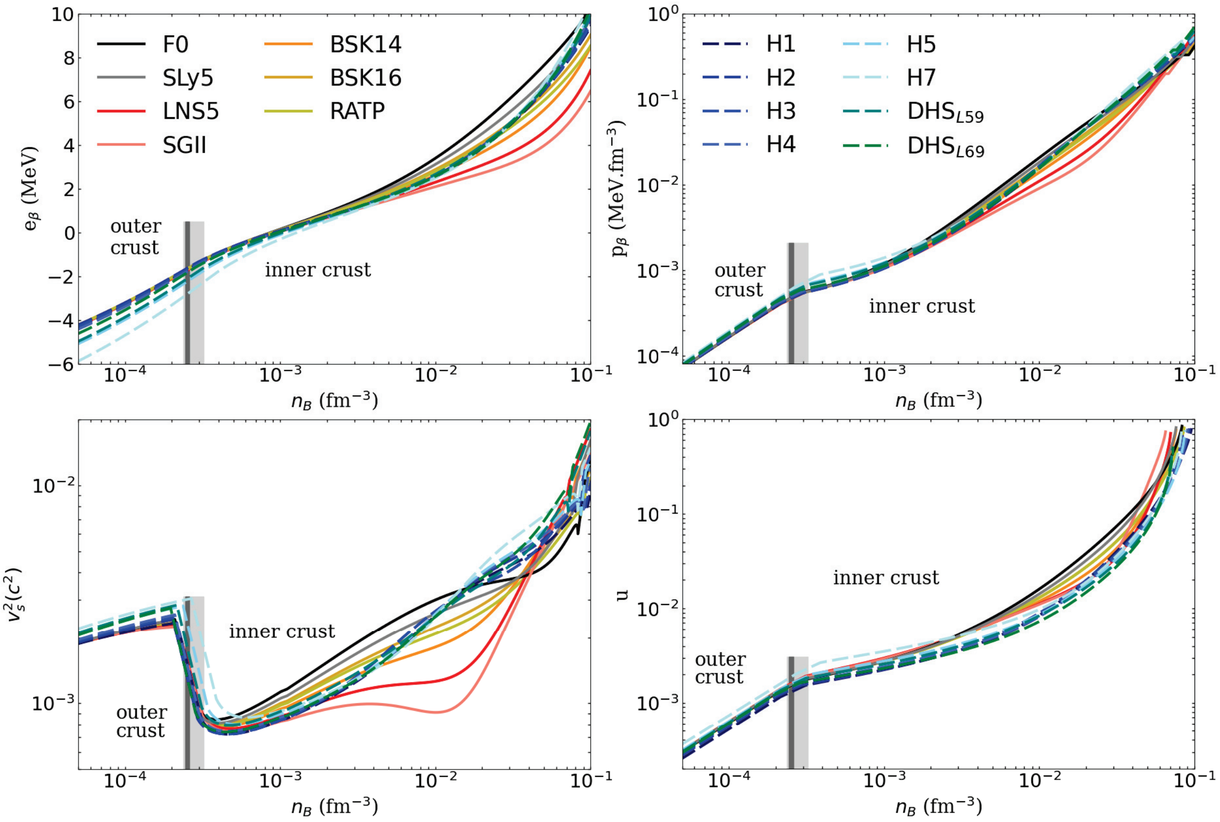

Figure 4.6: Energy per particle, pressure, sound speed and volume fraction at beta equilibrium in the NS crust. Dark gray band shows the prediction for the outer-inner crust transition for the models that better reproduce nuclear masses (all Skyrme and H1-H4). Light gray band shows the uncertainty including all models.

panel of Fig. 4.6 the end of the volume fraction curves indicate this transition. The spread of the ends of the curves shows the uncertainty in the crust-core transition given by the 15 models investigated in this work. In Tab. 4.6 we add the numerical values for the outer-inner crust transition together with the crust-core transition for the different models. Regarding the crust-core transition density, we see that models H1-H7 are consistent with the results of Table 4.1 within uncertainties. This indicates that the spinodal approach of Sec. 4.1 is a very useful tool to calculate the crust-core transition despite the fact that nuclear clusters are not taken into account.

The neutron, proton, electron and muon particle fractions are shown in Fig. 4.7. For densities lower than 10^{-3} fm^{-3} all models agree well together, except H7, which slightly overestimates Y_e. At higher densities however, a dispersion among the model predictions appears. Here also the low-density energy per particle in NM plays an important role: a reduction of the energy per particle in NM would facilitate the production of neutrons from electrons and protons via the β-process, and thus would reduce the electron fraction Y_e. This is exactly what happens: the stiffest models, e.g. F0 and SLy5, predict the largest particle fractions in the density range $10^{-3} - 10^{-1}$ fm^{-3}, while the softest ones, e.g. LNS5 and SGII, predict the lowest electron fractions.

Muons appear at around 0.1-0.2 fm^{-3}, and this onset density is rather model independent (at

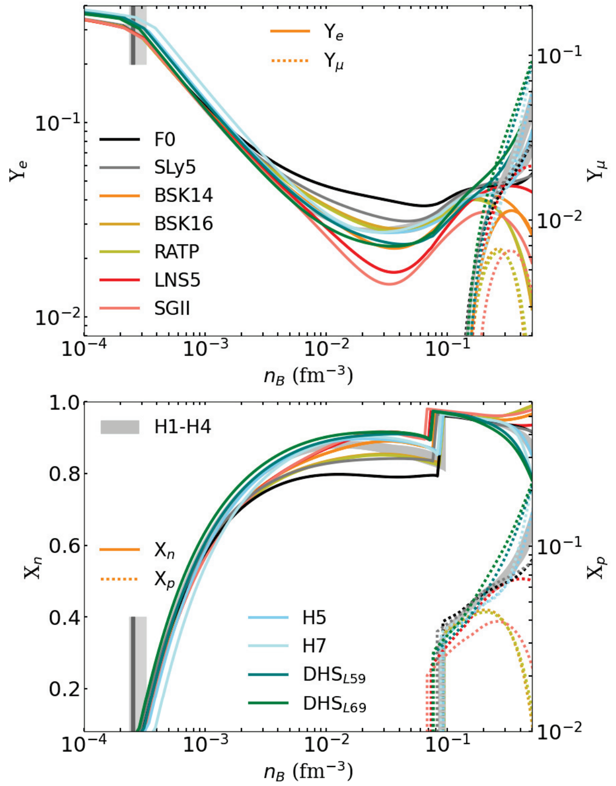

Figure 4.7: Particle fractions. Top: leptons, Y_e left axis (Y_μ right axis) in continuous (dotted) lines. Bottom: baryons, X_n left axis (X_p right axis) in continuous (dotted) lines.

least for the densities explored in this figure). The muon fraction increases with density for all models. At a few times saturation density, some models such as BSK14, BSK16, RATP, SGII and LNS5 predict however a bending down of the electron and muon density. This behavior results from the symmetry energy, see Fig. 4.3, which bends down to zero for these models as the density exceeds saturation density. As the symmetry energy reduces, it is more and more easy to produce neutrons and then the lepton fraction goes down to zero.

The neutron chemical potential is shown in Fig. 4.8. In the outer crust $\nu_n < 0$, since all neutrons are bound to nuclei. The neutron drip is defined as the density at which the first neutron drips out of nuclei or equivalently by the condition that the neutron chemical potential $\nu_n > 0$. Fig. 4.8 only shows this positive case. The small dispersion of the curves in the lower left side of Fig. 4.8 reflects the uncertainties in the position the outer-inner crust transition. As we already commented in the discussion of Fig. 4.6, the position of the inner-outer crust transition is better defined with Skyrme models than with χEFT ones. This indicates that the inner-outer crust transition is mainly determined by the experimental nuclear masses. As the density increases above the drip point, the neutron fluid contribution becomes more important. As a consequence a convergence of the χEFT models is observed, while the uncertainties on the Skyrme models predictions are getting larger and larger. As seen in the previous figures, we note that F0 and SLy5 (LNS5 and SGII) predicts higher (lower) values than the other models, while RATP, BSK14 and BSK16 predicts ν_n compatible with the χEFT models.

The cluster composition in the inner and outer crust is shown in Fig. 4.9. Our best predic-

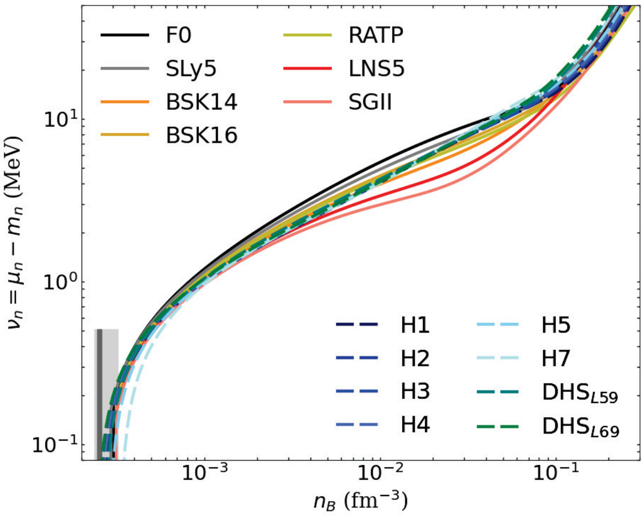

Figure 4.8: Neutron chemical potentials in the inner crust with respect to the baryon density.

tions from the χEFT models H1-H4 are bounded by the gray band. The Asy-Stiff models such as H5, H7, DHS$_{L59}$ and DHS$_{L69}$ predict lower $Z_{\rm cl}$ than the gray band, and the Asy-Soft models such as RATP, LNS5, SGII, BSK16 predict larger $Z_{\rm cl}$ than the gray band. Other models are compatible with the gray band. Note however than close to the core-crust transition density, the behavior of $A_{\rm cl}$ and $Z_{\rm cl}$ can be quite different from one model to another. This is reflecting the important role played by the isospin asymmetry parameter $p_{\rm surf}$, which is fixed to be $p_{\rm surf} = 3$ in our present study. The role of $p_{\rm surf}$ on the core-crust transition density has been discussed in Refs. [194, 208]. It is indeed a parameter which is difficult to determine, since finite nuclei do not explore isospin asymmetries large enough to be impacted by the value of $p_{\rm surf}$. This parameter could be determined from a slab configuration calculation exploring large asymmetries. In the present study, we however prefer to fix $p_{\rm surf}$ for simplicity, but a more accurate estimation of the core-crust transition density shall include a proper adjustment of the parameter $p_{\rm surf}$.

We also compare our results with other predictions in Fig. 4.9, such as the Bruxelles-Montreal Hartree-Fock Bogoliubov calculation (BSk22 and BSk25) [175], the Negele-Vautherin Hartree-Fock calculation [204], the Douchin-Haensel CLDM calculation [213, 166], and finally the original BBP model [214]. The oldest calculations, BBP, Negele-Vautherin and Douchin-Haensel, do not always overlap with our gray band, since they were performed before the recent χEFT achievement. The BSk22 model overlaps pretty well with our gray band, reflecting the good agreement already noticed for the symmetry energy. The model BSk25, which is stiffer than the χEFT H1-H4 models predicts larger $Z_{\rm cl}$ than us. Note also that while shell effects are absent from our calculation, our best predictions (gray band) is compatible with models which have them, e.g. BSk22 or Negele-Vautherin. This shows that while shell effects are important to get accurate $Z_{\rm cl}$, the actual value for $Z_{\rm cl}$ is still largely influenced by the contribution from the bulk term in the CLDM, in particular by the symmetry energy at low-density. The leptodermous expansion, which has been shown to provide a good ordering of the contribution of the different terms in the mass formula in NS crust, suggests that shell effects are comparable with curvature terms. In other words, shell effects are certainly important for accurate predictions of the crust properties, but they are not the main ingredient to understand the origin of the main

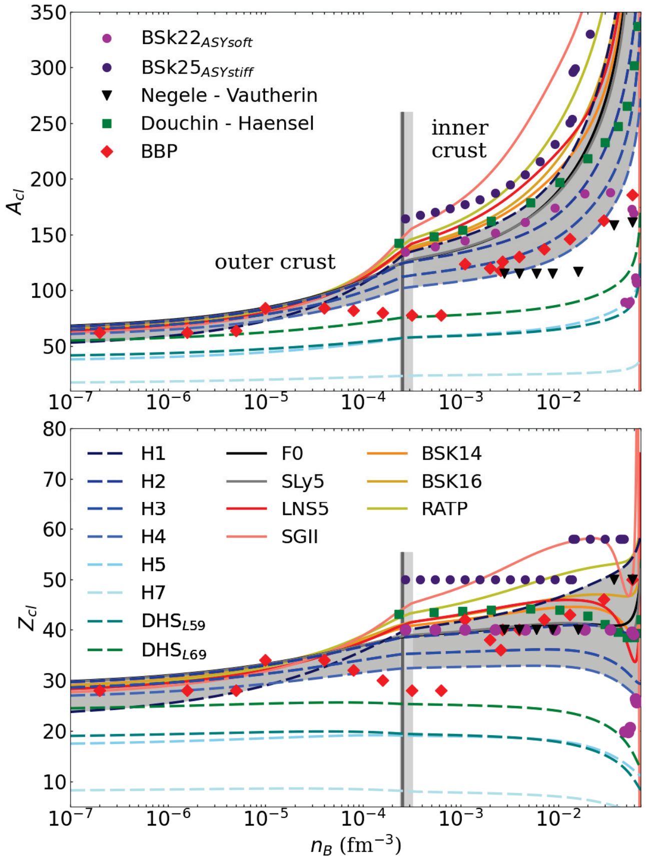

Figure 4.9: Cluster composition, $A_{\rm cl}$ (top) and $Z{\rm cl}$ (bottom), for the eight χEFT Hamiltonians and the seven Skyrme models. The silver band shows our best results including H1-H4.

uncertainties in these properties. The main source of uncertainties are originating from the bulk term, and in more detail by the low-density NM properties.

Several approximations have been made in this work, such as considering a fixed value for $p_{\rm surf}$, using a specific prescription for the finite-size terms (FS4), neglecting neutron skin and shell effects, etc. We end this section by performing a simple comparison that is indicative of the importance of the effects neglected in this work. In Fig. 4.10, we show $Z_{\rm cl}$ and $N_{\rm cl}$ as function of n_B obtained using the CLDM, the fourth order Extended Thomas Fermi (ETF) method and ETF plus the Strutinsky Integral correction (ETFSI). All three models employ the same BSk24 Skyrme interaction. The ETF method takes into account non-uniform density distributions which can be different for neutrons and protons (i.e. the neutron skin), and the ETFSI includes the proton shell effects within the Strutinsky approach. Note that, while the CLDM is expressed in the so-called r-representation [193] in which the neutron fluid does not penetrate inside the volume occupied by the cluster, the ETF and ETFSI are expressed in the e-representation where the neutron fluid overlaps the nuclear clusters. These two representations of the density distribution of the particles in the system are however approximate ways to describe the real quantum nature of the system based on wave functions [193]. We therefore relate the neutron numbers in the two representations as: $N^{\rm cl}_{e-{\rm rep}} = N^{\rm cl}_{r-{\rm rep}} - n_{ng}V_{\rm cl}$. The cluster neutron numbers in the r- and e- representations are shown in the middle and right panels of Fig. 4.10. The blue

Table 4.6: Neutron drip density, crust-core transition density and central density of the maximum causal mass. For some Skyrme models, F0, LNS5 and SLY5, the maximum mass is obtained without breaking causality.

Model	$n_{\rm drip}$ ($\times10^{-4}$ fm^{-3})	$n_{\rm cc}$ ($\times10^{-2}$ fm^{-3})	$n_{\rm causal}$ (fm^{-3})
H1$_{\rm MM}$	2.60	9.60	0.68
H2$_{\rm MM}$	2.94	8.67	0.65
H3$_{\rm MM}$	2.44	8.45	0.65
H4$_{\rm MM}$	2.52	9.06	0.65
H5$_{\rm MM}$	2.85	8.70	0.64
H7$_{\rm MM}$	3.22	8.31	0.57
DHS$^{L59}_{\rm MM}$	2.60	7.21	0.62
DHS$^{L69}_{\rm MM}$	2.37	7.32	0.64
BSK14$_{\rm MM}$	2.52	7.62	1.21
BSK16$_{\rm MM}$	2.52	8.46	1.20
F0$_{\rm MM}$	2.52	8.33	-
LNS5$_{\rm MM}$	2.60	7.04	-
RATP$_{\rm MM}$	2.52	8.60	1.34
SGII$_{\rm MM}$	2.60	6.53	1.35
SLY5$_{\rm MM}$	2.44	7.63	-

band contains CLDM predictions where the parameter $p_{\rm surf}$ is varied, and the different dashed lines show the impact of the FS description, see Ref. [208], ordered within the leptodermous expansion. The dotted dark purple line shows the ETF results. It is interesting to remark that by fixing $p_{\rm surf} \approx 3.1$ there is a very good overlap between the CLDM and the ETF predictions for $Z_{\rm cl}$. The same feature exists for $N_{\rm cl}$, but for $p_{\rm surf} \approx 3.3$. This small discrepancy may originate from the neutron skin, which is not included in the CLDM. The impact of the neutron skin is however small compared to the FS terms of higher rank in the leptodermous expansion. The shell effects shown in Fig. 4.10 can be seen as the difference between ETF and ETFSI predictions for $Z_{\rm cl}$ and $N_{\rm cl}$. The proton shell effects stabilises $Z_{\rm cl}$ to proton shell or sub-shell closure in almost all the inner crust ($Z_{\rm cl} = 40$ for BSk24). It is only in the densest region of the inner crust, the so-called pasta phase, that $Z_{\rm cl}$ departs from 40. Since shell or sub-shell closure occurs at fixed proton numbers, expected to be 20, 28, 40, 50 and 82 from nuclear

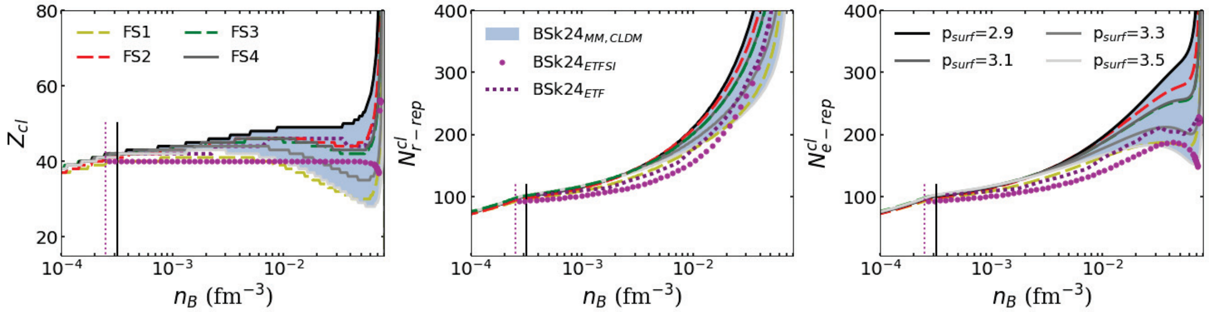

Figure 4.10: Crust composition $Z_{\rm cl}$, $N_{\rm cl}$ as function of the baryon density. The number of neutrons is calculated in the r-representation ($N_{\rm cl}^{r-\rm rep}$ middle panel) and in the e-representation ($N_{\rm cl}^{e-\rm rep}$ right panel). We explore the impact of the leptodermous expansion by showing the results for FS1-FS4 in the CLDM, the impact of $p_{\rm surf}$ by varying $p_{\rm surf}$ from 2.9 to 3.5 in the CLDM, and finally, we compare CLDM with EFT and EFTSI predictions. The blue band correspond to the CLDM uncertainty in the parameter $p_{\rm surf}$.

phenomenology, the impact of the shell effect could be larger on $Z_{\rm cl}$ and $N_{\rm cl}$ than the effect of FS terms or of the neutron skin. For BSk24, since CLDM and ETF predict values for $Z_{\rm cl}$ slightly above 40 (of the order of 42-44), the stabilization from the proton shell effects in ETFSI decreases $Z_{\rm cl}$ down to 40. As a consequence, $N_{\rm cl}$ is also reduced to approximately conserve the isospin asymmetry.

4.6 Global NS properties

The mass-radius relations for all the considered models are given in Fig. 4.11. Most of the Skyrme models considered here are softer than the χEFT ones and explore densities up to about $9n_{\rm sat}$ in the densest case. The central density is 5-6$n_{\rm sat}$ for χEFT models, which are stiffer. The M-R relations require extrapolations out of χEFT density domain which terminates at $\approx 2n_{\rm sat}$. We remind that we have fixed the values of the parameters Q and Z in such a way that these models reach $2M_\odot$. Some of the Skyrme models are so soft that they even miss to reproduce the observed lower limit of M$_{\rm TOV}$, e.g. F0, SGII, BSK14, BSK16 and RATP. These models predict however M$_{\rm TOV}$ ≥ 1.7 M$_\odot$, allowing them to predict the properties of canonical mass NS. We decided to keep these EoS in our analyses since the density at which these models fail are above the expected break-down of the nucleonic models, about 3-4$n_{\rm sat}$. The crosses on the figure show the central density in units of $n_{\rm sat}$, note that the central density at the maximum (causal) mass for the Skyrme models is of the order 7-8$n_{\rm sat}$. In the present tables, we limit ourself to pure nucleonic models, but it is possible to add a phase transition on top of these models. We have however not explored high-density phase transition yet, since we have concentrated our study in the properties of the crust. The Skyrme models explored here are all quite soft at high density. It is then interesting to study the consequence of such a soft EoS on the astrophysical predictions.

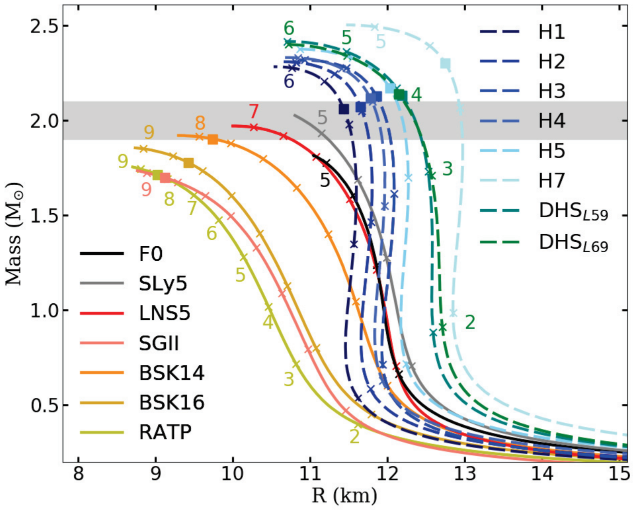

Figure 4.11: Neutron star M-R diagram, for the eight χEFT Hamiltonians and seven the Skyrme models. The squares indicate the density at which causality is violated. The light crosses mark the central density in units of n_{sat}: the numbers given in the diagram indicate the value of the central density in units of n_{sat}.

4.7 Conclusion

In this chapter, as a first estimate, we used the spinodal-instability criteria to calculate the influence of non-quadratic contributions to the symmetry energy on the crust-core transition point. We showed that the effects were of the order of a few percent. Furthermore, we showed that the spinodal instability criteria gives a crust-core transition point that is consistent with more sophisticated treatments of the crust developed in the subsequent parts of this chapter.

The bulk of this chapter was then devoted to the development of a unified description of the EoS of NSs, such that infinite nuclear matter present in the core and finite nuclear clusters present in the crust are treated consistently. We have employed the CLDM to model the finite size terms describing the nuclear clusters which allowed us to perform a detailed analysis of the crust. We used fifteen models for the nuclear interaction, including seven Skyrme and eight χEFT Hamiltonians. Our approach is adequate for the understanding of the origin of the model dependence in the prediction for the NS crust properties. The crust properties were analyzed in terms of bulk and FS contributions, where the bulk term explore the uncertainties in the uniform matter prediction, e.g. the low-density NM, and the FS terms are chosen to best reproduce experimental nuclear masses. The two main sources of uncertainties for the NS crust properties are then well identified. These two important factors which govern, at first order, our predictions are: i) the ability of the models to reproduce the nuclear experimental masses over the nuclear table, and ii) the low-density energy per particle in NM. For the models which satisfy i), the low-density energy per particle in NM is equivalent to the low-density properties of the symmetry energy. We have then observed that some quantities are more sensitive to the factor i), e.g. cluster composition A_{cl} and Z_{cl}, while others are more impacted by the factor ii), e.g. energy per particle, pressure, sound speed, volume fraction, electron fraction Y_e, neutron chemical potential, mentioning only the observables that we have analyzed.

For all the fifteen unified EoS presented here, we have generated tables in the CompOSE format. While a few of these models do not reach the lowest value of $\mathrm{M_{TOV}}$ set by radio-observations, we believe that the central densities explored for these soft EoS are so large that the table we provide here could be used to explicitly introduce a phase transition construction. Many nucleonic models presented here reach however the observed lowest value for $\mathrm{M_{TOV}}$.

Contributions left out of the CLDM such as the neutron skin and shell effects were studied by comparing the CLDM with the ETF and ETFSI approaches. We concluded that these effects, in particular the proton shell contribution could have an important impact on the composition of the nuclear clusters. Therefore extensions of the CLDM incorporating these effects would be beneficial. Investigations along these lines are in progress.

Part II

Relativistic Descriptions of Nuclear Matter

Chapter 5

A relativistic chiral model of nuclear matter with nucleon structure constraints

As stated in the chapter 1, the purpose of this thesis is to contribute to our understanding of dense nuclear matter. In part I, we employed Chiral Effective Field Theory in a non-relativistic framework to tackle this problem. This effective approach is well suited to address low-energy systems but as the energy, or equivalently the density, increases it faces a natural break-down, indicating that relativistic effects might have to be taken into account. In cold neutron matter, the break-down is expected to occur between $n_{\rm sat}$ and $2n_{\rm sat}$, see for instance Ref. [171] and references therein. Therefore, exploration of matter at densities beyond this breakdown scale requires extrapolations such as the one proposed in Ref. [215]. In part II, we adopt a different viewpoint and investigate relativistic modeling of nuclear matter. We focus on a relativistic framework because recent radio observations [58, 60, 56, 59] as well as X-ray observations from NICER [50, 52] of NSs with masses around two solar masses have indicated that the sound speed in the cores of NSs is expected to be larger than 10% of the velocity of light [171, 216]. Therefore the study of the densest phases in the cores of NSs requires the development of a relativistic description of nuclear matter.

Furthermore, for densities well above the saturation density, the question of possible phase transitions and the relevant degrees of freedom are important. We will discuss phase transitions in great detail in part III. Here, in part II, we restrict ourself to matter made of nucleons only. Usually nucleons are considered to be point-like degrees of freedom that exist in nuclei where energies up to some tens of MeV per nucleon are involved [217]. However, with the advent of QCD, it has been established that nucleons are not fundamental, but they are instead composed of colored quarks which interact through the exchange of colored gluons at a resolution scale of a few hundred MeV per nucleon [12]. Bridging the fundamental theory of QCD with the natural nucleonic degrees of freedom has thus became an important question in the recent developments of nuclear physics. Our exploration of relativistic nuclear matter thus emphasizes this connection. In order to do so, in this chapter, we will perform our investigation along the lines originally proposed in Refs. [218, 219] where spontaneous chiral symmetry breaking and confinement effects (i.e. QCD features at the quark level) are incorporated in the modeling of nuclear matter. In the next chapter 6, this model is compared to other effective approaches such as the Walecka-type model [220, 221] and the ones inspired from Refs. [222, 223, 224, 225].

The rest of this chapter is organized as follows. In Sec. 5.1 we present a review of relativistic theories with an emphasis on QCD aspects such as chiral symmetry and confinement. This will allow us to establish a historical background for this work. In Sec. 5.2, these notions are captured using the model developed in Refs. [218, 219]. In this section, we also present the ground state energy of nuclear matter derived from the relativistic Lagrangian in the Hartree approximation, thereby establishing our computational setup. The predictions of this model for the EoS are discussed in Sec. 5.3. We end this chapter with a brief summary in Sec. 5.4

5.1 Our understanding of the nuclear force

In order to understand the significance of the work presented in this part of the thesis, a brief reminder of the development of our understanding of low-energy nuclear interactions is necessary. In 1935, the Yukawa meson-exchange model [226] was the first theory for the nuclear force, where pions mediate the NN (nn, np, and pp) interaction. This meson-exchange approach, while now known as not being the fundamental theory, has however shaped the global understanding of nuclear physics in terms of nucleons and mesons, producing the first good qualitative results, by fixing the coupling constant and associating a particle exchange to the strong interaction. This first quantum field model for the strong interaction was however not successful enough to accurately reproduce the properties of atomic nuclei, e.g. the ground-state energy, because of its simplicity compared to more evolved and recent models (e.g. one-boson-exchange potentials or OBEP discussed hereafter) and of the unknown pion dynamics, which we now know is constrained by the chiral symmetry. In the early 1960's, the discovery of heavy mesons helped in the modeling of better one-boson-exchange potentials (OBEP) containing the exchange of well identified vector mesons namely the omega (ω) and rho (ρ) mesons. There were however still some problems, e.g., the scalar sigma boson-exchange (now named $f_0(600)$) for which the experimental evidence was polemic as well as its link to the broad 2π scalar resonance. Nevertheless, high-precision potentials based on the meson-exchange picture and including a scalar meson were constructed and successful, see for instance Ref. [227].

The first attempt to go beyond a non relativistic treatment of nuclear matter was the relativistic mean field (RMF) approach initiated by Walecka and collaborators [220, 221], which is based on meson exchange between nucleons whose wave functions are solution of the in-medium Dirac equation. In this framework nucleons move in an attractive (scalar field) and in a repulsive (vector field) backgrounds. This provides both the Walecka saturation mechanism and the correct magnitude of the spin-orbit potential. The parameters describing the meson-nucleon couplings are adjusted to the saturation properties of nuclear matter and/or nuclear ground state properties through the nuclear chart (binding energies, charge radii, etc). Hence there is no explicit or direct connection with the underlying QCD theory but instead this approach describes the nuclear properties in terms of a meson exchange potential renormalized around nuclear saturation density. The link with the bare nucleon-nucleon interaction could nevertheless be performed through the Dirac-Brueckner-Hartree-Fock (DBHF) approach [228, 229] which produces a mean-field potential which can guide the parametrization of the in-medium RMF theory with density-dependent coupling constants [230, 231]. Some recent RMF models accurately reproducing the properties of nuclei have included this link to DBHF in-medium modified potentials [232, 233]. However, the question of the very nature of these background mesonic fields has still to be elucidated or, said differently, it is highly desirable to clarify their relationship with the low-energy realization of chiral symmetry.

5.1.1 Chiral symmetry and color confinement

Chiral symmetry together with color confinement are the most prominent low-energy features of the gauge theory of colored quarks and gluons (QCD) established in the 1970's. In the low energy/large distance domain only light u and d quarks with masses of a few MeV are relevant. In this domain the QCD Lagrangian has essentially no dimensional parameter (when neglecting the quark masses). This scale invariance is however broken by quantum fluctuations [12], leading to the formation of the characteristic QCD scale $\Lambda_{\rm QCD}$. Much below $\Lambda_{\rm QCD} \approx 200$ MeV, the coupling constant of the theory becomes very large, a feature that occurs together with color confinement, and consequently renders QCD a non-perturbative theory in the energy range of nuclear physics, often referred to as low-energy. Lattice-QCD is one tool to tackle this problem by bridging the gap between unobserved quarks and gluons degrees of freedom and baryonic or mesonic degrees of freedom [234], however this method is presently feasible only at zero baryon density.

The concept of chiral symmetry was already briefly discussed in Sec. 2.3.1. However, for the sake of completeness, we shall recall some of the key notions again and discuss them in more detail. The $\mathrm{SU(N_f = 2)}$ chiral symmetry of QCD originating from the light quark masses means that in the limit of zero mass (called the chiral limit) non-interacting quarks with opposite parity are indistinguishable and do not couple to each other. For the description of hyper-nuclei, this concept of chiral symmetry can be extended to the s quark within $\mathrm{SU(N_f = 3)}$. In the present study, we however limit ourself to the $\mathrm{SU(2)}$ case. At low-energy, i.e. below a few $\Lambda_{\rm QCD}$, chiral symmetry is spontaneously broken due to the condensation of quark-antiquark pairs, mixing left handed and right handed quarks in the QCD vacuum: QCD prefers quark-antiquark pairs with negative parity to the quark-quark pairs with positive parity [103]. The chiral fields associated with the fluctuations of the resulting quark condensate $\langle \bar{q}q \rangle$ are usually parametrized in a $\mathrm{SU(2)}$ matrix M as:

$$M \;=\; \sigma + i\vec{\tau}\cdot\vec{\phi} \equiv S\,U \tag{5.1}$$

where $\vec{\tau}$ are the $\mathrm{SU(2)}$ isospin Pauli matrices, $S = s + f_\pi$ and $U = e^{i\,\vec{\tau}\cdot\vec{\pi}/f_\pi}$. The scalar field σ (S) and pseudoscalar fields $\vec{\phi}$ ($\vec{\pi}$) written in cartesian (polar) coordinates appear as the dynamical degrees of freedom. In particular the sigma field is not vanishing in vacuum since $\langle\sigma\rangle_{vac} = \langle S\rangle_{vac} = f_\pi \propto \sqrt{\langle\bar{q}q\rangle}_{vac}$, where the last relation is due to the Gellmann-Oakes-Renner relation [234], given hereafter. Note that, at finite density, the values taken by these dynamical degrees of freedom may deviate from their vacuum expectations.

In the chiral limit the potential energy, also called the chiral potential, exhibits a typical mexican hat shape in terms of the scalar and pseudoscalar fields. The bottom is a circle with radius f_π (the chiral circle defined from $\sigma^2 + \vec{\phi}^2 = f_\pi^2$) in a four dimensional space (an analogy can be made with the O(4) ferromagnet below the Curie temperature). The low-energy constant f_π is identified with the pion decay constant. As a result, one moves without cost of energy along the chiral circle and the pseudoscalar modes are massless in the chiral limit. These modes, called *Goldstone bosons*, are realized in terms of a few pseudoscalar mesons, e.g. the pions for $\mathrm{SU(2)}$ or the kaons for the $\mathrm{SU(3)}$ extension.

In addition to the spontaneous chiral symmetry breaking, one expects a small but explicit symmetry breaking. For small masses indeed, as it is the case in the physical world, chiral symmetry is explicitly broken and u and d quarks interact weakly. In reality the Goldstone bosons are quasi-Goldstone bosons with small masses. This explains why the quasi-Goldstone boson, identified as the pion, has a small mass $\simeq 140$ MeV compared to the other mesons. The Gellmann-Oakes-Renner relation, $f_\pi^2 m_\pi^2 = -2m_q \left<\bar{q}q\right>_{vac}$, relates the pion mass m_π to m_q, the small but finite mass of the light u and d quarks.

A simple realisation of the chiral symmetry breaking mechanism can be studied in the Nambu-Jona-Lasinio (NJL) model, see original Refs. [235, 236] and Ref. [237] for a review. In its simpler version, the complex QCD interaction is replaced by a contact 4-quark chirally invariant interaction, where the gluon degrees of freedom as frozen. In addition, quarks acquire a dynamical mass due to the spontaneous breaking of the chiral symmetry. This mass is called the constituent quark mass since it is approximately one third of the nucleon mass ($\simeq 330$ MeV). There is another mass, the scalar mass associated to the radial meson mode S, which is related to the curvature of the chiral potential. Since this mass is associated to two constituent quarks, it typically scales as twice the constituent quark mass in the NJL model. For this reason, in the following, we will take for the mass of the sigma typical values about 600 to 800 MeV.

These chiral properties can also be implemented in chiral perturbation theory. In the chiral Effective Field Theory (EFT) initiated by Weinberg [104], the radial mode S is frozen to its vacuum expectation value, f_π, and only low-energy displacements along the chiral circle are allowed. In this approach, the most general Lagrangian is expressed in terms of the matrix U, e.g., pionic degrees of freedom, dictated by symmetries, e.g. chiral symmetry. Recall that it was this framework that was used as our computational setup in part I.

Finally, let us remark that as the density of the medium increases, chiral symmetry is expected to be progressively restored. This is a general expectation: as the energy scale increases – in that case due to the increasing density – the symmetry of the QCD Lagrangian is recovered. It is typically demonstrated for an effective model of QCD such as the NJL model, see Ref. [237] for a review.

5.1.2 The *nuclear physics* sigma meson

To bridge the gap between relativistic theories of the Walecka type and approaches based on chiral symmetry, one has to map the *nuclear physics* sigma meson of the Walecka model at the origin of the nuclear binding (let us call it σ_W from now on) with a chiral quantity. For instance, one may be tempted to identify σ_W with σ, the chiral partner of the pion. It is however forbidden by chiral constraints. This point has been first addressed by Birse [238]: it would lead to the presence of terms of order m_π in the NN interaction which is not allowed.

It was instead proposed and justified to identify σ_W with the chiral invariant s $(= S - f_\pi)$ field associated with the radial fluctuation of the chiral condensate S about the "chiral radius" f_π: formally it imposes $\sigma_W \equiv s$ [218]. Equivalently the chiral invariant sigma field and the pion field appearing in the chiral field operator $M = S\,U \equiv (s + f_\pi)\,U \equiv (\sigma_W + f_\pi)\,U$ are promoted to the rank of effective degrees of freedom. This was originally formulated in the framework of the linear sigma model [218] but an explicit construction using a bosonization technique of the chiral effective potential can be done within the NJL model [239], where the linear sigma model potential is recovered through a second order expansion in $S^2 - f_\pi^2$ of the constituent quark Dirac sea energy. This proposal, which gives a plausible answer to the long standing problem of the chiral status of Walecka theories, has also the merit of respecting all the desired chiral constraints. In particuler the correspondance $s \equiv \sigma_W$ generates a coupling of the scalar field to the derivatives of the pion field. Hence the radial mode decouples from low-energy pions (as the pion is a quasi-Goldstone boson) whose dynamics is governed by chiral perturbation theory. A detailed discussion of this sometimes subtle topic is given in [218, 240]. From now on, we thus believe that the correct connection to the physical world is to identify $\sigma_W \equiv s$.

The very origin of this *nuclear physics* sigma meson is nevertheless still a controversial subject since there is no sharp scalar resonance observed in the expected mass range ≈ 600 MeV. Let us discuss this controversy in some detail, by repeating arguments already presented in Ref. [239]. As soon as we start from a model which gives a correct description of chiral symmetry breaking in the QCD vacuum such as the NJL model, the emergence of a scalar field linked to the quark condensate is predicted. This emergence is by construction a low momentum concept which does not imply the existence of a sharp scalar meson if the effect of confinement is taken into account. Indeed it has been demonstrated by Celenza et al [241, 242] that the inclusion of a confining interaction on top of the NJL model pushes the $q\bar{q}$ scalar state, located originally at twice the constituent quark mass, well above one GeV. The broad resonance, usually refereed as the $f_0(600)$, observed at around 600 MeV, is a $\pi\pi$ resonance which has no direct relation with the background scalar field introduced above. Coming back to this nuclear physics σ_W, its associated "scalar mass", which is around twice the constituent quark mass, is a low momentum parameter related to the inverse of the vacuum scalar susceptibility. As reminded in the previous sub-section, it is typically of the order of 600 to 800 MeV.

5.1.3 Nucleon response at finite density

There is a well identified problem concerning the nuclear saturation with usual chiral effective theories [243, 244, 245, 246]: Independently of the particular chiral model, the solution at finite density is moved away from the vacuum solution, located at the minimum of the chiral potential, into a region of smaller curvature. This single effect (equivalent to the lowering of the sigma mass) destabilizes the ground state solution, creating problems for the applicability of such effective theories in the nuclear context. The effect can be associated with a s^3 tadpole diagram generating an attractive three-body force and destroying saturation, even if an effective repulsive three-body force is present in the Walecka mechanism, because it is not strong enough.

In certain relativistic chiral approaches, this problem is cured by introducing a nucleon response to the scalar field, κ_{NS}, which is the central ingredient of the quark-meson coupling model (QMC), introduced in the seminal work of P. Guichon [247] and successfully applied to finite nuclei with an explicit connection to the Skyrme force [248]. The QMC model has since been applied to compute the EoS of NSs [249] and it has also been quite successful in reproducing the major features of the EMC [1] effect [250] which was one of the first methods to probe the internal structure of the nucleon, see Ref. [251] for a review of some of the recent developments regarding the QMC model. The physical motivation to introduce this nucleonic response is the observation that nucleons experience huge fields at finite density, e.g. the scalar field is of the order of a few hundred of MeV at saturation density. Nucleons, being in reality composite objects, will react against the nuclear environment (i.e., the background nuclear scalar fields) through a (self-consistent) modification of the quarks wave functions. This effect may generate a three body force which brings the desired repulsion if confinement dominates spontaneous chiral symmetry breaking, as discussed in Ref. [239] within particular models. In practice this

---

[1] The name originates from the European Muon Collaboration.

effect generates a non linear coupling of the nucleon to the scalar field, inducing a decrease of the effective scalar coupling constant with increasing density. This is the key ingredient of the saturation mechanism. The attractive chiral s^3 tadpole diagram responsible for the instability of the ground state at finite density is counterbalanced by the nucleon response. An estimate of the nucleon response parameter κ_{NS} can be extracted from lattice-QCD, providing an explicit connection between nuclear saturation mechanism and QCD itself. One may also notice that a similar mechanism occurs if confinement is simulated by an infrared cut-off in the NJL model as discussed in Ref. [245].

Note that the nucleon response largely contributes as well to the curvature coefficient at saturation – the incompressibility modulus K_{sat}. In a set of successive works [219, 252, 253, 254, 239, 255] this approach has been applied to the equation of state of nuclear matter and neutron stars as well as to the study of chiral properties of nuclear matter at different levels of approximation in the treatment of the many-body problem (RMF, Relativistic Hartree Fock or RHF, pion loop correlation energy). Note also that, the quark substructure plays also a crucial role for the spin-orbit potential as discussed in a recent paper [256].

In practice the introduction of the nucleon response is done by parametrizing the scalar field s dependence of the nucleon mass with the exception of Ref. [239] where explicit confinement models have been used to generate it. The parameter κ_{NS} can advantageously be replaced by the dimensionless parameter $C = f_\pi^2 \kappa_{NS}/2M_N \simeq 1.25$ as we will discuss later.

5.2 Computational Setup

We will now present our computational setup that will serve as the basis for the calculations presented in this chapter as well as in the next chapter 6. We begin by noting that, in relativistic approaches to nuclear matter, the Lagrangian can generically be written as the sum of a kinetic fermionic term,

$$\mathcal{L}_\psi = \bar{\psi} \left(i\gamma^\mu - M_N \right) \partial_\mu \psi \,,$$

where the field ψ represents the nucleon spinor, and the meson-nucleon interaction terms,

$$\mathcal{L}_m = \mathcal{L}_s + \mathcal{L}_\omega + \mathcal{L}_\rho + \mathcal{L}_\delta + \mathcal{L}_\pi \,, \tag{5.2}$$

where $\mathcal{L}_m$ collects all mesonic contributions considered in a given model. Using notation of Ref. [253] these can be enumerated as,

$$
\begin{aligned}
\mathcal{L}_s &= \big(M_N - M_N(s)\big)\bar{\psi}\psi - V(s) + \frac{1}{2}\partial^\mu s \partial_\mu s\,, \\
\mathcal{L}_\omega &= -g_\omega \omega_\mu \bar{\psi}\gamma^\mu \psi + \frac{1}{2}m_\omega^2 \omega^\mu \omega_\mu - \frac{1}{4}F^{\mu\nu}F_{\mu\nu}\,, \\
\mathcal{L}_\rho &= -g_\rho \rho_{a\mu}\bar{\psi}\gamma^\mu \tau_a \psi + g_\rho \frac{\kappa_\rho}{2M_N}\partial_\nu \rho_{a\mu}\bar{\psi}\sigma^{\mu\nu}\tau_a\psi \\
&\quad + \frac{1}{2}m_\rho^2 \rho_{a\mu}\rho_a^\mu - \frac{1}{4}G_a^{\mu\nu}G_{a\mu\nu}\,, \\
\mathcal{L}_\delta &= -g_\delta \delta_a \bar{\psi}\tau_a\psi - \frac{1}{2}m_\delta \delta_a \delta_a + \frac{1}{2}\partial^\mu \delta_a \partial_\mu \delta_a\,, \\
\mathcal{L}_\pi &= \frac{g_A}{2f_\pi}\partial_\mu \varphi_{\pi a}\bar{\psi}\gamma^\mu\gamma^5\tau_a\psi - \frac{1}{2}m_\pi^2 \varphi_{\pi a}\varphi_{\pi a} \\
&\quad + \frac{1}{2}\partial^\mu \varphi_{\pi a}\partial_\mu \varphi_{\pi a}\,,
\end{aligned}
\tag{5.3}
$$

where the symbols have their usual meaning. In Eq. (5.3), two quantities are of particular interest to us, the scalar potential $V(s)$ and the s-field dependent nucleon mass $M_N(s)$. Indeed, these are the two quantities that allow us to incorporate the notions of chiral symmetry breaking and nucleon polarization that were discussed in Sec. 5.1.

Chiral symmetry is enunciated via the chiral effective potential, which is a Mexican hat potential for the scalar field,

$$
V(s) = \frac{m_\sigma^2 - m_\pi^2}{8f_\pi^2}\left(\sigma^2 + \phi^2 - v^2\right)^2 - f_\pi m_\pi^2 \sigma\,,
\tag{5.4}
$$

with

$$
v^2 = f_\pi^2 \frac{m_\sigma^2 - 3m_\pi^2}{m_\sigma^2 - m_\pi^2}\,.
\tag{5.5}
$$

The chiral effective potential (5.4) corresponds to the original linear sigma model using the "cartesian" coordinates, namely the "chiral partners" σ and ϕ.

Employing the polar coordinates and keeping only the leading order mass term for the pion, the chiral potential can also be expressed as

$$
\begin{aligned}
V(s) &= \frac{m_\pi^2}{2}\left(S^2 - f_\pi^2\right) + \frac{m_\sigma^2 - m_\pi^2}{8f_\pi^2}\left(S^2 - f_\pi^2\right)^2 \\
&\quad + \frac{1}{2}m_\pi^2 \pi^2 + \ldots
\end{aligned}
\tag{5.6}
$$

In Eq. (5.6) the higher order terms generate pion-pion interactions which we can neglect as they disappear in the chiral limit.

We finally get the following expression that will be used for this model:

$$
V(s) = \frac{m_\sigma^2}{2}s^2 + \frac{m_\sigma^2 - m_\pi^2}{2f_\pi}\left(s^3 + \frac{s^4}{4f_\pi}\right)\,,
\tag{5.7}
$$

where we only keep the radial fluctuation field s (the field to be identified with the sigma meson

σ_W of Walecka theories) since at the Hartree mean field level, the pion exchange does not contribute. As explained in Sec 5.1, such a potential does not allow for SM to saturate because of the attractive contribution of the s^3 term in Eq. (5.7), i.e., the tadpole diagram mentioned earlier. This problem can be circumvented by introducing the nucleon response to the scalar field at finite density, driven by the susceptibility κ_{NS}, see discussion in Sec. 5.1.3:

$$M_N(s) = M_N + g_s s + \frac{1}{2}\kappa_{NS}\left(s^2 + \frac{s^3}{3f_\pi}\right). \tag{5.8}$$

In Eq. (5.8), the quadratic term leads to a non-zero nucleon susceptibility, and we have added a cubic term as well. The cubic term coupling constant is fixed such that the susceptibility $\kappa_{NS} = d^2M_N(s)/ds^2$ vanishes at full chiral restoration [219]. In the following, it will be convenient to introduce the dimensionless quantity

$$C = \frac{f_\pi^2}{2M_N}\kappa_{NS}. \tag{5.9}$$

In this work we will restrict our attention to only symmetric matter. The energy density at the Hartree level can be computed from the Lagrangian of Eq. (5.3) in the usual way [219]. It is expressed as

$$\begin{aligned}\varepsilon &= \int \frac{4d^3k}{(2\pi)^3}\left(\sqrt{k^2+M_N^2(s)} + g_\omega\,\omega_0\right)\Theta(k_F-k) \\ &\quad + V(s) - \frac{1}{2}m_\omega^2\,\omega_0^2,\end{aligned} \tag{5.10}$$

where the scalar and vector fields are obtained from the equations of motion :

$$m_\omega^2\,\omega_0 = g_\omega\,\rho \tag{5.11}$$

$$V'(s) = -g_S^*\rho_S \qquad \text{with} \qquad g_S^* = \frac{\partial M_N(s)}{\partial s}. \tag{5.12}$$

Note that in Eqs. (5.11) and (5.12), two densities are introduced, the vector density $\rho \equiv \langle\bar\psi\gamma^0\psi\rangle = \langle\psi^\dagger\psi\rangle$ and the scalar density $\rho_S \equiv \langle\bar\psi\psi\rangle$. The former is related to the Fermi momentum through

$$\rho = \int\frac{4d^3k}{(2\pi)^3}\Theta(k_F-k) = \frac{1}{3}\frac{2\,k_F^3}{\pi^2}, \tag{5.13}$$

whereas the scalar density is defined as

$$\rho_S = \int\frac{4d^3k}{(2\pi)^3}\frac{M_N(s)}{\sqrt{k^2+M_N^2(s)}}\Theta(k_F-k). \tag{5.14}$$

5.3 Results for the EoS

Our formalism can now be used to compute the EoS in symmetric matter. First, let us enumerate the free parameters (meson couplings and masses) in the model. Note that Eq. (5.3) contains three isovector coupling constants, g_ρ, g_δ and g_A. Since this chapter is dedicated to symmetric

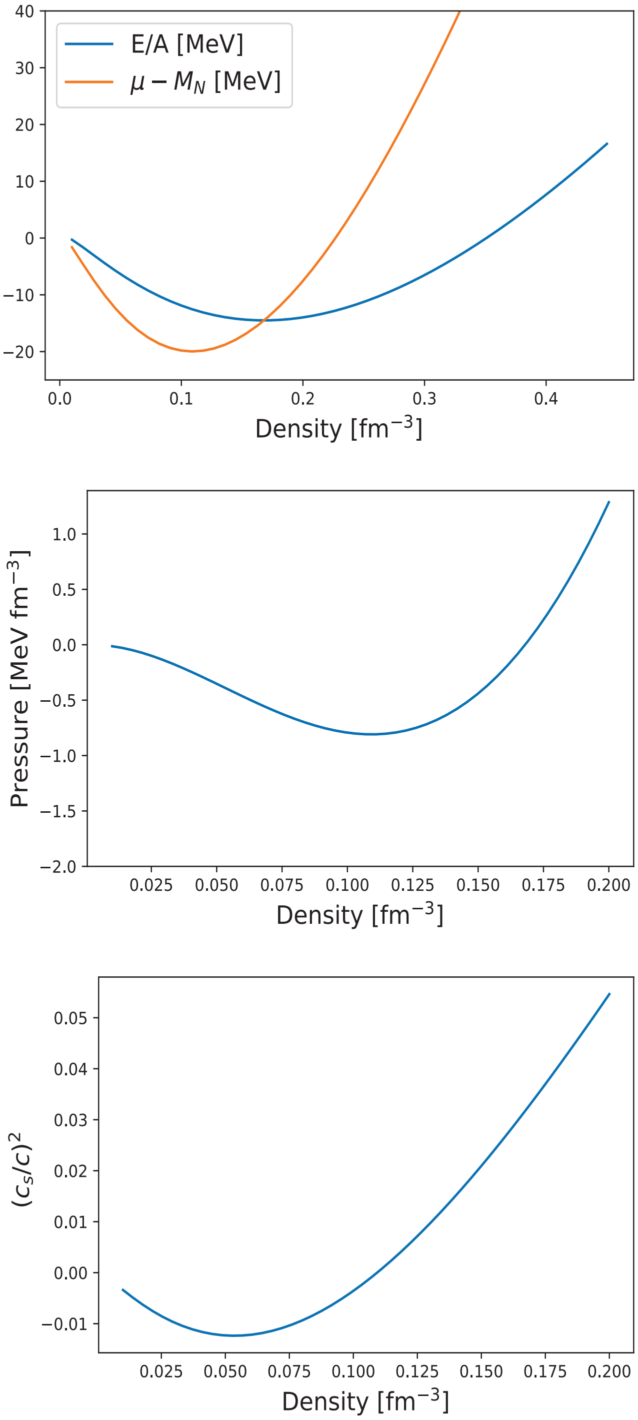

Figure 5.1: In the top panel, we show results for the energy per particle E/A (blue curve) and the chemical potential μ (orange curve) as function of the density. The middle and bottom panels depict the pressure and the sound speed respectively. All results are in symmetric nuclear matter.

matter, these parameters play no role (at the Hartree level) and are included in Eq. (5.3) only for the sake of completeness. Furthermore, the masses of all the mesons, except the σ, are taken from hadron phenomenology. It should however be noted that, in the Hartree approximation, only the ratio of the coupling constant to the mass (for all mesons) determines our results and not the masses themselves. This leaves us with four parameters, g_s, g_ω, m_σ and C. For these parameters, we shall use the values considered in Ref. [219] in order to reproduce the results of this reference. This sets $g_\omega = 6.8$, $m_\sigma = 750$ MeV, $C = 1$ and $g_s = M_N/f_\pi \approx 10$.

In the top panel on Fig. 5.1, we show the energy per particle E/A (blue curve) and the chemical potential μ (orange curve) as function of the density in symmetric matter. The former is obtained from Eq. (5.10) as $E/A = \epsilon/\rho - M_N$. The chemical potential μ can be obtained from the energy density as $\mu = \partial\epsilon/\partial\rho$. Interestingly, we see that at saturation density the chemical potential (without the rest mass contribution) is equal to the binding energy per particle. This is a simple consequence of Euler's identity $\epsilon + p = \mu\rho$, where p is the pressure, since the pressure vanishes at saturation density.

The middle panel of Fig. 5.1 depicts the pressure in symmetric nuclear matter. The pressure p is obtained from the energy per particle as $p = \rho^2 \frac{\partial(E/A)}{\partial\rho}$. As expected, the pressure is negative below saturation density and positive above it. Finally, the bottom panel of Fig. 5.1 shows the speed of sound as function of the number density in symmetric matter. The speed of sound c_s^2 can be obtained as $c_s^2 = c^2\partial p/\partial\epsilon$, where c is the speed of light. We find that the sound speed $c_s^2 \approx 0.025c^2$ at saturation density, as observed in typical energy density functionals. Note that the sound speed crosses 0 at around $0.1\,\mathrm{fm}^{-3}$. In symmetric matter, this crossing coincides with the onset of the spinodal instability, see discussion in Sec. 4.1. We therefore see that the spinodal onset density calcualted in this chapter is consistent with the Chiral EFT results discussed in Sec. 4.1.

5.4 Summary

In this chapter, we discussed the origins of our understanding of the nuclear force and enunciated on the importance of two fundamental aspects of QCD: spontaneous chiral symmetry breaking and confinement. We clarified that it is highly desirable to make a link between the low-energy realizations of these QCD aspects and the natural nucleonic degrees of freedom. In order to do so, we performed a detailed review of the model developed in Refs. [218, 219]. In this model, chiral symmetry is incorporated by taking the scalar potential to be the one given by the linear sigma model. Furthermore, the polarisation of the nucleon is taken into account by parametrizing the scalar field dependence of the nucleon mass. Using this model, we reproduced results for the EoS in symmetric nuclear matter and showed that the model predictions are qualitatively consistent with the empirical properties of symmetric nuclear matter.

In the next chapter, we will systematically confront this model with other relativistic models that differ by the treatment of chiral and confinement properties. Furthermore, we will employ Bayesian statistics to quantify the uncertainties in the model parameters and predictions. This will be an improvement over the calculations presented in this chapter where only fixed values for the model parameters were considered.

Chapter 6

Comparison of the Equation of State from different relativistic models

In the previous chapter, we explored the the properties of a relativistic model of nuclear matter originally proposed in Refs. [218, 219] in which chiral symmetry is incorporated via the linear sigma model and the in-medium polarization of the nucleon is taken into account. In this chapter, we compare this model with two other relativistic theories which differ by the treatment of chiral and confinement properties. As in the previous chapter, for simplicity, we consider the so-called Hartree approximation, also called the classical field case, and the properties of these models are explored in symmetric matter (SM), even though the question of the prediction of the symmetry energy is also addressed at the end of our study. The models are calibrated to reproduce the same properties in SM at saturation density and the uncertainty in the fitted quantities are propagated towards our prediction for nuclear matter properties using Bayesian statistics. The differences between the models are shown, and these differences while small at low density, appear to be significantly larger as the density increases.

The motivation for making such a link with other models is to better understand the role played by chiral symmetry and confinement in nuclear physics. Since the model presented in the previous chapter 5 incorporates both of these features, we shall refer to it as RMF-CC (Relativistic Mean Field with Chiral symmetry and Confinement). On the other hand, several chiral relativistic theories have indeed been formulated but without reference to the nucleon response [243, 257, 222, 223]. We shall refer to this class of models as RMF-C. Recently, such a RMF-C model has been used to study the possible mixed phase at the chiral transition in SM [224] and neutron stars [225]. In this approach the chiral potential deviates from the pure linear sigma model potential by terms of first and third order in $S^2 - f_\pi^2$ (our chiral invariant S field is named χ in the latter paper) with additional parameters. This is a legitimate attitude since any microscopic underlying model, including the above mentioned NJL model, will certainly generate such higher order many-body terms at low-energy.

One interesting question is whether this higher order terms may simulate the effect of the nucleon response. One main motivation of the present work is to make a comparison of the two classes of approaches by expanding the chiral effective potentials in powers of the scalar field s. Since a term in s^n corresponds to a $(n-1)$-body force, one may thus expect that the expansion in the scalar field s is perturbative (i.e. Taylor in nature), at least at low density: the 2-body force is expected to be larger than the 3-body one, itself larger than the 4-body force, and so on. Models violating this ordering will thus be referred as anomalous ones in the following.

Table 6.1: Nuclear Empirical Parameters (NEPs) (E_{sat} and n_{sat}) as given from Ref. [259] and Lattice parameters (a_2 and a_4) extracted from Ref. [260], used in the fits. For the NEPs the mean and standard deviations correspond to a Gaussian distribution, while for the Lattice parameters the standard deviation refers to the width of a uniform distribution.

Parameter	Mean	Standard deviation
E_{sat} (MeV)	-15.8	0.3
n_{sat} (fm^{-3})	0.155	0.005
a_2 (GeV^{-1})	1.533	0.136
a_4 (GeV^{-3})	-0.509	0.054

Anticipating our results, we found that this RMF-C model lead to anomalous chiral potentials.

Finally, in addition to RMF-CC and RMF-C models, we shall also consider the original Walecka model which makes no reference to the underlying properties of QCD. This model will hencefeorth be referred to as RMF. Note that however, the scalar potential $V(s)$ in RMF is possibly non-linear and has been introduced in a pragmatic way to better reproduce the incompressibility modulus and the effective mass. In summary, we have three different classes of models: RMF-CC, RMF-C and RMF. Moving forward, the purpose of the this chapter will be to perform a systematic comparison between these three models.

The organisation of this chapter is very similar to that of Ref. [258] on which this chapter is based. The three models, RMF-CC, RMF-C and RMF, are described in mathematical details in Secs. 6.1, 6.2 and 6.3. Although the RMF-CC model was already discussed in the previous chapter, the main equations are repeated again here for the sake of completeness. In these sections we also discuss the link between the parameters and the fitted data as well as their uncertainties. It is woth repeating that the parameter adjustment is done in such a way that all models are consistent at saturation density and extrapolation to high density is performed with Bayesian statistics. The predictions at high density therefore incorporate uncertainties from the model parameters. In Sec. 6.4 we begin the comparison of the relativistic models. In Sec. 6.4.1 we show that the predictions of the models do not agree at high density by studying the energy per particle and the self-energies. Secs. 6.4.2 and 6.4.3 focus on the interpretation of the scalar potential of the different models. Sec. 6.5 is devoted to a discussion of the Landau parameter F_0. Finally, in Sec. 6.6 we discuss the predictions for the symmetry energy, and describe limitations of the Hartree approximation and possible ways to cure those limitations. Finally we conclude our study by underlying the importance of consistently incorporating QCD ingredients such as confinement and chiral symmetry, since it provides a microscopically motivated and an economical way to incorporate in-medium corrections into dense matter.

6.1 Relativistic Mean Field including Chiral potential and Confinement effects (RMF-CC)

We first discuss the relativistic model that incorporates both chiral symmetry as well as the nucleon substructure, RMF-CC. Since this model was described in detail in the previous chapter,

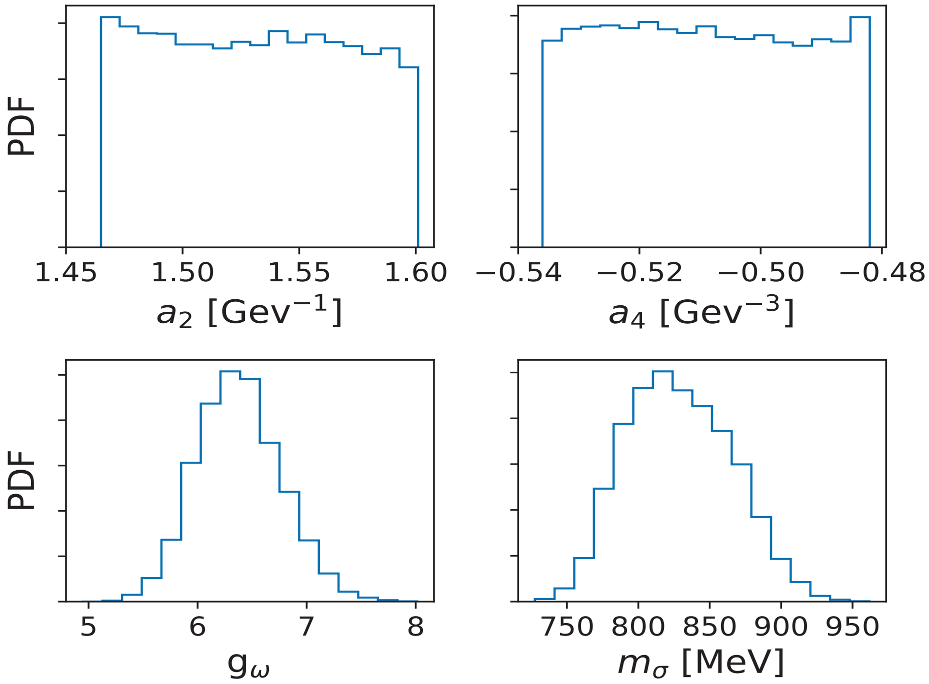

Figure 6.1: Probability Distribution Function (PDF) for the parameters of the RMF-CC model, adjusted to reproduce the NEPs $E_{\rm sat}$ and $n_{\rm sat}$ as well as the Lattice parameters a_2 and a_4, see Table 6.1 for more details.

we only summarize the main features here.

Recall from chapter 5 that the chiral effective potential of the linear sigma model can be expressed as:

$$V(s) = \frac{m_\sigma^2}{2}s^2 + \frac{m_\sigma^2 - m_\pi^2}{2f_\pi}\left(s^3 + \frac{s^4}{4f_\pi}\right) , \tag{6.1}$$

whereas the nucleon response to the scalar field at finite density is driven by the susceptibility κ_{NS}:

$$M_N(s) = M_N + g_s s + \frac{1}{2}\kappa_{NS}\left(s^2 + \frac{s^3}{3f_\pi}\right) . \tag{6.2}$$

Finally, recall that it is convenient to introduce the dimensionless quantity

$$C = \frac{f_\pi^2}{2M_N}\kappa_{NS} . \tag{6.3}$$

As discussed in the previous chapter 5 there are 4 parameters in the model: g_s, g_ω, m_σ and C. However, in this chapter, we improve our framework by making a connection with Lattice QCD by following the approach of Refs. [252, 253]. The structure of the nucleon, in particular its mass can be obtained from L-QCD, see for instance Ref. [261]. In this reference precise calculations were limited to quark masses much larger than the physical one. Therefore, extrapolation of L-QCD results to the physical value of the quark mass is required, but such extrapolations run into diffcutly due to the fact that M_N is a non-analytic function of m_q (or equivalently m_π^2). Such non-analytic behaviour arises due to contributions from pion loops.

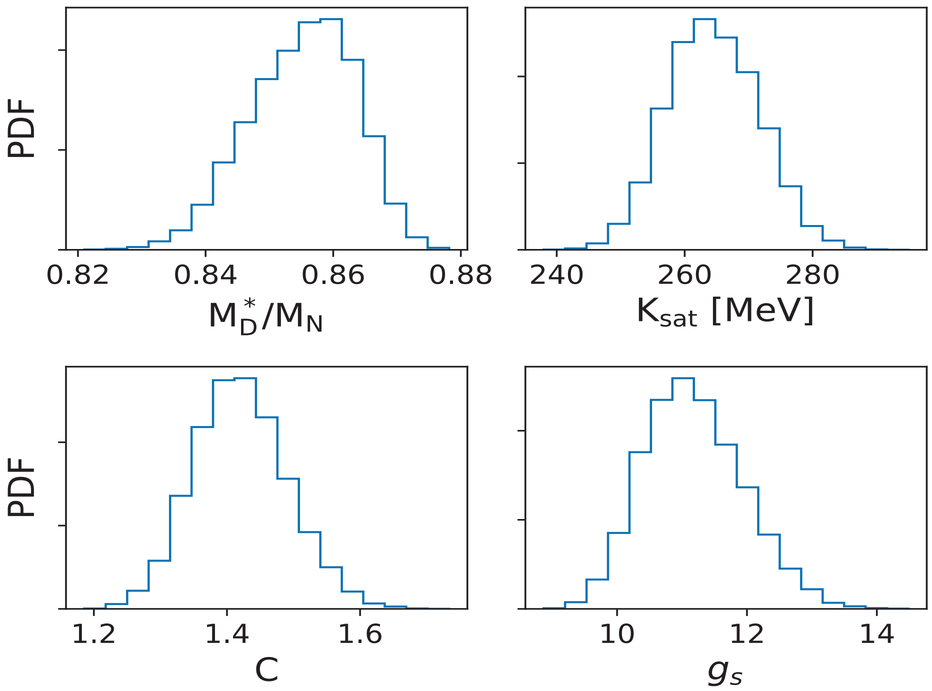

Figure 6.2: Prediction of the Dirac effective mass and the incompressibility modulus obtained from the RMF-CC model. The PDFs of C and g_s are also shown.

Following the strategy of Refs. [260, 262], we express the nucleon mass as

$$M_N(m_\pi^2) = a_0 + a_2 m_\pi^2 + a_4 m_\pi^4 + \cdots + \Sigma_\pi, \tag{6.4}$$

where we have isolated two contributions: one analytic in m_π^2 (the terms before the dots) and another, containing a non-analytic piece, denoted by Σ_π which is identified with the pion self energy contribution to the nucleon mass. Note that in reality Eq. (6.4) is an expansion in the quark mass m_q, but we have replaced the quark mass with the pion mass (squared) using the GOR relation $m_\pi^2 \propto m_q$ [253]. The derivative of Eq. (6.4) with respect to the pion mass gives the so-called sigma commutator σ_N, i.e.

$$\sigma_N \equiv m_\pi^2 \frac{dM_N}{d(m_\pi^2)} = a_2 m_\pi^2 + 2a_4 m_\pi^4 + \cdots + m_\pi^2 \frac{d\Sigma_\pi}{d(m_\pi^2)}. \tag{6.5}$$

The sigma commutator σ_N is an important quantity because on the one hand – on the theory side – it is related to symmetry properties and their explicit breaking and, on the other hand, it can be extracted from experimental results. It can also be calculated via L-QCD [239]. The authors of Refs. [260, 262] showed that it is possible to estimate the non-analytic pion self energy contribution Σ_π and its derivative in an essentially model independent way using chiral perturbation theory, with the pion loops suitably regularized. Then, the parameters a_2 and a_4 are fit to L-QCD results [261] and one obtains a range of values for a_2 and a_4, given in Table 6.1, due to the ambiguity in the regulator of the pion loops, for which four different functional forms are used: sharp-cutoff, monopole, dipole and Gaussian [262].

Furthermore, the parameters a_2 and a_4, which are related to the analytic, non-pionic piece of σ_N, can be used to determine the parameters of the RMF-CC model: g_s, m_σ and C (see Refs. [252, 253]) using the relations

$$a_2 = \frac{g_s f_\pi}{m_\sigma^2}, \tag{6.6}$$

and

$$a_4 = -\frac{f_\pi g_s}{2m_\sigma^4}\left(3 - 2C\frac{M_N}{f_\pi g_s}\right). \tag{6.7}$$

Notice that in the expression of a_4 the factor $M_N/f_\pi g_s$ was absent in [252, 253] since the nucleon mass was fixed to be $M_N = f_\pi g_s$.

Ultimately, in this approach, we have four fit parameters a_2, a_4, m_σ and g_ω. These are fixed by the analysis of the Lattice results and by two saturation properties, n_{sat} and E_{sat} (Table 6.1). Considering the uncertainties in these parameters, one can also predict the Probability Distribution Functions (PDF) for the parameters: $g_\sigma \equiv g_s$ and C from Eqs. (6.6) and (6.7), as well as K_{sat} and the Dirac mass M_D^*. Note that in SM, at the Hartree approximation, the Dirac mass is the same as the s-field dependent nucleon mass, i.e. $M_D^* = M_N(s)$. The uncertainties in the quantities to fit (given in Table 6.1) are explored within a Bayesian method using Markov-Chain Monte-Carlo (MCMC) approach. In this way full exploration of the uncertainties in the Nuclear Empirical Parameters (NEPs) and the Lattice parameters are translated into uncertainty in the model parameters. The PDFs obtained from the MCMC sampling over our fit parameters a_2, a_4, g_ω and m_σ are shown in Fig. 6.1. The distributions over a_2 and a_4 are almost flat (as imposed in the prior), and the confrontation against the NEPs changes very little. The distributions over g_ω and m_σ are much more peaked. The PDFs of g_ω is peaked around 6.5. The PDF of m_σ is peaked around 820 MeV which is consistent with the commonly assumed value of 800 MeV (see discussion in chapter 5).

Based on the parameter distributions shown in Fig. 6.1, we can now analyze the impact of the uncertainties in these parameters on several interesting properties of dense matter, e.g. the Dirac mass at saturation M_D^* and the incompressibility modulus K_{sat}. For completeness, we also show the distribution over the parameters C and g_σ. These results are shown in Fig. 6.2. The Dirac mass is peaked around $\approx 0.85 \pm 0.02 M_N$. The predictions for K_{sat}, with a PDF peaked at ≈ 265 MeV, are slightly larger than the expected empirical value around $230-250$ MeV [259]. We expect however that quantum corrections, e.g. Fock term or pion cloud [254], could change these quantities and shift them towards lower values. The PDF of C is consistent with the value used in Ref. [253] and g_s is consistent with the canonical value of $M_N/f_\pi \approx 9.98$.

6.2 Relativistic Mean Field with Chiral Symmetry only (RMF-C)

We now consider an approach where chiral symmetry is incorporated within a chiral potential $V(s)$, but without the effect of confinement in terms of nucleon polarisation. This so-called RMF-C model is inspired from Refs. [222, 223, 224, 225].

Since the non-trivial scalar response of the nucleon is neglected in this model, the s-field

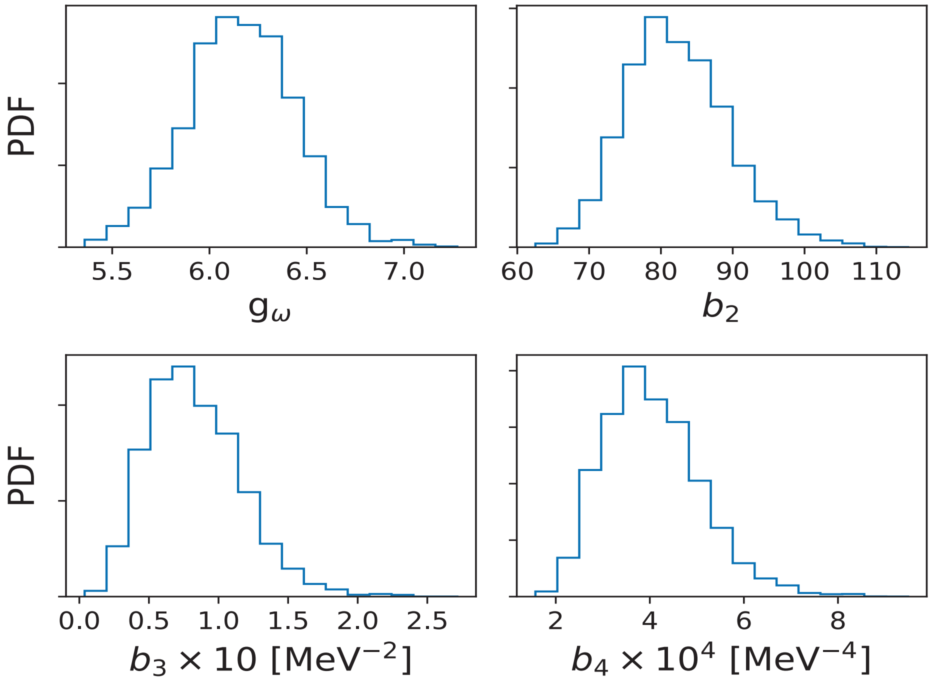

Figure 6.3: Results from the fit of the RMF-C model to the NEPs of Table 6.1 and the RMF-CC model's prediction of M_D^* and $K_{\rm sat}$ shown in Fig. 6.2.

dependent nucleon mass is simply given by

$$M_N(s) = M_N + g_s s\,, \tag{6.8}$$

as in the linear sigma model [263].

As mentioned in Sec. 5.1, the chiral potential is expressed in a very general way as

$$V(s) = \sum_{n=1}^{4} \frac{b_n}{n!} \frac{(S^2 - f_\pi^2)^n}{2^n} - f_\pi m_\pi^2 \sigma. \tag{6.9}$$

Notice that contrary to Eq. (5.6), this chiral potential contains terms of order $n = 3, 4$ in the $S^2 - f_\pi^2$ expansion.

An important specific point is that, as in the linear sigma model, the scalar coupling parameter is fixed, $g_s = M_N/f_\pi$. This leaves us with 4 unknown parameters g_ω, b_2, b_3 and b_4 that we fit in a consistent way compared to RMF-CC. To do so, we consider the two NEPs in Table 6.1, $E_{\rm sat}$ and $n_{\rm sat}$ as in the RMF-CC model and, additionally we use the predictions of the RMF-CC model for the Dirac effective mass and the incompressibility modulus shown in Fig. 6.2.

The result of sampling this distribution in the parameter space spanned by g_ω, b_2, b_3 and b_4 is shown in Fig. 6.3. First let us comment on the marginalized 1-dimensional PDF over g_ω. The distribution is peaked around ≈ 6.25. This is a rather low value given that the value of g_ω found in Ref. [225] is 9.47. This discrepancy is due to the fact that we have fitted g_ω to a Dirac effective mass M_D^* that is $\approx 0.85 M_N$ (see Fig. 6.2), whereas the value of M_D^* used in Ref. [225] is $0.75 M_N$. We have verified that if $M_D^* = 0.75 M_N$ is used in our approach, we are able to

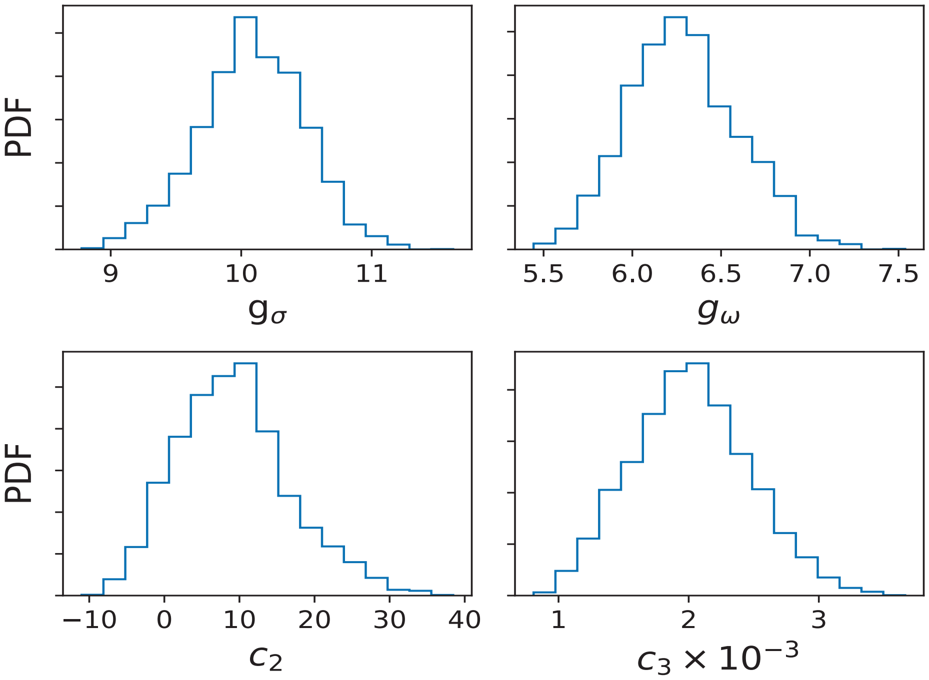

Figure 6.4: Results from the fit of the RMF model to the NEPs of Table 6.1 and the RMF-CC model's prediction of M_D^* and $K_{\rm sat}$ shown in Fig. 6.2.

reproduce the g_ω found in Ref. [225]. Regarding the other parameters b_2, b_3 and b_4, the PDFs are also peaked at values different from the ones found in Ref. [225]. This is due to the fact the NEPs used in this work are different from that used in Ref. [225], most notably $K_{\rm sat}$ but also $E_{\rm sat}$ and $n_{\rm sat}$, therefore a precise agreement of our results should not be expected. Indeed for this work what is important is that the three models are parametrized consistently at saturation density. In this way, the differences in the predictions at high density could only be related to the ingredients of the models.

Finally, let us note that the result of g_ω presented here is consistent with what one obtains in the RMF-CC model, see Fig. 6.1. We also remark that the PDFs are broad and thus the parameters cannot be very well constrained by empirical knowledge of SM saturation. We will comment more on the values of these parameters later when comparing the scalar potentials of different models.

6.3 Relativistic Mean Field Theory (RMF)

We now turn to a model in which both the chiral potential and the response of the nucleon is ignored. As in the original Walecka model, the scalar potential is limited to the mass term:

$$V(\sigma_W) = \frac{1}{2} m_\sigma^2 \sigma_W^2 \,, \tag{6.10}$$

and for the σ_W-field dependent mass one has:

$$M_N(\sigma_W) = M_N + g_\sigma \sigma_W \,, \tag{6.11}$$

where g_σ is the scalar coupling constant.

While the saturation mechanism arises from the equilibrium between the scalar and the vector fields and allows a good reproduction of the saturation density and binding energy – at the cost of large coupling constants – other properties of the model, e.g. the compression modulus, the effective nucleon mass and the symmetry energy, are in poor agreement with the empirical values. Boguta and Bodmer [264] have thus suggested an extension of the original Walecka model, whose main purpose is to bring the compression modulus and nucleon effective mass at saturation under control, by introducing self-interactions of the scalar field by modifying the potential (6.10) as,

$$V(\sigma_W) = \frac{1}{2}m_\sigma^2\sigma_W^2 + \frac{1}{3}c_2 M_N \sigma_W^3 + \frac{1}{4}c_3\sigma_W^4. \tag{6.12}$$

Such self-interacting scalar field potentials have been largely employed in what is commonly referred as the Relativistic Mean-Field (RMF), e.g. NL3 [265]. See also the book by Glendenning [15]. Note that other extensions based on density dependent coupling constant will not be considered in the present study. It is interesting to remark that the Euler-Lagrange equation for the scalar field is modified by the self-interaction terms, but the nucleon effective mass remains described by Eq. (6.11), as in the original Walecka model. This also makes the RMF model qualitatively similar to the RMF-C one, as we will illustrate it in the next section.

We have 4 parameters to fit, g_σ, g_ω, c_2 and c_3. As with the case of the RMF-C model, we use the two NEPs of Table 6.1 and the PDFs of M_D^* and K_{sat} shown in Fig. 6.2. The results of sampling this distribution is shown in Fig. 6.4. We see that the PDF of g_σ is peaked around 10, which is consistent with what is shown in Fig. 6.2 for the RMF-CC model. Note that we fix $m_\sigma = 800\,\mathrm{MeV}$ compatible with the peak predicted by the RMF-CC model. Fixing the value of m_σ in RMF is not constraining if g_σ is varied: only the ratio g_σ/m_σ matters. We remind that in the RMF-CC model however this degeneracy is broken by Eqs. (6.6) and (6.7). Additionally, the fixing of m_σ at a constant value can be seen as analogous to the RMF-C model where the parameter g_s is frozen instead of m_σ. For g_ω we again obtain a value ≈ 6.25 which is again due to the fact that we fit to a large value of $M_D^* \approx 0.85 M_N$. This value of g_ω is very close to those obtained previously for the RMF-CC and RMF-C models. Finally, we note that the PDF of the c_2 parameter has a peak around 10 but with an uncertainty of about 10, making it compatible with 0. The PDF of c_3 prefers very large values. We will comment extensively on our results for c_2 and c_3 later when we compare the scalar potentials of the different models.

Having obtained the values of $g_s(g_\sigma)$ and g_ω for the three models, we can study how the three models can be separated when the correlation between g_ω and g_s is analysed. In Fig. 6.5, this correlation is plotted for the three models in different colors, where the contours represent the 95% confidence level. For the RMF-C model, only a vertical line is shown since g_s is fixed in this case. We see that for the three models, the centroid of g_ω are very close (≈ 6.25). However, the models can be separated along the horizontal coordinate (g_s). The RMF-CC model prefers larger values of g_s, whereas the RMF-C and RMF models prefer the lower value close to M_N/f_π.

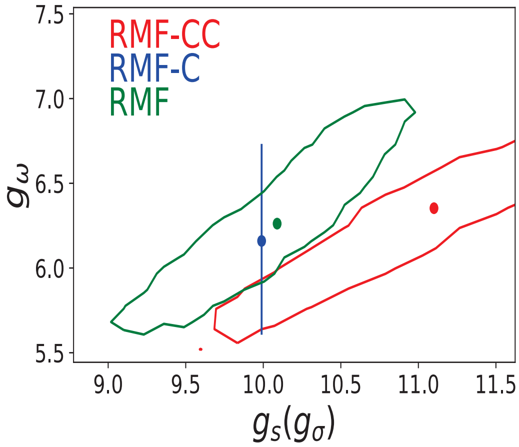

Figure 6.5: The correlation between g_s and g_ω for the three models. The 95 % confidence levels are shown. The dots represent the centroids of the distributions.

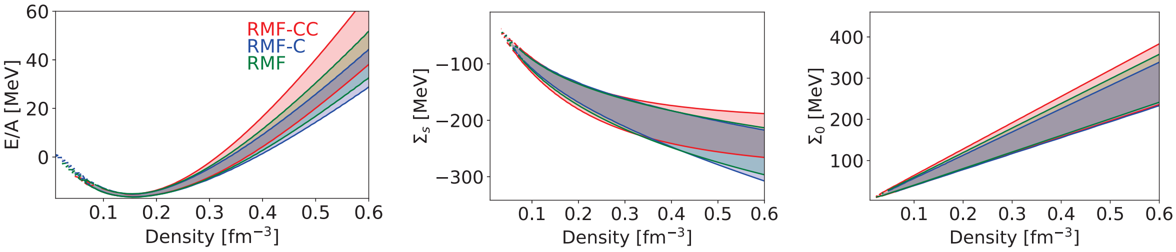

Figure 6.6: (left) The energy per particle in SM for the three models considered in this work. The contours show the 95% confidence level. The density dependence of the scalar self energy (center panel) and the time component of the vector self energy (right panel) are also shown.

6.4 Confrontation of the models

In the previous section, the three models have been fit to reproduce the same properties at saturation in SM. These properties are the saturation density and energy for all models, and the models RMF-C and RMF are adjusted to reproduce the same Dirac mass and incompressibility modulus as RMF-CC, which, for this model are deduced from fundamental L-QCD properties. The models are therefore treated on an equal footing by ensuring that they agree on the empirical parameters and their uncertainties: $n_{\rm sat}$, $E_{\rm sat}$, $K_{\rm sat}$ and $M^*_D(n = n_{\rm sat})$.

In this section we will show that although the predictions of these three models agree at saturation density, they differ quantitatively at larger densities since they represent different density functionals. Moreover, a detailed analysis of the scalar field properties leads us to believe that RMF-CC represents a more justified microscopic approach to in-medium corrections on top of the chiral potential defined in the vacuum.

6.4.1 The energy per particle, the self-energies and the effective masses

We first start with an analysis of the energy per particle in SM. In Fig. 6.6, the results are shown in the left panel. The three models correspond to the three colors. The upper and lower limits

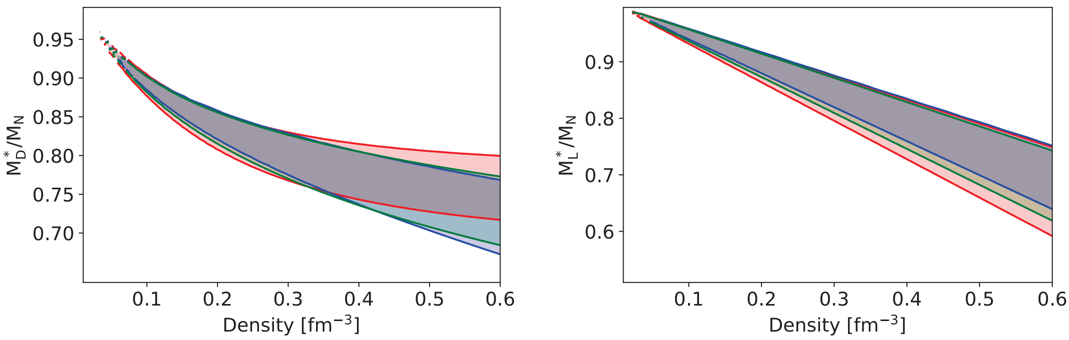

Figure 6.7: The density dependence of the Dirac and Landau masses are shown.

represent the 95% CL, allowing a visualization of the uncertainties in the model predictions as a function of density. Recall that these uncertainties originate from our imperfect knowledge of nuclear matter saturation properties and fundamental predictions of L-QCD. We see that the three models agree well at densities $n \approx n_{\text{sat}}$, since they are constrained to do so. The agreement also appears to be quite good at $n < n_{\text{sat}}$. However, at $n > 2n_{\text{sat}}$, RMF-CC model predicts the larger values for the energy per particle, while RMF-C model produces the smaller ones and RMF model lies in the intermediate range. Note however, that all model predictions are compatible with each other within the considered 95% confidence levels. Given that g_ω is similar for all three models, the reason for differences at high densities is most probably related to the scalar interaction, i.e. the scalar potential and/or the scalar coupling to the nucleons. In the next section, we will investigate the former in detail.

In the center and right panels of Fig. 6.6, the scalar and the vector (time component) self energies, Σ_s and Σ_0 are shown. At the mean-field level in SM, we have

$$\Sigma_s = M_N(s) - M_N \tag{6.13}$$

$$\Sigma_0 = g_\omega^2/m_\omega^2\rho\,. \tag{6.14}$$

We see again that the three models agree at low densities. At larger densities RMF-CC predicts a slightly larger value for Σ_s, however there is still significant overlap among the predictions. For Σ_0, the models still agree at large densities. This is expected since g_ω is the only parameter that controls the density dependence of Σ_0, and all three models have similar values of g_ω. Since correlations beyond the mean field lead to a more complicated density dependence of Σ_0 [266, 267], it would be interesting to re-analyse this quantity by including Fock contributions in the future.

Finally, in Fig. 6.7, the Dirac and Landau masses (M_D^* and M_L^*) are shown. The Landau mass has been computed by deriving the Schrödinger equivalent single-particle potential following Refs. [266, 267]. At the Hartree approximation, it reads

$$M_L^* = M_N - \Sigma_0. \tag{6.15}$$

On the other hand, the Dirac mass is the same as the s-field dependent nucleon mass, i.e. $M_D^* = M_N(s)$. All the comments made regarding Σ_s and Σ_0 are applicable to the Dirac and Landau masses respectively, since the relationship between the self energies and the effective

Table 6.2: Coefficients of the scalar potentials expressed as in Eq. (6.12) for the three models considered here. The quoted uncertainties represent the 95% CL.

Model	c_2	c_3
RMF-CC	$11.3^{+2.2}_{-1.7}$	$37.5^{+7.3}_{-5.6}$
RMF-C	$47.2^{+37.4}_{-23.5}$	5880^{+3870}_{-2470}
RMF	$8.9^{+17.2}_{-12.6}$	2010^{+940}_{-820}
NL3[265]	-29.89	-2.19

masses is quite straightforward in the mean-field level.

In summary, the 3 models presented here, while being calibrated on the same quantities at saturation, lead to slightly different predictions above saturation density: RMF-CC is more repulsive than RMF-C on the average, while RMF lies in between them. In the following, we investigate more closely the properties of the microscopic quantities at the base of the models: the scalar potential and the self-consistent equation for the scalar field.

6.4.2 Analysis of the scalar potential $V(s)$

The scalar potentials $V(s)$ have different expressions in the models considered in our analysis. For an easy comparison, we recast the chiral potential $V(s)$ for RMF-CC and RMF-C into the form of the scalar potential in RMF, see Eq. (6.12). In doing so, the chiral potential (5.7) in RMF-CC leads to the following coupling constants,

$$c_2^{\text{RMF-CC}} = \frac{3}{2f_\pi M_N}(m_\sigma^2 - m_\pi^2) \tag{6.16}$$

$$c_3^{\text{RMF-CC}} = \frac{1}{2f_\pi^2}(m_\sigma^2 - m_\pi^2) = \frac{M_N}{3f_\pi}c_2^{\text{RMF-CC}}, \tag{6.17}$$

and for RMF-C the chiral potential (6.9) gives

$$c_2^{\text{RMF-C}} = \frac{1}{M_N}\left(\frac{3}{2}b_2 f_\pi + \frac{1}{2}b_3 f_\pi^3\right) \tag{6.18}$$

$$c_3^{\text{RMF-C}} = \frac{1}{2}b_2 + b_3 f_\pi^2 + \frac{1}{6}b_4 f_\pi^4 . \tag{6.19}$$

The sign of the parameters c_2 and c_3 are important for the interpretation of the scalar potential in terms of a Mexican hat potential. It indeed implies that a positive c_2 generates an attractive term (since s is negative) and a positive c_3 a repulsive term. The magnitude of these parameters is also important in order to interpret the different terms of the potential as an expansion in terms of many-body interactions, since a term in s^n corresponds to an $(n-1)-$body force. Since these many-body forces are expected to be hierarchically ordered (at least at low densities), truncations at different orders of the scalar potential are expected to evolve smoothly. When this is not the case, we will interpret it as an anomaly of the scalar potential.

In Tab. 6.2 we compare the parameters c_2 and c_3 determined for the three models. For all

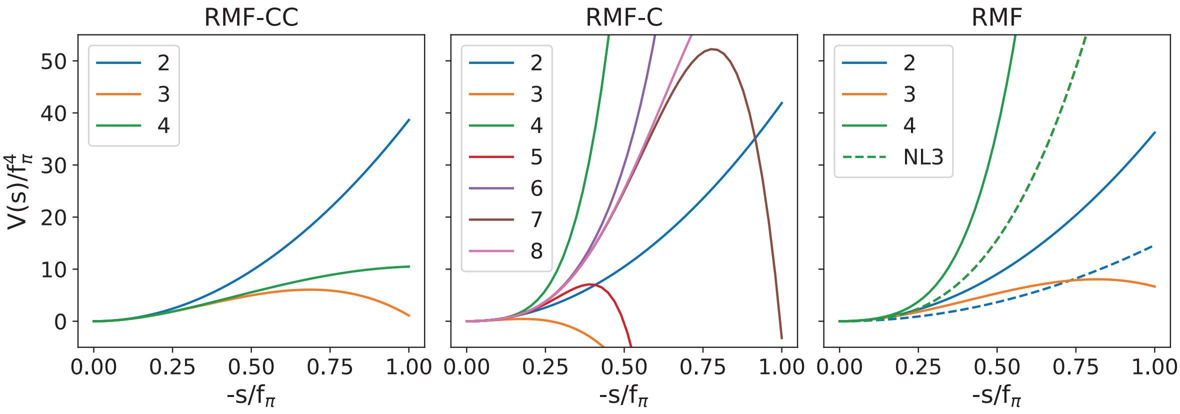

Figure 6.8: Analysis of the potential of the scalar field. Considering the potential as an expansion in s, the number in the legend refers to the order at which this expansion is truncated. The parameters of the scalar potential are taken to be the mean values reported in Table 6.2. In the right panel, for the NL3 parametrization (dashed lines) the orange dashed line is hidden behind the green one.

the models considered in this work, except NL3, the centroids of both c_2 and c_3 are positive, as expected. The parameters c_2 and c_3 of the RMF model are found to be different from the original NL3 model of Ref. [265], where c_2 and c_3 are both negative. Since the parameters c_2 and c_3 are obtained from a fit to the NEPs, their values are determined from the values considered for these NEPs. The values for E_{sat}, n_{sat}, $M^*_D(n = n_{\mathrm{sat}}) = M_N(s)$ and K_{sat} are indeed different for NL3 and the RMF case. Recall from Secs. 6.2 and 6.3 that this is because we constrain the three models RMF-CC, RMF-C and RMF to reproduce the same properties at saturation. If one were to break this constraint and allow RMF-C and RMF to explore different values for the NEPs, most notably the Dirac effective mass, some of the following results would have to be modified accordingly.

Large values of c_3 found for RMF and RMF-C indicate that $V(s)$, when considered as an expansion in s, might present an anomaly in the order hierarchy. In order to make it more clear, we show in Fig. 6.8 the chiral potential truncated at various orders in s, starting from order 2. In RMF-CC, the distinction between order 3 and order 4 curves appears only at large s, and this 4th order correction is relatively small. In the case of RMF-C however, we see that every addition of a higher order correction drastically changes the behaviour of the scalar potential. Indeed, a truncation at order 3 or 5 would result in an overall change of sign of $V(s)$ at $s \approx 0.5$. Therefore in the case of RMF-C, the correct reproduction of nuclear NEPs in SM is due to a fine tuning between the parameters b_2, b_3 and b_4, rendering difficult the interpretation of $V(s)$ in terms of many-body forces. We thus qualify the chiral potential in RMF-C as presenting an anomaly. We have a similar behaviour for RMF. The 4th order correction to the order 3 curve is very large, which is imposed by the saturation properties of RMF-CC. The scalar potential of RMF is thus also possibly anomalous. This conclusion is of course limited to the explored parameters region considered in our study - and related to the predictions of RMF-CC model - but different parameter sets could lead to a convergent expansion, as illustrated for instance by NL3 (RMF model), see the right panel of Fig. 6.8. Note that in this case the 4th order correction (dashed green line) is so small that it lies on top of and thus hides the 3rd order term.

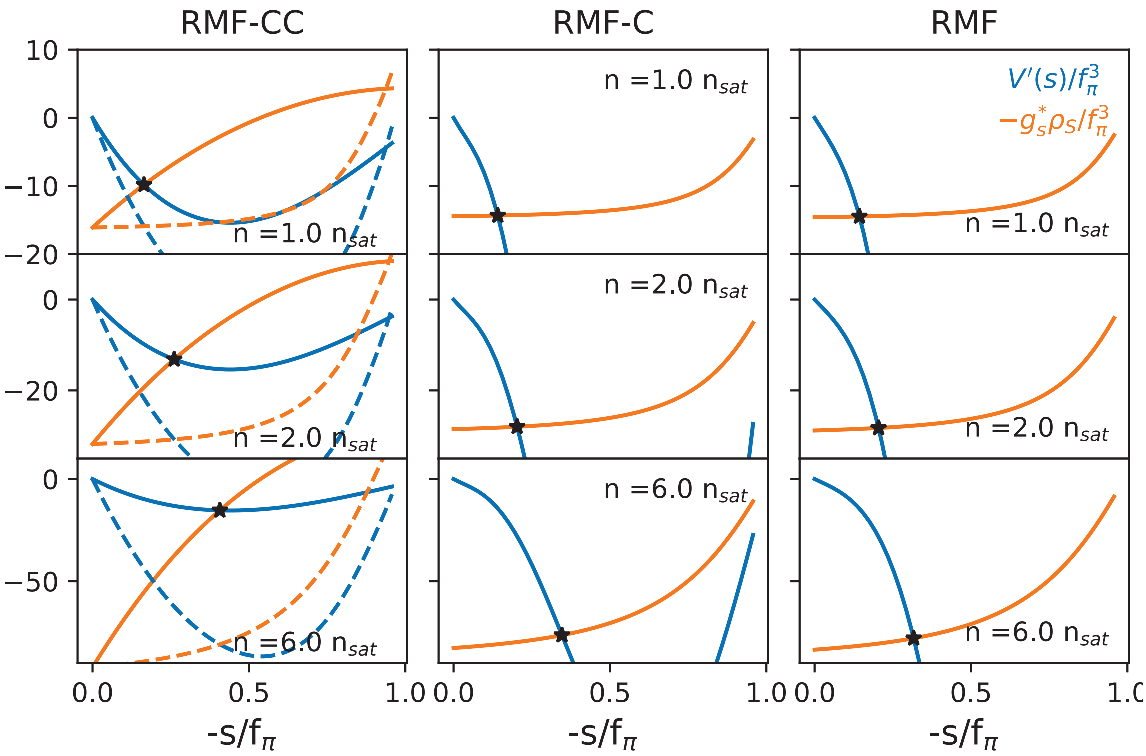

Figure 6.9: Analysis of the equation of motion of the scalar field. The different rows correspond to different densities. Dashed lines correspond to the equation of motion written for RMF-CC with the effective potential, see Eq. 6.21.

In conclusion, we observe that if the three models RMF-CC, RMF-C and RMF are constrained to reproduce the same properties at saturation, the s expansion of the scalar potential $V(s)$ may manifest an anomalous behaviour for RMF-C and RMF, at variance with RMF-CC. In the following section, we show that the origin of this anomaly for RMF-C and RMF can be related to the absence of the scalar nucleon response in their Lagrangian.

6.4.3 Analysis of the equation of motion of the scalar field

We now analyze in details the equation of motion (EoM) for the scalar field where the scalar potential plays naturally a crucial role. We will show that the anomaly of the scalar potential observed in the previous subsection for RMF-C and RMF models impacts the solution of the EoM.

The EoM for the scalar field s is, see Sec. 5.2,

$$V'(s) = -g_S^* \rho_S \qquad \text{with} \qquad g_S^* = \frac{\partial M_N(s)}{\partial s}, \tag{6.20}$$

where ρ_S is the scalar density. Note that for RMF-C and RMF models, $g_s^* = g_s$ since $M_N(s)$ is simply linear in the field s.

In Fig. 6.9, we represent the graphical solution of the EoM by drawing the two sides of the equation: $V'(s)$ is plotted as the solid blue lines and $-g_S^*\rho_S$ as the solid orange lines for the

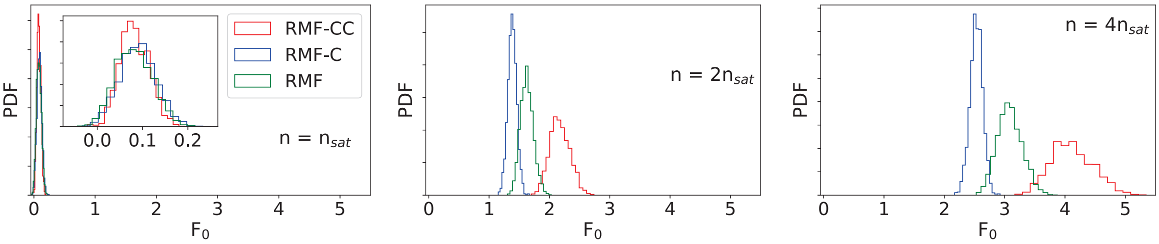

Figure 6.10: The Landau parameter evaluated at different densities. In the top panel, the inset shows a zoom of the region where the PDFs are nonzero.

three models (by columns) and at different densities (by rows). The parameters of the scalar potential are taken to be the mean values reported in Table 6.2, and similarly we consider the centroid of the PDFs for g_s which are 11.10, 9.98 and 10.08 for RMF-CC, RMF-C and RMF respectively. In case of several solutions, the physical one is the smallest one and it is identified as a black star. We see that as the density increases, the solution for the s-field (abscissa of the black star) of the scalar EoM increases. It is interesting to note that for all three models, at a given density, the value of this solution is quite similar. This is due to the fact that the quantity $g_s s$ defines the in-medium Dirac mass (except for RMF-CC where the nucleon response is also included) which remains almost identical for the three models, see Fig. 6.7 and g_s does not differs by more than about 10% between the different models, see Fig. 6.5. As a consequence the values of the field s are very close between the three models considered here.

The absolute value of the y-coordinate of the solution ($\propto V'(s)$) is however always smaller for RMF-CC compared to the RMF-C and RMF models. Since $V(s)$ is the vacuum chiral potential in the case of RMF-CC, the vertical position of the intersection point informs us about the derivatives of this potential for various values of the field s. In other words, for RMF-CC density scans the chiral potential function of s and the in-medium effects are entirely captured by the nucleon response given by g_s^*.

The situation is however different for RMF-C and RMF models. These models share two important features: i) they do not incorporate explicitly the nucleon response as in RMF-CC, and ii) the scalar potential is determined from the fit to saturation properties. If the fit imposes a modification of the scalar potential making it different from the vacuum one, it is interpreted as an in-medium correction to the scalar potential. It is interesting to remark that the result of the fit, which is made differently for RMF-C and RMF, is to impose larger absolute values for $V'(s)$ as function of s compared to the vacuum values represented by RMF-CC model. As a consequence, the intersection points in RMF-C and RMF happen at larger absolute values compared to RMF-CC. The vertical intersection point therefore informs us either on the role of the nucleon response in the EoM (6.20) (for RMF-CC), or on the in-medium modification of the scalar potential (for RMF-C and RMF).

At first sight, the models fitted to saturation and disregarding nucleon response (RMF-C and RMF) suggest large in-medium modification of the scalar potential, while the models considering the vacuum chiral potential complemented with nucleon response (RMF-CC) do not require any in-medium modification of the chiral potential. One may however wonder to which extend these two opposite conclusions do not reflect a similar reality suggesting that the nucleon polarization may modify in an effective way the vacuum scalar potential. It may even be the dominant in-medium correction to the scalar EoM.

In order to address this question, we rewrite the EoM for RMF-CC to absorb the effects of the nucleon response in an effective scalar potential $\tilde{V}'(s) = V'(s) + g_S^* \rho_S - g_S \tilde{\rho}_S$, as

$$\tilde{V}'(s) = -g_S \tilde{\rho}_S \, . \tag{6.21}$$

This leaves the standard scalar coupling g_S on the RHS of Eq. (6.21) (as in the other models). Note that this re-arrangement has been done by ensuring that it is still the same self-consistent equation of motion that is being solved for the RMF-CC. Finally, $\tilde{\rho}_S$ denotes that the dependence of the scalar density on s via the nucleon mass $M_N(s)$ is obtained by using a linear relation for $M_N(s)$ (as in RMF-C and RMF) and not the non-linear one used in RMF-CC. In this way, Eq. (6.21) is formally equivalent to the EoM (6.20) solved for RMF-C and RMF models.

In Fig. 6.9, the left column (for RMF-CC) displays dashed blue and dashed orange lines corresponding to the graphical solution of Eq. (6.21) in terms of the effective potential $\tilde{V}'(s)$. With such a construction, we see that the dashed blue line intersects the dashed orange line for lager absolute values of $\tilde{V}'(s)$, similar to RMF-C and RMF. This clearly demonstrates that the smaller absolute values of $V'(s)$ obtained for RMF-CC is a consequence of the inclusion of the scalar response of the nucleon. In other words, the nucleon polarisation captures most of the in-medium correction to the vacuum scalar potential.

While Fig. 6.9 clearly demonstrates that the nucleon polarisation is the dominant in-medium correction to the scalar EoM, a similar conclusion may have been obtained in the previous section based on the values for c_2 given in Tab. 6.5. In the RMF-CC model, the (positive) c_2 parameter controls the magnitude of the above mentioned attractive tadpole diagram which destroys saturation. For hierarchically ordered scalar potentials, it has been shown that after an appropriate shift of the scalar field, $\sigma_W = s + (\kappa_{NS}/2g_s)s^2$, where the term $\propto \kappa_{NS}$ represents the nucleon response, the Dirac mass of the nucleon becomes $M_N(s) = M_N + g_s \sigma_W$ and the nucleon polarizability modifies the cubic term of the scalar potential as $c_2\,(1-2C) \simeq -2\,c_2$ if $C \simeq 1.5$ [268] . One sees that this is qualitatively compatible with the values of c_2 for RMF-CC and NL3 quoted in Tab. 6.2. One can thus remark that the negative value of c_2 in the original NL3 model Ref. [265] simulates in an effective way the nucleon response. Note also that this discussion is not applicable to the RMF model since its scalar potential displays an anomalous behaviour. However it is interesting to note that while having a positive centroid for c_2, negative values for c_2 are also allowed in the PDF for the RMF model.

In conclusion, we have shown that the in-medium modification of the scalar potential which is captured in RMF-C and RMF models by the fit to saturation properties can also be simulated in RMF-CC by a single in-medium term in the Lagrangian: the nucleon response generated by the coupling of the constituent quarks to the large scalar field at finite density. The nucleon response effect, being characterized by a single coupling constant (κ_{NS} or C) in the RMF-CC Lagrangian represents therefore a very economical way to capture in-medium correction to the scalar EoM, on top of being well motivated from a microscopic viewpoint. In RMF-CC the chiral potential at finite density is identical to the vacuum one and one could interpret the solution of the scalar EoM as a scan of $V'(s)$ at different values of s. This latter point suggests that the solution of the EoM at finite density may be a way to probe the properties of the chiral potential in vacuum.

6.5 Collective states in dense matter

In the previous section, we have illustrated the equivalence between actual in-medium modification of the scalar potential guided by the fit to saturation properties (as in RMF-C and RMF) and in-medium effect of the nucleon polarization (as in RMF-CC). We have also suggested that the nucleon polarization is an economical way to treat in-medium correction to the scalar EoM. One may however wonder if the effect of the nucleon polarization could influence other in medium properties. It is therefore natural to come to the exploration of the excitation spectrum of dense matter.

We limit ourself to the scalar-isoscalar excitation channel, which is determined by the scalar-isoscalar Landau parameter F_0 at low excitation energy (and zero momentum transferred). Following Ref. [219], we have computed the fully relativistic Landau parameter F_0 for the three models. The outline of the derivation is as follows.

Derivation of the Landau parameter F_0 in relativistic theory

We begin by computing the first derivative of the energy density (5.10) with respect to the number density. We obtain

$$\frac{\partial \varepsilon}{\partial \rho} = E_F + \frac{g_\omega^2}{m_\omega^2}\,\rho \equiv \mu. \tag{6.22}$$

The second derivative is:

$$\frac{\partial^2 \varepsilon}{\partial \rho^2} = \left[\frac{k_F}{E_F} + \frac{M_N(s)}{E_F}\,g_S^*\,\frac{\partial s}{\partial k_F}\right]\frac{\partial k_F}{\partial \rho} + \frac{g_\omega^2}{m_\omega^2}. \tag{6.23}$$

The derivative of s with respect to the Fermi momentum is obtained by taking the derivative of the equation of motion (Eq. 5.12):

$$V''(s)\frac{\partial s}{\partial k_F} = -\tilde{\kappa}_{NS}\,\frac{\partial s}{\partial k_F}\rho_S + g_S^*\rho_S \quad \text{with} \quad \tilde{\kappa}_{NS} = \frac{\partial g_S^*}{\partial s}. \tag{6.24}$$

We introduce an effective sigma meson mass, such as $m_\sigma^{*2} = m_\sigma^2 + \tilde{\kappa}_{NS}\,\rho_S$, to obtain:

$$\frac{\partial s}{\partial k_F} = -\frac{1}{m_\sigma^{*2}}\,\frac{\partial \rho_S}{\partial k_F} \tag{6.25}$$

and the derivative of the scalar density has the form:

$$\begin{aligned}
\frac{\partial \rho_S}{\partial k_F} &= \frac{\partial}{\partial k_F}\left[\int \frac{4d^3k}{(2\pi)^3}\frac{M_N(s)}{\sqrt{k^2+M_N^2(s)}}\,\Theta(k_F-k)\right]\\
&= \frac{\partial \rho}{\partial k_F}\frac{M_N(s)}{E_F} + I_3(k_F)\,g_S^*\,\frac{\partial s}{\partial k_F}\\
\text{with} \qquad I_3 &= \int \frac{4d^3k}{(2\pi)^3}\,\frac{k^2}{\left(k^2+M_N^2(s)\right)^{3/2}}\Theta(k_F-k).
\end{aligned} \tag{6.26}$$

Combining Eqs. (6.25) and (6.26), we obtain:

$$\begin{aligned}\frac{\partial \rho_S}{\partial \rho} &= \frac{\partial \rho_S}{\partial k_F}\frac{\partial k_F}{\partial \rho} \\ &= -\frac{g_S^{*2}}{m_\sigma^{*2}}\frac{M_N(s)}{E_F}\left[1 + \frac{g_S^{*2}}{m_\sigma^{*2}} I_3(k_F)\right]^{-1} .\end{aligned} \tag{6.27}$$

Using the previous results, the compressibility modulus can be written in the following form:

$$K_{\rm sat} = 9\rho \frac{\partial^2 \varepsilon}{\partial \rho^2} = \frac{3\, k_F^2}{E_F}\,(1 \,+\, F_0)\,, \tag{6.28}$$

which depends on the relativistic generalization of the Landau parameter F_0:

$$F_0 = N_{0R}\left(\frac{g_\omega^2}{m_\omega^2} - \frac{g_S^{*2}}{m_\sigma^{*2}}\left(\frac{M_N(s)}{E_F}\right)^2\left[1 + \frac{g_S^{*2}}{m_\sigma^{*2}} I_3(k_F)\right]^{-1}\right). \tag{6.29}$$

This result derived in a different manner has been quoted in [219] but omitting the (small) correction arising from the I_3 integral. Notice that, as demonstrated in Ref. [269], $g_S^{*2}\, I_3(k_F)$ corresponds to the nuclear response associated with $N\bar{N}$ excitation. Also notice that our result coincides with the one derived by T. Matsui [270] but in the absence of medium modification (i.e., in the absence of the nucleon susceptibility term) of the scalar mass and coupling constant.

Numerical results for F_0

Fig. 6.10 shows the Landau parameter F_0, for the three models evaluated at three different densities, $n_{\rm sat}, 2n_{\rm sat}$ and $4n_{\rm sat}$. We see that at saturation density, the results agree for the three models, as it could be expected because the three models are calibrated such that they reproduce the same incompressibility modulus ($K_{\rm sat}$), see Eq. (6.28). However, at larger densities, the RMF-CC models predict larger values of F_0, followed by RMF and then RMF-C. At $4n_{\rm sat}$ the values for F_0 suggested by RMF-CC are almost twice the ones predicted by RMF-C.

This distinction in the predictions of F_0 by the three models at large densities may have important phenomenological consequences for dense matter in neutron stars. As an example, since it modifies the nuclear response functions, it may have implications for neutrino scattering and other phenomena in the core of neutron stars. Furthermore, our result suggests that the differences that we observe among the three models in this chapter would become even more enhanced at finite temperature. It would thus be interesting to, in the future, preform this comparison at finite temperature and also to apply these models in the simulation of binary NS mergers and heavy ion collisions.

6.6 The symmetry Energy

In this paper, we have restricted our many-body treatment to the Hartree approximation (classical fields) and to SM. In the future, we will also include the contribution of the Fock terms and we will explore asymmetric matter. At the Hartree level, the symmetry energy is however only determined by the ρ vector iso-vector meson. The small contribution from the δ scalar-isovector

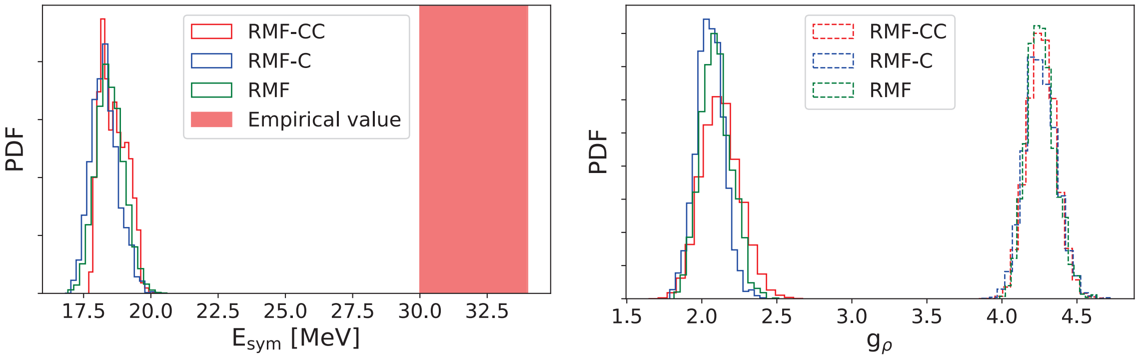

Figure 6.11: (TOP) The Symmetry Energy predicted by the three models assuming the quark model relation between g_ρ and g_ω. The empirical value is shaded in red. (BOTTOM) The coupling constant predicted by the quark model is shown as solid lines and the value required to obtain the empirical value is shown as dashed lines.

meson is disregarded here, and one obtains

$$E_{\rm sym} = \frac{k_F^2}{6\sqrt{k_F^2 + M_N^2(s)}} + \frac{g_\rho^2}{2m_\rho^2}\rho \tag{6.30}$$

where g_ρ and m_ρ are the coupling constant and the mass of the ρ meson. If the quark model is assumed, then $g_\rho = g_\omega/3$. In this case, the predictions for the symmetry energy at saturation density $E_{\rm sym}$ is shown for the three models in the upper panel of Fig. 6.11. The empirical value is shown as a red band. We see that there is a difference of about $12 - 15$ MeV (about half the expected value for $E_{\rm sym}$) between the predicted value and the empirical one. In the lower panel, in solid lines the value of g_ρ assuming the quark model (as in the upper panel) is confronted to the dashed lines showing the value of g_ρ required to reproduce the empirical value for $E_{\rm sym}$. There is a factor 2 difference between the solid and the dashed curves.

We interpret the discrepancy between the quark model prediction and the empirical value for $E_{\rm sym}$ as originating from the corrections beyond the Hartree approximation. In a future work, we will illustrate this point by adding to the present modeling the contribution of the Fock term, without modification of the fitting procedure. Preliminary results give us confidence in our interpretation.

6.7 Conclusions

In this chapter we have analysed the important role of chiral symmetry breaking and scalar nucleon response in the study of nuclear matter. We have done this, for the first time, by systematically comparing a model that takes these features into account (RMF-CC) versus models that neglect some or all of these aspects (RMF-C and RMF).

The systematic analysis was performed by ensuring a democratic treatment of the three models: we constrained the three models to agree with each other in the vicinity of saturation density of SM. In particular, the fit of the RMF-CC parameters to SM properties was performed in a novel way by simultaneously varying Lattice QCD parameters during the Bayesian fit, establishing a direct link with the underlying QCD theory. The fit of all three models to SM properties was performed in a consistent Bayesian manner which allows us to properly explore the uncertainties in our empirical knowledge of nuclear matter saturation.

In RMF-CC the modification of the effective potential at high density is driven by a microscopic mechanism, while in RMC-C and RMF approaches the scalar potential already encompasses finite density properties at saturation, that are simply extrapolated. In addition, we have shown that if the nucleon response is neglected, the scalar potential become anomalous since the hierarchy in the orders of s is not respected as it is expected in a many-body framework. Moreover the ground state and excited states in the scalar-isoscalar channel are predicted to be noticeably different as the density increases (2 to $4n_{\mathrm{sat}}$).

The RMF-CC approach represents a step in the modeling of matter properties beyond saturation density since the model parameters are mainly given by fundamental properties, e.g., L-QCD predictions or quark model constraints, and only saturation density n_{sat} and energy E_{sat} have actually been used in the model calibration. All other empirical parameters are predicted, e.g., K_{sat} or E_{sym}. We have shown for instance that the Hartree approximation of the mean field is not sufficient to reproduce the empirical values for E_{sym}. In our RMF-CC approach E_{sym} can thus be used to evaluate the contribution of the correlations beyond the Hartree approximation, as well as of the missing interaction terms, e.g., the pion contribution. This could have important phenomenological consequences in the description of very dense matter.

Finally, phase transitions are expected to occur in the very dense matter found in the core of massive neutron stars. These phase transitions could lead to the appearance of other (non-nucleonic) hadronic degrees of freedom such as pion and kaon condensates as well as hyperons. Other phenomena such as chiral symmetry restoration and transition to deconfined quark matter might also take place. These exciting possibilities are explored in part III.

Part III

Exotic degrees of freedom in dense matter

Chapter 7

First Order Phase Transitions and Quarkyonic Matter

Previously, in parts I and II, we explored the properties of dense matter under the assumption that it is composed of only nucleonic degrees of freedom. Based on the empirical properties of finite, heavy nuclei, this purely-nucleonic hypothesis can be confirmed up-to about nuclear matter saturation density. However, in the inner cores of NSs where the density can be much larger than saturation density, it is certainly possible that non-nucleonic degrees of freedom play a role. For the sake of generality, we will henceforth refer to matter consisting of any non-nucleonic particle as Exotic Matter (EM). Such EM can consist of pion and/or kaon condensates [271, 32] as well as hyperons [154, 155]. Other examples of EM include deconfined quark matter (QM) and/or matter in which chiral symmetry is restored [272]. Recent multimessenger observations of NSs, i.e., radio [58, 60, 56, 59], X-ray [50, 49, 51, 52], gravitational-wave (GW) observations [38, 39] have renewed theoretical efforts to address the question of the existence of EM, in particular QM, in the inner cores of NSs.

The existence of QM in the cores of NSs has a long history starting from the early works by Seidov [273], Bodmer [274] and Witten [275]. In particular, Ref. [275] explored the strange quark matter hypothesis stating that the absolute ground-state of matter may be composed of u,d,s quarks instead of the observed u,d matter that builds nucleons. Since then, typical questions such as the nature of the transition, its location in the space of thermodynamic variables and implications for the resulting EoS have attracted a lot of attention [276, 277, 278, 279, 280, 281, 282, 283, 284]. Theoretical modeling of QM has been investigated from the simple MIT bag model to more advanced field-theory based NJL models, see Ref. [285] for a review of the latter. Besides these "microscopic approaches", more agnostic types of modeling in which the phase transition is described in terms of physical quantities, instead of coupling constants, have also been proposed [278, 286].

The transition from nucleonic matter to EM occurs via a *phase transition*. Different kinds of phase transitions are possible in dense matter [15, 28]. The phase transition could be an abrupt First-Order Phase transition (FOPT) which creates a discontinuity in the sound speed as a function of the density. Second Order Phase transitions as well as hyperonization are also possible. Furthermore, the transition could be fully analytic, as observed at finite temperature and zero chemical potential [5]. An example of such a crossover is the transition to Quarkyonic matter (QycM) [287], which has been shown to be quite attractive to NS phenomenology [288]. In Secs. 7.1 and 7.2 we will discuss the features of some of these kinds of phase transitions in detail.

The rest of the chapter is organized as follows. In Sec. 7.1, we will discuss our formalism for the construction of FOPTs. In Sec. 7.2, the theory of Quarkyonic matter as presented in Refs. [288] and [289] will be reviewed. The main purpose of this work is to explore the consequences of FOPTs on the radii of NSs, with special attention to the radii of very massive ($M \geq 2M_\odot$) NSs. We also confront these calculations to the predictions of the Quarkyonic model. Sec. 7.3 will be devoted to our results where we present calculations of NS masses and radii obtained from models exhibiting FOPTs and a transition to QycM. The behaviour of the sound speed of these models is analysed in Sec. 7.4. The analysis presented in Sec. 7.4 will serve as our main motivation for the developments of chapter 8. We present our conclusions in Sec. 7.5.

7.1 First Order Phase Transitions

In this work, we assume that the FOPT to EM in the inner cores of NSs is described by the Maxwell construction. Following the approach of Refs. [278, 286], the EoS is

$$p(n) = \begin{cases} p_{\text{Had}}(n) & \text{if } n < n_{\text{FO}} \\ p_{\text{FO}} & \text{if } n_{\text{FO}} < n < n_{\text{FO}} + \delta n_{\text{FO}} \\ p_{\text{FO}} + c_{\text{FO}}^2\big(\rho(n) - \rho_{\text{FO}}\big) & \text{if } n > n_{\text{FO}} + \delta n_{\text{FO}} \end{cases} \tag{7.1}$$

where $p(n)$ is the pressure as a function of the baryon number density, with $p_{\text{Had}}(n)$ denoting the purely hadronic case that is valid below the transition density n_{FO} (the subscript refers to First-Order). Also, p_{FO} is the constant pressure in the mixed phase which exists in the density interval δn_{FO}, with $p_{\text{FO}} = p_{\text{Had}}(n_{\text{FO}})$. The variable $\rho(n)$ is the energy density and ρ_{FO} is the energy density at $n = n_{\text{FO}} + \delta n_{\text{FO}}$. Finally, c_{FO} is the sound speed in the EM phase, which is assumed to be a constant, at least for the explored densities immediately after the FOPT. The qualitative features of this construction is illustrated in Fig. 7.1. Note that in this approach there is no assumption about the nature of the EM, which is not necessarily deconfined QM, and thus this approach is quite agnostic regarding the composition of the exotic phase.

Below the FOPT point, we require a model for the hadronic EoS. The hadronic EoS can, in principle, include more than just nucleons, e.g. nucleon resonances, hyperons, meson condensates. For simplicity, we consider in the following only nucleonic EoSs below the phase transition. For this purely nucleonic EoS the energy density $\rho_{\text{Nuc}}(p)$ is calculated based on the meta-model (MM) [64, 131, 192] that has been used extensively in part I of this thesis. Recall that this is a density functional approach, similar to the Skyrme approach [185], that allows one to incorporate nuclear physics knowledge directly encoded in terms of the Nuclear Empirical Parameters (NEPs), see Eqs. 3.18 and 3.19 for their definition. By varying the empirical parameters within their uncertainties, the MM is able to reproduce the EoSs predicted by a large number of existing nucleonic models [64, 131], such as the Skyrme SLy4 interaction [185] that is shown in Fig. 7.5 for instance. Note however that it is not the purpose of the this chapter to explore nuclear physics uncertainties from the MM. As we detail hereafter, the nucleonic EoS will be fixed such that we will focus on the effects of different approaches to describe the transition to EM.

Let us now discuss some of the features of Eq. (7.1) qualitatively. As can be seen in Fig. 7.1,

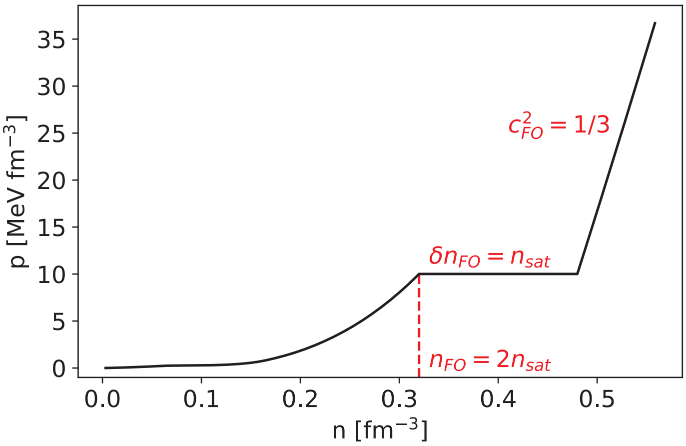

Figure 7.1: The pressure as function of the baryon number density for an EoS undergoing a FOPT as described by Eq. (7.1).

the pressure remains constant as a function of n, during the gap δn_{FO}. This leads to the so called *softening* of the EoS. Although one might think that such soft EoSs may not support NSs with $M \geq 2M_\odot$ (a condition which is required by radio observations of heavy pulsars, see Refs. [59, 61, 56] for the most recent of them), studies have shown that FOPTs can lead to maximum masses $M_{\mathrm{TOV}} \sim 2.5M_\odot$ [286]. Additionally, large radii (~ 14 km) for massive NSs have been constructed in previous works, see for instance Refs. [290, 279]. In particular, the authors of Ref. [290] have constrained the properties of FOPTs by imposing upper and lower bounds on M_{TOV} along with bounds on the radii of massive NSs. In Ref. [279], the authors obtain radii as large as 15.8 km for maximally massive stars. However this value decreases significantly if the condition of thermodynamic stability is imposed, i.e. the condition that the exotic phase should have a lower free energy per baryon than the nucleonic phase. This stability suggests that the nucleonic free energy represents a viable solution for the ground-state of matter at all densities, even for the largest ones found after the phase transition. Such a condition might be over constraining since it may reject solutions which can be physical after the phase transition. Since the break-down density of the nucleonic solution is not well known, we fix it to be located just after the phase transition, for $n > n_{\mathrm{FO}} + \delta n_{\mathrm{FO}}$.

Finally, we remark that at variance with Eq. (7.1), the FOPT might proceed via a Gibbs construction [291]. In the Gibbs construction, the pressure is not required to be constant in the mixed phase [28] implying that an extended mixed phase can exist inside NSs. This is contrary to the Maxwell construction in which there is only a sharp interface between the hadronic and exotic phases, since there exists a one-to-one correspondence between the pressure and the radial coordinate inside the NS. Furthermore, the mixed phase in the Gibbs construction might contain inhomogeneous bubbles (or pasta) of one phase immersed inside the homogenous medium composed of the other phase [15, 28]. The shapes and sizes of these bubbles depend of their surface tension, which is practically unknown. While the Gibbs construction is the more general one, it can be shown that if the surface tension exceeds a certain critical value [292, 293, 286], the FOPT reduces to one that is described by the Maxwell construction, i.e. the transition proceeds via a sharp interface between the two phases. Since the uncertainties in the surface tension, in the case of QM, allow for this scenario, in this study we will work only with the Maxwell construction, i.e Eq. (7.1).

7.2 Quarkyonic Matter

After the original conjecture of QycM by McLerran and Pisarski [287], a model for QycM has been developed to produce an EoS relevant to NSs [288]. By considering the case of pure neutron matter rather than beta-equilibrated matter, McLerran and Reddy have shown that the resulting EoS is stiff by nature and thereby attractive to NS phenomenology. Following their study, extensions have been proposed to incorporate beta-equilibrium by Refs. [294, 289], and here we follow the proposal of Ref. [289].

The basic picture of QycM is that the ground state of dense matter is composed of free quarks, having a constituent quark mass, that occupy states deep inside the Fermi sea. Baryons are generated by the strong confining force close to the Fermi level and therefore occupy a shell lying on top of the quark states. This momentum shell has a width that is taken to be $\Delta_{\text{Qyc}} \approx \Lambda_{\text{Qyc}}$, where Λ_{Qyc} is the typical QCD momentum scale. The low energy excitations around the Fermi level therefore involve only quasi-particles of nucleonic type. As in Ref. [288], the thickness of the shell inside which the nucleons reside is taken to be

$$\Delta_{\text{Qyc}} = \frac{\Lambda_{\text{Qyc}}^3}{k_{F_N}^2} + \kappa_{\text{Qyc}} \frac{\Lambda_{\text{Qyc}}}{N_c^2}, \tag{7.2}$$

where k_{F_N} is the nucleon Fermi momentum. There are two parameters: the Qyc scale $\Lambda_{\text{Qyc}} \approx 250 - 300$ MeV, which is similar to the QCD scale, and the coefficient $\kappa_{\text{Qyc}} \approx 0.3$.

The relationship between isoscalar quark Fermi momentum k_{F_Q} and the nucleon Fermi momentum is given by

$$k_{F_Q} = \frac{k_{F_N} - \Delta_{\text{Qyc}}}{N_c} \Theta(k_{F_N} - \Delta_{\text{Qyc}}). \tag{7.3}$$

We can therefore remark that the isoscalar nucleon Fermi momentum k_{F_N} drives the behaviour of the nucleon gap (7.2) as well as the isoscalar quark Fermi momentum (7.3). It follows that the nucleon and quark densities are given by

$$n_N = \frac{2}{3\pi^2} \left[k_{F_N}^3 - (k_{F_N} - \Delta_{\text{Qyc}})^3 \Theta(k_{F_N} - \Delta_{\text{Qyc}}) \right], \tag{7.4}$$

and

$$n_Q = \frac{2}{3\pi^2} k_{F_Q}^3 \Theta(k_{F_Q}) \,. \tag{7.5}$$

The total baryon density is given by

$$n_B = n_N + n_Q. \tag{7.6}$$

In asymmetric matter, one additionally has to deal with the 4 particle densities: n_n, n_p, n_u and n_d which are the densities of neutrons, protons, up-quarks and down-quarks respectively. Their relationship with the isoscalar nucleon and quark densities are straightforward and given by

$$\begin{aligned} n_N &= n_n + n_p \qquad (7.7) \\ n_Q &= (n_d + n_u)/N_c \,. \qquad (7.8) \end{aligned}$$

In order to obtain the densities n_n, n_p, n_u and n_d, the authours of Ref. [289] proposed the imposition that the two phases conserve isospin/flavor asymmetry. Since $n : (udd)$ and $p : (uud)$, this gives

$$\delta_N = N_c \delta_Q, \qquad (7.9)$$

where $\delta_N = (n_n - n_p)/n_N$ and $\delta_Q = (n_d - n_u)/(n_d + n_u)$.

Therefore, knowing δ_N and k_{F_N}, one can determine all the particle densities:

$$\begin{aligned} n_n &= \frac{1+\delta_N}{2} n_N \qquad (7.10) \\ n_p &= \frac{1-\delta_N}{2} n_N \qquad (7.11) \\ n_d &= \frac{1+\delta_Q}{2} N_c n_Q \qquad (7.12) \\ n_u &= \frac{1-\delta_Q}{2} N_c n_Q . \qquad (7.13) \end{aligned}$$

Furthermore, the neutron and proton densities can be related to the corresponding Fermi momenta as

$$n_n = \frac{1}{3\pi^2}\left(k^3_{F_n} - k^3_{F_n^{\min}}\right) \,, \; n_p = \frac{1}{3\pi^2}\left(k^3_{F_p} - k^3_{F_p^{\min}}\right) \,, \qquad (7.14)$$

where

$$k^3_{F_n} = (1+\delta_N) k^3_{F_N} \,, \qquad k^3_{F_p} = (1-\delta_N) k^3_{F_N} \,, \qquad (7.15)$$

and the lower bounds of the nucleon shells are given as

$$\begin{aligned} k^3_{F_n^{\min}} &= (1+\delta_N)\left(N_c k_{F_Q}\right)^3 \qquad (7.16) \\ k^3_{F_p^{\min}} &= (1-\delta_N)\left(N_c k_{F_Q}\right)^3 \,. \qquad (7.17) \end{aligned}$$

Finally, the energy density contributions from the nucleons and the quarks are given by

$$\begin{aligned} \rho_N &= 2\sum_{i=n,p} \int_{k^{\min}_{F_i}}^{k_{F_i}} \frac{d^3k}{(2\pi)^3} \sqrt{k^2 + M_N^2} + V_N(k_{F_n}, k_{F_p}), \\ \rho_Q &= 2\sum_{q=u,d} N_c \int_0^{k_{F_q}} \frac{d^3k}{(2\pi)^3} \sqrt{k^2 + M_Q^2}. \qquad (7.18) \end{aligned}$$

As in Sec. 7.1, the nucleonic residual interaction V_N is taken from the MM approach . Note that, under the assumption that chiral symmetry remains broken, we take $M_Q = M_N/N_c$ even in the quarkyonic matter. Having thus established the EoS of quarkyonic matter for arbitrary

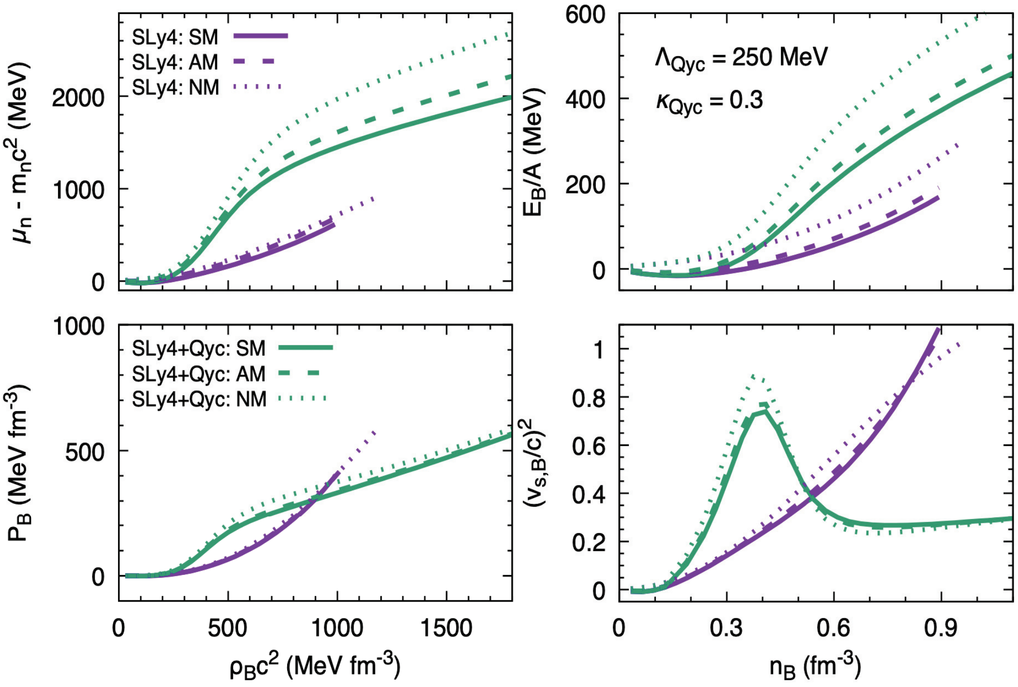

Figure 7.2: The baryon chemical potential μ_B, energy per particle E_B/A, pressure P_B and sound speed $(v_{s,B}/c)^2$ in symmetric ($\delta_N = 0$), asymmetric ($\delta_N = 0.5$), and neutron matter ($\delta_N = 1.0$) for $\Lambda_{\mathrm{Qyc}} = 250$ MeV and $\kappa_{\mathrm{Qyc}} = 0.3$. Figure taken from Ref. [289].

isospin asymmetries, the condition of beta-equilibrium can now be imposed easily [289].

Results for the EoS of the QycM is shown in Figs. 7.2 and 7.3. In Fig. 7.2, we show the baryon chemical potential μ_B, energy per particle E_B/A, pressure P_B and sound speed $(v_{s,B}/c)^2$ in symmetric ($\delta_N = 0$), asymmetric ($\delta_N = 0.5$), and neutron matter ($\delta_N = 1.0$) for $\Lambda_{\mathrm{Qyc}} = 250$ MeV and $\kappa_{\mathrm{Qyc}} = 0.3$. Similar thermodynamical quantities are shown in Fig. 7.3 but at β-equilibrium. These results were obtained from QycMs constructed on top of the SLy4 model [185]. This purely nucleonic SLy4 model is also shown in Figs. 7.2 and 7.3 as violet lines for comparison. We see that, by suggesting a crossover between the nucleonic and the quark phases, the QycM implies a rapid increase in pressure upon the onset of quarks. This induces an hardening of the EoS in a density interval associated to the cross-over transition between hadronic and quarkyonic matter. At higher density, the sound speed decreases again, producing the expected softening of the EoS, but at densities that may not be explored in nature. The qualitative features of QycM thus seem to be opposite to those of a FOPT. Note that, in addition to the QycM, other models exhibiting crossover transitions have been explored in the literature [295, 296]. In this work however, we will restrict our attention to QycM since it qualitatively captures the stiffness of the EoS generic to crossover transitions.

7.3 Prediction of NS Masses and Radii

The purpose of this chapter is to challenge the *a priori* difference between FOPT and QycM by testing to which extent FOPTs can also predict *hard* dense matter EoSs. In Fig. 7.4 we show

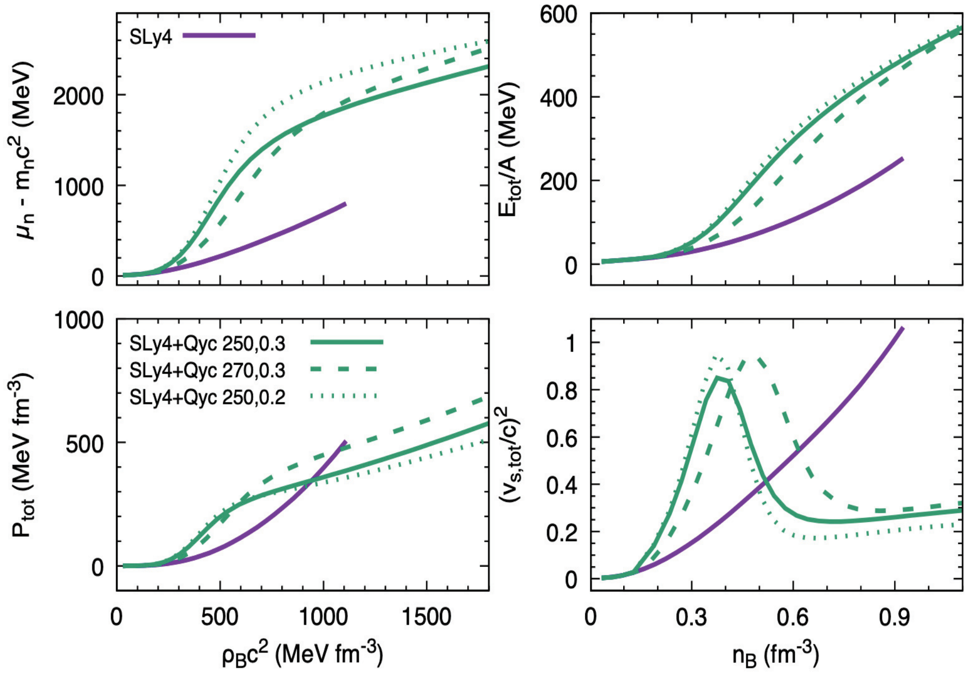

Figure 7.3: The neutron chemical potential μ_n, total energy per particle E_{tot}/A, total pressure P_{tot} and total sound speed $(v_{s,tot}/c)^2$ at β-equilibrium. Figure taken from Ref. [289].

various examples of EoSs with a FOPT as described by Eq. (7.1). These are shown as the black lines with different line-styles. We consider the purely nucleonic SLy4 EoS [185] shown as the red dashed line. Interestingly, the SLy4 EoS is quite soft and it predicts radii lower than the recent NICER radius estimate [50, 52] of PSR J0740+6620 shown in magenta (68% CL). In order to increase the repulsion and create a stiffer nucleonic EoS, the value of K_{sym}, see Eq. (3.19), was increased from -120 MeV to 125 MeV and the result is shown as the solid red line which is consistent with the NICER result. In the following this EoS is used as a reference one, so for simplicity it is labelled "Nucleonic". Additionally, we show two extreme instances of quarkyonic EoSs as solid and dashed blue lines (with $\Lambda_{\mathrm{Qyc}} = 250$ and 332 MeV) and fill up the region described by intermediate values for Λ_{Qyc}. The value of $\Lambda_{\mathrm{Qyc}} = 332$ MeV implies that the onset of quarks occurs at a density of 0.33 fm^{-3}, whereas for $\Lambda_{\mathrm{Qyc}} = 250$ MeV, the quarks appear at 0.14 fm^{-3}. Thus, while the former corresponds to what one may consider as a typical value of the quarkyonic transition density, the latter serves only as an example of an extreme case where the quarks start appearing around the saturation density. We also show existing astrophysical data on NS masses and radii. The yellow contour depicts constraints from the GW170817 event obtained from Ref. [39], the green one is obtained from the NICER observation reported in Ref. [49] and the magenta contour is obtained by combining the PSR J0740+6620 NICER observations of Refs. [50] and [52]. All measurements are reported at the 68% CL. In this chapter some astrophysical data are shown only for illustrative purposes and we leave for a later study the complete Bayesian analysis, exploring the nucleonic uncertainties in addition to the ones from EM.

In Fig. 7.4, various values of the FOPT parameters are considered. Recall that n_{FO} is the baryon number density at the transition point, δn_{FO} is the transition gap and c^2_{FO} is the square of

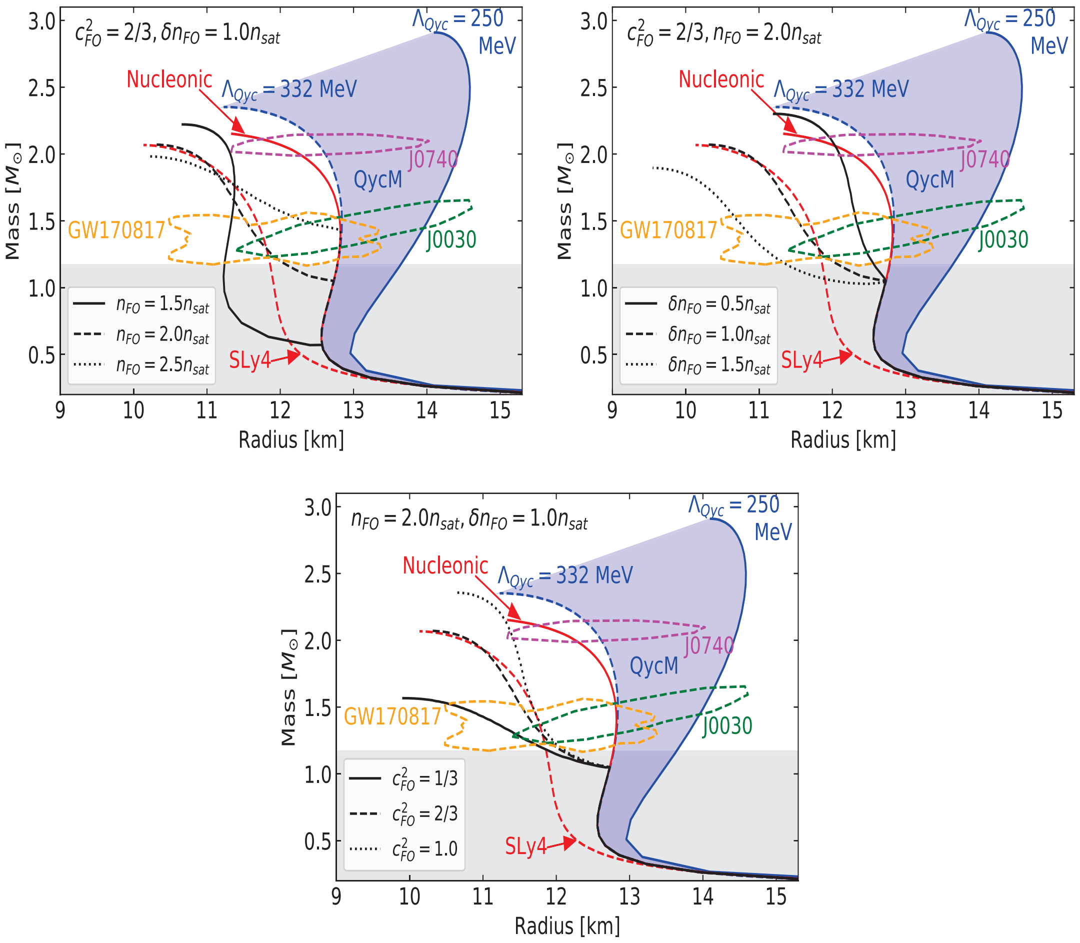

Figure 7.4: The mass-radius curves for various FOPT EoSs in the *soft* case, shown in black with the different line-styles referring to different values of the parameters governing the FOPT. The dashed red line displays the purely nucleonic SLy4 EoS and the solid one is a more repulsive nucleonic EoS which matches with the NICER's constraints (see text). The blue lines depict area explored by the Quarkyonic EoSs. We also show constraints from GW170817 (yellow contour), NICER's PSR J0030+0451 observation (green contour) and NICER's PSR J0740+6620 measurement (magenta contour).

the sound speed in the exotic matter present in NSs after the phase transition. Here, we consider values for these parameters in the ranges: $n_{\rm FO} = (1.5 - 2.5)n_{\rm sat}$, $\delta n_{\rm FO} = (0.5 - 1.5)n_{\rm sat}$, and $c^2_{\rm FO} = 1/3 - 1$. Note that some of these EoSs can support more massive NSs than the most massive one that can be supported by the purely nucleonic EoS. It was indeed already noticed in Ref. [289] that the Qyc model can change a nucleonic EoS failing to get the observed $2M_\odot$ into an EoS passing over this limit. However, the generic feature of all these first-order EoSs is that they predict smaller radii compared to the nucleonic and quarkyonic EoSs. Thus the FOPT considered here clearly illustrate the prevalent picture mentioned earlier, i.e. FOPT soften the EoS and lead to smaller radii [278, 286, 279]. Also note that all FOPT curves (except the solid one in the top right panel) predict smaller radii than the recent NICER estimate shown in magenta, and would therefore be simply rejected by the new NICER observation.

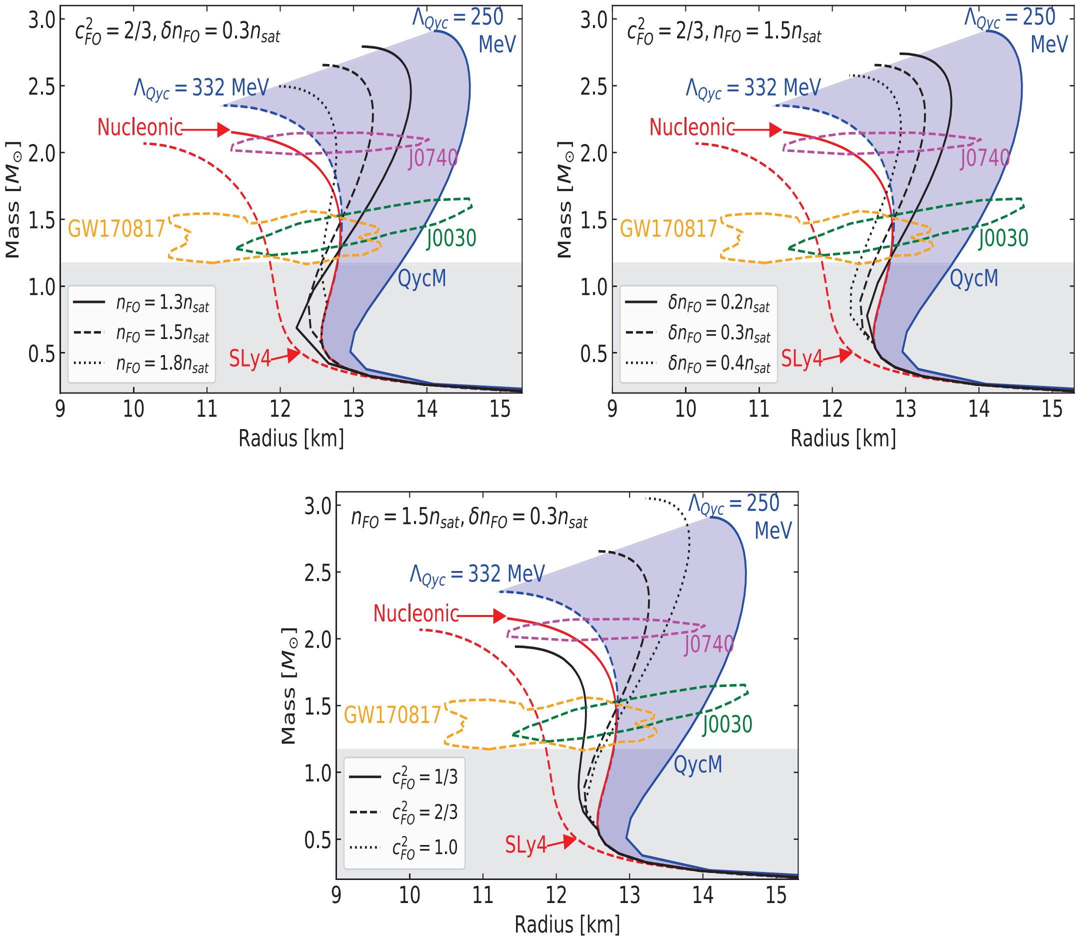

Figure 7.5: Same as Fig. 7.4 for FOPT EoSs in the *stiff* case.

In Fig. 7.4, the parameters controlling the transition point where chosen to coincide with typical values expected for a transition to QM, i.e. the transition does not occur at very low densities ($n_{\rm FO} \gtrsim 2.0 n_{\rm sat}$) and the sound speed is close to the expected conformal limit in QM, $c^2_{\rm cl} = 1/3$. This is what leads to the consensus that FOPTs lead to soft EoSs. However, we argue that another set of values, with $n_{\rm FO} \lesssim 2.0 n_{\rm sat}$, $c^2_{\rm FO} \gtrsim 0.6$ and $\delta n_{\rm FO} \approx 0.3 n_{\rm sat}$, cannot be ignored just because they result in the appearance of quarks (or any other exotic matter) at relatively low densities. The first reasoning is that these sets of parameter values results in EoSs that could not be excluded by experimental or observational constraints. Further, a recent study [297] estimating the posterior distribution over these parameters via a Bayesian analysis of astrophysical data has shown that the most probable values are $n_{\rm FO} \approx 1.6 n_{\rm sat}$ and $c^2_{\rm FO} \approx 0.95$. This shows that parameters resulting in an early phase transition to EM with large sound speeds should not be overlooked and, additionally, they may even be favoured by astrophysical observations. See also Ref. [298] which came to a similar conclusion in the context of the analysis of locations for the special point of hybrid stars in the mass-radius diagram.

With such a motivation, in Fig. 7.5 we construct examples of EoSs with a FOPT that are relatively stiff. We have considered low values for the transition point $n_{\rm FO} \leq 1.8 n_{\rm sat}$, small density gaps $\delta n_{\rm FO} = 0.2 - 0.4 n_{\rm sat}$ and again, a large prior for the EM sound speed $c^2_{\rm FO} = 1/3$,

$2/3$, 1. As before, we contrast these EoSs against the nucleonic EoS (in solid red) and two Qyc EoSs (in blue) with $\Lambda_{\mathrm{Qyc}} = 250$ and 332 MeV. Several of the EoSs with FOPTs lie inside the blue band encapsulating various possible quarkyonic EoSs. For instance, in the middle panel ($c^2_{\mathrm{FO}} = 2/3$ and $n_{\mathrm{FO}} = 1.5n_{\mathrm{sat}}$), the first-order EoSs with $\delta n_{\mathrm{FO}} = 0.2n_{\mathrm{sat}}$ and $\delta n_{\mathrm{FO}} = 0.3n_{\mathrm{sat}}$ give radii that are comfortably larger than those corresponding to the quarkyonic EoS (with $\Lambda_{\mathrm{Qyc}} = 332$ MeV) and the nucleonic EoS for $M \gtrsim 1.5M_{\odot}$. The EoS with $\delta n_{\mathrm{FO}} = 0.4n_{\mathrm{sat}}$ predicts larger radii only in the range $M \gtrsim 1.75M_{\odot}$. Similar comments can be made for the EoSs with a FOPT shown in the other panels with the lone exception being the EoS with $c^2_{\mathrm{FO}} = 1/3$ (bottom panel) that predicts lower radii for all NSs. This demonstrates that EoSs with FOPTs can give radii comparable to and larger than those resulting from quarkyonic and nucleonic EoSs at the condition that the sound speed in the EM exceeds the conformal limit in EM. We also observe that all EoSs with a FOPT (except the one with $c^2_{\mathrm{FO}} = 1/3$) are compatible with the considered astrophysical observations, most notably the NICER radius observation of the most massive NS known (magenta contour).

Let us also note that all the first-order EoSs shown in Fig. 7.5 do lead to smaller radii at very low NS masses ($\approx 1\mathrm{M}_{\odot}$). This is below the observed mass lower limit, $1.17M_{\odot}$ [299], which is shown in the figure as the upper limit of the grey area. A way to differentiate between the FOPT (for the parameters explored in Fig. 7.5) and Qyc matter would be to observe, if they exist, very low mass NSs ($\approx 1\mathrm{M}_{\odot}$). Indeed, the importance of such low mass NSs has been pointed out in Ref. [300] in the context of chiral effective field theory. Another quantitative difference between FOPT and Qyc matter is observed for the predicted radii associated to a canonical mass NS. At around $1.5M_{\odot}$, no FOPT could predict radii as large as the ones allowed by the Qyc model with typical $\Lambda_{\mathrm{Qyc}} \approx 250$ MeV. The main takeaway message illustrated by this figure is that EoSs with a FOPT can predict radii that are comparable to or larger than those corresponding to the nucleonic EoS as well as almost all the possible quarkyonic EoSs, in the range of observed NS masses.

In addition to the radii, Figs. 7.4 and 7.5 can be analyzed in terms of the maximum masses $\mathrm{M}_{\mathrm{TOV}}$ explored by FOPTs and Qyc models. It is known that FOPT can lead to large maximum masses, e.g. $\mathrm{M}_{\mathrm{TOV}} \approx 2.5\mathrm{M}_{\odot}$ with $c^2_{\mathrm{FO}} = 1$ [286]. We show that under special choice of parameters, FOPT can even reach $\mathrm{M}_{\mathrm{TOV}} \approx 3\mathrm{M}_{\odot}$, see the bottom panel of Fig. 7.5. The detection of GWs from binary NS mergers have been used to infer new constraints on $\mathrm{M}_{\mathrm{TOV}}$. Indeed, as mentioned in Sec. 1.2.1, an analysis of the GW170817 event by Ref. [47] found $\mathrm{M}_{\mathrm{TOV}} \lesssim 2.16^{+0.17}_{-0.15}\mathrm{M}_{\odot}$, and Ref. [48] found that $\mathrm{M}_{\mathrm{TOV}} \lesssim 2.3\mathrm{M}_{\odot}$. Using these values, several Qyc and FOPT models shown in Figs. 7.4 and 7.5 could be ruled out. However, more refined GW observations and numerical simulations may be required before FOPT and Qyc models could be definitively selected according to their prediction for $\mathrm{M}_{\mathrm{TOV}}$.

A Statistical analysis

Until now, we have show examples of EoSs with typical values for the FOPT parameters. In order to understand the role played by the three parameters ($n_{\mathrm{FO}}, \delta n_{\mathrm{FO}}, c^2_{\mathrm{FO}}$) in the global properties of NS such as the radius of a $1.6\mathrm{M}_{\odot}$ NS, we now perform a more extensive analysis based on a set of 5000 EoS, where the FOPT parameters are varied in a systematical way. We consider a sampling of uniformly distributed parameters in the following ranges, $c^2_{\mathrm{FO}} = [0.15, 1.00]$, $\delta n_{\mathrm{FO}} = [0.05, 1.50]n_{\mathrm{sat}}$, $n_{\mathrm{FO}} = [1.5, 2.5]n_{\mathrm{sat}}$, and we reject all samples for which $\mathrm{M}_{\mathrm{TOV}} < 1.6\mathrm{M}_{\odot}$. For all the remaining first-order EoS samples, the quantity $\mathrm{R}_{1.6} - \mathrm{R}^{\mathrm{nuc}}_{1.6}$

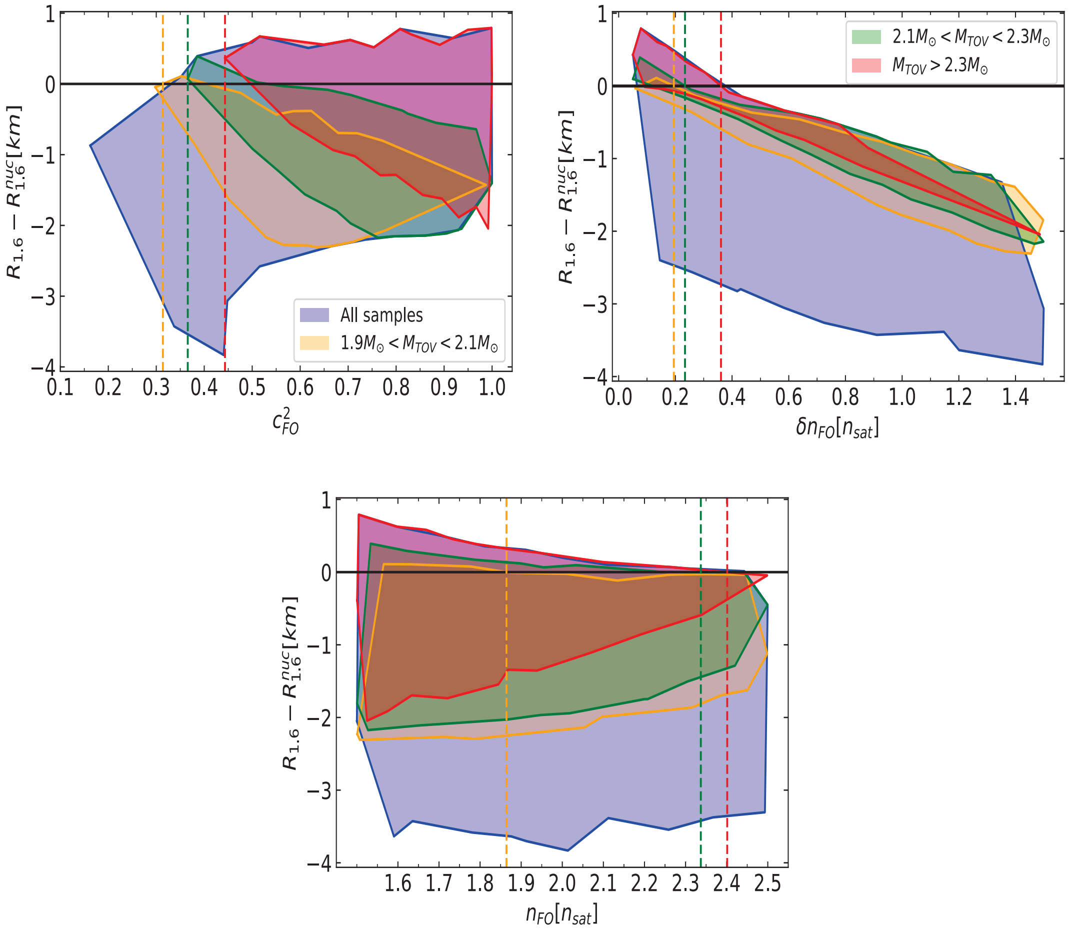

Figure 7.6: Plots depicting the correlation of $R_{1.6} - R_{1.6}^{nuc}$ versus the three transition parameters: $c^2_{\rm FO}$, $\delta n_{\rm FO}$, $n_{\rm FO}$. $R_{1.6}$ refers to the radius at $1.6M_\odot$ resulting from a FOPT. $R_{1.6}^{nuc}$ is the same quantity but for the purely nucleonic case. The contour colors correspond to different selection rules, as indicated in the figure legend. The different vertical lines correspond to extremum values of the FOPT parameters such that the condition $R_{1.6} > R_{1.6}^{nuc}$ is satisfied. See text for more details.

is plotted as a function of the three transition parameters in Fig. 7.6. Here $\rm R_{1.6}$ refers to the radius of a $\rm 1.6M_\odot$ NS resulting from a FOPT whereas $\rm R_{1.6}^{nuc}$ is the same quantity but for the purely nucleonic case. The results are show as contours for TOV masses given in the legend. Notice that, by analyzing the difference $\rm R_{1.6} - R_{1.6}^{nuc}$, we reduce the influence of the considered nucleonic EoS on which the FOPT is built. There is however a remaining effect of the nucleonic EoS which slightly impact the numbers given below.

In the top left panel of Fig. 7.6, we plot $\rm R_{1.6} - R_{1.6}^{nuc}$ against $c^2_{\rm FO}$. The vertical lines correspond to the minimum values of $c^2_{\rm FO}$ such that the condition $\rm R_{1.6} > R_{1.6}^{nuc}$ is satisfied, for different constraints on $\rm M_{TOV}$ (differently colored contours). For instance, if $\rm M_{TOV} > 2.1M_\odot$ as it is likely, then $\rm R_{1.6} > R_{1.6}^{nuc}$ is satisfied only if $c^2_{\rm FO} \gtrsim 0.37$. Therefore we can now confirm our earlier observation that $c^2_{\rm FO} > c^2_{\rm cl}$ allows FOPT EoS to predict larger radii than the one based on nucleonic EoS. We also observe that the quantity $\rm R_{1.6} - R_{1.6}^{nuc}$ increases with the increase in $c^2_{\rm FO}$.

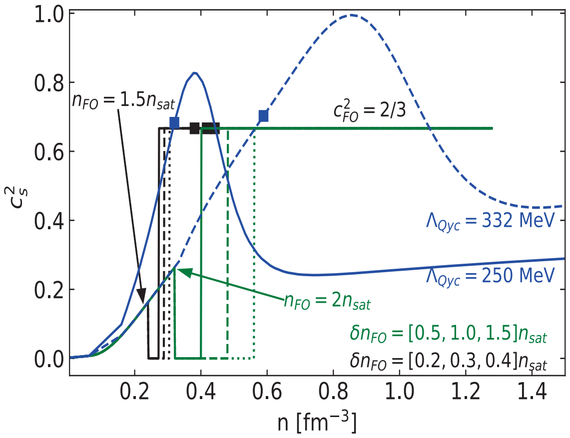

Figure 7.7: The sound-speed density profile for the various EoSs show in the middle panels of Figs. 7.4 and 7.5. The blue lines depict Quarkyonic EoSs. The black and green lines correspond to FOPTs for different values of $n_{\rm FO}$, $\delta n_{\rm FO}$ and $c^2_{\rm FO}$. The squares indicate the central density associated to a $2.1M_\odot$ NS for each EoS.

It shows that larger sound speeds support larger TOV masses. For instance, if $\rm M_{TOV} > 2.3M_\odot$, then $\rm R_{1.6} > R^{nuc}_{1.6}$ is satisfied only if $c^2_{\rm FO} \gtrsim 0.45$.

In the top right panel of Fig. 7.6, we plot $\rm R_{1.6} - R^{nuc}_{1.6}$ against $\delta n_{\rm FO}$. The vertical lines correspond to the maximum values of $\delta n_{\rm FO}$ allowed to satisfy $\rm R_{1.6} > R^{nuc}_{1.6}$. Note for instance that $\rm R_{1.6} > R^{nuc}_{1.6}$ (stiffer first-order EoS) is possible only if $\delta n_{\rm FO} \lesssim 0.23 n_{\rm sat}$ if $\rm 2.1M_\odot < M_{TOV} < 2.3M_\odot$. Unlike the top panel, EoS samples with $\rm M_{TOV} > 2.3M_\odot$ can be obtained at all values of $\delta n_{\rm FO}$. Restricting $\rm M_{TOV}$ to be inside small intervals but $> \rm 1.9M_\odot$ induces a tight correlation between $\rm R_{1.6} - R^{nuc}_{1.6}$ and $\delta n_{\rm FO}$. The correlation is even tighter for $\delta n_{\rm FO} > n_{\rm sat}$ if $\rm M_{TOV} > 2.3M_\odot$, and for $\delta n_{\rm FO} < 0.6 n_{\rm sat}$ if $\rm 1.9M_\odot < M_{TOV} < 2.3M_\odot$.

Finally, in the bottom panel of Fig. 7.6, we see that $\rm R_{1.6} > R^{nuc}_{1.6}$ is possible at the condition that $n_{\rm FO} \lesssim 2.3 n_{\rm sat}$ if $\rm 2.1M_\odot < M_{TOV} < 2.3M_\odot$, and at $n_{\rm FO} \lesssim 2.4 n_{\rm sat}$ if $\rm M_{TOV} > 2.3M_\odot$. Note that these values for $n_{\rm FO}$ are above $2n_{\rm sat}$ (not so low). Larger values for $\rm R_{1.6}$, i.e. increasingly repulsive EoS, are obtained for the lower values for $n_{\rm FO}$, predicting as well larger TOV masses.

7.4 Behaviour of the sound-speed

Since FOPT and QycM can predict very similar mass-radius relations, one could ask if the sound speed predicted by these two different models share similar features as well. In Fig. 7.7, the speed of sound is shown for the various EoSs considered in the middle panel of Figs. 7.4 and 7.5. The blue curves correspond to the $\rm Qyc$ EoSs for the two extreme cases where $\Lambda_{\rm Qyc} = 250$ and 332 MeV, whereas the black and green ones depict the EoSs with FOPTs. The squares indicate the central density of the $2.1M_\odot$ NS (the squares for the green EoSs are not shown). We see the familiar bumps in the sound speed profiles shown in blue, that characterize the quarkyonic EoS. The sound-speed density profiles associated to the FOPT models are qualitatively different from the QycM. Their density dependence is simpler since they first drop to zero for densities inside the transition domain, and after the phase transition they get to a constant value. However, the mass-radius curves generated by the FOPTs in black and the QycM in blue are quite similar, while the FOPTs in green predict different mass-radius curves (with a reduction of the radius after the phase transition). In conclusion, Fig. 7.5 illustrates that the bump in the Qyc EoS can be replaced with a simple, trivial structure such as a horizontal line corresponding to sound speeds around $c_{\mathrm{FO}}^2 \approx 2/3$, as shown here for the FOPT in black, albeit it implies a fine tuning of the parameters. If the value of δn_{FO} is not too large, such a replacement does not affect the mass-radius curve in a significant manner, leading to the possibility that first-order EoSs can mimic quarkyonic ones with a good accuracy. This remark moderates the findings of Ref. [27], where the authors argued that massive NSs and stiff EoSs are likely the result of non-trivial sound speed structures.

7.5 Conclusions

The purpose of this chapter is to challenge the *a priori* difference between FOPT and QycM, and to show that FOPT solutions could realistically masquerade QycM and predict *hard* dense matter EoSs. We construct explicit examples of EoSs undergoing a FOPT that are significantly stiffer than their purely hadronic counterparts, where by *stiff* we typically refer to the radii of NSs. Stiffer EoSs also predict larger TOV mass. Additionally, we show that the stiffness of such EoSs can be such that their mass-radius relations can realistically mimic the ones corresponding to the QycM. This can be seen as an extension of the results of Ref. [301] where it was shown that the mass-radius relations of first-order EoSs are quite similar to those predicted for NSs made of purely nucleonic matter. We have also confirmed that large TOV masses are possible with such FOPT EoSs. These EoSs arise from a certain set of values for the FOPT parameters, and we have performed a detailed analysis of the correlation between the stiffness of the EoS and the FOPT parameters. We have argued that such FOPT parameter sets are not ruled out by present astrophysical data and may even be favoured by them, as shown in Ref. [297]. These results have clear and important implications for phenomenology-based studies of the hadron-quark phase transitions in NSs and for the confrontation of EoS to the latest results from the NICER observation [50, 52]. An interesting extension of this work would be to confront systematically the various EoSs presented in this chapter to the wealth of available astrophysical data (radio, x-rays, and GW). Work along these lines is presently in progress.

Furthermore, we have analysed the behaviour of the sound speed of the models exhibiting transitions to EM. We showed that, while the sound speeds of the FOPT models have a different density dependence as compared to the QcyM model, the mass-radius curve remains unaffected by this difference. However, it is interesting to note that all the models undergoing phase transitions we have analysed in this chapter exhibit a non-monotonous behaviour of the sound speed as function of the density, see Fig. 7.7. It is therefore extremely interesting to ask if such non-monotonous (or non-trivial) structures can be inferred from astrophysical data in a physics-agnostic manner. This will the topic of chapter 8.

Chapter 8

Signatures of Phase Transitions from Astrophysical Data

In the previous chapter 7, the question of phase transitions was studied using two specific models: the Quarkyonic model (QycM) and the First-Order Phase Transition (FOPT). We observed that a change in the degrees of freedom to exotic forms of matter, such as quark matter likely manifests itself in terms of non-trivial structures in the sound-speed profile, see also Refs [27, 55]. In particular, an abrupt FOPT creates a discontinuous drop in the sound speed as a function of density [302, 303]. Particularly in a Maxwell construction for a FOPT, the speed of sound vanishes because the pressure is required to be constant in the mixed phase. Other forms of phase transitions, such as hyperonization or generic Second-Order Phase Transitions (SOPTs) such as kaon condensation, can also lead to a sudden reduction in pressure and therefore to a decrease in the speed of sound. In stark contrast to such softening phase transitions, a transition to quarkyonic matter could stiffen the EoS, leading to a sharp peak in the sound speed [288, 294, 289]. Similar stiffening of the EoS has also been observed in models that incorporate quark Pauli blocking, i.e. the exchange energy obtained by the antisymmetrization of the wave functions of the quarks that constitute multi-nucleon systems [304].

Recently, studies investigated non-trivial structures in the EoS above saturation density such as bumps in the sound speed [27, 55] or a kink in the EoS [272]. The authors of Ref. [272], using a general extension scheme in the speed of sound constrained by chiral effective field theory (EFT) calculations at low densities, perturbative QCD (pQCD) calculations at large densities, astrophysical observations of pulsars with masses around $2\mathrm{M}_\odot$, and the GW observation GW170817, observed a change in the adiabatic index γ of the envelope of all EoS models. By comparing this to expectations for hadronic and quark matter and by comparing central densities in heavy NSs for selected hadronic EoS models[1] and EoSs constructed within their extension scheme, they concluded to have found evidence for a phase transition to quark matter in the heaviest NSs, appearing at an onset energy density of approximately 700 MeV fm^{-3}. On the other hand, the authors of Ref. [27] explicitly considered non-trivial structures in the speed of sound such as kinks, dips and peaks. This allowed the authors to construct massive NSs consistent with the mass of the secondary component of GW190814. They concluded that such non-trivial structures are likely present at densities probed in very massive NSs ($\approx 2.5\,\mathrm{M}_\odot$).

In this chapter, we re-investigate if non-trivial structures in the speed of sound can be in-

---

[1] We note that some of the hadronic EoS models studied in Ref. [272] are non-relativistic.

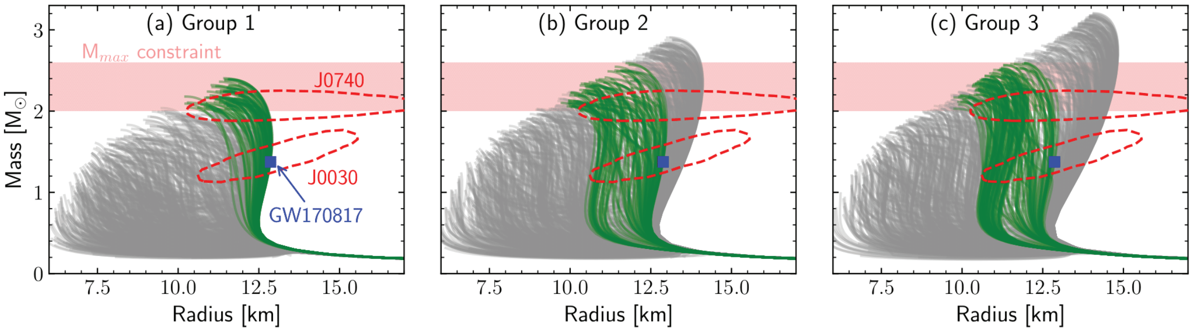

Figure 8.1: Mass-radius curves for all EoSs that we employ in our work (gray). The samples are divided into three panels corresponding to three EoS groups (see text). Note that for each group only 1000 samples (chosen randomly) out of the total 10000 EoSs are shown. We also show the observational constraints enforced in this work. EoSs that pass all observational constraints at the 90% confidence level are shown in green. See text for more details.

ferred from present astrophysical data. At variance with the previous chapter 7 where specific models where used for the phase transition, we use a fully physics-agnostic approach. For this, we employ general schemes for the EoS that are able to describe a wide range of density behaviors of the sound speed. We use a systematic approach to model the EoS in the speed of sound vs. density plane, employing a piece-wise linear model for the speed of sound which is a modified version of the scheme of Ref. [46] and similar to Ref. [272] but with more model parameters. We then group different EoS realizations according to the slope in the speed of sound, the appearance of non-trivial structures, or explicit FOPT, and analyze the effect of astrophysical NS observations. We compare our results with those presented in the literature and comment on the evidence for phase transitions linked to astrophysical data.

The rest of the chapter is organized as follows. Our computational framework is presented in Sec. 8.1 where we describe how we model the EoS in physics-agnostic manner. In Sec. 8.2, we analyse our results for the pressure of dense matter as function of the energy density. Sec. 8.3 is devoted to our results for the existence of phase transitions in dense matter inferred from the possible presence of non-trivial structures in the speed of sound and the adiabatic index. We present our conclusions in Sec. 8.4.

8.1 Equation of State Model

We use an extension scheme for the EoS in the speed of sound, c_s. At low densities, up to nuclear saturation density $n_{\rm sat}$, we fix our EoS to be given by the SLy4 energy-density functional [305], a phenomenological force that is well calibrated to nuclear matter as well as finite nuclei properties, and commonly used in astrophysical applications. Beyond $n_{\rm sat}$, for each EoS we create a non-uniform grid in density between $n_{\rm sat}$ and $12n_{\rm sat}$ by randomizing an initial uniform grid with a spacing of $n_{\rm sat}$: at each grid point, a density shift drawn from a uniform distribution between $-0.4n_{\rm sat}$ and $0.4n_{\rm sat}$ is added and defines the set $\{n_i\}_{i=1,11}$. We then sample random values for $c_s^2(n_i)$ between 0 and c^2 with c being the speed of light (we set $c = 1$ in the following). Finally, we connect all points $c_{s,i}^2(n_i)$ using linear segments.

We sort the resulting EoSs into three groups according to the maximal slope in the speed of

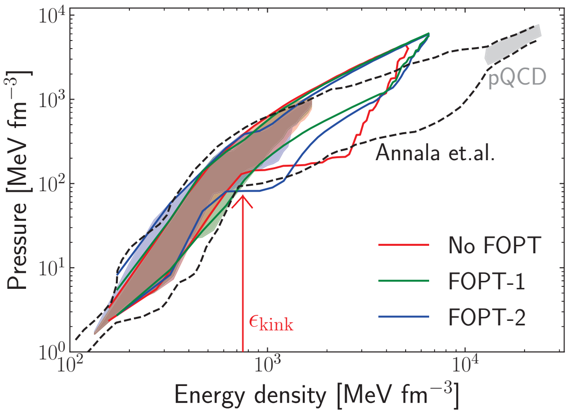

Figure 8.2: EoSs of this work that satisfy observational constraints. We show envelopes for EoSs without FOPT (red) and EoSs with FOPT with different onset density ranges (green and blue), see details in the text. The shaded bands correspond to stable NS configurations, whereas the solid lines show the EoSs extended beyond the maximally massive NS configurations. The black contour depicts the results of Ref. [272], and the gray contour represents the perturbative QCD constraint.

sound $c'_{\rm max} = \max\{dc_s^2/dn\}$: defining the slope at $n_{\rm sat}$ to be $c'_{\rm sat} = dc_s^2/dn(n_{\rm sat}) = 0.55$ fm^3, group 1 contains EoSs whose maximal slope is less than three times the slope at $n_{\rm sat}$, $c'_{\rm max} \leq 3c'_{\rm sat}$, group 2 contains all EoSs with $3c'_{\rm sat} < c'_{\rm max} \leq 6c'_{\rm sat}$, and group 3 contains all EoSs with $6c'_{\rm sat} < c'_{\rm max} \leq 9c'_{\rm sat}$. These groups are thus mutually exclusive. The upper limit in group 3 allows us to disregard EoSs for which the sound speed strongly oscillates with density, a case which is not observed in any EoS models besides those which incorporate a FOPT. We explicitly construct FOPTs later in the manuscript and analyze their impact on our results. We have generated 10,000 EoSs in each group.

By inverting the expression $c_s^2 = dp/d\epsilon = (nd\mu)/(\mu dn)$, we obtain the chemical potential μ in the interval $n_i \leq n \leq n_{i+1}$, the pressure and the energy density,

$$\log\left(\frac{\mu(n)}{\mu_i}\right) = \int_{n_i}^{n} \frac{c_s^2(n')}{n'} dn' \,, \tag{8.1}$$

$$p(n) = p(n_i) + \int_{n_i}^{n} c_s^2(n')\mu(n')dn' \,, \tag{8.2}$$

$$\epsilon(n) = \epsilon(n_i) + \int_{n_i}^{n} \mu(n')dn' \,. \tag{8.3}$$

More details regarding the computation of these integrals are given in Appendix B. Finally, we solve the TOV equations for each EoS to determine NS radii (R) and dimensionless tidal deformabilities (Λ) as functions of masses (M), see for instance Ref. [46] for more details.

In Fig. 8.1, we show the resulting mass-radius families together with the astrophysical observations that we consider in this work: the NICER observations of millisecond pulsars J0030+0451 [49, 51] and J0740+6620 [50, 52], the gravitational-wave observation GW170817 [38, 306], and upper and lower limits on the maximum NS mass, M$_{\rm TOV}$. For NICER's observation of J0740+6620, we have averaged over the analyses of Ref. [50] and Ref. [52]. For

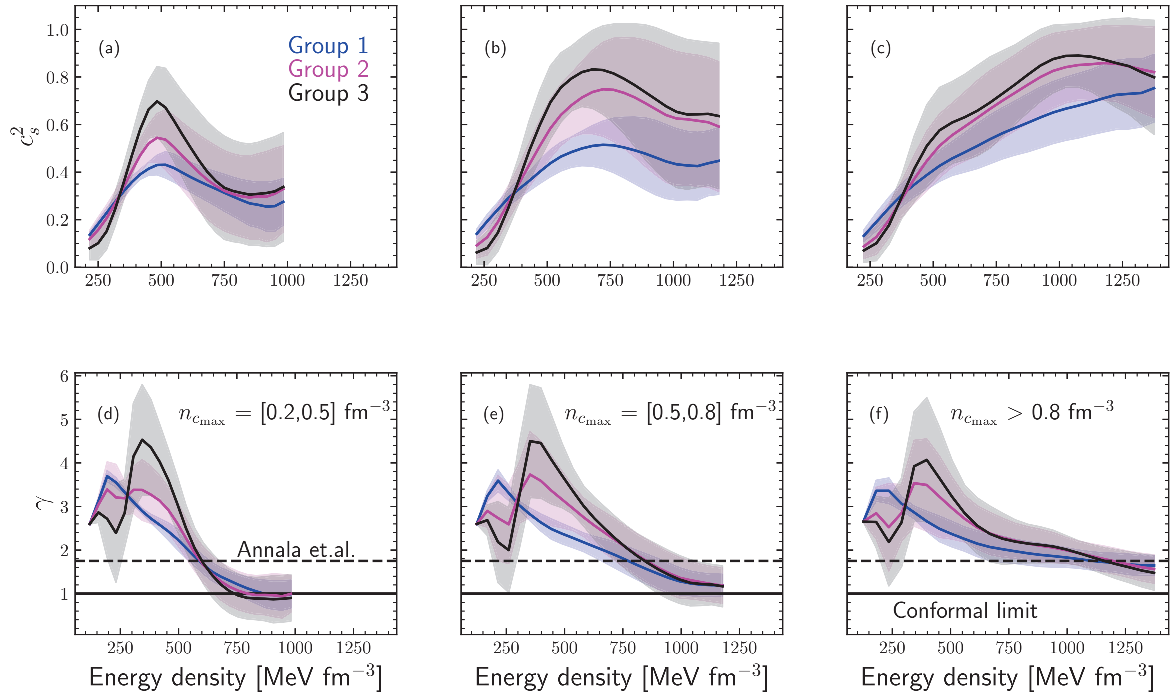

Figure 8.3: The squared sound speed (top) and adiabatic index (bottom) versus the energy density. We show the model-averaged bands for EoS that fulfill the astrophysical constraints (mean values with solid lines, band width representing the standard deviation). The different panels correspond to different locations of the maximum of the sound speed (see text).

GW170817, we transformed the estimation of the tidal deformability, considering $\tilde{\Lambda} = 222^{+420}_{-138}$ at 90% confidence level (CL) from Ref. [306], into a single constraint on the radius for the mass $m = 1.38\,\mathrm{M}_\odot$. This constraint gives an upper value of the radius obtained by running over all our EoSs compatible with GW170817 and by fixing the mass ratio $q = m_1/m_2 = 1$. This upper radius is 12.9 km and it is indicated by a blue dot in the figure. For $\mathrm{M}_{\mathrm{TOV}}$, we impose the constraint $2\,\mathrm{M}_\odot < \mathrm{M}_{\mathrm{TOV}} < 2.6\,\mathrm{M}_\odot$. The lower bound of $2\,\mathrm{M}_\odot$ is chosen to account for heavy pulsar radio observations [58, 60, 56, 59]. The upper bound of $2.6\,\mathrm{M}_\odot$ is consistent with the mass of the secondary object in the GW190814 event, which is likely a black hole [307, 308]. The EoSs that satisfy all constraints at the 90% CL are shown in green in Fig. 8.1.

8.2 Results for the EoS

The range of radii explored by our EoSs constrained by the astrophysical data previously reviewed is about 11-13 km. The upper radius limit is set by GW170817 (see Fig. 8.1) while the lower radius limit is a result of both the NICER and maximum-mass constraints. The envelopes of EoSs that survive all imposed astrophysical constraints are shown in Fig. 8.2. The filled contours encompass EoSs on the stable NS branch while the dashed contours encompass the EoSs on the unstable branch as well, i.e. for densities going above the maximum-mass NS, $\mathrm{M}_{\mathrm{TOV}}$. Fig. 8.2 illustrates that when we represent EoSs for densities above $\mathrm{M}_{\mathrm{TOV}}$ we find a kink similar to the one from Annala *et al.* [272] at $\epsilon_{\mathrm{kink}} \gtrapprox 700$ MeV fm^{-3}. More precisely, we observe

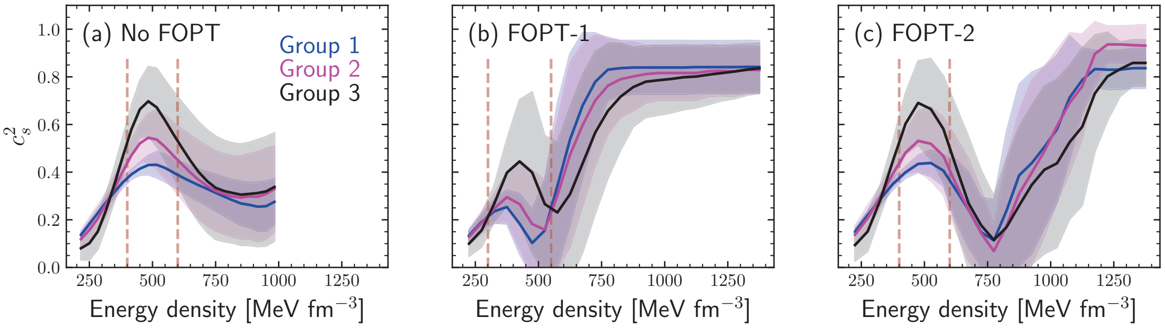

Figure 8.4: We compare the speed-of-sound bands for the various groups without including a FOPT (left panel, similar to left panel of Fig. 8.3) and when a FOPT is explicitly included. We show results for two ranges of the onset density of the FOPT. The dashed vertical lines encapsulate the region inside which a peak in the sound-speed occurs.

that EoSs can be arbitrarily soft above ϵ_{kink} since this regime is not probed in stable NSs (with $\mathrm{M} \leq \mathrm{M}_{\mathrm{TOV}}$). At even larger densities, our EoS envelopes broaden compared to Ref. [272], this time allowing stiff EoSs, but these differences have no impact for stable NSs. Note that unlike Ref. [272], we do not incorporate constraints from pQCD since the objective of this work is to study the influence of astrophysical data alone. In a future work, we will address the theoretical constraints from pQCD.

We also show results for EoSs with an explicit FOPT, built upon each original EoS. It is implemented in terms of three parameters: the transition energy density ϵ_t, the width of the transition $\Delta\epsilon$ and a constant sound speed after the transition $c^2_{s,t}$ [278, 286, 279]. The choice of imposing a constant sound speed allows us to control the stiffness of the EoS with a single parameter. By using a single value for the sound speed, it is easier to distinguish between soft and stiff quark matter. However, we note that exploring density dependent sound speeds after the FOPT could increase the variety of EoSs that satisfy the observational data. We aim to explore this systematically in a future analysis. For each EoS, random values are drawn from the uniform ranges $\epsilon_t = [400, 800]\,\mathrm{MeV\,fm}^{-3}$, $\Delta\epsilon = [0.2, 0.6]\epsilon_t$ and $c^2_{s,t} = [1/3, 1]$, and the EoSs are compared with astrophysical constraints as before. The lower bound on $c^2_{s,t}$ is not strictly necessary but it allows us to provide a uniform prior over a reasonable range in which we expect to find EoSs that satisfy astrophysical constraints. We show later in this chapter that this lower bound does not bias our results since all accepted EoSs (with FOPT) populate regions of sound speed with values above $1/3$. Finally, we separate the EoSs into two subgroups: $\epsilon_t = [400, 600]\,\mathrm{MeV\,fm}^{-3}$ (FOPT-1) and $\epsilon_t = [600, 800]\,\mathrm{MeV\,fm}^{-3}$ (FOPT-2). For the group with larger onset density, we again observe a kink of the EoS, while the other EoS group shows a smooth behavior.

The softening of the EoSs without FOPT observed in Fig. 8.2 at ϵ_{kink} is somewhat similar to the softening of the FOPT EoSs with $\epsilon_t = [600, 800]\,\mathrm{MeV\,fm}^{-3}$. It is, therefore, tempting to conclude that this softening is a signal of a phase transition to exotic matter. The adiabatic index $\gamma \equiv \frac{d\log p}{d\log\epsilon} = (\epsilon/p)\,c_s^2$ was computed in Ref. [272] and a value of $\gamma = 1.75$ was chosen to distinguish between hadronic and quark-matter models. In the following, we will study the behaviour of the adiabatic index γ and the sound speed c_s^2 for all EoSs shown in Fig. 8.2.

8.3 Results for the existence of phase transitions

In Fig. 8.3, we show sound speed distributions as function of energy density, for all EoSs fulfilling the observational constraints previously described. The model-averaged bands are terminated when the NSs enter the unstable branch. The precise value for which this happens, while slightly different for different models, has been fixed for the graphical representation shown in the figures. We separate each group into subgroups according to the density where the speed of sound reaches its maximum, $n_{c_{\max}}$: panel (a) shows all the EoSs for which $n_{c_{\max}}$ is between 0.2-$0.5\,\mathrm{fm}^{-3}$, in panel (b) $n_{c_{\max}}$ lies between 0.5-$0.8\,\mathrm{fm}^{-3}$, and panel (c) shows those for which $n_{c_{\max}}$ is beyond $0.8\,\mathrm{fm}^{-3}$. As one can see, while some groups contain EoSs with clear peaks, astrophysical observations do *not* require the EoS to have significant structures the speed of sound, in particular a decrease to $c_s^2 \approx 1/3$, see Fig. 8.3(c). The more pronounced peaks in Fig. 8.3(a) are reminiscent of the quarkyonic model [288] and the quark Pauli blocking effect [304], whereas the broader peaks in Fig. 8.3(b) can potentially be interpreted as a weaker change of phases.

We have found that the peaks in Fig. 8.3 disappear if we change the maximum mass constraint from $2\,\mathrm{M}_\odot <\mathrm{M}_{\mathrm{TOV}} < 2.6\,\mathrm{M}_\odot$ to $\mathrm{M}_{\mathrm{TOV}} > 2.6\,\mathrm{M}_\odot$. Therefore, the upper limit on $\mathrm{M}_{\mathrm{TOV}}$ is crucial for the appearance of a peak as it requires the EoS to soften at sufficiently high densities. These findings are consistent with those presented in Ref. [55] which concluded that existing astrophysical data does not necessarily enforce a bump in the c_s^2. For the behavior below the peak, both the stiffness required by the $2\,\mathrm{M}_\odot$ observations and the NICER observations and the softness required by GW170817 play an important role. This explains the agreement of the individual groups at low densities but their deviations at higher densities.

We show the adiabatic index γ in the bottom panels of Fig. 8.3. We find that basically all γ bands drop below $\gamma = 1.75$ at higher densities, corroborating the findings of Ref. [272]. However, we stress that this is only a *necessary but not a sufficient condition* for the appearance of quark matter. Indeed, a straightforward comparison of the top and bottom panels in Fig. 8.3 shows that while γ asymptotically approaches 1 in all cases, the sound speeds exhibit no preferred asymptotic value that can be identified as the conformal quark matter limit. Also, contrary to the findings of Ref. [272], we did not find that EoSs with $\gamma > 2$ in the maximally massive configuration have a significant softening at lower densities.

We finally analyze the impact of explicitly including a FOPT on the sound speed profiles. The results are shown in Fig. 8.4, where we compare (panel (a)) EoSs without FOPT but predicting a significant peak (as shown in Fig. 8.3a) with EoSs undergoing a FOPT. The EoSs with FOPTs are separated into two groups, as FOPT-1 (panel (b)) and FOPT-2 (panel (c)). When including a FOPT, we always observe the formation of a clear peak in the speed of sound profile, located at an energy density inside the region indicated by the dashed brown lines, similar to what we observe in Fig. 8.4(a). This suggests that if a FOPT occurs in dense matter, it is preceeded by a sharp increase in the sound speed beyond the conformal limit, reaching its maximum at approximately 400-$500\,\mathrm{MeV\,fm}^{-3}$. However, we stress once again that present astrophysical data does *not* necessarily imply that the EoS undergoes a FOPT.

8.4 Conclusions

We have used a framework based on the speed-of-sound extension to address the question of phase transitions in dense matter in a systematic way. We have classified EoSs agreeing with present astrophysical data based on the behaviour of their sound speed profiles. We were able to identify EoSs with a bump in the sound-speed profiles, resembling quarkyonic matter for instance, while for others we have explicitly included a FOPT. However, our analysis also revealed the presence of (sub)groups of EoSs that have neither a clear structure nor an asymptotic tendency to the conformal limit. This leads us to conclude that present astrophysical data does *not* favour exotic matter over the standard hadronic matter or a crossover feature. Nevertheless, our analysis also shows that, in the near future, new astrophysical data has the clear potential to be decisive, one way or the other, regarding the long-standing question of phase transitions in dense matter. With more data or a few accurate observations, we could anticipate two kind of scenarios: (i) If super-stiff EoSs survive from these new observations, then they will point towards a behavior like the one shown in Fig. 8.3(a), (ii) while if moderately-stiff EoSs survive, they will prefer the behavior represented in Fig. 8.3(c). We therefore expect that the future detections will prefer one of the scenarios suggested in Fig. 8.3. In addition, an information about phase transition could be extracted from BNS mergers if the post-merger GW signal is observed, as expected in the future. Such future detections will provide information that will also select among the behaviors illustrated in Fig. 8.4(a)-(c).

We believe that the tools developed in this work – by classifying the type of sound-speed density dependence in terms of simple properties – paves the way for further research in this direction. Finally it might be interesting to systematically investigate whether pQCD calculations have an impact on the findings of this work. This will be the subject explored in the next chapter.

Chapter 9

Perturbative QCD and the Neutron Star Equation of State

The overarching theme of this thesis is a consistent description of the Equation of State (EoS) of dense matter from low densities, where nuclear effective field theories (EFTs) are valid, $n \lessapprox 2n_{\text{sat}}$, [171], up to the highest densities explored in the universe, $n \approx 8n_{\text{sat}}$. As explored in detail in part I, at densities $n \lessapprox 2n_{\text{sat}}$, advances in Chiral Effective Field Theory (χEFT) [309, 310] allow for an *ab-initio* description of nuclear matter consistent with the symmetries of the QCD Lagrangian. Furthermore, properties of matter at these densities can be studied in experiments with heavy atomic nuclei [11, 66, 311, 312, 313], allowing for the calibration of high-precision nuclear Energy Density Functionals (EDF) [305, 185, 64, 131, 95] that accurately reproduce such properties.

At larger densities, the situation changes drastically, as we saw in part II. In this regime, effective nuclear potentials based on χEFT are no longer expected to be applicable due to the breakdown of the EFT [171, 172]. Furthermore, the extrapolation of EDFs well beyond the density regime where they were fit comes with systematic uncertainties that cannot be quantified [258]. Therefore, at these densities, our understanding of dense neutron-rich matter comes mostly from the observation of neutron stars (NS) [314, 45, 44, 315, 316]. As discussed in chapter 1, recent multimessenger observations of NSs, i.e., radio [58, 60, 56, 59], X-ray [50, 51, 52, 49] and gravitational-wave (GW) observations [38, 39], have provided valuable new insights into the EoS of dense matter. Nevertheless, many open questions remain that might be elucidated by upcoming measurements [317].

To the picture of dense matter that emerges due to a combination of low-density theoretical constraints and observational data on NSs, an additional piece of information can be added. At asymptotically large densities, $n \equiv n_{\text{pQCD}} \approx 40n_{\text{sat}}$, the fundamental theory of quarks and gluons, QCD, becomes perturbative, allowing for an *ab-inito* calculation of the EoS of weakly interacting quark matter via a perturbative treatment of the QCD Lagrangian [318, 319]. Such perturbative QCD (pQCD) calculations have previously been incorporated in studies of matter at NS densities [320, 45, 272]. For example, Ref. [272] claimed to have found evidence for the presence of quark matter in NS cores by employing a general extension scheme in the speed of sound constrained by χEFT at low densities, perturbative QCD (pQCD) calculations at large densities, astrophysical observations of pulsars with masses around $2\text{M}_{\odot}$, and the GW observation GW170817. While intriguing, pQCD calculations are valid above $n_{\text{pQCD}} \approx 40n_{\text{sat}}$, whereas the inner cores of NSs are not expected to explore densities larger than $n_c^{\text{TOV}} \approx 8\, n_{\text{sat}}$.

Given the order of magnitude that separates these two density regimes, the importance of pQCD calculations in analyses of NS matter might be smaller than expected. Furthermore, the particularities of the interpolation between these vastly disconnected density regimes might introduce systematic uncertainties that overemphasize the impact of pQCD.

Komoltsev and Kurkela have recently suggested a new method to link both density regimes, allowing them to "integrate backwards", i.e., to propagate the pQCD constraints to lower densities in a completely general, analytical, and model-agnostic manner using only the thermodynamic potential and the conditions of causality and mechanical stability [321]. They concluded that, independently of NS observations, pQCD calculations exclude about 65% of the area in the pressure-energy density plane at $n = 5n_{\text{sat}}$. Given these findings, the question remains whether pQCD constraints affect the neutron-star EoS at a level comparable to constraints from astrophysical observations.

In this chapter, we quantify to which extent pQCD constraints add to our knowledge of the NS EoS and compare with information extracted from astrophysical constraints, to identify the unique impact of pQCD calculations. The rest of the chapter is organized as follows. In Sec. 9.1, we present our EoS model and discuss the imposition of astrophysical and pQCD constraints. We present our results for the EoS in Sec. 9.2. Implications for the masses and radii of NSs are discussed in this section as well. In Sec. 9.3, we discuss the potential implications of a future radius measurement of a $2\,\mathrm{M}_\odot$ NS that is more constraining than the NICER observation of PSR J0740+6620 [50, 52]. We provide a comparison of the results presented in this chapter with the recent work of Ref. [322] in Sec. 9.4 and we present our conclusions in Sec. 9.5.

9.1 Computational Setup

To reliably analyze the impact of the pQCD at asymptotically high densities and compare it to astrophysical and experimental constraints at lower densities, we rely here on the computational setup presented in Ref. [317]. This formalism is general enough to (i) capture our knowledge of the low-density EoS where nuclear physics constraints exist, (ii) fully explore the present uncertainties in observational NS data, and (iii) allow for the implementation of pQCD constraints minimizing the effects of uncontrolled interpolations over vastly separated density regions. For simplicity, the EoS up to n_{sat} is given by the Douchin-Haensel SLY model [213] based on the Skyrme SLy4 EDF [305] that is well calibrated to the properties of nuclear matter and finite nuclei and commonly used in astrophysical applications. Beyond n_{sat}, we describe the EoS using an extension in the speed of sound plane, the details of which are provided in chapter 8. For each EoS, we then calculate the NS mass-radius-tidal deformability relations and analyze astrophysical observations of NSs.

Regarding the astrophysical data, we consider:

- The tidal deformability $\tilde{\Lambda} = 222^{+420}_{-138}$ at 90% confidence level (CL) for GW170817 [306], which is consistent with other analyses [38, 39].
- The independent analyses of X-ray observations of pulsars J0740+6620 and J0030+0451 by the NICER telescope [50, 51, 52, 49] (by averaging over different results for the same source).
- Radio observations of heavy NSs imposing $\mathrm{M}_{\text{TOV}} \gtrsim 2\,\mathrm{M}_\odot$ [56, 58, 60].

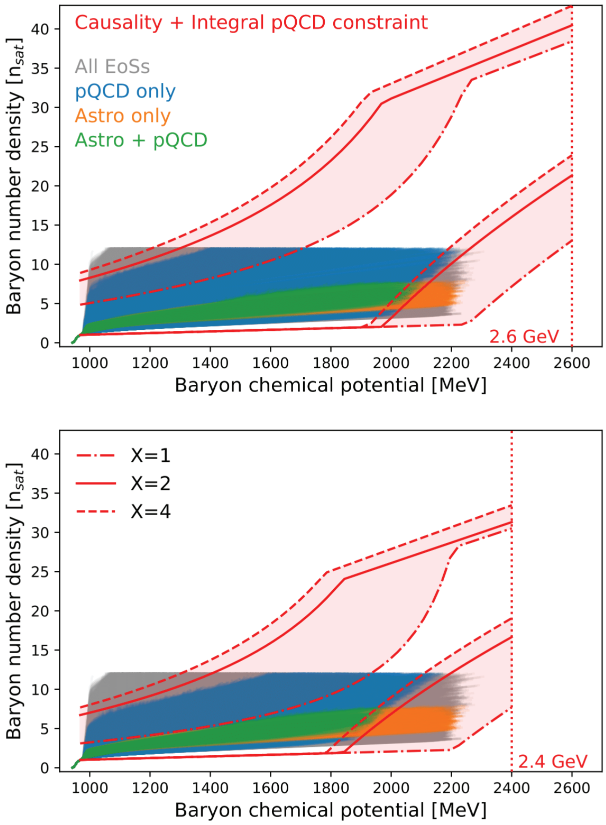

Figure 9.1: The baryon number density as function of the chemical potential. The red boundaries depict integrated constraints from pQCD with the red band showing the uncertainty (see text). The top (bottom) panel is constructed using the pQCD EoS down to $\mu_{\rm pQCD} = 2.6$ GeV ($\mu_{\rm pQCD} = 2.4$ GeV). We show all EoS in our set (gray), the EoS constrained by pQCD, at $X = 2$, only (blue), by astrophysical constraints only (orange), and by both astrophysical and pQCD constraints, at $X = 2$, (green). All EoSs are terminated at the TOV limit.

Note that, unlike in chapter 8, we do not include any upper limit on $\mathrm{M}_{\rm TOV}$ so as to not mask any effects of the pQCD constraints. The number density n as function of the chemical potential μ is shown for each EoS satisfying these observations in Fig. 9.1.

In order to implement pQCD constraints, we follow the approach of Ref. [321] by first imposing that $n_{\rm min}(\mu) < n(\mu) < n_{\rm max}(\mu)$ for $\mu \leq \mu_c^{\rm TOV}$, where $\mu_c^{\rm TOV}$ is the central chemical potential at the TOV limit and

$$n_{\rm max}(\mu) = \begin{cases} \frac{\mu^3 n_L - \mu\mu_L(\mu_L n_L + 2\Delta p)}{(\mu^2 + \mu_H^2)\mu_L} & \mu_L \leq \mu < \mu_c \\ n_H \mu/\mu_H & \mu_c \leq \mu \leq \mu_H \end{cases} \tag{9.1}$$

and

$$n_{\rm min}(\mu) = \begin{cases} n_L \mu/\mu_L & \mu_L \leq \mu \leq \mu_c \\ \frac{\mu^3 n_H - \mu\mu_H(\mu_H n_H - 2\Delta p)}{(\mu^2 - \mu_L^2)\mu_H} & \mu_c < \mu \leq \mu_H \end{cases} \tag{9.2}$$

where μ_L is the chemical potential of the low-density Skyrme EoS at $n_L = n_{\rm sat}$ and n_H, μ_H are the corresponding pQCD values evaluated at $\mu_H = \mu_{\rm pQCD}$. Also, $\Delta p = p_H - p_L$ and μ_c

is given by the intercept of the causal line and the integral constraint, see Ref. [321]. Note that the actual location of the TOV point, i.e. $(\mu_c^{\mathrm{TOV}}, n_c^{\mathrm{TOV}})$ changes from one EoS to another, as shown in Fig. 9.1. Beyond n_c^{TOV} the NS branch is unstable and not observable: n_c^{TOV} is therefore the natural density above which the connection to pQCD can be performed. However, we discuss the impact of changing the matching density to $10 n_{\mathrm{sat}}$ in Sec. 9.4. The contours defined by Eqs. (9.1)-(9.2) are shown in Fig. 9.1 in red. Note that the region encapsulated by the red contours represent a necessary but not sufficient condition to fulfill the pQCD constraint, since every EoS has to satisfy the additional criteria $p_{\mathrm{min}}(\mu, n) < p(\mu, n) < p_{\mathrm{max}}(\mu, n)$ where

$$p_{\mathrm{min}}(\mu, n) = p_L + \frac{\mu^2 - \mu_L^2}{2\mu} n_{\mathrm{min}}(\mu) \tag{9.3}$$

and

$$p_{\mathrm{max}}(\mu, n) = \begin{cases} p_L + \frac{\mu^2 - \mu_L^2}{2\mu} n & n < n_c(\mu) \\ p_H - \frac{\mu_H^2 - \mu^2}{2\mu} n & n > n_c(\mu) \end{cases} \tag{9.4}$$

where $n_c(\mu) = n_{\mathrm{max}}(\mu_L)\mu/\mu_L$. Note that the blue and green curves stop before the $X = 2$ contour, illustrating the impact of satisfying the sufficient conditions, Eqs. (9.1)-(9.4). In the top panel of Fig 9.1, we have considered $\mu_{\mathrm{pQCD}} = 2.6$ GeV as suggested in Ref. [319], and we explore the sensitivity of the results to this choice in the bottom panel for $\mu_{\mathrm{pQCD}} = 2.4$ GeV. At fixed μ_{pQCD}, the uncertainties in the pQCD EoS can be estimated by varying the renormalization scale parameter X as in Ref. [321]. In Fig. 9.1, we show results for $X = [1, 2, 4]$.

9.2 Results for the EoS and global NS properties

Several EoSs in our set are consistent with astrophysical NS observations but inconsistent with pQCD constraints for $X = 2$ and $X = 4$, see Fig. 9.1. These EoSs are too stiff below n_c^{TOV}, leading to a fast rise of the chemical potential with the number density. The chemical potential then becomes too large to be connected to the pQCD limit. This violation of the pQCD constraint is even more pronounced for $\mu_{\mathrm{pQCD}} = 2.4$ GeV, leading to an interesting interplay between the pQCD constraining power and astrophysical observations. Current astrophysical observations of NSs are consistent with stiffer EoSs at high densities to account for the existence of $2\,\mathrm{M}_{\odot}$ NSs [56] and their possibly large radii suggested by NICER [50, 52]. Hence, these data require a rapid increase of the pressure as function of the energy density ϵ, which in turn, implies large values for the speed of sound $c_s^2 = \partial p/\partial \epsilon$. Because the speed of sound can also be expressed as $c_s^2 = (n\partial\mu)/(\mu\partial n)$, this implies that the chemical potential rises rapidly with the number density. In Fig. 9.1, we see that for some EoSs, chemical potentials as large as $\mu \approx 2.2$ GeV can be reached in the center of maximally massive NSs, which is comparable to μ_{pQCD}. If the number density for this configuration is too low, the asymptotic pQCD limit cannot be reached in a thermodynamically consistent manner and, therefore, such EoSs are ruled out. This clarifies how pQCD impacts dense matter at NS densities even though pQCD itself is valid only at much larger densities: while NSs never explore densities close to n_{pQCD}, they might explore chemical potentials close to μ_{pQCD}. This is an interesting finding of our study.

While several EoSs in our set violate the pQCD constraint for $X = 2$ or $X = 4$, this is not the case anymore when allowing $X = 1$. In this case, all EoSs lie within the uncertainty band for the pQCD constraint, depicted by the red bands. Therefore, improvements for the precision

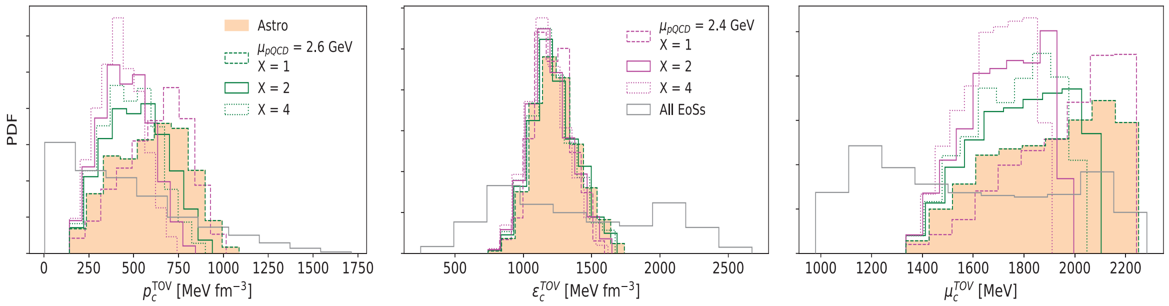

Figure 9.2: The PDFs for the central pressure (left), the central energy density (middle) and central chemical potential (right) in maximally massive NSs. The shaded orange PDF is obtained by imposing astrophysical constraints only, whereas the green and magenta PDFs impose pQCD constraints on top of the astrophysical constraints. Different linestyles correspond to different choices for the pQCD renormalization scale X.

of the pQCD calculations would have a great potential in increasing the pQCD constraining power.

As shown in Fig. 9.1, imposing constraints from pQCD can impact the EoS posterior. We have quantified in more details the effects of enforcing pQCD constraints on the EoS in Fig. 9.2 by examining the Probability Density Functions (PDF) for the central pressure, the central energy density, and the central chemical potential in maximally massive NSs. Note that the pQCD constraints are imposed "on top of" the astrophysical constraints. We see that the dashed lines corresponding to $X = 1$, with $\mu_{\rm pQCD} = 2.6$ GeV, coincide with the astro-only PDF, showing that pQCD has no impact in this case. For $p_c^{\rm TOV}$, pQCD constraints with $X = 2$ and $X = 4$ reduce the maximal pressure explored in NSs, with the effect being more pronounced for larger values of X and lower values of $\mu_{\rm pQCD}$. Interestingly the case $X = 1$ with $\mu_{\rm pQCD} = 2.4$ GeV clearly impacts the PDF for $p_c^{\rm TOV}$ and $\mu_c^{\rm TOV}$ by excluding certain soft EoS. The pQCD constraints play no role for $\epsilon_c^{\rm TOV}$.

In the left panel of Fig. 9.3, we show envelopes for the pressure as function of the energy density around all the EoSs allowed in a certain set. The bands are terminated at the TOV limit. For the cases $X = 2$ and $X = 4$, we find that incorporating pQCD constraints reduces the allowed region in the $p - \epsilon$ plane by lowering the maximum allowed pressures. Again, the pQCD constraints do not reduce the number of EoSs if $X = 1$ and $\mu_{\rm pQCD} = 2.6$ GeV. Note the impact of pQCD if $X = 1$ and $\mu_{\rm pQCD} = 2.4$ GeV as previously discussed.

Now, we analyze if pQCD impacts the global structure of NSs such as their masses and radii. In the middle and right panels of Fig. 9.3, we show the PDFs over the maximal NS mass $\rm M_{TOV}$ and the radius of the corresponding NS, $\rm R_{TOV}$. For $\rm M_{TOV}$, the effects of pQCD are most significant when the case $X = 1$ and $\mu_{\rm pQCD} = 2.4$ GeV is considered. For $X = 2$ and $X = 4$, we find that pQCD constraints slightly shift the distributions for $\rm M_{TOV}$ to lower values when added on top of astrophysical constraints but the corresponding PDF over $\rm R_{TOV}$ show no significant change. These results indicate that present pQCD calculations do not impact the masses and radii of observable NSs, but they are on the brink of becoming constraining.

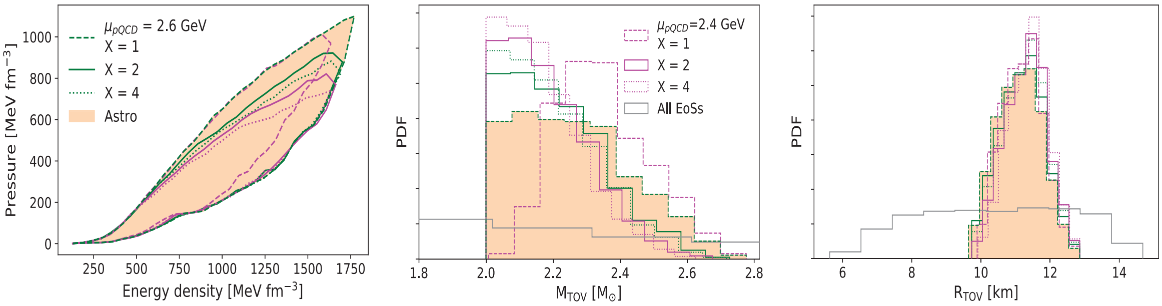

Figure 9.3: Left panel: pressure as a function of the energy density where the upper and lower edges of the contours represent the envelop over all the EoSs allowed in the corresponding set. PDFs over the maximum NS mass (middle panel) and its corresponding radius (right panel) are also shown.

9.3 A more constraining future measurement

Thus far, we have addressed the interplay of astrophysical observations, requiring a stiffening of the EoS, and pQCD calculations, requiring a softening of the EoS. Now, we investigate how an improved future measurement of the radius $R_{2.0}$ of a two solar mass NS would influence our findings. In the left panel of Fig. 9.4, we show constraints on the sound speed including observational NS data to date. Additionally imposing constraints from pQCD slightly lowers the average sound speed when larger values of X are considered, but we find a significant overlap of EoS ranges with or without pQCD constraint. In the right panel of Fig. 9.4, we now impose the additional constraint $R_{2.0} > 13$ km, which is a possible future scenario given the NICER measurement of PSR J0740+6620 [50, 52]. We find that in this case, adding pQCD constraints on top of astrophysical data shows a more significant impact, leading to the formation of a pronounced peak in the sound speed for $X = 2$ and $X = 4$: At low energy densities, the sound speed rises rapidly due to the imposed constraint $R_{2.0} > 13$ km; at $\epsilon \gtrsim 500\,\text{MeV fm}^{-3}$, the speed of sound plateaus if only astrophysical data are considered, while it decreases significantly if pQCD (at larger X values) is added. Such non-monotonous behaviour of the sound speed is expected to be indicative of the appearance of exotic, non-nucleonic degrees of freedom [317, 27, 323], such as quarkyonic matter as suggested in Ref. [288].

9.4 Comparison with analysis of Gorda et al.

The impact of pQCD calculations on the inference of the NS EoS has been studied recently in Ref. [322] in a Bayesian framework. The authors of Ref. [322] employ a Gaussian Process (GP) regression which is conditioned with an EoS computed in χEFT up to $1.1n_{\text{sat}}$. Using this GP, the EoS is extrapolated up to $10n_{\text{sat}}$ and this resulting EoS is used to analyse astrophysical observations of NSs. Finally, pQCD constraints are imposed similar to the work presented in this chapter, i.e. the methodology of Ref. [321] is used. However, in Ref. [322] the endpoint of the EoS at which the pQCD integrals are connected is fixed to be $10n_{\text{sat}}$ for all EoSs, whereas in this work the endpoint is taken to be n_c^{TOV} which is different for each EoS. Finally, the authors take pQCD uncertainties into account by integrating over X in the range 1 to 4.

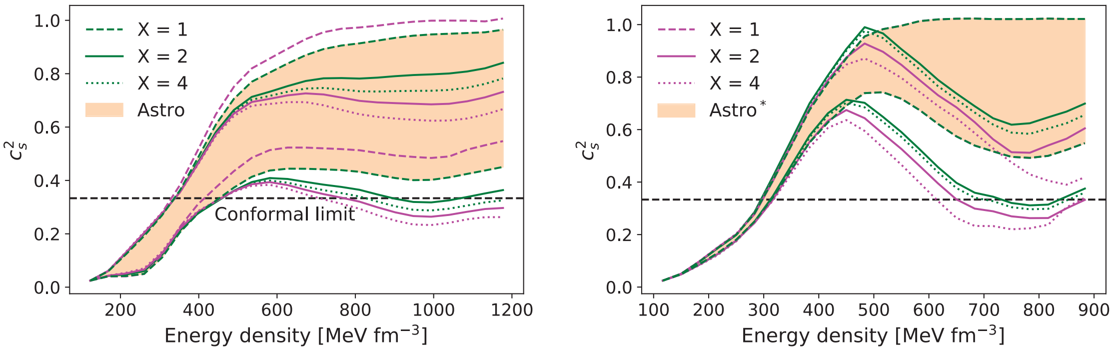

Figure 9.4: The speed of sound as function of the energy density. The upper and lower edges represent a 2σ uncertainty where σ is the sample standard deviation of our EoS ensemble. Left: Constraints on the speed of sound for NS observational data to date for a variation of the pQCD renormalization scale X. Right: Constraints on the speed of sound for NS observational data when additionally imposing $R_{2.0} > 13$ km (Astro*). Note that the $X = 1$ magenta dashed lines are not visible since they overlap with the $X = 1$ green case.

Using this setup, the authors of Ref. [322] claim that pQCD offers strong constraints in addition to the astrophysical observations. Furthermore, they state that the pQCD input reduces the pressure and speed of sound at high densities, and it predicts that binary collisions of equal-mass neutron stars will produce a black hole with greater than 95% credence for masses M $\geq 1.38\,\mathrm{M}_{\odot}$. These results are slightly in contradiction with this work given that we have found that pQCD does not rule out any EoS when imposed on top of astrophysical data, if the case $X = 1$ is considered. In this section, we investigate the differences between our approaches that could explain the tension between our results. The main differences between our methods are:

- We match to the pQCD constraint at n_c^{TOV} while Ref. [322] matches at $10n_{\mathrm{sat}}$,
- Ref. [322] uses Gaussian Processes (GPs) to generate EoS models while we use a speed-of-sound model,
- and Ref. [322] uses a probabilistic approach while we study envelopes.

Regarding point 3, when studying the impact of pQCD on the nuclear EoS it is most conservative to study envelopes as they account for all possible EoS behavior. Probabilistic treatments, on the other, could smear out the existence of phase transitions because these are more fine-tuned EoS models. Regarding the second point, while different EoS parametrizations might impact results in a probabilistic framework (see, e.g., Ref. [324]), EoS envelopes are less sensitive to this choice and the speed-of-sound parametrization can equally well capture extreme behavior compared to GPs. Furthermore, previous EoS inferences using similar astrophysical and EoS constraints agree well, independent of using GPs or a speed-of-sound parametrizations [325, 326]. Hence, we do not expect this choice to influence our results drastically.

We, therefore, expect that the difference between our results and those of Ref. [322] arise primarily due to point 1. To investigate this, we repeated our study using a matching density of $10n_{\mathrm{sat}}$; see Figs. 9.5 and 9.6. In Fig. 9.5, the result obtained using a matching density

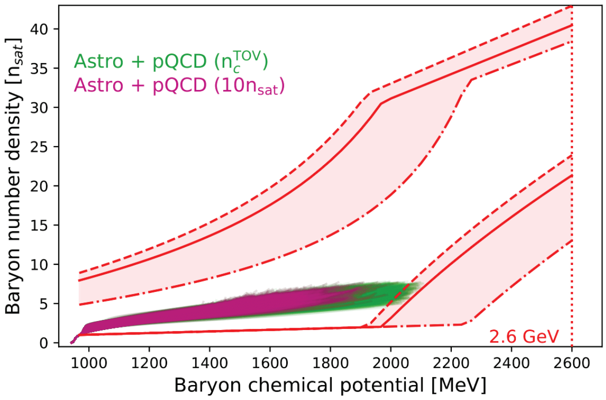

Figure 9.5: The baryon number density as function of the chemical potential, similar to the top panel of Fig. 9.1. Additionally, we show results for a matching density of $10n_{\rm sat}$ in purple. As before, each EoS is plotted up to the TOV limit.

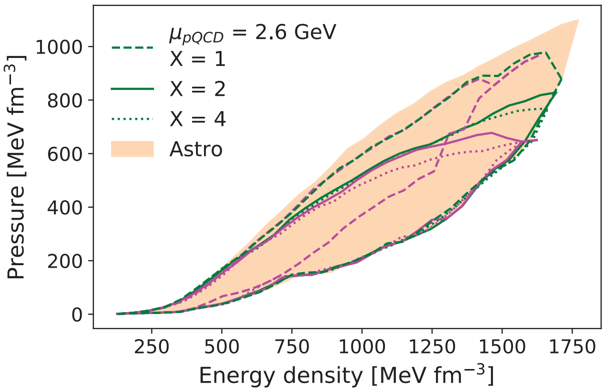

Figure 9.6: Pressure as a function of the energy density similar to the left panel of Fig. 9.3 but for a matching density of $10n_{\rm sat}$. As before, the upper and lower edges of the contours represent the envelop over all the EoS allowed in the corresponding set.

of $10n_{\rm sat}$ is compared with that obtained using $n_c^{\rm TOV}$, whereas in Fig. 9.6, we show results only for the $10n_{\rm sat}$ case. The EoSs that are very stiff inside NSs have a larger probability of remaining somewhat stiff beyond $n_c^{\rm TOV}$ than for the EoS to undergo a phase transition, leading to a likely violation of the pQCD limit if the matching is performed at larger densities. We find that changing this matching density to $10n_{\rm sat}$ leads to an exclusion of stiff EoS, in complete agreement with the findings of Ref. [322].

Because the density where pQCD integrals are connected plays an important role for making claims about the constraining power of pQCD, constraints from pQCD are very sensitive to model assumptions. This emphasizes our findings that pQCD is currently not constraining but might be so in future, when uncertainties are reduced such that simple model choices do not matter as much.

9.5 Conclusion

We have systematically studied the effects of incorporating pQCD calculations when analyzing the EoS of NSs. Using a model-independent approach to the EoS, we concluded that pQCD does not significantly constrain the EoS, if it is imposed on top of current observational constraints on NSs taking their uncertainties into account. However, the calculations are at the brink of being constraining for NSs: improved pQCD constraints or new astrophysical data preferring stiff EoSs will reveal the potential of pQCD for EoS selection. We found an interesting interplay of astrophysical observation and pQCD calculations: While certain astrophysical observations of NSs are consistent with stiff EoSs, supporting large NS masses and radii, such EoSs are disfavored upon imposing pQCD constraints.

These findings have important implications for the study of dense matter. In particular, while an analysis of future astrophysical data alone might be inconclusive with respect to the existence of exotic matter in neutron-star cores, the combined analysis of astrophysical and pQCD data might help answering this question. Therefore, future work on improving pQCD constraints is crucial for the studies of dense neutron-star matter.

Chapter 10

Summary and outlook

In this thesis, we systematically studied the nature of dense matter explored in neutron stars using a variety of theoretical and experimental tools. In this final chapter, we will briefly summarize the major results obtained in this thesis. We will also present an outlook for future research along the lines of this thesis.

Part I of this thesis was devoted to low-density matter, $n \lessapprox 2n_{\text{sat}}$. In chapter 3, we analyzed the properties of asymmetric nuclear matter based on six commonly used chiral EFT Hamiltonians with NN and 3N interactions. The global symmetry energy as well as its quadratic and quartic contributions have been determined with theoretical uncertainty estimates. The non-quadratic contribution to the symmetry energy was found to be $0.74^{+0.11}_{-0.08}$ MeV. Later, in chapter 4, we presented a unified description of the EoS of NSs. We employed the compressible liquid drop model to account for the finite size terms describing the nuclear clusters present in the NS crust. We used fifteen models for the nuclear interaction, including seven Skyrme and eight χEFT Hamiltonians. We found that there are two important factors which govern our predictions: i) the ability of the models to reproduce the nuclear experimental masses over the nuclear table, and ii) the low-density energy per particle in neutron matter. The work presented in part I can be improved by future analyses that explore a wider range of nuclear interactions and additional asymmetric-matter calculations using different many-body approaches and regularization schemes. This requires the development of improved chiral NN and 3N interactions up to $\mathrm{N^3LO}$, which will enable order-by-order analyses of the neutron-rich matter EoS.

In part II, we discussed different relativisitic approaches to dense nuclear matter. In particular, we have analysed the important role of chiral symmetry breaking and scalar nucleon response in the study of dense nuclear matter. We have done this, for the first time, by systematically comparing a model that takes these features into account (RMF-CC) versus models that neglect some or all of these aspects (RMF-C and RMF). The RMF-CC approach represents a step in the modeling of matter properties beyond saturation density since the model parameters are mainly given by fundamental properties, e.g., L-QCD predictions or quark model constraints, and only saturation density n_{sat} and energy E_{sat} have actually been used in the model calibration. Future work in this direction would involve the incorporation of correlations beyond the Hartree approximation such as the Fock terms as well as the pion loop correlation energy. Indeed, we have shown for instance that the Hartree approximation is not sufficient to reproduce the empirical values for E_{sym}. The inclusion of these correlation could therefore have important phenomenological consequences for the description of extreme matter.

Finally, part III was devoted to phase transitions in dense matter. Different kinds of phase transitions such as first-order phase transitions and a crossover to quarkyonic matter were introduced. Their features and predictions for NS masses and radii were enunciated and confronted against existing astrophysical observations. In chapter 8, we systematically investigated the possibility of inferring the existence of phase transitions from astrophysical data in a physics-agnostic manner. We concluded that the present data does not necessarily require the presence of a phase transition, but new astrophysical data has the potential to be decisive. Finally, in chapter 9, we systematically studied the effects of incorporating perturbative QCD calculations when analyzing the EoS of NSs. We concluded that pQCD does not significantly constrain the EoS, if it is imposed on top of current observational constraints on NSs and its uncertainties are accounted for. However, the calculations are at the brink of being constraining for NSs: improving the pQCD constraints or having new astrophysical data preferring large radii will reveal the potential of pQCD for EoS selection. With additional data expected from NICER and the LVC, future work along these lines promises to be extremely interesting.

Appendix A

Bayesian Fits using the meta-model

The details of the fitting procedure used in chapter 3 as well as other related technical details are given here. We also briefly describe the GitHub repository where the data and Python code used in this chapter 3 are hosted under the MIT license.

A.1 Details of the Fitting Procedure

In this chapter 3, we treat the calculations of Drischler *et al.* [94] as input data. Ref. [94] evaluated the energy per particle $E/A(n, \delta)$ at 11 isospin asymmetries ($\delta = 0.0, 0.1, \ldots, 1.0$) using MBPT up to second order. For each proton fraction, the energy per particle is sampled on an equidistant grid in the neutron Fermi momentum (not the density), and available up to $k_{\mathrm{F}} = 2\,\mathrm{fm}^{-1}$ leading to 385 points in total for each Hamiltonian. On the other hand, the single-particle energies were sampled on an equidistant grid in density from $0.01 - 0.21\,\mathrm{fm}^{-3}$ in SNM and PNM.

To obtain the parameter values, we perform a Bayesian analysis using the nonlinear least-square fitting package LSQFIT developed in Python [121]. LSQFIT uses SCIPY's least-squares minimization routine to optimize our model with respect to data y_i. The index i runs over all data sampling points (e.g., the density grid). The propagation of the Gaussian uncertainties from the model parameters, p_α, to the functions of those parameters, $f(\{p_\alpha\})$, requires calculating derivatives of those functions with respect to the parameters, which is achieved by automatic differentiation. In this work, the spread of the six Hamiltonians is interpreted as a fair representation of the width σ of a normal distribution that reflects theoretical uncertainties.

The fitting procedure requires the minimization of the objective function, hereafter noted the χ^2 function, which, in general, receives contributions from both the input data (χ^2_{data}) and the prior information on the model parameters (χ^2_{prior}). We can write these two contributions as

$$\chi^2_{\text{data}} = \sum_{ij} \Delta y(p)_i \, \mathrm{cov}^{-1}_{ij} \, \Delta y(p)_j \,, \tag{A.1}$$

$$\chi^2_{\text{prior}} = \sum_{\alpha} \frac{(p_\alpha - \mu_\alpha)^2}{\sigma^2_\alpha} \,, \tag{A.2}$$

with the total χ^2 being the sum of the two terms,

$$\chi^2 = \chi^2_{\text{data}} + \chi^2_{\text{prior}} \,. \tag{A.3}$$

In Eq. (A.1), $\Delta y(p)_i = f(\{p_\alpha\})_i - E(y_i)$, where the expectation value $E(y_i)$ is defined as

$$E(y_i) = \frac{1}{6}\sum_{\mu=1}^{6}(y_i)_\mu \,, \tag{A.4}$$

the summation index μ runs over the six nuclear Hamiltonians, and cov_{ij} is the co-variance matrix between the data points y_i and y_j, which is given by

$$\text{cov}_{ij} \equiv \text{cov}(y_i, y_j) = E(y_i y_j) - E(y_i)E(y_j) \,. \tag{A.5}$$

The correlation matrix corr_{ij} is then defined by its matrix elements,

$$\text{corr}_{ij} = \frac{\text{cov}_{ij}}{\sqrt{\text{cov}_{ii}\,\text{cov}_{jj}}} \,. \tag{A.6}$$

If the data are independent from each other, the co-variance and correlation matrices are diagonal and χ^2_{data} is associated with a normal distribution, as it is for χ^2_{prior}. Here, the data are not independent because of correlations in density: the knowledge of the predictions of the Hamiltonians at a few density points can be used to determine other points by interpolation or—to some extent—by extrapolation. We, thus, expect a non-diagonal co-variance matrix. While the Hamiltonians are by construction strongly correlated, we do not account for their correlations in the co-variance matrix. It only includes the correlations between the different data points, see Eq. (A.5).

In Eq. (A.2), μ_α is the prior mean value of the parameter p_α, and σ_α is its standard deviation. Note that, in this work, we only consider uncorrelated Gaussian prior distributions for our fit parameters.

The best-fit values of the parameters $\bar{p}_\alpha$ are those that minimize the total χ^2. The inverse co-variance matrix corresponding to the posterior distribution of the best-fit parameters is defined as,

$$(\text{cov}_p^{-1})_{\alpha\beta} = \frac{\partial\chi^2}{\partial p_\alpha \partial p_\beta}(\bar{p}) \,. \tag{A.7}$$

This expression is used by *lsqfit* to define the uncertainties in the fit parameters p_α.

A.2 Correlations in the data sample

The data analysis performed in this work involves parametric fits to data that are highly correlated across densities (or equivalently, Fermi momenta). It was found that this correlation had to be taken into account in order to achieve compatibility between the obtained posterior distributions and the data. In this appendix, we provide an estimate of this correlation.

As mentioned in the previous section, the correlation in the input data is captured by the co-varaince matrix (A.5). The strong positive correlation in the data points across densities results in large off-diagonal elements with respect to the diagonal ones. We analyse the strength of these off-diagonal elements as follow. We first diagonalize the correlation matrix (A.6) and obtain the eigenvalues and associated eigenvectors. In the case of maximum correlation all but one eigenvalue are 0. In our case, we found that the largest eigenvalue contributes to about 96% of the trace of the correlation matrix. Then, the eigenvector corresponding to this dominant eigenvalue captures the correlation (or mixing) between the data, which needs to be quantified. Let λ be this eigenvector with components $(\lambda_1, \ldots, \lambda_{N_D})$, where N_D is the number of data points. In the case of maximum correlation, the quantities $|\lambda_1|, \ldots, |\lambda_{N_D}|$ have zero dispersion about their average value, and in the case of minimum correlation, this dispersion takes a maximum value. We thus define the dispersion about the mean as

$$d^2 = \frac{1}{N_D} \sum_{i=1}^{N_D} (|\lambda_i| - \bar{\lambda})^2 \, , \tag{A.8}$$

where $\bar{\lambda}$ is the average value of the $|\lambda_i|$. In the case of a maximum correlation $d^2 = 0$, whereas in the case of minimum correlation $d^2 = \frac{1}{N_D}[1 - \frac{1}{N_D}]$.

We then define the level of correlation as

$$l_{\text{corr}} \equiv 1 - N_D \, d^2 \, , \tag{A.9}$$

where $l_{\text{corr}} = 1$ in the case of maximum correlation and, for zero correlation $l_{\text{corr}} = 1/N_D$, which approaches 0 in the limit of infinitely many data points. This parameter is similar to the correlation coefficient, ρ which one introduces in the case of identical off-diagonal elements in the covariance matrix.

The values of l_{corr} for the various fits presented in chapter 3 are as follows. In the fits to the effective masses presented in Fig. 2, for the linear fit, l_{corr} is 0.96 in SNM and 0.92 in PNM; for the quadratic fit, 0.54 in SNM and 0.54 in PNM. For the fits shown in Fig. 3, l_{corr} is $0.91, 0.53, 0.46$ in the scalings 1, 2 and 3, respectively, in SNM. Similarly in PNM, it is $0.92, 0.38, 0.39$. Finally, for the fits presented Fig. 5, $l_{\text{corr}} = 0.50$ for the analysis with the expansion around SNM and $l_{\text{corr}} = 0.58$ for the expansion around PNM. In all cases, we see that there is a significant correlation in the data. This is, as mentioned before, an important ingredient of our analysis, and is required for agreement between the obtained posterior distributions and the data.

A.3 Goodness of the fit and Q–Q plots

In this section we quantify the goodness of the fits using the Q–Q plot method. We consider the two illustrative fits in Fig. A.1: the fit of the Landau mass in SNM using a quadratic density functional (top panel in Fig. 2) and the energy per particle in PNM as a function of density (lower right panel in Fig. 3).

For the analysis of the Landau mass, we found $\chi^2/\text{dof} \approx 1.1$, and for the energy per particle, we find that $\chi^2/\text{dof} \approx 1.4$. These numbers are already indications for a successful fit.

We further investigate the goodness of the fit by examining the normalized residuals of the fit, which are defined as the differences between the data and the best fit model. These differences are expressed in the basis formed by the eigenvectors of the correlation matrix (A.6). Then, each component of the eigenvectors are divided by the square root of the corresponding

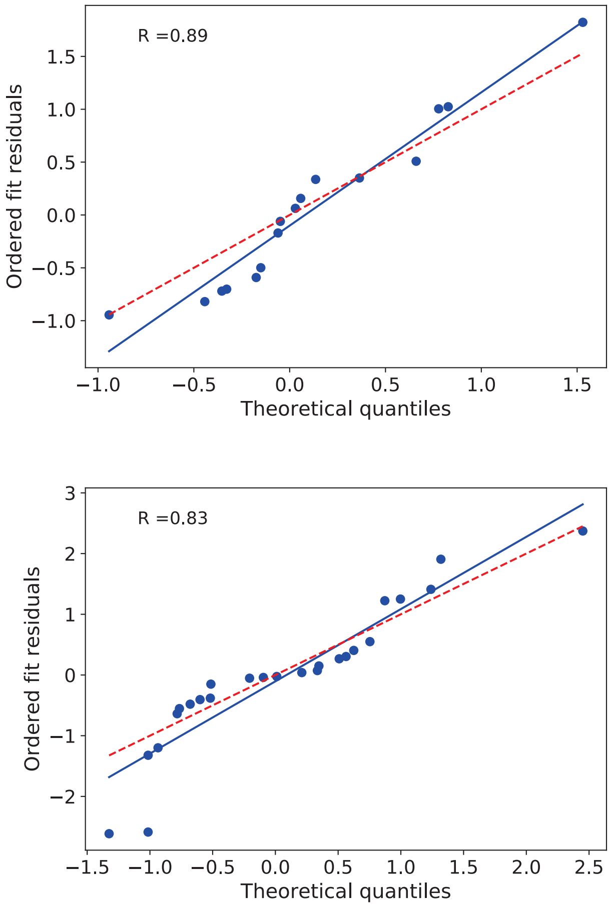

Figure A.1: Q–Q plot for the analysis of the Landau mass in SNM (top row) and energy per particle in PNM (bottom row). The reported R score, see Eq. (A.10), is a measure of how well the blue points lie on the dashed red line.

eigenvalue. The assumption of this analysis for a good fit is that the normalized residuals should be uncorrelated and randomly distributed around the mean value following a normal distribution.

Q–Q plots are a way for testing that the residuals follow a normal distribution. They are obtained as follow. First, the residuals are ordered from the smallest to the largest on the y-axis, then they are plotted against an ordered list of samples drawn from a normal distribution (centered at zero, with a width of one). If the residuals are perfectly normal distributed, then the result aligns on a straight line with slope 1. This alignment can be captured by the coefficient of determination, R defined as

$$R = 1 - \frac{\sum_{i=1}^{n}(r_i - \hat{r}_i)^2}{\sum_{i=1}^{n}(r_i - \bar{r})^2} \tag{A.10}$$

where n is the number of residuals, r_i are the residuals, $\hat{r}_i$ are the values expected for those residuals and $\bar{r} = \frac{1}{n}\sum_{i=1}^{n} r_i$. The best possible R score is 1 and it can be negative for arbitrarily worse fits.

The top panel of Fig. A.1 shows the Q–Q plot for our analysis of the Landau mass in SNM. The ideal straight line with unit slope is shown as the dashed-red line, while the ordered residuals are shown as blue circles. The blue solid line is a fit to the blue points. The R score, see Eq. (A.10), is 0.89, which leads us to the conclusion that the ordered fit residuals are consistent with a normal distribution with a mean one, so close to $\chi^2/\mathrm{dof} = 1$. We also give similar results for the analysis of the energy per particle in PNM in the bottom panel of Fig. A.1. Here, the coefficient of determination is 0.83, indicating a good fit.

A.4 Description of the GitHub repository

The repository [132] contains the Python codes used to perform the analysis as well as generate all the figures presented in chapter 3. This repository is publicly available on GitHub [132] and distributed under the MIT license.

The model parameters are obtained from a Bayesian analysis using the nonlinear least-square fitting *lsqfit* package developed in Python [121], which uses the SCIPY least-squares minimization routine to optimize our model with respect to data.

A.4.1 List of Folders

There are two main directories at the root of the repository: data and results.

- data: contains the predictions (that we treat as data) from each of the six Hamiltonians considered in this work. They are given as ASCII files.
    - data/Effective_mass: consists of the single particle energies for the six Hamiltonians in symmetric and neutron matter.
    - data/EOS_Drischler: contains the data files for the energy per particle for different values of iso-spin asymmetry.
- results: contains the figures as pdf files. The following sub-folders contain the various figures presented in Ref. [192] as follows,
    - results/3_scales: Figs. 1 and 3.
    - results/crust_core: Fig. 8.
    - results/effective_mass: Figs. 2, 9, 10 and 11.
    - results/esym_esym2: Figs. 4 and 5.
    - results/non_quadraticities: Figs. 6 and 7.
    - results/goodness: plots presented in the Supplemental Material.

A.4.2 List of Python codes

The Python codes are located in the main folder. They depend on the following Python libraries: scipy, numpy, matplotlib, gvar, lsqfit [121], sklearn.metrics.

- EM.py: performs the analysis of the single particle energies and produces the plots stored in the folder results/effective_mass.
- SM_NM.py: performs the analysis of the energy per particle in symmetric and neutron matter and produces the plots stored in the folder results/3_scales.
- symmetry_energy.py: calculates the global symmetry energy and creates the corresponding plot stored in the folder results/esym_esym2.
- quadratic_symmetry_energy.py: calculates the quadratic symmetry energy and creates the corresponding plot stored in the folder results/esym_esym2.
- non_quadraticities.py calculates the non-quadratic contributions to the symmetry energy as well as the final fit residuals and creates the plots stored in the folder results/non_quadraticities.
- crust_core.py calculates the crust-core transition and produces the plot in the folder results/crust_core.

A.4.3 Launch the Python script

The scripts are written in Python 3, and can be launched from a terminal as:

```
python3 ScriptName.py
```

where “ScriptName.py” is one of the scripts listed in Sec. A.4.2.

Appendix B

Speed of sound extension scheme

In this appendix, we provide the details of the extension scheme in the speed of sound that was used in chapters 8 and 9. We detail the construction of the EoS i.e. the sound speed, baryon chemical potential, energy density and pressure as functions of the number density.

Consider a discretized grid in the number density with elements n_i. Let c_i be the square of the sound speed at the density $n = n_i$. Note that, in this appendix, we shall use the symbol c for the speed of sound instead of c_s for the sake of clarity of the following equations. It should not be confused with the speed of light which is set to 1. Our task is to interpolate linearly between two consequent grid points i and $i + 1 \equiv j$. For $n_i < n < n_j$, the constant slope of the squared sound speed is

$$s_{ij} = \frac{c_j^2 - c_i^2}{n_j - n_i}. \tag{B.1}$$

The analytic expression $c^2(n)$ for the density dependent sound speed is then

$$c^2(n) = s_{ij}(n - n_i) + c_i^2. \tag{B.2}$$

The next step is to obtain an analytical expression for the chemical potential in the range $n_i < n < n_j$. For this, we use the relation

$$\frac{d\mu}{dn} = c^2 \frac{\mu}{n}. \tag{B.3}$$

Injecting Eq. (B.2) in Eq. (B.3), we obtain

$$\frac{d\mu}{\mu} = \big(s_{ij}(n - n_i) + c_i^2\big)\frac{dn}{n}. \tag{B.4}$$

Integrating from n_i to $n < n_j$,

$$\begin{aligned} \log\left(\frac{\mu(n)}{\mu_i}\right) &= s_{ij}\int_{n_i}^{n} \frac{n' - n_i}{n'} dn' + c_i^2 \int_{n_i}^{n} \frac{dn'}{n'} \\ &= s_{ij}\left(n - n_i - n_i \log\left(\frac{n}{n_i}\right)\right) + c_i^2 \log\left(\frac{n}{n_i}\right), \end{aligned} \tag{B.5}$$

where $\mu_i \equiv \mu(n_i)$. Therefore,

$$\mu(n) = \mu_i \exp\left\{ s_{ij}\left(n - n_i - n_i \log\left(\frac{n}{n_i}\right)\right) + c_i^2 \log\left(\frac{n}{n_i}\right)\right\}. \tag{B.6}$$

Finally, we require the energy density ϵ and pressure p as functions of the number density. The energy density is given by the integral

$$\epsilon(n) \quad = \quad \epsilon_i + \int_{n_i}^{n} \mu(n')dn', \tag{B.7}$$

where $\epsilon_i \equiv \epsilon(n_i)$. The pressure is

$$p(n) \quad = \quad p_i + \int_{n_i}^{n} c^2(n')\mu(n')dn', \tag{B.8}$$

with $p_i \equiv p(n_i)$.

The integrals in Eqs. (B.7) and (B.8) have to be computed numerically. The results presented in this appendix can be checked using Euler's relation

$$\frac{p(n) + \epsilon(n)}{\mu(n)} = n. \tag{B.9}$$

Bibliography

[1] L. McLerran. “The Phase Diagram of QCD and Some Issues of Large N(c)”. In: *Nucl. Phys. B Proc. Suppl.* 195 (2009). Ed. by C. Gattringer, L. Y. Glozman, and C. B. Lang, pp. 275–280. DOI: `10.1016/j.nuclphysbps.2009.10.020`. arXiv: `0906.2651 [hep-ph]`.

[2] D. J. Gross and Frank Wilczek. “Asymptotically Free Gauge Theories - I”. In: *Phys. Rev. D* 8 (1973), pp. 3633–3652. DOI: `10.1103/PhysRevD.8.3633`.

[3] D. J. Gross and Frank Wilczek. “Asymptotically Free Gauge Theories - 2”. In: *Phys. Rev. D* 9 (1974), pp. 980–993. DOI: `10.1103/PhysRevD.9.980`.

[4] David J. Gross and Frank Wilczek. “Ultraviolet Behavior of Nonabelian Gauge Theories”. In: *Phys. Rev. Lett.* 30 (1973). Ed. by J. C. Taylor, pp. 1343–1346. DOI: `10.1103/PhysRevLett.30.1343`.

[5] Szabocls Borsanyi, Zoltan Fodor, Christian Hoelbling, Sandor D. Katz, Stefan Krieg, and Kalman K. Szabo. “Full result for the QCD equation of state with 2+1 flavors”. In: *Phys. Lett. B* 730 (2014), pp. 99–104. DOI: `10.1016/j.physletb.2014.01.007`. arXiv: `1309.5258 [hep-lat]`.

[6] A. Bazavov et al. “Equation of state in (2+1)-flavor QCD”. In: *Phys. Rev. D* 90 (2014), p. 094503. DOI: `10.1103/PhysRevD.90.094503`. arXiv: `1407.6387 [hep-lat]`.

[7] Ulrich W. Heinz and Maurice Jacob. “Evidence for a new state of matter: An Assessment of the results from the CERN lead beam program”. In: (Jan. 2000). arXiv: `nucl-th/0002042`.

[8] Hiroaki Menjo et al. “Status and Prospects of the LHCf and RHICf experiments”. In: *PoS* ICRC2021 (2021), p. 301. DOI: `10.22323/1.395.0301`.

[9] Peter Senger. “Exploring terra incognita in the phase diagram of strongly interacting matter – Experiments at FAIR and NICA”. In: (Apr. 2022). arXiv: `2204.01056 [nucl-ex]`.

[10] J. P. Blaizot. “Nuclear Compressibilities”. In: *Phys. Rept.* 64 (1980), pp. 171–248. DOI: `10.1016/0370-1573(80)90001-0`.

[11] M.B. Tsang et al. “Constraints on the symmetry energy and neutron skins from experiments and theory”. In: *Phys. Rev. C* 86 (2012), p. 015803. DOI: `10.1103/PhysRevC.86.015803`. arXiv: `1204.0466 [nucl-ex]`.

[12] Francisco J. Yndurain. *The Theory of Quark and Gluon Interactions*. Theoretical and Mathematical Physics. Berlin, Germany: Springer, 2006. DOI: `10.1007/3-540-33210-3`.

[13] J.M. Lattimer and M. Prakash. "The physics of neutron stars". In: *Science* 304 (2004), pp. 536–542. arXiv: `astro-ph/0405262`.

[14] Mikhail A. Stephanov. "QCD phase diagram and the critical point". In: *Prog. Theor. Phys. Suppl.* 153 (2004). Ed. by Berndt Muller and C. I. Tan, pp. 139–156. DOI: `10.1142/S0217751X05027965`. arXiv: `hep-ph/0402115`.

[15] N. K. Glendenning. *Compact stars: Nuclear physics, particle physics, and general relativity*. 1997.

[16] Subrahmanyan Chandrasekhar. "The maximum mass of ideal white dwarfs". In: *Astrophys. J.* 74 (1931), pp. 81–82. DOI: `10.1086/143324`.

[17] Adam Burrows and James M. Lattimer. "The birth of neutron stars". In: *Astrophys. J.* 307 (1986), pp. 178–196. DOI: `10.1086/164405`.

[18] A. Burrows. "Supernova explosions in the universe". In: *Nature* 403 (2000), pp. 727–733. DOI: `10.1038/35001501`.

[19] K. Hirata et al. "Observation of a Neutrino Burst from the Supernova SN 1987a". In: *Phys. Rev. Lett.* 58 (1987). Ed. by K. C. Wali, pp. 1490–1493. DOI: `10.1103/PhysRevLett.58.1490`.

[20] R. M. Bionta et al. "Observation of a Neutrino Burst in Coincidence with Supernova SN 1987a in the Large Magellanic Cloud". In: *Phys. Rev. Lett.* 58 (1987), p. 1494. DOI: `10.1103/PhysRevLett.58.1494`.

[21] John M. Blondin, Anthony Mezzacappa, and Christine DeMarino. "Stability of standing accretion shocks, with an eye toward core collapse supernovae". In: *Astrophys. J.* 584 (2003), pp. 971–980. DOI: `10.1086/345812`. arXiv: `astro-ph/0210634`.

[22] John M. Blondin and Anthony Mezzacappa. "Pulsar spins from an instability in the accretion shock of supernovae". In: *Nature* 445 (2007), p. 58. DOI: `10.1038/nature05428`. arXiv: `astro-ph/0611680`.

[23] Hans-Thomas Janka, K. Langanke, A. Marek, G. Martinez-Pinedo, and B. Mueller. "Theory of Core-Collapse Supernovae". In: *Phys. Rept.* 442 (2007), pp. 38–74. DOI: `10.1016/j.physrep.2007.02.002`. arXiv: `astro-ph/0612072`.

[24] Hans-Thomas Janka. "Explosion Mechanisms of Core-Collapse Supernovae". In: *Ann. Rev. Nucl. Part. Sci.* 62 (2012), pp. 407–451. DOI: `10.1146/annurev-nucl-102711-094901`. arXiv: `1206.2503 [astro-ph.SR]`.

[25] Richard C. Tolman. "Static Solutions of Einstein's Field Equations for Spheres of Fluid". In: *Phys. Rev.* 55 (4 1939), pp. 364–373. DOI: `10.1103/PhysRev.55.364`. URL: `https://link.aps.org/doi/10.1103/PhysRev.55.364`.

[26] J. R. Oppenheimer and G. M. Volkoff. "On Massive Neutron Cores". In: *Phys. Rev.* 55 (4 1939), pp. 374–381. DOI: `10.1103/PhysRev.55.374`. URL: `https://link.aps.org/doi/10.1103/PhysRev.55.374`.

[27] Hung Tan, Jacquelyn Noronha-Hostler, and Nico Yunes. “Neutron Star Equation of State in light of GW190814”. In: *Phys. Rev. Lett.* 125.26 (2020), p. 261104. DOI: `10.1103/PhysRevLett.125.261104`. arXiv: `2006.16296 [astro-ph.HE]`.

[28] P. Haensel, A. Y. Potekhin, and D. G. Yakovlev. *Neutron stars 1: Equation of state and structure*. Vol. 326. New York, USA: Springer, 2007.

[29] Andrew W. Steiner. In: *Phys. Rev. C* 77 (3 2008), p. 035805. DOI: `10.1103/PhysRevC.77.035805`.

[30] Jurgen Schaffner and Igor N. Mishustin. “Hyperon rich matter in neutron stars”. In: *Phys. Rev. C* 53 (1996), pp. 1416–1429. DOI: `10.1103/PhysRevC.53.1416`. arXiv: `nucl-th/9506011`.

[31] Norman K. Glendenning and Jeurgen Schaffner-Bielich. “Kaon condensation and dynamical nucleons in neutron stars”. In: *Phys. Rev. Lett.* 81 (1998), pp. 4564–4567. DOI: `10.1103/PhysRevLett.81.4564`. arXiv: `astro-ph/9810284`.

[32] Norman K. Glendenning and Jurgen Schaffner-Bielich. “First order kaon condensate”. In: *Phys. Rev. C* 60 (1999), p. 025803. DOI: `10.1103/PhysRevC.60.025803`. arXiv: `astro-ph/9810290`.

[33] Mark Alford, David Blaschke, Alessandro Drago, Thomas Klahn, Giuseppe Pagliara, and Juergen Schaffner-Bielich. “Quark matter in compact stars?” In: *Nature* 445 (2007), E7–E8. DOI: `10.1038/nature05582`. arXiv: `astro-ph/0606524`.

[34] R. A. Hulse and J. H. Taylor. “Discovery of a pulsar in a binary system”. In: *Astrophys. J. Lett.* 195 (1975), pp. L51–L53. DOI: `10.1086/181708`.

[35] J. H. Taylor and J. M. Weisberg. “A new test of general relativity - Gravitational radiation and the binary pulsar PSR 1913+16”. In: *Astrophys. J. Lett.* 253 (Feb. 1982), pp. 908–920. DOI: `10.1086/159690`.

[36] R N Manchester, G B Hobbs, A Teoh, and M Hobbs. “The Australia Telescope National Facility pulsar catalogue”. In: *Astron. J.* 129 (2005), p. 1993. DOI: `10.1086/428488`. arXiv: `astro-ph/0412641`.

[37] B. P. Abbott et al. “Prospects for observing and localizing gravitational-wave transients with Advanced LIGO, Advanced Virgo and KAGRA”. In: *Living Rev. Rel.* 21.1 (2018), p. 3. DOI: `10.1007/s41114-020-00026-9`. arXiv: `1304.0670 [gr-qc]`.

[38] B. P. Abbott et al. “GW170817: Observation of Gravitational Waves from a Binary Neutron Star Inspiral”. In: *Phys. Rev. Lett.* 119.16 (2017), p. 161101. DOI: `10.1103/PhysRevLett.119.161101`. arXiv: `1710.05832 [gr-qc]`.

[39] B. P. Abbott et al. “GW170817: Measurements of neutron star radii and equation of state”. In: *Phys. Rev. Lett.* 121.16 (2018), p. 161101. DOI: `10.1103/PhysRevLett.121.161101`. arXiv: `1805.11581 [gr-qc]`.

[40] B. P. Abbott et al. “Multi-messenger Observations of a Binary Neutron Star Merger”. In: *Astrophys. J. Lett.* 848.2 (2017), p. L12. DOI: `10.3847/2041-8213/aa91c9`. arXiv: `1710.05833 [astro-ph.HE]`.

[41] Katerina Chatziioannou. “Neutron star tidal deformability and equation of state constraints”. In: *Gen. Rel. Grav.* 52.11 (2020), p. 109. DOI: `10.1007/s10714-020-02754-3`. arXiv: `2006.03168 [gr-qc]`.

[42] Tanja Hinderer. "Tidal Love Numbers of Neutron Stars". In: *The Astrophysical Journal* 677.2 (2008), pp. 1216–1220. DOI: `10.1086/533487`. URL: `https://doi.org/10.1086/533487`.

[43] Éanna É. Flanagan and Tanja Hinderer. "Constraining neutron-star tidal Love numbers with gravitational-wave detectors". In: *Phys. Rev. D* 77 (2 2008), p. 021502. DOI: `10.1103/PhysRevD.77.021502`. URL: `https://link.aps.org/doi/10.1103/PhysRevD.77.021502`.

[44] Collin D. Capano, Ingo Tews, Stephanie M. Brown, Ben Margalit, Soumi De, Sumit Kumar, Duncan A. Brown, Badri Krishnan, and Sanjay Reddy. "Stringent constraints on neutron-star radii from multimessenger observations and nuclear theory". In: *Nature Astron.* 4.6 (2020), pp. 625–632. DOI: `10.1038/s41550-020-1014-6`. arXiv: `1908.10352 [astro-ph.HE]`.

[45] Eemeli Annala, Tyler Gorda, Aleksi Kurkela, and Aleksi Vuorinen. "Gravitational-wave constraints on the neutron-star-matter Equation of State". In: *Phys. Rev. Lett.* 120.17 (2018), p. 172703. DOI: `10.1103/PhysRevLett.120.172703`. arXiv: `1711.02644 [astro-ph.HE]`.

[46] I. Tews, J. Margueron, and S. Reddy. "Critical examination of constraints on the equation of state of dense matter obtained from GW170817". In: *Phys. Rev. C* 98.4 (2018), p. 045804. DOI: `10.1103/PhysRevC.98.045804`. arXiv: `1804.02783 [nucl-th]`.

[47] Luciano Rezzolla, Elias R. Most, and Lukas R. Weih. "Using gravitational-wave observations and quasi-universal relations to constrain the maximum mass of neutron stars". In: *Astrophys. J. Lett.* 852.2 (2018), p. L25. DOI: `10.3847/2041-8213/aaa401`. arXiv: `1711.00314 [astro-ph.HE]`.

[48] Masaru Shibata, Enping Zhou, Kenta Kiuchi, and Sho Fujibayashi. "Constraint on the maximum mass of neutron stars using GW170817 event". In: *Phys. Rev. D* 100.2 (2019), p. 023015. DOI: `10.1103/PhysRevD.100.023015`. arXiv: `1905.03656 [astro-ph.HE]`.

[49] M. C. Miller et al. "PSR J0030+0451 Mass and Radius from $NICER$ Data and Implications for the Properties of Neutron Star Matter". In: *Astrophys. J. Lett.* 887.1 (2019), p. L24. DOI: `10.3847/2041-8213/ab50c5`. arXiv: `1912.05705 [astro-ph.HE]`.

[50] M. C. Miller et al. "The Radius of PSR J0740+6620 from NICER and XMM-Newton Data". In: *Astrophys. J. Lett.* 918.2 (2021), p. L28. DOI: `10.3847/2041-8213/ac089b`. arXiv: `2105.06979 [astro-ph.HE]`.

[51] Thomas E. Riley et al. "A $NICER$ View of PSR J0030+0451: Millisecond Pulsar Parameter Estimation". In: *Astrophys. J. Lett.* 887.1 (2019), p. L21. DOI: `10.3847/2041-8213/ab481c`. arXiv: `1912.05702 [astro-ph.HE]`.

[52] Thomas E. Riley et al. "A NICER View of the Massive Pulsar PSR J0740+6620 Informed by Radio Timing and XMM-Newton Spectroscopy". In: *Astrophys. J. Lett.* 918.2 (2021), p. L27. DOI: `10.3847/2041-8213/ac0a81`. arXiv: `2105.06980 [astro-ph.HE]`.

[53] Slavko Bogdanov et al. “Constraining the Neutron Star Mass–Radius Relation and Dense Matter Equation of State with $NICER$. II. Emission from Hot Spots on a Rapidly Rotating Neutron Star”. In: *Astrophys. J. Lett.* 887.1 (2019), p. L26. DOI: `10.3847/2041-8213/ab5968`. arXiv: `1912.05707 [astro-ph.HE]`.

[54] Slavko Bogdanov et al. “Constraining the Neutron Star Mass-Radius Relation and Dense Matter Equation of State with NICER. III. Model Description and Verification of Parameter Estimation Codes”. In: *Astrophys. J. Lett.* 914.1 (2021), p. L15. DOI: `10.3847/2041-8213/abfb79`. arXiv: `2104.06928 [astro-ph.HE]`.

[55] Hung Tan, Travis Dore, Veronica Dexheimer, Jacquelyn Noronha-Hostler, and Nicolás Yunes. “Extreme matter meets extreme gravity: Ultraheavy neutron stars with phase transitions”. In: *Phys. Rev. D* 105.2 (2022), p. 023018. DOI: `10.1103/PhysRevD.105.023018`. arXiv: `2106.03890 [astro-ph.HE]`.

[56] H. T. Cromartie, E. Fonseca, S. M. Ransom, P. B. Demorest, Z. Arzoumanian, H. Blumer, P. R. Brook, M. E. DeCesar, T. Dolch, J. A. Ellis, R. D. Ferdman, E. C. Ferrara, N. Garver-Daniels, P. A. Gentile, M. L. Jones, M. T. Lam, D. R. Lorimer, R. S. Lynch, M. A. McLaughlin, C. Ng, D. J. Nice, T. T. Pennucci, R. Spiewak, I. H. Stairs, K. Stovall, J. K. Swiggum, and W. W. Zhu. In: *Nature Astronomy* 4 (Jan. 2020), pp. 72–76. DOI: `10.1038/s41550-019-0880-2`. arXiv: `1904.06759 [astro-ph.HE]`.

[57] E. Fonseca et al. “Refined Mass and Geometric Measurements of the High-mass PSR J0740+6620”. In: *Astrophys. J. Lett.* 915.1 (2021), p. L12. DOI: `10.3847/2041-8213/ac03b8`. arXiv: `2104.00880 [astro-ph.HE]`.

[58] Paul Demorest, Tim Pennucci, Scott Ransom, Mallory Roberts, and Jason Hessels. “Shapiro Delay Measurement of A Two Solar Mass Neutron Star”. In: *Nature* 467 (2010), pp. 1081–1083. DOI: `10.1038/nature09466`. arXiv: `1010.5788 [astro-ph.HE]`

[59] Emmanuel Fonseca et al. “The NANOGrav Nine-year Data Set: Mass and Geometric Measurements of Binary Millisecond Pulsars”. In: *Astrophys. J.* 832.2 (2016), p. 167. DOI: `10.3847/0004-637X/832/2/167`. arXiv: `1603.00545 [astro-ph.HE]`.

[60] John Antoniadis et al. “A Massive Pulsar in a Compact Relativistic Binary”. In: *Science* 340 (2013), p. 6131. DOI: `10.1126/science.1233232`. arXiv: `1304.6875 [astro-ph.HE]`.

[61] Manuel Linares, Tariq Shahbaz, and Jorge Casares. “Peering into the dark side: Magnesium lines establish a massive neutron star in PSR J2215+5135”. In: *Astrophys. J.* 859.1 (2018), p. 54. DOI: `10.3847/1538-4357/aabde6`. arXiv: `1805.08799 [astro-ph.HE]`.

[62] James M. Lattimer. “The nuclear equation of state and neutron star masses”. In: *Ann. Rev. Nucl. Part. Sci.* 62 (2012), pp. 485–515. DOI: `10.1146/annurev-nucl-102711-095018`. arXiv: `1305.3510 [nucl-th]`.

[63] James M. Lattimer and Andrew W. Steiner. “Constraints on the symmetry energy using the mass-radius relation of neutron stars”. In: *Eur. Phys. J. A* 50 (2014), p. 40. DOI: `10.1140/epja/i2014-14040-y`. arXiv: `1403.1186 [nucl-th]`.

[64] Jérôme Margueron, Rudiney Hoffmann Casali, and Francesca Gulminelli. “Equation of state for dense nucleonic matter from metamodeling. I. Foundational aspects”. In: *Phys. Rev. C* 97.2 (2018), p. 025805. DOI: `10.1103/PhysRevC.97.025805`. arXiv: `1708.06894 [nucl-th]`.

[65] C. Drischler, R. J. Furnstahl, J. A. Melendez, and D. R. Phillips. “How Well Do We Know the Neutron-Matter Equation of State at the Densities Inside Neutron Stars? A Bayesian Approach with Correlated Uncertainties”. In: *Phys. Rev. Lett.* 125.20 (2020), p. 202702. DOI: `10.1103/PhysRevLett.125.202702`. arXiv: `2004.07232`.

[66] Brendan T. Reed, F. J. Fattoyev, C. J. Horowitz, and J. Piekarewicz. “Implications of PREX-2 on the Equation of State of Neutron-Rich Matter”. In: *Phys. Rev. Lett.* 126.17 (2021), p. 172503. DOI: `10.1103/PhysRevLett.126.172503`. arXiv: `2101.03193 [nucl-th]`.

[67] H. A. Bethe and R. F. Bacher. “Nuclear Physics A. Stationary States of Nuclei”. In: *Rev. Mod. Phys.* 8 (1936), pp. 82–229. DOI: `10.1103/RevModPhys.8.82`.

[68] C. F. V. Weizsacker. “Zur Theorie der Kernmassen”. In: *Z. Phys.* 96 (1935), pp. 431–458. DOI: `10.1007/BF01337700`.

[69] Peter Möller, William D. Myers, Hiroyuki Sagawa, and Satoshi Yoshida. “New Finite-Range Droplet Mass Model and Equation-of-State Parameters”. In: *Phys. Rev. Lett.* 108.5 (2012), p. 052501. DOI: `10.1103/PhysRevLett.108.052501`.

[70] Pawel Danielewicz and Jenny Lee. “Symmetry Energy I: Semi-Infinite Matter”. In: *Nucl. Phys. A* 818 (2009), pp. 36–96. DOI: `10.1016/j.nuclphysa.2008.11.007`. arXiv: `0807.3743 [nucl-th]`.

[71] Pawel Danielewicz, Pardeep Singh, and Jenny Lee. “Symmetry Energy III: Isovector Skins”. In: *Nucl. Phys. A* 958 (2017), pp. 147–186. DOI: `10.1016/j.nuclphysa.2016.11.008`. arXiv: `1611.01871 [nucl-th]`.

[72] G. Fricke, C. Bernhardt, K. Heilig, L. A. Schaller, L. Schellenberg, E. B. Shera, and C. W. de Jager. “Nuclear Ground State Charge Radii from Electromagnetic Interactions”. In: *Atom. Data Nucl. Data Tabl.* 60 (1995), pp. 177–285. DOI: `10.1006/adnd.1995.1007`.

[73] C. J. Horowitz. “Parity violating elastic electron scattering and Coulomb distortions”. In: *Phys. Rev. C* 57 (1998), pp. 3430–3436. DOI: `10.1103/PhysRevC.57.3430`. arXiv: `nucl-th/9801011`.

[74] S. Abrahamyan et al. “Measurement of the Neutron Radius of 208Pb Through Parity-Violation in Electron Scattering”. In: *Phys. Rev. Lett.* 108 (2012), p. 112502. DOI: `10.1103/PhysRevLett.108.112502`. arXiv: `1201.2568 [nucl-ex]`.

[75] D. Adhikari et al. “Accurate Determination of the Neutron Skin Thickness of ^{208}Pb through Parity-Violation in Electron Scattering”. In: *Phys. Rev. Lett.* 126.17 (2021), p. 172502. DOI: `10.1103/PhysRevLett.126.172502`. arXiv: `2102.10767 [nucl-ex]`.

[76] J. Piekarewicz. “Implications of PREX-2 on the electric dipole polarizability of neutron-rich nuclei”. In: *Phys. Rev. C* 104.2 (2021), p. 024329. DOI: `10.1103/PhysRevC.104.024329`. arXiv: `2105.13452 [nucl-th]`.

[77] Andrew W. Steiner, Madappa Prakash, James M. Lattimer, and Paul J. Ellis. “Isospin asymmetry in nuclei and neutron stars”. In: *Phys. Rept.* 411 (2005), pp. 325–375. DOI: 10.1016/j.physrep.2005.02.004. arXiv: nucl-th/0410066.

[78] M. Baldo and G.F. Burgio. “The nuclear symmetry energy”. In: *Prog. Part. Nucl. Phys.* 91 (2016), pp. 203–258. DOI: 10.1016/j.ppnp.2016.06.006. arXiv: 1606.08838 [nucl-th].

[79] M. Oertel, M. Hempel, T. Klähn, and S. Typel. “Equations of state for supernovae and compact stars”. In: *Rev. Mod. Phys.* 89 (1 Mar. 2017), p. 015007. DOI: 10.1103/RevModPhys.89.015007. URL: https://link.aps.org/doi/10.1103/RevModPhys.89.015007.

[80] G. Fiorella Burgio and Anthea F. Fantina. “Nuclear Equation of State for Compact Stars and Supernovae”. In: *The Physics and Astrophysics of Neutron Stars*. Ed. by Luciano Rezzolla, Pierre Pizzochero, David Ian Jones, Nanda Rea, and Isaac Vidaña. Cham: Springer International Publishing, 2018, pp. 255–335. ISBN: 978-3-319-97616-7. DOI: 10.1007/978-3-319-97616-7_6. URL: https://doi.org/10.1007/978-3-319-97616-7_6.

[81] K. Hebeler, J. D. Holt, J. Menendez, and A. Schwenk. “Nuclear forces and their impact on neutron-rich nuclei and neutron-rich matter”. In: *Ann. Rev. Nucl. Part. Sci.* 65 (2015), pp. 457–484. DOI: 10.1146/annurev-nucl-102313-025446. arXiv: 1508.06893 [nucl-th].

[82] K. Hebeler, J.M. Lattimer, C.J. Pethick, and A. Schwenk. “Constraints on neutron star radii based on chiral effective field theory interactions”. In: *Phys. Rev. Lett.* 105 (2010), p. 161102. DOI: 10.1103/PhysRevLett.105.161102. arXiv: 1007.1746 [nucl-th].

[83] S. Gandolfi, J. Carlson, and Sanjay Reddy. “The maximum mass and radius of neutron stars and the nuclear symmetry energy”. In: *Phys. Rev. C* 85 (2012), p. 032801. DOI: 10.1103/PhysRevC.85.032801. arXiv: 1101.1921 [nucl-th].

[84] A.W. Steiner and S. Gandolfi. “Connecting Neutron Star Observations to Three-Body Forces in Neutron Matter and to the Nuclear Symmetry Energy”. In: *Phys. Rev. Lett.* 108 (2012), p. 081102. DOI: 10.1103/PhysRevLett.108.081102. arXiv: 1110.4142 [nucl-th].

[85] C.J. Horowitz, E.F. Brown, Y. Kim, W.G. Lynch, R. Michaels, A. Ono, J. Piekarewicz, M.B. Tsang, and H.H. Wolter. “A way forward in the study of the symmetry energy: experiment, theory, and observation”. In: *J. Phys. G* 41 (2014), p. 093001. DOI: 10.1088/0954-3899/41/9/093001. arXiv: 1401.5839 [nucl-th].

[86] Nuclear Science Advisory Committee (NSAC). *2015 Long Range Plan for Nuclear Science*. 2015. URL: https://www.aps.org/units/dnp/resources/nuclear.cfm.

[87] C. J. Horowitz, K. S. Kumar, and R. Michaels. “Electroweak Measurements of Neutron Densities in CREX and PREX at JLab, USA”. In: *Eur. Phys. J. A* 50 (2014), p. 48. DOI: 10.1140/epja/i2014-14048-3. eprint: 1307.3572.

[88] X. Roca-Maza, M. Brenna, B.K. Agrawal, P.F. Bortignon, G. Colò, Li-Gang Cao, N. Paar, and D. Vretenar. “Giant Quadrupole Resonances in 208Pb, the nuclear symmetry energy and the neutron skin thickness”. In: *Phys. Rev. C* 87.3 (2013), p. 034301. DOI: `10.1103/PhysRevC.87.034301`. arXiv: `1212.4377 [nucl-th]`.

[89] Andrew W. Steiner. “The High-density symmetry energy and direct Urca”. In: *Phys. Rev. C* 74 (2006), p. 045808. DOI: `10.1103/PhysRevC.74.045808`. arXiv: `nucl-th/0607040`.

[90] Lie-Wen Chen, Bao-Jun Cai, Che Ming Ko, Bao-An Li, Chun Shen, and Jun Xu. “High-order effects on the incompressibility of isospin asymmetric nuclear matter”. In: *Phys. Rev. C* 80 (2009), p. 014322. DOI: `10.1103/PhysRevC.80.014322`. arXiv: `0905.4323 [nucl-th]`.

[91] Bao-Jun Cai and Lie-Wen Chen. “Nuclear matter fourth-order symmetry energy in the relativistic mean field models”. In: *Phys. Rev. C* 85 (2012), p. 024302. DOI: `10.1103/PhysRevC.85.024302`. arXiv: `1111.4124 [nucl-th]`.

[92] Bao-Jun Cai and Bao-An Li. “The isospin quartic term in the kinetic energy of neutron-rich nucleonic matter”. In: *Phys. Rev. C* 92.1 (2015), p. 011601. DOI: `10.1103/PhysRevC.92.011601`. arXiv: `1503.01167 [nucl-th]`.

[93] W.M. Seif and D.N. Basu. “Higher-order symmetry energy of nuclear matter and the inner edge of neutron star crusts”. In: *Phys. Rev. C* 89.2 (2014), p. 028801. DOI: `10.1103/PhysRevC.89.028801`. arXiv: `1401.0090 [nucl-th]`.

[94] Christian Drischler, Kai Hebeler, and Achim Schwenk. “Asymmetric nuclear matter based on chiral two- and three-nucleon interactions”. In: *Phys. Rev. C* 93.5 (2016), p. 054314. DOI: `10.1103/PhysRevC.93.054314`. arXiv: `1510.06728 [nucl-th]`.

[95] Michael Bender, Paul-Henri Heenen, and Paul-Gerhard Reinhard. “Self-consistent mean-field models for nuclear structure”. In: *Rev. Mod. Phys.* 75 (1 Jan. 2003), pp. 121–180. DOI: `10.1103/RevModPhys.75.121`. URL: `https://link.aps.org/doi/10.1103/RevModPhys.75.121`.

[96] G. Wlazłowski, J.W. Holt, S. Moroz, A. Bulgac, and K.J. Roche. “Auxiliary-Field Quantum Monte Carlo Simulations of Neutron Matter in Chiral Effective Field Theory”. In: *Phys. Rev. Lett.* 113.18 (2014), p. 182503. DOI: `10.1103/PhysRevLett.113.182503`. arXiv: `1403.3753 [nucl-th]`.

[97] I. Bombaci and U. Lombardo. “Asymmetric nuclear matter equation of state”. In: *Phys. Rev. C* 44 (1991), pp. 1892–1900. DOI: `10.1103/PhysRevC.44.1892`.

[98] C.-H. Lee, T.T.S. Kuo, G.Q. Li, and G.E. Brown. “Nuclear symmetry energy”. In: *Phys. Rev. C* 57 (1998), pp. 3488–3491. DOI: `10.1103/PhysRevC.57.3488`.

[99] T. Frick, H. Muther, A. Rios, A. Polls, and A. Ramos. “Correlations in hot asymmetric nuclear matter”. In: *Phys. Rev. C* 71 (2005), p. 014313. DOI: `10.1103/PhysRevC.71.014313`. arXiv: `nucl-th/0409067`.

[100] Isaac Vidana, Constanca Providencia, Artur Polls, and Arnau Rios. “Density dependence of the nuclear symmetry energy: A Microscopic perspective”. In: *Phys. Rev. C* 80 (2009), p. 045806. DOI: `10.1103/PhysRevC.80.045806`. arXiv: `0907.1165 [nucl-th]`.

[101] N. Kaiser. “Quartic isospin asymmetry energy of nuclear matter from chiral pion-nucleon dynamics”. In: *Phys. Rev. C* 91.6 (2015), p. 065201. DOI: `10.1103/PhysRevC.91.065201`. arXiv: `1504.00604 [nucl-th]`.

[102] Corbinian Wellenhofer, Jeremy W. Holt, and Norbert Kaiser. “Divergence of the isospin-asymmetry expansion of the nuclear equation of state in many-body perturbation theory”. In: *Phys. Rev. C* 93.5 (2016), p. 055802. DOI: `10.1103/PhysRevC.93.055802`. arXiv: `1603.02935 [nucl-th]`.

[103] G. Ripka. *Quarks bound by chiral fields: The quark-structure of the vacuum and of light mesons and baryons*. 1997.

[104] Steven Weinberg. “Nuclear forces from chiral Lagrangians”. In: *Phys. Lett. B* 251 (1990), pp. 288–292. DOI: `10.1016/0370-2693(90)90938-3`.

[105] Jeremy W. Holt, Mannque Rho, and Wolfram Weise. “Chiral symmetry and effective field theories for hadronic, nuclear and stellar matter”. In: *Phys. Rept.* 621 (2016), pp. 2–75. DOI: `10.1016/j.physrep.2015.10.011`. arXiv: `1411.6681 [nucl-th]`.

[106] J. Simonis, K. Hebeler, J.D. Holt, J. Menendez, and A. Schwenk. “Exploring sd-shell nuclei from two- and three-nucleon interactions with realistic saturation properties”. In: *Phys. Rev. C* 93.1 (2016), p. 011302. DOI: `10.1103/PhysRevC.93.011302`. arXiv: `1508.05040 [nucl-th]`.

[107] S. Kaufmann et al. “Charge Radius of the Short-Lived ^{68}Ni and Correlation with the Dipole Polarizability”. In: *Phys. Rev. Lett.* 124.13 (2020), p. 132502. DOI: `10.1103/PhysRevLett.124.132502`. arXiv: `2003.06353 [nucl-ex]`.

[108] G. Hagen, A. Ekström, C. Forssén, G. R. Jansen, W. Nazarewicz, T. Papenbrock, K. A. Wendt, S. Bacca, N. Barnea, B. Carlsson, C. Drischler, K. Hebeler, M. Hjorth-Jensen, M. Miorelli, G. Orlandini, A. Schwenk, and J. Simonis. “Neutron and weak-charge distributions of the ^{48}Ca nucleus”. In: *Nat. Phys.* 12.2 (2016), p. 186. DOI: `10.1038/nphys3529`. eprint: `1509.07169`.

[109] R. F. Garcia Ruiz, M. L. Bissell, K. Blaum, A. Ekström, N. Frömmgen, G. Hagen, M. Hammen, K. Hebeler, J. D. Holt, G. R. Jansen, M. Kowalska, K. Kreim, W. Nazarewicz, R. Neugart, G. Neyens, W. Nörtershäuser, T. Papenbrock, J. Papuga, A. Schwenk, J. Simonis, K. A. Wendt, and D. T. Yordanov. “Unexpectedly large charge radii of neutron-rich calcium isotopes”. In: *Nat. Phys.* 12 (2016), p. 594. DOI: `10.1038/nphys3645`. eprint: `1602.07906`.

[110] G. Hagen, G. R. Jansen, and T. Papenbrock. “Structure of ^{78}Ni from first-principles computations”. In: *Phys. Rev. Lett.* 117.17 (2016), p. 172501. DOI: `10.1103/PhysRevLett.117.172501`. eprint: `1605.01477`.

[111] J. Simonis, S. R. Stroberg, K. Hebeler, J. D. Holt, and A. Schwenk. “Saturation with chiral interactions and consequences for finite nuclei”. In: *Phys. Rev. C* 96.1 (2017), p. 014303. DOI: `10.1103/PhysRevC.96.014303`. eprint: `1704.02915`.

[112] J. Birkhan, M. Miorelli, S. Bacca, S. Bassauer, C. A. Bertulani, G. Hagen, H. Matsubara, P. von Neumann-Cosel, T. Papenbrock, N. Pietralla, V. Yu. Ponomarev, A. Richter, A. Schwenk, and A. Tamii. “Electric dipole polarizability of ^{48}Ca and implications for the neutron skin”. In: *Phys. Rev. Lett.* 118.25 (2017), p. 252501. DOI: `10.1103/PhysRevLett.118.252501`. eprint: `1611.07072`.

[113] T. D. Morris, J. Simonis, S. R. Stroberg, C. Stumpf, G. Hagen, J. D. Holt, G. R. Jansen, T. Papenbrock, R. Roth, and A. Schwenk. “Structure of the Lightest Tin Isotopes”. In: *Phys. Rev. Lett.* 120 (15 Apr. 2018), p. 152503. DOI: `10.1103/PhysRevLett.120.152503`.

[114] J.D. Holt, S.R. Stroberg, A. Schwenk, and J. Simonis. “Ab initio limits of atomic nuclei”. In: (May 2019). arXiv: `1905.10475 [nucl-th]`.

[115] M. Mougeot et al. “Examining the $N = 28$ shell closure through high-precision mass measurements of $^{46-48}$Ar”. In: *Phys. Rev. C* 102.1 (2020), p. 014301. DOI: `10.1103/PhysRevC.102.014301`. arXiv: `2006.02712 [nucl-ex]`.

[116] D. R. Entem and R. Machleidt. “Accurate charge-dependent nucleon-nucleon potential at fourth order of chiral perturbation theory”. In: *Phys. Rev. C* 68 (4 Oct. 2003), p. 041001. DOI: `10.1103/PhysRevC.68.041001`. URL: `https://link.aps.org/doi/10.1103/PhysRevC.68.041001`.

[117] K. Hebeler, S. K. Bogner, R. J. Furnstahl, A. Nogga, and A. Schwenk. “Improved nuclear matter calculations from chiral low-momentum interactions”. In: *Phys. Rev. C* 83 (3 Mar. 2011), p. 031301. DOI: `10.1103/PhysRevC.83.031301`. URL: `https://link.aps.org/doi/10.1103/PhysRevC.83.031301`.

[118] M. C. M. Rentmeester, R. G. E. Timmermans, and J. J. de Swart. “Determination of the chiral coupling constants c_3 and c_4 in new pp and np partial-wave analyses”. In: *Phys. Rev. C* 67 (4 Apr. 2003), p. 044001. DOI: `10.1103/PhysRevC.67.044001`. URL: `https://link.aps.org/doi/10.1103/PhysRevC.67.044001`.

[119] A. Akmal, V. R. Pandharipande, and D. G. Ravenhall. “Equation of state of nucleon matter and neutron star structure”. In: *Phys. Rev. C* 58 (3 Sept. 1998), pp. 1804–1828. DOI: `10.1103/PhysRevC.58.1804`. URL: `https://link.aps.org/doi/10.1103/PhysRevC.58.1804`.

[120] I. Tews, S. Gandolfi, A. Gezerlis, and A. Schwenk. “Quantum Monte Carlo calculations of neutron matter with chiral three-body forces”. In: *Phys. Rev. C* 93.2 (2016), p. 024305. DOI: `10.1103/PhysRevC.93.024305`. arXiv: `1507.05561 [nucl-th]`.

[121] Peter Lepage and Christoph Gohlke. *gplepage/lsqfit: lsqfit version 11.5.1*. Version v11.5.1. Mar. 2020. DOI: `10.5281/zenodo.3707868`. URL: `https://doi.org/10.5281/zenodo.3707868`.

[122] Robert B. Wiringa, V.G.J. Stoks, and R. Schiavilla. “An Accurate nucleon-nucleon potential with charge independence breaking”. In: *Phys. Rev. C* 51 (1995), pp. 38–51. DOI: `10.1103/PhysRevC.51.38`. arXiv: `nucl-th/9408016`.

[123] B.S. Pudliner, V.R. Pandharipande, J. Carlson, and Robert B. Wiringa. “Quantum Monte Carlo calculations of A <= 6 nuclei”. In: *Phys. Rev. Lett.* 74 (1995), pp. 4396–4399. DOI: `10.1103/PhysRevLett.74.4396`. arXiv: `nucl-th/9502031`.

[124] L. Coraggio, A. Covello, A. Gargano, N. Itaco, D.R. Entem, T.T.S. Kuo, and R. Machleidt. “Low momentum nucleon-nucleon interactions and shell-model calculations”. In: *Phys. Rev. C* 75 (2007), p. 024311. DOI: `10.1103/PhysRevC.75.024311`. arXiv: `nucl-th/0701065`.

[125] L. Coraggio, J.W. Holt, N. Itaco, R. Machleidt, and F. Sammarruca. “Reduced regulator dependence of neutron-matter predictions with perturbative chiral interactions”. In: *Phys. Rev. C* 87.1 (2013), p. 014322. DOI: `10.1103/PhysRevC.87.014322`. arXiv: `1209.5537 [nucl-th]`.

[126] A. Gezerlis, I. Tews, E. Epelbaum, S. Gandolfi, K. Hebeler, A. Nogga, and A. Schwenk. “Quantum Monte Carlo Calculations with Chiral Effective Field Theory Interactions”. In: *Phys. Rev. Lett.* 111.3 (2013), p. 032501. DOI: `10.1103/PhysRevLett.111.032501`. arXiv: `1303.6243 [nucl-th]`.

[127] A. Gezerlis, I. Tews, E. Epelbaum, M. Freunek, S. Gandolfi, K. Hebeler, A. Nogga, and A. Schwenk. “Local chiral effective field theory interactions and quantum Monte Carlo applications”. In: *Phys. Rev. C* 90.5 (2014), p. 054323. DOI: `10.1103/PhysRevC.90.054323`. arXiv: `1406.0454 [nucl-th]`.

[128] J.E. Lynn, I. Tews, J. Carlson, S. Gandolfi, A. Gezerlis, K.E. Schmidt, and A. Schwenk. “Chiral Three-Nucleon Interactions in Light Nuclei, Neutron-α Scattering, and Neutron Matter”. In: *Phys. Rev. Lett.* 116.6 (2016), p. 062501. DOI: `10.1103/PhysRevLett.116.062501`. arXiv: `1509.03470 [nucl-th]`.

[129] E. Epelbaum, H. Krebs, and U.G. Meißner. “Improved chiral nucleon-nucleon potential up to next-to-next-to-next-to-leading order”. In: *Eur. Phys. J. A* 51.5 (2015), p. 53. DOI: `10.1140/epja/i2015-15053-8`. arXiv: `1412.0142 [nucl-th]`.

[130] C. Drischler, J. A. Melendez, R. J. Furnstahl, and D. R. Phillips. “Quantifying uncertainties and correlations in the nuclear-matter equation of state”. In: *Phys. Rev. C* 102.5 (2020), p. 054315. DOI: `10.1103/PhysRevC.102.054315`. arXiv: `2004.07805`.

[131] Jérôme Margueron, Rudiney Hoffmann Casali, and Francesca Gulminelli. “Equation of state for dense nucleonic matter from metamodeling. II. Predictions for neutron star properties”. In: *Phys. Rev. C* 97.2 (2018), p. 025806. DOI: `10.1103/PhysRevC.97.025806`. arXiv: `1708.06895 [nucl-th]`.

[132] Rahul Somasundaram. *Somasundaram-Rahul/Nuclear-Symmetry-Energy*. Version v1.1.0. Sept. 2020. DOI: `10.5281/zenodo.4012355`. URL: `https://doi.org/10.5281/zenodo.4012355`.

[133] K. Hebeler and A. Schwenk. “Chiral three-nucleon forces and neutron matter”. In: *Phys. Rev. C* 82 (1 July 2010), p. 014314. DOI: `10.1103/PhysRevC.82.014314`. URL: `https://link.aps.org/doi/10.1103/PhysRevC.82.014314`.

[134] J.P. Jeukenne, A. Lejeune, and C. Mahaux. “Many Body Theory of Nuclear Matter”. In: *Phys. Rept.* 25 (1976), pp. 83–174. DOI: `10.1016/0370-1573(76)90017-X`.

[135] Kh.S.A. Hassaneen and H. Muther. “Correlations and spectral functions in asymmetric nuclear matter”. In: *Phys. Rev. C* 70 (2004), p. 054308. DOI: `10.1103/PhysRevC.70.054308`. arXiv: `nucl-th/0408035`.

[136] E.N.E. van Dalen, C. Fuchs, and Amand Faessler. “Effective nucleon masses in symmetric and asymmetric nuclear matter”. In: *Phys. Rev. Lett.* 95 (2005), p. 022302. DOI: `10.1103/PhysRevLett.95.022302`. arXiv: `nucl-th/0502064`.

[137] L.G. Cao, U. Lombardo, C.W. Shen, and Nguyen Van Giai. “From Brueckner approach to Skyrme-type energy density functional”. In: *Phys. Rev. C* 73 (2006), p. 014313. DOI: `10.1103/PhysRevC.73.014313`. arXiv: `nucl-th/0507071`.

[138] X. Roca-Maza, G. Colo, and H. Sagawa. “A new Skyrme interaction with improved spin-isospin properties”. In: *Phys. Rev. C* 86 (2012), p. 031306. DOI: `10.1103/PhysRevC.86.031306`. arXiv: `1205.3958 [nucl-th]`.

[139] W. Zuo, I. Bombaci, and U. Lombardo. “Asymmetric nuclear matter from extended Brueckner-Hartree-Fock approach”. In: *Phys. Rev. C* 60 (1999), p. 024605. DOI: `10.1103/PhysRevC.60.024605`. arXiv: `nucl-th/0102035`.

[140] W. Zuo, A. Lejeune, U. Lombardo, and J.F. Mathiot. “Interplay of three-body interactions in the EOS of nuclear matter”. In: *Nucl. Phys. A* 706 (2002), pp. 418–430. DOI: `10.1016/S0375-9474(02)00750-9`. arXiv: `nucl-th/0202076`.

[141] Bengt Fornberg. “Generation of Finite Difference Formulas on Arbitrarily Spaced Grids”. In: *Math. Comp.* 51 (184 1988), p. 699. DOI: `10.1090/S0025-5718-1988-0935077-0`. URL: `https://www.ams.org/journals/mcom/1988-51-184/S0025-5718-1988-0935077-0/`.

[142] Jérôme Margueron and Francesca Gulminelli. “Effect of high-order empirical parameters on the nuclear equation of state”. In: *Phys. Rev. C* 99.2, 025806 (Feb. 2019), p. 025806. DOI: `10.1103/PhysRevC.99.025806`. arXiv: `1807.01729 [nucl-th]`.

[143] S. Typel, G. Ropke, T. Klahn, D. Blaschke, and H. H. Wolter. “Composition and thermodynamics of nuclear matter with light clusters”. In: *Phys. Rev. C* 81 (2010), p. 015803. DOI: `10.1103/PhysRevC.81.015803`. arXiv: `0908.2344 [nucl-th]`.

[144] Bao-An Li, Plamen G. Krastev, De-Hua Wen, and Nai-Bo Zhang. “Towards Understanding Astrophysical Effects of Nuclear Symmetry Energy”. In: *Eur. Phys. J. A* 55.7 (2019), p. 117. DOI: `10.1140/epja/i2019-12780-8`. arXiv: `1905.13175 [nucl-th]`.

[145] D. Lonardoni, I. Tews, S. Gandolfi, and J. Carlson. “Nuclear and neutron-star matter from local chiral interactions”. In: *Phys. Rev. Res.* 2 (2020), p. 022033. DOI: `10.1103/PhysRevResearch.2.022033`. arXiv: `1912.09411 [nucl-th]`.

[146] I. Tews, T. Krüger, K. Hebeler, and A. Schwenk. “Neutron matter at next-to-next-to-next-to-leading order in chiral effective field theory”. In: *Phys. Rev. Lett.* 110.3 (2013), p. 032504. DOI: `10.1103/PhysRevLett.110.032504`. arXiv: `1206.0025 [nucl-th]`.

[147] Aurel Bulgac, Michael Mcneil Forbes, Shi Jin, Rodrigo Navarro Perez, and Nicolas Schunck. “Minimal nuclear energy density functional”. In: *Phys. Rev. C* 97.4 (2018), p. 044313. DOI: `10.1103/PhysRevC.97.044313`. arXiv: `1708.08771 [nucl-th]`.

[148] G. Audi, F. G. Kondev, Meng Wang, W.J. Huang, and S. Naimi. “The NUBASE2016 evaluation of nuclear properties”. In: *Chinese Physics C* 41.3 (Mar. 2017), p. 030001. DOI: `10.1088/1674-1137/41/3/030001`. URL: `https://doi.org/10.1088%2F1674-1137%2F41%2F3%2F030001`.

[149] L. Coraggio, J. W. Holt, N. Itaco, R. Machleidt, L. E. Marcucci, and F. Sammarruca. “Nuclear-matter equation of state with consistent two- and three-body perturbative chiral interactions”. In: *Phys. Rev. C* 89 (4 Apr. 2014), p. 044321. DOI: `10.1103/PhysRevC.89.044321`. URL: `https://link.aps.org/doi/10.1103/PhysRevC.89.044321`.

[150] Pengsheng Wen and Jeremy W. Holt. “Constraining the nonanalytic terms in the isospin-asymmetry expansion of the nuclear equation of state”. In: (Dec. 2020). arXiv: `2012.02163`.

[151] C. Drischler, K. Hebeler, and A. Schwenk. “Chiral interactions up to next-to-next-to-next-to-leading order and nuclear saturation”. In: *Phys. Rev. Lett.* 122.4 (2019), p. 042501. DOI: `10.1103/PhysRevLett.122.042501`. arXiv: `1710.08220 [nucl-th]`.

[152] J. Hoppe, C. Drischler, K. Hebeler, A. Schwenk, and J. Simonis. “Probing chiral interactions up to next-to-next-to-next-to-leading order in medium-mass nuclei”. In: *Phys. Rev. C* 100.2 (2019), p. 024318. DOI: `10.1103/PhysRevC.100.024318`. arXiv: `1904.12611 [nucl-th]`.

[153] Thomas Hüther, Klaus Vobig, Kai Hebeler, Ruprecht Machleidt, and Robert Roth. “Family of Chiral Two- plus Three-Nucleon Interactions for Accurate Nuclear Structure Studies”. In: *Phys. Lett. B* 808 (2020), p. 135651. DOI: `10.1016/j.physletb.2020.135651`. arXiv: `1911.04955 [nucl-th]`.

[154] I. Vidana, A. Polls, A. Ramos, L. Engvik, and M. Hjorth-Jensen. “Hyperon-hyperon interactions and properties of neutron star matter”. In: *Phys. Rev. C* 62 (2000), p. 035801. DOI: `10.1103/PhysRevC.62.035801`. arXiv: `nucl-th/0004031`.

[155] Diego Lonardoni, Alessandro Lovato, Stefano Gandolfi, and Francesco Pederiva. “Hyperon Puzzle: Hints from Quantum Monte Carlo Calculations”. In: *Phys. Rev. Lett.* 114.9 (2015), p. 092301. DOI: `10.1103/PhysRevLett.114.092301`. arXiv: `1407.4448 [nucl-th]`.

[156] A. Gal, E. V. Hungerford, and D. J. Millener. “Strangeness in nuclear physics”. In: *Rev. Mod. Phys.* 88.3 (2016), p. 035004. DOI: `10.1103/RevModPhys.88.035004`. arXiv: `1605.00557 [nucl-th]`.

[157] Laura Tolos and Laura Fabbietti. “Strangeness in Nuclei and Neutron Stars”. In: *Prog. Part. Nucl. Phys.* 112 (2020), p. 103770. DOI: `10.1016/j.ppnp.2020.103770`. arXiv: `2002.09223 [nucl-ex]`.

[158] C.J. Pethick, D.G. Ravenhall, and C.P. Lorenz. “The inner boundary of a neutron-star crust”. In: *Nuclear Physics A* 584.4 (1995), pp. 675–703. ISSN: 0375-9474. DOI: `https://doi.org/10.1016/0375-9474(94)00506-I`. URL: `http://www.sciencedirect.com/science/article/pii/037594749400506I`.

[159] Camille Ducoin, Jerome Margueron, and Constanca Providencia. “Nuclear symmetry energy and core-crust transition in neutron stars: a critical study”. In: *EPL* 91.3 (2010), p. 32001. DOI: 10.1209/0295-5075/91/32001. arXiv: 1004.5197 [nucl-th].

[160] Camille Ducoin, Jerome Margueron, Constanca Providencia, and Isaac Vidana. “Core-crust transition in neutron stars: predictivity of density developments”. In: *Phys. Rev. C* 83 (2011), p. 045810. DOI: 10.1103/PhysRevC.83.045810. arXiv: 1102.1283 [nucl-th].

[161] Peter Lepage, Christoph Gohlke, and Daniel Hackett. *gplepage/gvar: gvar version 11.7*. Version v11.7. July 2020. DOI: 10.5281/zenodo.3948666. URL: https://doi.org/10.5281/zenodo.3948666.

[162] James M. Lattimer and Madappa Prakash. “The Equation of State of Hot, Dense Matter and Neutron Stars”. In: *Phys. Rept.* 621 (2016), pp. 127–164. DOI: 10.1016/j.physrep.2015.12.005. arXiv: 1512.07820 [astro-ph.SR].

[163] G. F. Burgio, H. -J. Schulze, I. Vidana, and J. -B. Wei. “Neutron stars and the nuclear equation of state”. In: *Prog. Part. Nucl. Phys.* 120 (2021), p. 103879. DOI: 10.1016/j.ppnp.2021.103879. arXiv: 2105.03747 [nucl-th].

[164] M. Fortin, C. Providencia, A. R. Raduta, F. Gulminelli, J. L Zdunik, P. Haensel, and M. Bejger. “Neutron star radii and crusts: uncertainties and unified equations of state”. In: *Phys. Rev. C* 94.3 (2016), p. 035804. DOI: 10.1103/PhysRevC.94.035804. arXiv: 1604.01944 [astro-ph.SR].

[165] Lami Suleiman, Morgane Fortin, Julian Leszek Zdunik, and Pawel Haensel. “Influence of the crust on the neutron star macrophysical quantities and universal relations”. In: *Phys. Rev. C* 104.1 (2021), p. 015801. DOI: 10.1103/PhysRevC.104.015801. arXiv: 2106.12845 [astro-ph.HE].

[166] F. Douchin and P. Haensel. “A unified equation of state of dense matter and neutron star structure”. In: *Astron. Astrophys.* 380 (2001), p. 151. DOI: 10.1051/0004-6361:20011402. arXiv: astro-ph/0111092.

[167] A. F. Fantina, N. Chamel, J. M. Pearson, and S. Goriely. “Constraints on the equation of state of cold dense matter from nuclear physics and astrophysics”. In: *EPJ Web Conf.* 66 (2014). Ed. by Santo Lunardi, P. G. Bizzeti, Carlo | Bucci, Massimo Chiari, Andrea Dainese, Pasquale Di Nezza, Roberto Menegazzo, Adriana Nannini, Cosimo Signorini, and Jose Javier Valiente-Dobon, p. 07005. DOI: 10.1051/epjconf/20146607005.

[168] Henning Heiselberg and Vijay Pandharipande. “Recent Progress in Neutron Star Theory”. In: *Annual Review of Nuclear and Particle Science* 50.1 (2000), pp. 481–524. DOI: 10.1146/annurev.nucl.50.1.481. eprint: https://doi.org/10.1146/annurev.nucl.50.1.481. URL: https://doi.org/10.1146/annurev.nucl.50.1.481.

[169] J. Carlson, J. Morales, V. R. Pandharipande, and D. G. Ravenhall. In: *Phys. Rev. C* 68 (2 2003), p. 025802. DOI: 10.1103/PhysRevC.68.025802. URL: https://link.aps.org/doi/10.1103/PhysRevC.68.025802.

[170] Evgeny Epelbaum, Hans-Werner Hammer, and Ulf-G. Meissner. “Modern Theory of Nuclear Forces”. In: *Rev. Mod. Phys.* 81 (2009), pp. 1773–1825. DOI: `10.1103/RevModPhys.81.1773`. arXiv: `0811.1338 [nucl-th]`.

[171] Ingo Tews, Joseph Carlson, Stefano Gandolfi, and Sanjay Reddy. “Constraining the speed of sound inside neutron stars with chiral effective field theory interactions and observations”. In: *ApJ* 860.2 (2018), p. 149. arXiv: `1801.01923 [nucl-th]`.

[172] C. Drischler, R. J. Furnstahl, J. A. Melendez, and D. R. Phillips. “How Well Do We Know the Neutron-Matter Equation of State at the Densities Inside Neutron Stars? A Bayesian Approach with Correlated Uncertainties”. In: *Phys. Rev. Lett.* 125.20 (2020), p. 202702. DOI: `10.1103/PhysRevLett.125.202702`. arXiv: `2004.07232 [nucl-th]`.

[173] N. Chamel and P. Haensel. “Physics of Neutron Star Crusts”. In: *Living Rev. Rel.* 11 (2008), p. 10. DOI: `10.12942/lrr-2008-10`. arXiv: `0812.3955 [astro-ph]`.

[174] William D. Myers. “Geometric properties of leptodermous distributions with applications to nuclei”. In: *Nucl. Phys. A* 204 (1973), pp. 465–484. DOI: `10.1016/0375-9474(73)90388-6`.

[175] J. M. Pearson, N. Chamel, A. Y. Potekhin, A. F. Fantina, C. Ducoin, A. K. Dutta, and S. Goriely. “Unified equations of state for cold non-accreting neutron stars with Brussels–Montreal functionals – I. Role of symmetry energy”. In: *Mon. Not. Roy. Astron. Soc.* 481.3 (2018). [Erratum: Mon.Not.Roy.Astron.Soc. 486, 768 (2019)], pp. 2994–3026. DOI: `10.1093/mnras/sty2413`. arXiv: `1903.04981 [astro-ph.HE]`.

[176] Christian Drischler, Kai Hebeler, and Achim Schwenk. “Asymmetric nuclear matter based on chiral two- and three-nucleon interactions”. In: *Phys. Rev. C* 93.5 (2016), p. 054314. DOI: `10.1103/PhysRevC.93.054314`. arXiv: `1510.06728 [nucl-th]`.

[177] C. Drischler, J. W. Holt, and C. Wellenhofer. “Chiral Effective Field Theory and the High-Density Nuclear Equation of State”. In: *Ann. Rev. Nucl. Part. Sci.* 71 (2021), pp. 403–432. DOI: `10.1146/annurev-nucl-102419-041903`. arXiv: `2101.01709 [nucl-th]`.

[178] J Dobaczewski, W Nazarewicz, and P-G Reinhard. “Error estimates of theoretical models: a guide”. In: *Journal of Physics G: Nuclear and Particle Physics* 41.7 (May 2014), p. 074001. DOI: `10.1088/0954-3899/41/7/074001`. URL: `https://doi.org/10.1088/0954-3899/41/7/074001`.

[179] S. Goriely, M. Samyn, and J. M. Pearson. “Further explorations of Skyrme-Hartree-Fock-Bogoliubov mass formulas. VII. Simultaneous fits to masses and fission barriers”. In: *Phys. Rev. C* 75 (2007), p. 064312. DOI: `10.1103/PhysRevC.75.064312`.

[180] N. Chamel, S. Goriely, and J. M. Pearson. “Further explorations of Skyrme-Hartree-Fock-Bogoliubov mass formulas. IX. Constraint of pairing force to S(0)-1 neutron-matter gap”. In: *Nucl. Phys. A* 812 (2008), pp. 72–98. DOI: `10.1016/j.nuclphysa.2008.08.015`. arXiv: `0809.0447 [nucl-th]`.

[181] T. Lesinski, K. Bennaceur, T. Duguet, and J. Meyer. “Isovector splitting of nucleon effective masses, ab-initio benchmarks and extended stability criteria for Skyrme energy functionals”. In: *Phys. Rev. C* 74 (2006), p. 044315. DOI: `10.1103/PhysRevC.74.044315`. arXiv: `nucl-th/0607065`.

[182] L. G. Cao, U. Lombardo, C. W. Shen, and Nguyen Van Giai. “From Brueckner approach to Skyrme-type energy density functional”. In: *Phys. Rev. C* 73 (2006), p. 014313. DOI: `10.1103/PhysRevC.73.014313`. arXiv: `nucl-th/0507071`.

[183] M. Rayet, M. Arnould, G. Paulus, and F. Tondeur. “Nuclear forces and the properties of matter at high temperature and density”. In: *Astron. Astrophys.* 116.1 (Dec. 1982), pp. 183–187.

[184] Nguyen van Giai and H. Sagawa. “Spin-isospin and pairing properties of modified Skyrme interactions”. In: *Phys. Lett. B* 106 (1981), pp. 379–382. DOI: `10.1016/0370-2693(81)90646-8`.

[185] E. Chabanat, P. Bonche, P. Haensel, J. Meyer, and R. Schaeffer. “A Skyrme parametrization from subnuclear to neutron star densities. 2. Nuclei far from stablities”. In: *Nucl. Phys. A* 635 (1998). [Erratum: Nucl.Phys.A 643, 441–441 (1998)], pp. 231–256. DOI: `10.1016/S0375-9474(98)00180-8`.

[186] Alessandro Roggero, Abhishek Mukherjee, and Francesco Pederiva. “Constraining the Skyrme energy density functional with quantum Monte Carlo calculations”. In: *Phys. Rev. C* 92.5 (2015), p. 054303. DOI: `10.1103/PhysRevC.92.054303`. arXiv: `1406.1631 [nucl-th]`.

[187] Guilherme Grams, Jérôme Margueron, Rahul Somasundaram, and Sanjay Reddy. “Properties of Neutron Star Crust with Improved Nuclear Physics: Impact of Chiral EFT Interactions and Experimental Nuclear Masses”. In: *Few Body Syst.* 62.4 (2021), p. 116. DOI: `10.1007/s00601-021-01697-y`. arXiv: `2109.11857 [nucl-th]`.

[188] J. Carlson and Sanjay Reddy. “Superfluid Pairing Gap in Strong Coupling”. In: *Phys. Rev. Lett.* 100 (2008), p. 150403. DOI: `10.1103/PhysRevLett.100.150403`. arXiv: `0711.0414 [cond-mat.str-el]`.

[189] Aurel Bulgac, Michael McNeil Forbes, and Piotr Magierski. “The Unitary Fermi Gas: From Monte Carlo to Density Functionals”. In: *Lect. Notes Phys.* 836 (2012), pp. 305–373. DOI: `10.1007/978-3-642-21978-8_9`. arXiv: `1008.3933 [cond-mat.quant-ga`

[190] Isaac Vidaña. “Low-density neutron matter and the unitary limit”. In: *Front. in Phys.* 9 (2021), p. 170. DOI: `10.3389/fphy.2021.660622`. arXiv: `2101.11903 [nucl-th]`.

[191] N. Navon, S. Nascimbene, F. Chevy, and C. Salomon. “The Equation of State of a Low-Temperature Fermi Gas with Tunable Interactions”. In: *Science* 328.5979 (2010), pp. 729–732. DOI: `10.1126/science.1187582`. arXiv: `1004.1465 [cond-mat.quant-`

[192] R. Somasundaram, C. Drischler, I. Tews, and J. Margueron. “Constraints on the nuclear symmetry energy from asymmetric-matter calculations with chiral NN and $3N$ interactions”. In: *Phys. Rev. C* 103.4 (2021), p. 045803. DOI: `10.1103/PhysRevC.103.045803`. arXiv: `2009.04737 [nucl-th]`.

[193] P. Papakonstantinou, J. Margueron, F. Gulminelli, and Ad. R. Raduta. “Densities and energies of nuclei in dilute matter at zero temperature”. In: *Phys. Rev. C* 88.4 (2013), p. 045805. DOI: `10.1103/PhysRevC.88.045805`. arXiv: `1305.0282 [nucl-th]`.

[194] Thomas Carreau, Francesca Gulminelli, and Jérôme Margueron. “Bayesian analysis of the crust-core transition with a compressible liquid-drop model”. In: *Eur. Phys. J. A* 55.10 (2019), p. 188. DOI: `10.1140/epja/i2019-12884-1`. arXiv: `1902.07032 [nucl-th]`.

[195] W. D. Myers and W. J. Swiatecki. “Droplet-model theory of the neutron skin”. In: *Nucl. Phys. A* 336 (1980), pp. 267–278. DOI: `10.1016/0375-9474(80)90623-5`.

[196] X. Viñas, B. K. Sharma, C. Gonzalez-Boquera, and M. Centelles. “Crust-Core Transitions in Neutron Stars Revisited”. In: *Bulg. J. Phys.* 44.S1 (2017). Ed. by Mitko Gaidarov, pp. 081–092.

[197] Haensel P. In: *Physics of Neutron Star Interiors* 578 (2001), p. 127.

[198] F. Gulminelli and Ad. R. Raduta. “Unified treatment of subsaturation stellar matter at zero and finite temperature”. In: *Phys. Rev. C* 92.5 (2015), p. 055803. DOI: `10.1103/PhysRevC.92.055803`. arXiv: `1504.04493 [nucl-th]`.

[199] William D. Myers and W. J. Swiatecki. “Average nuclear properties”. In: *Annals Phys.* 55 (1969), p. 395. DOI: `10.1016/0003-4916(69)90202-4`.

[200] B. Alex Brown. “Neutron Radii in Nuclei and the Neutron Equation of State”. In: *Phys. Rev. C* 85.25 (Dec. 2000), pp. 5296–5299. DOI: `10.1103/PhysRevLett.85.5296`.

[201] X. Roca-Maza, M. Centelles, X. Viñas, and M. Warda. “Neutron Skin of Pb208, Nuclear Symmetry Energy, and the Parity Radius Experiment”. In: *Phys. Rev. C* 106.25, 252501 (June 2011), p. 252501. DOI: `10.1103/PhysRevLett.106.252501`. arXiv: `1103.1762 [nucl-th]`.

[202] Thomas Carreau, Francesca Gulminelli, and Jérôme Margueron. “General predictions for the neutron star crustal moment of inertia”. In: *Phys. Rev. C* 100.5 (2019), p. 055803. DOI: `10.1103/PhysRevC.100.055803`. arXiv: `1810.00719 [nucl-th]`.

[203] Gordon Baym, Hans A. Bethe, and Christopher J. Pethick. “Neutron star matter”. In: *Nucl. Phys. A* 175.2 (Nov. 1971), pp. 225–271. DOI: `10.1016/0375-9474(71)90281-8`.

[204] John W. Negele and D. Vautherin. “Neutron star matter at subnuclear densities”. In: *Nucl. Phys. A* 207 (1973), pp. 298–320. DOI: `10.1016/0375-9474(73)90349-7`.

[205] B. K. Sharma, M. Centelles, X. Viñas, M. Baldo, and G. F. Burgio. “Unified equation of state for neutron stars on a microscopic basis”. In: *A&A* 584, A103 (Dec. 2015), A103. DOI: `10.1051/0004-6361/201526642`. arXiv: `1506.00375 [nucl-th]`.

[206] James M. Lattimer and F. Douglas Swesty. “A Generalized equation of state for hot, dense matter”. In: *Nucl. Phys. A* 535 (1991), pp. 331–376. DOI: `10.1016/0375-9474(91)90452-C`.

[207] W. G. Newton, M. Gearheart, and Bao-An Li. “A survey of the parameter space of the compressible liquid drop model as applied to the neutron star inner crust”. In: *Astrophys. J. Suppl.* 204 (2013), p. 9. DOI: 10.1088/0067-0049/204/1/9. arXiv: 1110.4043 [astro-ph.SR].

[208] G. Grams, R. Somasundaram, J. Margueron, and S. Reddy. “Properties of the neutron star crust: Quantifying and correlating uncertainties with improved nuclear physics”. In: (Oct. 2021). arXiv: 2110.00441 [nucl-th].

[209] A. Bohr and B. R. Mottelson. *Nuclear structure vol I*. Addison-Wesley, 1969.

[210] P. Vogel, B. Jonson, and P. G. Hansen. “Is there neutron-proton pairing in medium heavy nuclei?” In: *Phys. Lett. B* 139 (1984), pp. 227–230. DOI: 10.1016/0370-2693(84)91068-2.

[211] J. M. Pearson, N. Chamel, S. Goriely, and C. Ducoin. “Inner crust of neutron stars with mass-fitted Skyrme functionals”. In: *Phys. Rev. C* 85.6, 065803 (June 2012), p. 065803. DOI: 10.1103/PhysRevC.85.065803. arXiv: 1206.0205 [nucl-th].

[212] A. F. Fantina, S. De Ridder, N. Chamel, and F. Gulminelli. “Crystallization of the outer crust of a non-accreting neutron star”. In: *Astron. Astrophys.* 633 (2020), A149. DOI: 10.1051/0004-6361/201936359. arXiv: 1912.02849 [astro-ph.HE].

[213] F Douchin, P Haensel, and J Meyer. “Nuclear surface and curvature properties for SLy Skyrme forces and nuclei in the inner neutron-star crust”. In: *Nucl. Phys. A* 665 (2000), pp. 419–446. DOI: 10.1016/S0375-9474(99)00397-8.

[214] Gordon Baym, Hans A. Bethe, and Christopher Pethick. “Neutron star matter”. In: *Nucl. Phys. A* 175 (1971), pp. 225–271. DOI: 10.1016/0375-9474(71)90281-8.

[215] K. Hebeler, J. M. Lattimer, C. J. Pethick, and A. Schwenk. “Equation of state and neutron star properties constrained by nuclear physics and observation”. In: *Astrophys. J.* 773 (2013), p. 11. DOI: 10.1088/0004-637X/773/1/11. arXiv: 1303.4662 [astro-ph.SR].

[216] Paulo Bedaque and Andrew W. Steiner. “Sound velocity bound and neutron stars”. In: *Phys. Rev. Lett.* 114.3 (2015), p. 031103. DOI: 10.1103/PhysRevLett.114.031103. arXiv: 1408.5116 [nucl-th].

[217] S. S. M. Wong. *Introductory nuclear physics*. Wiley, 1998.

[218] G. Chanfray, Magda Ericson, and Pierre A. M. Guichon. “Chiral symmetry and quantum hadrodynamics”. In: *Phys. Rev. C* 63 (2001), p. 055202. DOI: 10.1103/PhysRevC.63.055202. arXiv: nucl-th/0012013.

[219] G. Chanfray and M. Ericson. “QCD susceptibilities and nuclear-matter saturation in a relativistic chiral theory”. In: *Eur. Phys. J. A* 25 (2005), pp. 151–157. DOI: 10.1140/epja/i2005-10074-6.

[220] Brian D. Serot and John Dirk Walecka. “The Relativistic Nuclear Many Body Problem”. In: *Adv. Nucl. Phys.* 16 (1986), pp. 1–327.

[221] Brian D. Serot and John Dirk Walecka. “Recent progress in quantum hadrodynamics”. In: *Int. J. Mod. Phys. E* 6 (1997), pp. 515–631. DOI: 10.1142/S0218301397000299. arXiv: nucl-th/9701058.

[222] Stefan Floerchinger and Christof Wetterich. “Chemical freeze-out in heavy ion collisions at large baryon densities”. In: *Nucl. Phys. A* 890-891 (2012), pp. 11–24. DOI: `10.1016/j.nuclphysa.2012.07.009`. arXiv: `1202.1671 [nucl-th]`.

[223] Matthias Drews, Thomas Hell, Bertram Klein, and Wolfram Weise. “Thermodynamic phases and mesonic fluctuations in a chiral nucleon-meson model”. In: *Phys. Rev. D* 88.9 (2013), p. 096011. DOI: `10.1103/PhysRevD.88.096011`. arXiv: `1308.5596 [hep-ph]`.

[224] Eduardo S. Fraga, Maurício Hippert, and Andreas Schmitt. “Surface tension of dense matter at the chiral phase transition”. In: *Phys. Rev. D* 99.1 (2019), p. 014046. DOI: `10.1103/PhysRevD.99.014046`. arXiv: `1810.13226 [hep-ph]`.

[225] Andreas Schmitt. “Chiral pasta: Mixed phases at the chiral phase transition”. In: *Phys. Rev. D* 101.7 (2020), p. 074007. DOI: `10.1103/PhysRevD.101.074007`. arXiv: `2002.01451 [hep-ph]`.

[226] Hideki Yukawa. “On the Interaction of Elementary Particles I”. In: *Proc. Phys. Math. Soc. Jap.* 17 (1935), pp. 48–57. DOI: `10.1143/PTPS.1.1`.

[227] K. Erkelenz. “Current status of the relativistic two-nucleon one boson exchange potential”. In: *Physics Reports* 13.5 (1974), pp. 191–258. ISSN: 0370-1573. DOI: `https://doi.org/10.1016/0370-1573(74)90008-8`. URL: `https://www.sciencedirect.com/science/article/pii/0370157374900088`.

[228] R. Brockmann and R. Machleidt. “Nuclear saturation in a relativistic Brueckner-Hartree-Fock approach”. In: *Phys. Lett. B* 149 (1984), p. 283. DOI: `10.1016/0370-2693(84)90407-6`.

[229] B. Ter Haar and R. Malfliet. “Nucleons, Mesons and Deltas in Nuclear Matter. A Relativistic Dirac-Bruckner Approach”. In: *Phys. Rept.* 149 (1987), pp. 207–286. DOI: `10.1016/0370-1573(87)90085-8`.

[230] S. Typel and H. H. Wolter. “Relativistic mean field calculations with density dependent meson nucleon coupling”. In: *Nucl. Phys. A* 656 (1999), pp. 331–364. DOI: `10.1016/S0375-9474(99)00310-3`.

[231] E. N. E. van Dalen and H. Muther. “Relativistic Description of Finite Nuclei Based on Realistic NN Interactions”. In: *Phys. Rev. C* 84 (2011), p. 024320. DOI: `10.1103/PhysRevC.84.024320`. arXiv: `1106.3157 [nucl-th]`.

[232] G. A. Lalazissis, T. Niksic, D. Vretenar, and P. Ring. “New relativistic mean-field interaction with density-dependent meson-nucleon couplings”. In: *Phys. Rev. C* 71 (2005), p. 024312. DOI: `10.1103/PhysRevC.71.024312`.

[233] Wen Hui Long, Hiroyuki Sagawa, Nguyen Van Giai, and Jie Meng. “Shell Structure and rho-Tensor Correlations in Density-Dependent Relativistic Hartree-Fock theory”. In: *Phys. Rev. C* 76 (2007), p. 034314. DOI: `10.1103/PhysRevC.76.034314`. arXiv: `0706.3497 [nucl-th]`.

[234] Wolfram Weise. “Nuclear chiral dynamics and phases of QCD”. In: *Prog. Part. Nucl. Phys.* 67 (2012). Ed. by Amand Faessler and Vadim Rodin, pp. 299–311. DOI: `10.1016/j.ppnp.2011.12.034`. arXiv: `1201.0950 [nucl-th]`.

[235] Yoichiro Nambu and G. Jona-Lasinio. “Dynamical model of elementary particles based on an analogy with superconductivity. I”. In: *Phys. Rev.* 122 (1961), pp. 345–358. DOI: 10.1103/PhysRev.122.345.

[236] Yoichiro Nambu and G. Jona-Lasinio. “Dynamical model of elementary particles based on an analogy with superconductivity. II”. In: *Phys. Rev.* 124 (1961), pp. 246–254. DOI: 10.1103/PhysRev.124.246.

[237] S. P. Klevansky. “The Nambu–Jona-Lasinio model of quantum chromodynamics”. In: *Rev. Mod. Phys.* 64 (1992), pp. 649–708. DOI: 10.1103/RevModPhys.64.649.

[238] Michael C. Birse. “What does a change in the quark condensate say about restoration of chiral symmetry in matter?” In: *Phys. Rev. C* 53 (1996), R2048–R2051. DOI: 10.1103/PhysRevC.53.R2048. arXiv: hep-ph/9602266.

[239] G. Chanfray and M. Ericson. “Scalar field in nuclear matter: the roles of spontaneous chiral symmetry breaking and nucleon structure”. In: *Phys. Rev. C* 83 (2011), p. 015204. DOI: 10.1103/PhysRevC.83.015204. arXiv: 1011.4280 [nucl-th].

[240] G. Chanfray, D. Davesne, M. Ericson, and M. Martini. “Two-pion production processes, chiral symmetry and N N interaction in the medium”. In: *Eur. Phys. J. A* 27 (2006), pp. 191–198. DOI: 10.1140/epja/i2005-10245-5. arXiv: nucl-th/0406003.

[241] L. S. Celenza, C. M. Shakin, Wei-Dong Sun, J. Szweda, and Xi-quan Zhu. “Quark model calculations of current correlators in the nonperturbative domain”. In: *Annals Phys.* 241 (1995), pp. 1–36. DOI: 10.1006/aphy.1995.1053.

[242] L. S. Celenza, Huangsheng Wang, and C. M. Shakin. “Application of a generalized Nambu-Jona-Lasinio model to the calculation of the properties of scalar mesons and nuclear matter”. In: *Phys. Rev. C* 63 (2001), p. 025209. DOI: 10.1103/PhysRevC.63.025209.

[243] J. Boguta. “A SATURATING CHIRAL FIELD THEORY OF NUCLEAR MATTER”. In: *Phys. Lett. B* 120 (1983), pp. 34–38. DOI: 10.1016/0370-2693(83)90617-2.

[244] A. K. Kerman and L. D. Miller. “Field Theory Methods for Finite Nuclear Systems and the Possibility of Density Isomerism.” In: *1974 PEP Summer Study*. 1974.

[245] Wolfgang Bentz and Anthony William Thomas. “The Stability of nuclear matter in the Nambu-Jona-Lasinio model”. In: *Nucl. Phys. A* 696 (2001), pp. 138–172. DOI: 10.1016/S0375-9474(01)01119-8. arXiv: nucl-th/0105022.

[246] G. Chanfray. “Theoretical approaches to hadrons in nuclear matter”. In: *Nucl. Phys. A* 721 (2003). Ed. by H. Toki, K. Imai, and T. Kishimoto, pp. 76–83. DOI: 10.1016/S0375-9474(03)01019-4. arXiv: nucl-th/0212085.

[247] Pierre A. M. Guichon. “A Possible Quark Mechanism for the Saturation of Nuclear Matter”. In: *Phys. Lett. B* 200 (1988), pp. 235–240. DOI: 10.1016/0370-2693(88)90762-9.

[248] Pierre A. M. Guichon and Anthony William Thomas. “Quark structure and nuclear effective forces”. In: *Phys. Rev. Lett.* 93 (2004), p. 132502. DOI: 10.1103/PhysRevLett.93.132502. arXiv: nucl-th/0402064.

[249] Jesper Leong, Theo F. Motta, Anthony W. Thomas, and P. A. M. Guichon. “Dense Nuclear Matter with Baryon Overlap”. In: (Aug. 2022). arXiv: `2208.09331 [nucl-th]`.

[250] Donald F. Geesaman, K. Saito, and Anthony William Thomas. “The nuclear EMC effect”. In: *Ann. Rev. Nucl. Part. Sci.* 45 (1995), pp. 337–390. DOI: `10.1146/annurev.ns.45.120195.002005`.

[251] Theo F. Motta and Anthony W. Thomas. “The role of baryon structure in neutron stars”. In: *Mod. Phys. Lett. A* 37.01 (2022), p. 2230001. DOI: `10.1142/S0217732322300014`. arXiv: `2201.11549 [nucl-th]`.

[252] G. Chanfray and M. Ericson. “QCD susceptibilities and nuclear matter saturation in a chiral theory: inclusion of pion loops”. In: *Phys. Rev. C* 75 (2007), p. 015206. DOI: `10.1103/PhysRevC.75.015206`. arXiv: `nucl-th/0611042`.

[253] E. Massot and G. Chanfray. “Relativistic Chiral Hartree-Fock description of nuclear matter with constraints from nucleon structure and confinement”. In: *Phys. Rev. C* 78 (2008), p. 015204. DOI: `10.1103/PhysRevC.78.015204`. arXiv: `0803.1719 [nucl-th]`.

[254] E. Massot and G. Chanfray. “Relativistic calculation of the pion loop correlation energy in nuclear matter in a theory including confinement”. In: *Phys. Rev. C* 80 (2009), p. 015202. DOI: `10.1103/PhysRevC.80.015202`. arXiv: `0905.0605 [nucl-th]`.

[255] E. Massot, J. Margueron, and G. Chanfray. “On the maximum mass of hyperonic neutron stars”. In: *EPL* 97.3 (2012), p. 39002. DOI: `10.1209/0295-5075/97/39002`. arXiv: `1201.2772 [nucl-th]`.

[256] Guy Chanfray and Jérôme Margueron. “Contribution of the rho-meson and quark substructure to the nuclear spin-orbit potential”. In: *Phys. Rev. C* 102.2 (2020), p. 024331. DOI: `10.1103/PhysRevC.102.024331`. arXiv: `2006.02698 [nucl-th]`.

[257] J. Boguta and J. Kunz. “CHIRAL NUCLEAR INTERACTIONS”. In: *Nucl. Phys. A* 501 (1989), pp. 637–652. DOI: `10.1016/0375-9474(89)90153-X`.

[258] R. Somasundaram, J. Margueron, G. Chanfray, and H. Hansen. “Confrontation of Different Relativistic Descriptions of Nuclear Matter”. In: (Sept. 2021). arXiv: `2109.05374 [nucl-th]`.

[259] Jérôme Margueron, Rudiney Hoffmann Casali, and Francesca Gulminelli. “Equation of state for dense nucleonic matter from metamodeling. I. Foundational aspects”. In: *Phys. Rev. C* 97.2 (2018), p. 025805. DOI: `10.1103/PhysRevC.97.025805`. arXiv: `1708.06894 [nucl-th]`.

[260] Derek Bruce Leinweber, Anthony William Thomas, and Ross Daniel Young. “Physical nucleon properties from lattice QCD”. In: *Phys. Rev. Lett.* 92 (2004), p. 242002. DOI: `10.1103/PhysRevLett.92.242002`. arXiv: `hep-lat/0302020`.

[261] A. Ali Khan et al. “Light hadron spectroscopy with two flavors of dynamical quarks on the lattice”. In: *Phys. Rev. D* 65 (2002). [Erratum: Phys.Rev.D 67, 059901 (2003)], p. 054505. DOI: `10.1103/PhysRevD.65.054505`. arXiv: `hep-lat/0105015`.

[262] Anthony William Thomas, Pierre A. M. Guichon, Derek Bruce Leinweber, and Ross Daniel Young. "Towards a connection between nuclear structure and QCD". In: *Prog. Theor. Phys. Suppl.* 156 (2004), pp. 124–136. DOI: 10.1143/PTPS.156.124. arXiv: nucl-th/0411014.

[263] R. K. Bhaduri. *Models of the Nucleon: From Quarks to Soliton*. 1988.

[264] J. Boguta and A. R. Bodmer. "Relativistic Calculation of Nuclear Matter and the Nuclear Surface". In: *Nucl. Phys. A* 292 (1977), pp. 413–428. DOI: 10.1016/0375-9474(77)90626-1.

[265] G. A. Lalazissis, J. Konig, and P. Ring. "A New parametrization for the Lagrangian density of relativistic mean field theory". In: *Phys. Rev. C* 55 (1997), pp. 540–543. DOI: 10.1103/PhysRevC.55.540. arXiv: nucl-th/9607039.

[266] Zhong-yu Ma, Jian Rong, Bao-Qiu Chen, Zhi-Yuan Zhu, and Hong-Qiu Song. "Isospin dependence of nucleon effective mass in Dirac Brueckner-Hartree-Fock approach". In: *Phys. Lett. B* 604 (2004), pp. 170–174. DOI: 10.1016/j.physletb.2004.11.004. arXiv: nucl-th/0412030.

[267] M. Jaminon and C. Mahaux. "Effective masses in relativistic approaches to the nucleon-nucleus mean field". In: *Phys. Rev. C* 40 (1 July 1989), pp. 354–367. DOI: 10.1103/PhysRevC.40.354. URL: https://link.aps.org/doi/10.1103/PhysRevC.40.354.

[268] M. Ericson and G. Chanfray. "Constraints on nuclear matter properties from QCD susceptibilities". In: *Eur. Phys. J. A* 34 (2007), pp. 215–222. DOI: 10.1140/epja/i2007-10498-x. arXiv: 0707.3025 [nucl-th].

[269] G. Chanfray, Magda Ericson, and Pierre A. M. Guichon. "Scalar susceptibility and chiral symmetry restoration in nuclei". In: *Phys. Rev. C* 68 (2003), p. 035209. DOI: 10.1103/PhysRevC.68.035209. arXiv: nucl-th/0305058.

[270] T. Matsui. "Fermi Liquid Properties of Nuclear Matter in a Relativistic Mean - Field Theory". In: *Nucl. Phys. A* 370 (1981), pp. 365–388. DOI: 10.1016/0375-9474(81)90103-2.

[271] P. Haensel and M. Proszynski. "Pion condensation in cold dense matter and neutron stars". In: *Astrophys. J.* 258 (1982), pp. 306–320. DOI: 10.1086/160080.

[272] Eemeli Annala, Tyler Gorda, Aleksi Kurkela, Joonas Nättilä, and Aleksi Vuorinen. "Evidence for quark-matter cores in massive neutron stars". In: *Nature Phys.* 16.9 (2020), pp. 907–910. DOI: 10.1038/s41567-020-0914-9. arXiv: 1903.09121 [astro-ph.HE].

[273] Z. F. Seidov. "The Stability of a Star with a Phase Change in General Relativity Theory". In: *Soviet Astronomy* 15 (Oct. 1971), p. 347.

[274] A.R. Bodmer. "Collapsed nuclei". In: *Phys. Rev. D* 4 (1971), pp. 1601–1606. DOI: 10.1103/PhysRevD.4.1601.

[275] Edward Witten. "Cosmic Separation of Phases". In: *Phys. Rev. D* 30 (1984), pp. 272–285. DOI: 10.1103/PhysRevD.30.272.

[276] R. Schaeffer, L. Zdunik, and P. Haensel. "Phase transitions in stellar cores. I - Equilibrium configurations". In: *Astronomy and Astrophysics* 126.1 (Sept. 1983), pp. 121–145.

[277] Lee Lindblom. "Phase transitions and the mass radius curves of relativistic stars". In: *Phys. Rev. D* 58 (1998), p. 024008. DOI: `10.1103/PhysRevD.58.024008`. arXiv: `gr-qc/9802072`.

[278] Zdunik, J. L. and Haensel, P. "Maximum mass of neutron stars and strange neutron-star cores". In: *A&A* 551 (2013), A61. DOI: `10.1051/0004-6361/201220697`. URL: `https://doi.org/10.1051/0004-6361/201220697`.

[279] Chamel, N., Fantina, A. F., Pearson, J. M., and Goriely, S. "Phase transitions in dense matter and the maximum mass of neutron stars". In: *A&A* 553 (2013), A22. DOI: `10.1051/0004-6361/201220986`. URL: `https://doi.org/10.1051/0004-6361/201220986`.

[280] Elias R. Most, L. Jens Papenfort, Veronica Dexheimer, Matthias Hanauske, Stefan Schramm, Horst Stöcker, and Luciano Rezzolla. "Signatures of quark-hadron phase transitions in general-relativistic neutron-star mergers". In: *Phys. Rev. Lett.* 122.6 (2019), p. 061101. DOI: `10.1103/PhysRevLett.122.061101`. arXiv: `1807.03684 [astro-ph.HE]`.

[281] Lukas R. Weih, Matthias Hanauske, and Luciano Rezzolla. "Postmerger Gravitational-Wave Signatures of Phase Transitions in Binary Mergers". In: *Phys. Rev. Lett.* 124.17 (2020), p. 171103. DOI: `10.1103/PhysRevLett.124.171103`. arXiv: `1912.09340 [gr-qc]`.

[282] Andreas Bauswein, Niels-Uwe F. Bastian, David B. Blaschke, Katerina Chatziioannou, James A. Clark, Tobias Fischer, and Micaela Oertel. "Identifying a first-order phase transition in neutron star mergers through gravitational waves". In: *Phys. Rev. Lett.* 122.6 (2019), p. 061102. DOI: `10.1103/PhysRevLett.122.061102`. arXiv: `1809.01116 [astro-ph.HE]`.

[283] Andreas Bauswein, Sebastian Blacker, Vimal Vijayan, Nikolaos Stergioulas, Katerina Chatziioannou, James A. Clark, Niels-Uwe F. Bastian, David B. Blaschke, Mateusz Cierniak, and Tobias Fischer. "Equation of state constraints from the threshold binary mass for prompt collapse of neutron star mergers". In: *Phys. Rev. Lett.* 125.14 (2020), p. 141103. DOI: `10.1103/PhysRevLett.125.141103`. arXiv: `2004.00846 [astro-ph.HE]`.

[284] I. Bombaci, A. Drago, D. Logoteta, G. Pagliara, and I. Vidaña. "Was GW190814 a Black Hole–Strange Quark Star System?" In: *Phys. Rev. Lett.* 126.16 (2021), p. 162702. DOI: `10.1103/PhysRevLett.126.162702`. arXiv: `2010.01509 [nucl-th]`.

[285] Michael Buballa. "NJL model analysis of quark matter at large density". In: *Phys. Rept.* 407 (2005), pp. 205–376. DOI: `10.1016/j.physrep.2004.11.004`. arXiv: `hep-ph/0402234`.

[286] Mark G. Alford, Sophia Han, and Madappa Prakash. "Generic conditions for stable hybrid stars". In: *Phys. Rev. D* 88.8 (2013), p. 083013. DOI: `10.1103/PhysRevD.88.083013`. arXiv: `1302.4732 [astro-ph.SR]`.

[287] Larry McLerran and Robert D. Pisarski. "Phases of cold, dense quarks at large N(c)". In: *Nucl. Phys. A* 796 (2007), pp. 83–100. DOI: `10.1016/j.nuclphysa.2007.08.013`. arXiv: `0706.2191 [hep-ph]`.

[288] Larry McLerran and Sanjay Reddy. "Quarkyonic Matter and Neutron Stars". In: *Phys. Rev. Lett.* 122.12 (2019), p. 122701. DOI: `10.1103/PhysRevLett.122.122701`. arXiv: `1811.12503 [nucl-th]`.

[289] J. Margueron, H. Hansen, P. Proust, and G. Chanfray. "Quarkyonic stars with isospin-flavor asymmetry". In: *Phys. Rev. C* 104.5 (2021), p. 055803. DOI: `10.1103/PhysRevC.104.055803`. arXiv: `2103.10209 [nucl-th]`.

[290] Sophia Han and Madappa Prakash. "On the Minimum Radius of Very Massive Neutron Stars". In: *Astrophys. J.* 899.2 (2020), p. 164. DOI: `10.3847/1538-4357/aba3c7`. arXiv: `2006.02207 [astro-ph.HE]`.

[291] Norman K. Glendenning. "First order phase transitions with more than one conserved charge: Consequences for neutron stars". In: *Phys. Rev. D* 46 (1992), pp. 1274–1287. DOI: `10.1103/PhysRevD.46.1274`.

[292] Marcus B. Pinto, Volker Koch, and Jorgen Randrup. "The Surface Tension of Quark Matter in a Geometrical Approach". In: *Phys. Rev. C* 86 (2012), p. 025203. DOI: `10.1103/PhysRevC.86.025203`. arXiv: `1207.5186 [hep-ph]`.

[293] K. Maslov, N. Yasutake, A. Ayriyan, D. Blaschke, H. Grigorian, T. Maruyama, T. Tatsumi, and D. N. Voskresensky. "Hybrid equation of state with pasta phases and third family of compact stars". In: *Phys. Rev. C* 100.2 (2019), p. 025802. DOI: `10.1103/PhysRevC.100.025802`. arXiv: `1812.11889 [nucl-th]`.

[294] Tianqi Zhao and James M. Lattimer. "Quarkyonic Matter Equation of State in Beta-Equilibrium". In: *Phys. Rev. D* 102.2 (2020), p. 023021. DOI: `10.1103/PhysRevD.102.023021`. arXiv: `2004.08293 [astro-ph.HE]`.

[295] Yong-Liang Ma and Mannque Rho. "Topology change, emergent symmetries and compact star matter". In: *AAPPS Bull.* 31.1 (2021), p. 16. DOI: `10.1007/s43673-021-00016-1`. arXiv: `2103.00744 [nucl-th]`.

[296] J. I. Kapusta and T. Welle. "Neutron stars with a crossover equation of state". In: *Phys. Rev. C* 104.1 (2021), p. L012801. DOI: `10.1103/PhysRevC.104.L012801`. arXiv: `2103.16633 [nucl-th]`.

[297] Wen-Jie Xie and Bao-An Li. "Bayesian inference of the dense-matter equation of state encapsulating a first-order hadron-quark phase transition from observables of canonical neutron stars". In: *Phys. Rev. C* 103.3 (2021), p. 035802. DOI: `10.1103/PhysRevC.103.035802`. arXiv: `2009.13653 [nucl-th]`.

[298] Mateusz Cierniak and David Blaschke. "Hybrid neutron stars in the mass-radius diagram". In: *Astron. Nachr.* 342.5 (2021), pp. 819–825. DOI: `10.1002/asna.202114000`. arXiv: `2106.06986 [nucl-th]`.

[299] J. G. Martinez, K. Stovall, P. C. C. Freire, J. S. Deneva, F. A. Jenet, M. A. McLaughlin, M. Bagchi, S. D. Bates, and A. Ridolfi. "Pulsar J0453+1559: A Double Neutron Star System with a Large Mass Asymmetry". In: *Astrophys. J.* 812.2 (2015), p. 143. DOI: `10.1088/0004-637X/812/2/143`. arXiv: `1509.08805 [astro-ph.HE]`.

[300] Christian Drischler, Sophia Han, James M. Lattimer, Madappa Prakash, Sanjay Reddy, and Tianqi Zhao. "Limiting masses and radii of neutron stars and their implications". In: *Phys. Rev. C* 103.4 (2021), p. 045808. DOI: 10.1103/PhysRevC.103.045808. arXiv: 2009.06441 [nucl-th].

[301] Mark Alford, Matt Braby, M.W. Paris, and Sanjay Reddy. "Hybrid stars that masquerade as neutron stars". In: *Astrophys. J.* 629 (2005), pp. 969–978. DOI: 10.1086/430902. arXiv: nucl-th/0411016.

[302] Jan-Erik Christian and Jürgen Schaffner-Bielich. "Twin Stars and the Stiffness of the Nuclear Equation of State: Ruling Out Strong Phase Transitions below $1.7n_0$ with the New NICER Radius Measurements". In: *Astrophys. J. Lett.* 894.1 (2020), p. L8. DOI: 10.3847/2041-8213/ab8af4. arXiv: 1912.09809 [astro-ph.HE].

[303] Jan-Erik Christian, Andreas Zacchi, and Jürgen Schaffner-Bielich. "Signals in the tidal deformability for phase transitions in compact stars with constraints from GW170817". In: *Phys. Rev. D* 99.2 (2019), p. 023009. DOI: 10.1103/PhysRevD.99.023009. arXiv: 1809.03333 [astro-ph.HE].

[304] David Blaschke, Hovik Grigorian, and Gerd Röpke. "Chirally improved quark Pauli blocking in nuclear matter and applications to quark deconfinement in neutron stars". In: *Particles* 3.2 (2020), pp. 477–499. DOI: 10.3390/particles3020033. arXiv: 2005.10218 [nucl-th].

[305] E. Chabanat, J. Meyer, P. Bonche, R. Schaeffer, and P. Haensel. "A Skyrme parametrization from subnuclear to neutron star densities". In: *Nucl. Phys. A* 627 (1997), pp. 710–746. DOI: 10.1016/S0375-9474(97)00596-4.

[306] Soumi De, Daniel Finstad, James M. Lattimer, Duncan A. Brown, Edo Berger, and Christopher M. Biwer. "Tidal Deformabilities and Radii of Neutron Stars from the Observation of GW170817". In: *Phys. Rev. Lett.* 121.9 (2018). [Erratum: Phys.Rev.Lett. 121, 259902 (2018)], p. 091102. DOI: 10.1103/PhysRevLett.121.091102. arXiv: 1804.08583 [astro-ph.HE].

[307] R. Abbott et al. "GW190814: Gravitational Waves from the Coalescence of a 23 Solar Mass Black Hole with a 2.6 Solar Mass Compact Object". In: *Astrophys. J. Lett.* 896.2 (2020), p. L44. DOI: 10.3847/2041-8213/ab960f. arXiv: 2006.12611 [astro-ph.HE].

[308] Ingo Tews, Peter T. H. Pang, Tim Dietrich, Michael W. Coughlin, Sarah Antier, Mattia Bulla, Jack Heinzel, and Lina Issa. "On the Nature of GW190814 and Its Impact on the Understanding of Supranuclear Matter". In: *Astrophys. J. Lett.* 908.1 (2021), p. L1. DOI: 10.3847/2041-8213/abdaae. arXiv: 2007.06057 [astro-ph.HE].

[309] E. Epelbaum, H.-W. Hammer, and Ulf-G. Meißner. "Modern Theory of Nuclear Forces". In: *Rev. Mod. Phys.* 81 (2009), pp. 1773–1825. DOI: 10.1103/RevModPhys.81.1773. arXiv: 0811.1338 [nucl-th].

[310] R. Machleidt and D. R. Entem. "Chiral effective field theory and nuclear forces". In: *Phys. Rept.* 503 (2011), pp. 1–75. DOI: 10.1016/j.physrep.2011.02.001. arXiv: 1105.2919 [nucl-th].

[311] Reed Essick, Ingo Tews, Philippe Landry, and Achim Schwenk. “Astrophysical Constraints on the Symmetry Energy and the Neutron Skin of Pb208 with Minimal Modeling Assumptions”. In: *Phys. Rev. Lett.* 127.19 (2021), p. 192701. DOI: 10.1103/PhysRevLett.127.192701. arXiv: 2102.10074 [nucl-th].

[312] S. Huth et al. “Constraining Neutron-Star Matter with Microscopic and Macroscopic Collisions”. In: (July 2021). arXiv: 2107.06229 [nucl-th].

[313] Elias R. Most, Anton Motornenko, Jan Steinheimer, Veronica Dexheimer, Matthias Hanauske, Luciano Rezzolla, and Horst Stoecker. “Probing neutron-star matter in the lab: connecting binary mergers to heavy-ion collisions”. In: (Jan. 2022). arXiv: 2201.13150 [nucl-th].

[314] Andreas Bauswein, Oliver Just, Hans-Thomas Janka, and Nikolaos Stergioulas. “Neutron-star radius constraints from GW170817 and future detections”. In: *Astrophys. J.* 850.2 (2017), p. L34. DOI: 10.3847/2041-8213/aa9994. arXiv: 1710.06843 [astro-ph.HE].

[315] Ingo Tews. “Spectrum of shear modes in the neutron-star crust: Estimating the nuclear-physics uncertainties”. In: *Phys. Rev. C* 95.1 (2017), p. 015803. DOI: 10.1103/PhysRevC.95.015803. arXiv: 1607.06998 [nucl-th].

[316] G. Raaijmakers, S. K. Greif, K. Hebeler, T. Hinderer, S. Nissanke, A. Schwenk, T. E. Riley, A. L. Watts, J. M. Lattimer, and W. C. G. Ho. “Constraints on the Dense Matter Equation of State and Neutron Star Properties from NICER’s Mass-Radius Estimate of PSR J0740+6620 and Multimessenger Observations”. In: *Astrophys. J. Lett.* 918.2 (2021), p. L29. DOI: 10.3847/2041-8213/ac089a. arXiv: 2105.06981 [astro-ph.HE].

[317] Rahul Somasundaram, Ingo Tews, and Jérôme Margueron. “Investigating Signatures of Phase Transitions in Neutron-Star Cores”. In: (Dec. 2021). arXiv: 2112.08157 [nucl-th].

[318] Tyler Gorda, Aleksi Kurkela, Paul Romatschke, Matias Säppi, and Aleksi Vuorinen. “Next-to-Next-to-Next-to-Leading Order Pressure of Cold Quark Matter: Leading Logarithm”. In: *Phys. Rev. Lett.* 121.20 (2018), p. 202701. DOI: 10.1103/PhysRevLett.121.202701. arXiv: 1807.04120 [hep-ph].

[319] Tyler Gorda, Aleksi Kurkela, Risto Paatelainen, Saga Säppi, and Aleksi Vuorinen. “Soft Interactions in Cold Quark Matter”. In: *Phys. Rev. Lett.* 127.16 (2021), p. 162003. DOI: 10.1103/PhysRevLett.127.162003. arXiv: 2103.05658 [hep-ph].

[320] Aleksi Kurkela, Eduardo S. Fraga, Jürgen Schaffner-Bielich, and Aleksi Vuorinen. “Constraining neutron star matter with Quantum Chromodynamics”. In: *Astrophys. J.* 789 (2014), p. 127. DOI: 10.1088/0004-637X/789/2/127. arXiv: 1402.6618 [astro-ph.HE].

[321] Oleg Komoltsev and Aleksi Kurkela. “How Perturbative QCD Constrains the Equation of State at Neutron-Star Densities”. In: *Phys. Rev. Lett.* 128.20 (2022), p. 202701. DOI: 10.1103/PhysRevLett.128.202701. arXiv: 2111.05350 [nucl-th].

[322] Tyler Gorda, Oleg Komoltsev, and Aleksi Kurkela. “Ab-initio QCD calculations impact the inference of the neutron-star-matter equation of state”. In: (Apr. 2022). arXiv: `2204.11877 [nucl-th]`.

[323] Hung Tan, Veronica Dexheimer, Jacquelyn Noronha-Hostler, and Nicolas Yunes. “Finding Structure in the Speed of Sound of Supranuclear Matter from Binary Love Relations”. In: *Phys. Rev. Lett.* 128.16 (2022), p. 161101. DOI: `10.1103/PhysRevLett.128.161101`. arXiv: `2111.10260 [astro-ph.HE]`.

[324] Isaac Legred, Katerina Chatziioannou, Reed Essick, and Philippe Landry. “Implicit correlations within phenomenological parametric models of the neutron star equation of state”. In: *Phys. Rev. D* 105.4 (2022), p. 043016. DOI: `10.1103/PhysRevD.105.043016`. arXiv: `2201.06791 [astro-ph.HE]`.

[325] Tim Dietrich, Michael W. Coughlin, Peter T. H. Pang, Mattia Bulla, Jack Heinzel, Lina Issa, Ingo Tews, and Sarah Antier. “New Constraints on the Supranuclear Equation of State and the Hubble Constant from Nuclear Physics – Multi-Messenger Astronomy”. In: *Science* 370.6523 (Feb. 2020), pp. 1450–1453. DOI: `10.1126/science.abb4317`. arXiv: `2002.11355 [astro-ph.HE]`.

[326] Reed Essick, Ingo Tews, Philippe Landry, Sanjay Reddy, and Daniel E. Holz. “Direct Astrophysical Tests of Chiral Effective Field Theory at Supranuclear Densities”. In: *Phys. Rev. C* 102.5 (2020), p. 055803. DOI: `10.1103/PhysRevC.102.055803`. arXiv: `2004.07744 [astro-ph.HE]`.